Space Programs Summary 37-64, Vol. II

The Deep Space Network

For the Period June 1 to July 31, 1970

JET PROPULSION LABORATORY
CALIFORNIA INSTITUTE OF TECHNOLOGY
PASADENA, CALIFORNIA

August 31, 1970

NATIONAL AERONAUTICS AND SPACE ADMINISTRATION

Space Programs Summary 37-64, Vol. II

The Deep Space Network

For the Period June 1 to July 31, 1970

JET PROPULSION LABORATORY
CALIFORNIA INSTITUTE OF TECHNOLOGY
PASADENA, CALIFORNIA

August 31, 1970

SPACE PROGRAMS SUMMARY 37-64, VOL. II

Prepared Under Contract No. NAS 7-100
National Aeronautics and Space Administration

Preface

The Space Programs Summary is a multivolume, bimonthly publication that presents a review of technical information resulting from current engineering and scientific work performed, or managed, by the Jet Propulsion Laboratory for the National Aeronautics and Space Administration. The Space Programs Summary is currently composed of four volumes:

Vol. I. *Flight Projects* (Unclassified)

Vol. II. *The Deep Space Network* (Unclassified)

Vol. III. *Supporting Research and Advanced Development* (Unclassified)

Vol. IV. *Flight Projects and Supporting Research and Advanced Development* (Confidential)

Foreword

Volume II of the Space Programs Summary reports the results of work performed by the Deep Space Network (DSN). Information is presented, as appropriate, in the following categories:

Introduction
- Description of the DSN
- Description of DSN Systems

Mission Support
- Interplanetary Flight Projects
- Planetary Flight Projects
- Manned Space Flight Project
- Advanced Flight Projects

Advanced Engineering
- Tracking and Navigational Accuracy Analysis
- Communications Systems Research
- Communications Elements Research
- Supporting Research and Technology

Development and Implementation
- Space Flight Operations Facility Development
- Ground Communications Facility Development
- Deep Space Instrumentation Facility Development
- DSN Project and System Development

Operations and Facilities
- DSN Operations
- Space Flight Operations Facility Operations
- Ground Communications Facility Operations
- Deep Space Instrumentation Facility Operations
- Facility Engineering

In each issue, the section entitled "Description of DSN Systems" reports the current configuration of one of the six DSN systems (tracking, telemetry, command, monitoring, simulation, and operations control). The fundamental research carried out in support of the DSN is reported in Vol. III.

Contents

I. Introduction 1

A. Description of the DSN 1

II. Mission Support 4

A. Planetary Flight Projects 4

1. *Mariner* Mars 1971 Mission Support
R. P. Laeser 4

B. Manned Space Flight Project 7

1. *Apollo* Mission Support
R. B. Hartley 7

III. Advanced Engineering 12

A. Tracking and Navigational Accuracy Analysis 12

1. Introduction
T. W. Hamilton and D. W. Trask 12

2. Charged-Particle Calibration System Analysis
B. D. Mulhall 13

3. The Ionospheric Electron Content as Determined From Faraday Rotation Measurements of an Earth Satellite and Deep-Space Probe
B. D. Mulhall and C. T. Stelzried 21

4. Evaluation of the Ionospheric Model
B. D. Mulhall 25

B. Communications Systems Research 27

1. Digital Telemetry and Command: Mean-Square Error and Bias of Phase Estimator for the JPL Sequential Ranging System
J. Molinder 27

2. Digital Telemetry and Command: The Asymptotic Complexity of the Green Decoding Procedure
J. E. Savage 29

3. Digital Telemetry and Command: The Effective Computing Power of Computer Memory
J. E. Savage 30

4. Digital Acquisition and Detection: Minimum Switching Network for Generating the Weight, in Binary Notation, of a Binary Vector
T. O. Anderson 33

5. Digital Acquisition and Detection: Numerical Interactive Controller
S. Brokl 35

Contents (contd)

6. Digital Acquisition and Detection: Solution of a Toeplitz Set of Linear Homogeneous Equations
S. Zohar 38

7. Information Systems: Performance of Short Constraint Length Convolutional Codes and a Heuristic Code-Construction Algorithm
J. W. Layland 41

8. Information Systems: Synchronizability of Convolutional Codes
J. W. Layland 44

9. Information Systems: Multiple-Mission Sequential Decoder—Comparing Performance Among Three Rate $1/2$, $K = 32$ Codes
J. W. Layland 50

10. Information Systems: Multiple-Mission Sequential Decoder Interface Buffer
A. Zygielbaum 53

11. Frequency Generation and Control: The Measurement of Phase Jitter
R. Meyer and A. Sward 55

12. Frequency Generation and Control: Computer-Assisted Acquisition
K. Schreder 59

13. Loop Stress Diminution
R. M. Goldstein, R. F. Emerson, W. L. Sjogren, and L. Sydnor 61

C. Communications Elements Research 67

1. Tracking and Data Acquisition Elements Research: Improved RF Calibration Techniques—Precision Compact Rotary Vane Attenuator
T. Y. Otoshi 67

2. Tracking and Data Acquisition Elements Research: Improved RF Calibration Techniques—System Operating Noise Temperature Calibrations of Low Noise Cones
M. S. Reid and C. T. Stelzried 69

D. Supporting Research and Technology 70

1. DSS 13 Operations
E. B. Jackson 70

2. Planetary Ranging Demodulator
D. W. Brown 71

3. Thirty-Degree Reflector Mockup Study: Comparisons of Measured and Predicted Deflections
R. Levy 74

4. Welded Joint Integrity Study
V. Lobb and W. Kissane 79

Contents (contd)

IV. Development and Implementation 87

A. DSIF Development 87

1. DSIF Monitor System Development
F. B. Leppla 87

2. Simulation Conversion Assembly
E. Garcia 88

3. Transmitter Phase Modulation as a Result of Beam Voltage Ripple
C. P. Wiggins, E. B. Jackson, and T. W. Rathbun 96

4. Antenna Acceleration: Impact Damage Modifications
V. Lobb 97

5. Clock-Sync Antenna Installation at the U.S. Naval Observatory
W. Kissane 97

6. DSS 51 Antenna Mechanical Subsystem Upgrade
J. Carpenter, V. Lobb, A. Nicula, and D. Nelson 98

V. Operations and Facilities 105

A. DSN Operations 105

1. Network Allocation Schedules
D. G. Tustin 105

B. SFOF Operations 107

1. SFOF *Mariner* Mars 1971 Mission Support Area
B. M. Hayes 107

I. Introduction

A. Description of the DSN

The Deep Space Network (DSN), established by the NASA Office of Tracking and Data Acquisition under the system management and technical direction of JPL, is designed for two-way communications with unmanned spacecraft traveling approximately 10,000 mi from earth to planetary distances. It supports, or has supported, the following NASA deep space exploration projects: *Ranger*, *Surveyor*, *Mariner* Venus 1962, *Mariner* Mars 1964, *Mariner* Venus 67, *Mariner* Mars 1969, *Mariner* Mars 1971 (JPL); *Lunar Orbiter* and *Viking* (Langley Research Center); *Pioneer* (Ames Research Center); *Helios* (West Germany); and *Apollo* (Manned Spacecraft Center), to supplement the Manned Space Flight Network (MSFN).

The DSN is distinct from other NASA networks such as the MSFN, which has primary responsibility for tracking the manned spacecraft of the *Apollo* Project, and the Space Tracking and Data Acquisition Network (STADAN), which tracks earth-orbiting scientific and communications satellites. With no future unmanned lunar spacecraft presently planned, the primary objective of the DSN is to continue its support of planetary and interplanetary flight projects.

To support flight projects, the DSN simultaneously performs advanced engineering on components and systems, integrates proven equipment and methods into the network,[1] and provides direct support of each project through that project's Tracking and Data System. This management element and the project's Mission Operations personnel are responsible for the design and operation of the data, software, and operations systems required for the conduct of flight operations. The organization and procedures necessary to carry out these activities are described in SPS 37-50, Vol. II, pp. 15–17.

By tracking the spacecraft, the DSN is involved in the following data types:

(1) *Metric:* generate angles, one- and two-way doppler, and range.

(2) *Telemetry:* receive, record, and retransmit engineering and scientific data.

(3) *Command:* send coded signals to the spacecraft to activate equipment to initiate spacecraft functions.

[1]When a new piece of equipment or new method has been accepted for integration into the network, it is classed as Goldstone duplicate standard (GSDS), thus standardizing the design and operation of identical items throughout the network.

The DSN operation is characterized by six DSN systems: (1) tracking, (2) telemetry, (3) command, (4) monitoring, (5) simulation, and (6) operations control.

The DSN can be characterized as being comprised of three facilities: the Deep Space Instrumentation Facility (DSIF), the Ground Communications Facility (GCF), and the Space Flight Operations Facility (SFOF).

1. Deep Space Instrumentation Facility

a. Tracking and data acquisition facilities. A worldwide set of deep space stations (DSSs) with large antennas, low-noise phase-lock receiving systems, and high-power transmitters provide radio communications with spacecraft. The DSSs and the deep space communications complexes (DSCCs) they comprise are given in Table 1.

Radio contact with a spacecraft usually begins when the spacecraft is on the launch vehicle at Cape Kennedy, and it is maintained throughout the mission. The early part of the trajectory is covered by selected network stations of the Air Force Eastern Test Range (AFETR) and the MSFN of the Goddard Space Flight Center.[2] Normally, two-way communications are established between the spacecraft and the DSN within 30 min after the spacecraft has been injected into lunar, planetary, or interplanetary flight. A compatibility test station at Cape Kennedy (discussed later) monitors the spacecraft continuously during the launch phase until it passes over the local horizon. The deep space phase begins with acquisition by either DSS 51, 41, or 42. These and the remaining DSSs given in Table 1 provide radio communications to the end of the flight.

To enable continuous radio contact with spacecraft, the DSSs are located approximately 120 deg apart in longitude; thus, a spacecraft in deep space flight is always within the field-of-view of at least one DSS, and for several hours each day may be seen by two DSSs. Furthermore, since most spacecraft on deep space missions travel within 30 deg of the equatorial plane, the DSSs are located within latitudes of 45 deg north or south of the equator. All DSSs operate at S-band frequencies: 2110–2120 MHz for earth-to-spacecraft transmission and 2290–2300 MHz for spacecraft-to-earth transmission.

To provide sufficient tracking capability to enable useful data returns from around the planets and from the edge of the solar system, a 210-ft-diam-antenna network will be required. Two additional 210-ft-diam-antenna DSSs are under construction at Madrid and Canberra, which will operate in conjunction with DSS 14 to provide this capability. These stations are scheduled to be operational by early 1973.

b. Compatibility test facilities. In 1959, a mobile L-band compatibility test station was established at Cape Kennedy to verify flight-spacecraft–DSN compatibility prior to the launch of the *Ranger* and *Mariner* Venus 1962 spacecraft. Experience revealed the need for a permanent facility at Cape Kennedy for this function. An S-band compatibility test station with a 4-ft-diam antenna became operational in 1965. In addition to supporting the preflight compatibility tests, this station monitors the spacecraft continuously during the launch phase until it passes over the local horizon.

Spacecraft telecommunications compatibility in the design and prototype development phases was formerly verified by tests at the Goldstone DSCC. To provide a more economical means for conducting such work and because of the increasing use of multiple-mission telemetry and command equipment by the DSN, a compatibility test area (CTA) was established at JPL in 1968. In all essential characteristics, the configuration of this facility is identical to that of the 85- and 210-ft-diam-antenna stations.

The JPL CTA is used during spacecraft system tests to establish the compatibility with the DSN of the proof test model and development models of spacecraft, and the Cape Kennedy compatibility test station is used for final flight spacecraft compatibility validation testing prior to launch.

2. Ground Communications Facility

The GCF, using, in part, facilities of the worldwide NASA Communications Network (NASCOM),[3] provides voice, high-speed data, and teletype communications between the SFOF and all DSSs, except those of the Goldstone DSCC. Communications between the Goldstone DSCC and the SFOF are provided by a microwave link leased from a common carrier. Early missions were

[2]The 30-ft-diam-antenna station established by the DSN on Ascension Island during 1965 to act in conjunction with the MSFN orbital support 30-ft-diam-antenna station was transferred to the MSFN in July 1968.

[3]Managed and directed by the Goddard Space Flight Center.

Table 1. Tracking and data acquisition stations of the DSN

DSCC	Location	DSS	DSS serial designation	Antenna		Year of initial operation
				Diameter, ft	Type of mounting	
Goldstone	California	Pioneer	11	85	Polar	1958
		Echo[a]	12	85	Polar	1962
		(Venus)[b]	13	(85)	(Az–El)	(1962)
		Mars	14	210	Az-El	1966
Canberra	Australia	Woomera[c]	41	85	Polar	1960
		Tidbinbilla[c]	42	85	Polar	1965
—	South Africa	Johannesburg[c]	51	85	Polar	1961[d]
Madrid	Spain	Robledo[c]	61	85	Polar	1965
		Cebreros[c]	62	85	Polar	1967

[a]Established in 1959 to support NASA's *Echo* Project to explore the feasibility of transcontinental two-way communications using a passive satellite; DSS 12 was originally configured with an 85-ft-diam az–el-mounted antenna. In 1962, when the need arose for a second 85-ft-diam polar-mounted antenna at the Goldstone site, the 85-ft-diam az–el-mounted antenna was moved to DSS 13, and an 85-ft-diam polar-mounted antenna was constructed at DSS 12.

[b]A research-and-development facility used for ground-based radio science experiments, and to demonstrate the feasibility of new equipment and methods to be integrated into the operational network. Besides the 85-ft-diam az–el-mounted anenna, DSS 13 has a 30-ft-diam az–el-mounted antenna that is used for the transmission of lunar radar time signals to all stations in the network.

[c]Staffed and operated by government agencies of the respective countries.

[d]Between 1958 and 1962, a temporary mobile tracking station was located near Johannesburg to provide L-band communications required by the Ranger and *Mariner* Venus 1962 spacecraft.

supported with voice and teletype circuits only, but increased data rates necessitated the use of wide-band circuits from all DSSs.

3. Space Flight Operations Facility

Network and mission control functions are performed at the SFOF at JPL. (Prior to 1964, these functions were performed in temporary facilities at JPL.) The SFOF receives data from all DSSs and processes that information required by the flight project to conduct mission operations. The following services are provided: (1) real-time processing and display of metric data; (2) real-time and non-real-time processing and display of telemetry data; (3) simulation of flight operations; (4) near-real-time evaluation of DSN performance; (5) operations control, and status and operational data display; and (6) general support such as internal communications by telephone, intercom, public address, closed-circuit TV, documentation, and reproduction of data packages. Master data records of science data received from spacecraft are generated. Technical areas are provided for flight project personnel who analyze spacecraft performance, trajectories, and generation of commands.

The SFOF is equipped to support many spacecraft in flight and those under test in preparation for flight. Over a 24-h period in 1967, as many as eight in-flight spacecraft or operational-readiness tests for flight were supported by the SFOF.

II. Mission Support

A. Planetary Flight Projects

1. *Mariner* Mars 1971 Mission Support, R. P. Laeser

a. Introduction. In order to determine the readiness of the DSN to support a complex pair of missions (i.e., the *Mariner* Mars 1971 missions), a thorough test program is required.

Proposition 1: Thorough test programs require long periods of time to accomplish.

Proposition 2: Because some key developments will be delivered later than required, there won't be as much test time as required.

These two opposed propositions are both true for *Mariner* Mars 1971 support. This article will study the constraints imposed on the program and the planned solution.

b. Constraint 1: Project requirements. Considering a May 5, 1971 launch readiness date and a November 14, 1971 Mars orbit insertion date for the first spacecraft, the Project requirements call for the following performance demonstrations:

(1) All capabilities to be used for transit support by January 1, 1971.

(2) Essential orbital operations support capabilities by March 1, 1971.

(3) All orbital operations support capabilities by July 1, 1971.

On these dates, the delivered capabilities are to support launch–cruise training, verify a minimal orbital support capability before launch, and support orbital operations training, respectively. One additional requirement that applies to each of the three dates is that the DSN integrate mission-dependent elements (Project-supplied as well as DSN-supplied), and that the performance demonstration include these mission-dependent elements.

c. Constraint 2: DSN testing philosophy. As the Network Systems concept evolves, it is natural that a corresponding testing philosophy should evolve. This philosophy splits testing into (1) the testing and verification of multimission systems, and (2) the testing and verification of mission-dependent configurations that include mission-dependent elements. Generally, the former is the responsibility of the implementation and system engineering organizations, and the latter is the responsibility of the project interface organization. In both cases, support for the actual conduct of the tests is provided by the DSN operations organization.

Specifically, the multimission Network Systems are to be tested and verified by the Network System Engineer prior to the operational use of any new capability that may affect the performance of the system. The System Engineer expects, as a prerequisite, the implementing facility to fully test the new capabilities at the assembly, subsystem, and system levels.

The mission-dependent Network System configurations are to be tested by the DSN Project Engineer. He also tests all configured systems simultaneously under full load conditions. The DSN Project Engineer expects, as a prerequisite, the implementing facilities (or interfacing facilities in the case of Project-supplied hardware or software) to integrate mission-dependent hardware or software and to conduct sufficient subsystem and system testing.

d. Constraint 3: DSN training. It is desired that the DSN operations organization be fully trained in the operation of all hardware and software, and in all procedures to be used for mission support, prior to the start of Project training.

e. Constraint 4: implementation schedules. At this time, the implementation of two key elements in the system design have been split into deliverable phases so that minimum capabilities will be available on the required dates: telemetry and command processor (TCP) software and the SFOF Mark IIIA Central Processing System (IBM 360/75s). The version of the TCP program available at supporting DSSs will not have teletype backup capabilities; if possible, these capabilities will be incorporated into a subsequent version of the TCP program. In addition, for DSS 14, a special TCP program that processes two engineering streams and one command stream will be on a separate schedule.

The 360/75 capabilities will be available in four deliverable models, each new model adding more capabilities. Table 1 summarizes the current plans for the contents of each model.

Several capabilities will be late and workarounds have been developed. For instance, the GCF High-Speed Data (HSD) System implementation at DSSs 51 and 71 will not

Table 1. IBM 360/75 phased capability summary

Model	Command system	Tracking system	Telemetry system	Monitor and operations control system
1	Generate and transmit messages from keyboard, cards, or comgen Perform most system control functions (except those below) No digital TV displays	Receive, process, and display DSN, MSFN, and AFETR formats Generate system data record–tape interface to Univac 1108 Compute and display pseudo-residuals High-speed predictions to DSS	Receive, log, sync, decommutate, convert to engineering units, alarm, and display (no digital TV) low-rate data	Batch process schedule and sequence of events and transmit to DSS Monitor processing and display (except below)
2	Add: Automatic enable generation Generate system data record TCP recall Digital TV display	Add: Electrical interface to Univac 1108 Data validation Digital TV display	Add: Tabular digital TV display Generate system data record for low-rate	Add: Real-time schedule of sequence of events Digital TV display
3	Add: Generate master data record More than one spacecraft at a time	Add: Pseudo-residual recall from system data record Real-time initialization of tracking data processor, predicts, and pseudo-residuals	Add: Generate master data record for low-rate Format request box for digital TV Digital TV graphics Process high-rate data except video	Add: Generate system data record Recall and display from storage Expanded sequence of events
4	Add: Nothing	Add: DSIF tracking subsystem HSD interface Tracking system analytic calibration Analysis of pseudo-residuals	Add: High-rate master data record Video processing Mission TV system interface	Add: Nothing

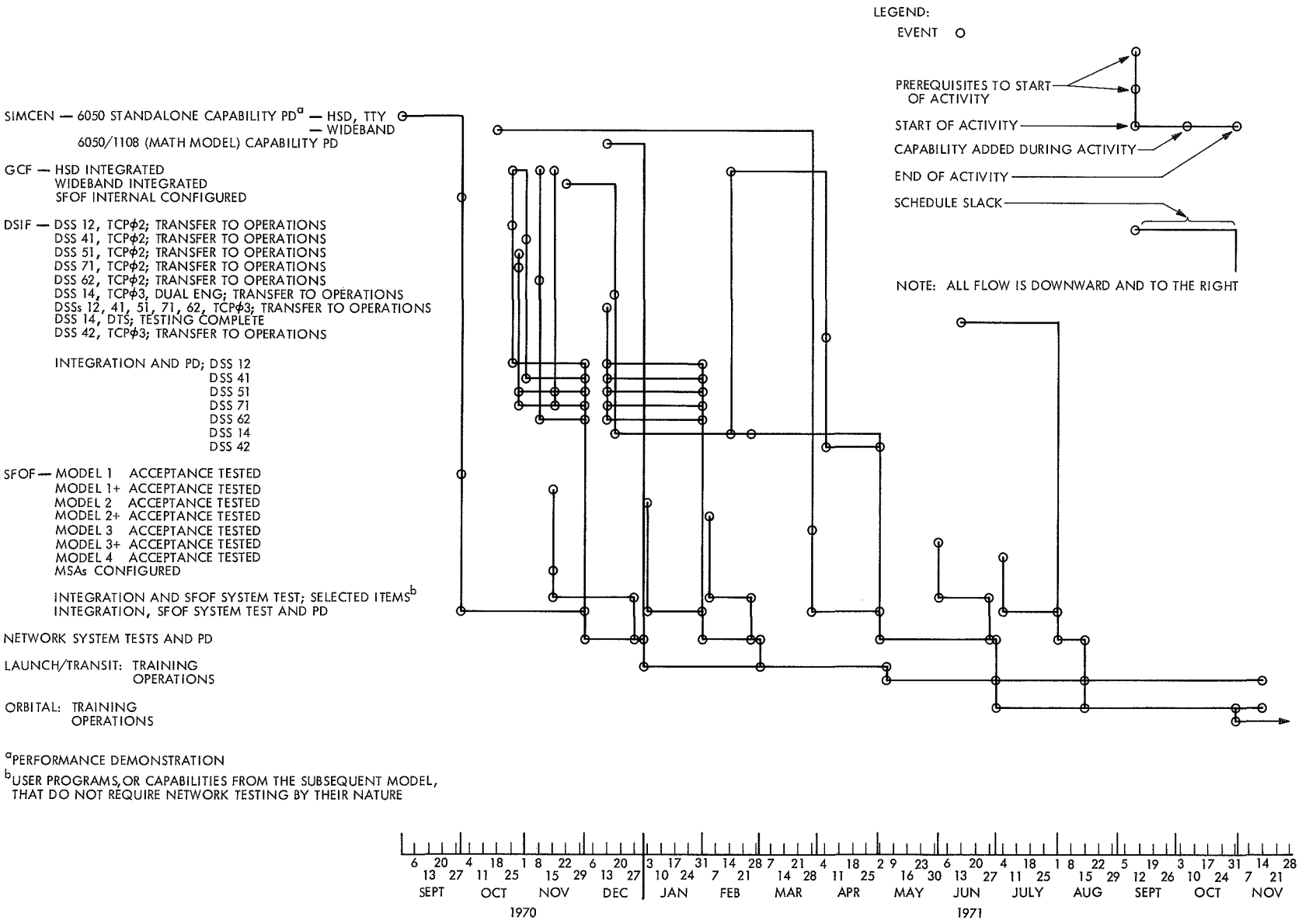

Fig. 1. Schedule for activity leading to *Mariner* Mars 1971 operations

be complete until two weeks after DSS integration has been initiated; however, initial use of the old HSD capability and DSS and GCF cooperation during the new HSD installation should bypass the problem.

The aspect of this constraint that may cause the most difficulty is the chance of schedule slippage of some key development. The test program must be flexible enough to cope with such schedule slippage.

f. A possible best-match solution. Figure 1 depicts a possible solution to best match all of the constraints; it is a combined flow plan and schedule showing all key activities and events from delivery of Network Facility elements through operational use for mission support. Figure 1 should be considered as a sample; similar actual schedules will be published by the DSN interface organization for *Mariner* Mars 1971. In general, Figure 1 represents current plans. The salient concepts are:

(1) Simulation "standalone" capability is demonstrated in time to support facility integration testing.

(2) Where possible, GCF capability is integrated before SFOF and DSIF integration testing starts, and, as a minimum, before the end of SFOF and DSIF integration testing.

(3) The SFOF integration and system testing plan is followed; i.e., all components (multimission, mission-dependent, and analysis programs) are (a) accepted for integration, (b) integrated, (c) facility system tested, and (d) turned over to the DSN for Network System tests. Four such sequences are planned, one for each model.

(4) For the SFOF, user programs or capabilities from a subsequent model which, by their nature, do not require Network System testing are allowed to follow a slightly delayed SFOF integration and system testing schedule. They are merged into the scheme at the Network Performance Demonstration.

(5) DSIF integration and system testing follows standard procedure, with DSSs and capabilities that are required only for orbital operations support being tested at a later date.

(6) Four sets of Network System tests and performance demonstrations are planned, picking up phased-in facility capabilities. No distinction is made between multimission and mission-dependent Network testing since it is planned to combine the two activities. The DSN Project Engineer will control all tests, with the appropriate DSN System Engineer(s) acting as subcontroller(s). The DSN operations organization will actually conduct the tests.

(7) Training the DSN operations organization at the facility level will coincide with facility integration and system testing; at the Network level, it will coincide with the Network System testing.

(8) Capabilities, in general, will not be available for Project training and/or operations until Network System testing is complete.

(9) Simulation math-model capability will be demonstrated in time to support Project training.

B. Manned Space Flight Project

1. *Apollo* Mission Support, *R. B. Hartley*

a. Introduction. The DSN support provided to the MSFN for the first two manned lunar landing missions is described in SPS 37-59, Vol. II, pp. 27–32 and SPS 37-61, Vol. II, pp. 22–26. This article describes the support provided for the *Apollo 13* (AS-508) mission, the abortive attempt at a third manned lunar landing.

b. Mission description. Apollo 13 was the sixth manned *Apollo* mission flown aboard the three-stage *Saturn V* launch vehicle and carried astronauts James A. Lovell, Jr. (Commander), Thomas K. Mattingly III (Command Module Pilot), and Fred W. Haise, Jr. (Lunar Module Pilot). The mission goal was to land in the Fra Mauro uplands for a stay of 33 h, including two EVA (extra-vehicular activity) periods as for the *Apollo 12* mission. These plans were aborted, however, long before the spacecraft reached the vicinity of the moon.

Launch from Cape Kennedy Pad 39A occurred at 19:13:00.65 GMT on April 11, 1970, at a launch azimuth of 72.04 deg. Injection into translunar trajectory occurred midway through the second revolution in earth parking orbit with a 5-min, 57-s burn of the S-IVB stage engine. Following translunar injection, the Command/Service Module separated from the booster and docked with the unattended Lunar Module, extracting it from the S-IVB third-stage booster.

For the first time in *Apollo* history, the discarded S-IVB was directed toward an impact on the moon to generate seismic waves for the seismometer package left on the moon during the *Apollo 12* mission. Lunar impact occurred some 78 h after launch at 01:09:39 GMT on April 15 at lunar coordinates 2.4 deg S, 27.9 deg W, 74 mi from the *Apollo 12* seismometer. The impact velocity was 3280 ft/s,

creating an impulse equivalent to 10 tons of TNT. These data compare with the crash of the *Apollo 12* Lunar Module, which was 42 miles from the seismometer with an equivalent energy of one ton of TNT. The seismic waves recorded were of similar character, but the S-IVB impact waves were 20 to 30 times larger and lasted four times longer (approximately 4 h).

The accuracy of the translunar injection maneuver eliminated the need for Command/Service Module–Lunar Module midcourse correction 1, which had been planned for 11:41 GET (Ground Elapsed Time or time after launch). The spacecraft at this point was on a "free-return" trajectory; i.e., should all propulsion be lost, the spacecraft would swing around the moon and return to a normal re-entry into the earth's atmosphere. At 30:41 GET, midcourse correction 2 altered the spacecraft's free-return trajectory to a "hybrid" trajectory that would enable a saving of fuel for the lunar landing sequence. However, with a hybrid trajectory, loss of all propulsion would doom the spacecraft to miss the earth and enter perpetual solar orbit.

The mission continued nominally until 55:00 GET, when the crew entered the Lunar Module in order to check the pressure of the supercritical helium following premission indications of an anomalous heat-leak rate. After being satisfied that no problem existed, the crew was re-entering the Command Module when a loud bang was heard. The sound did not cause immediate anxiety because one of the Lunar Module systems often makes this same noise. However, warning signals soon indicated problems in the Service Module power subsystem, the first indication being at 55:55 GET (03:08 GMT on April 14). An apparent oxygen tank explosion forced the crew to shut down first one fuel cell, and then all three fuel cells, which left the Command Module with no electrical power and no oxygen. The crew then returned to the Lunar Module, powered up its systems, and prepared to use it as an emergency lifeboat for the remainder of the mission. From its complete shutdown at 58:40 GET until the re-entry phase, the Command Module was used for nothing but cold (38°F) sleeping quarters.

The unthinkable had happened—the entire capability of the Service Module, with all its many redundant systems, had been lost. All mission objectives except return to earth were abandoned. A quick analysis showed that the Lunar Module consumables (water, power, and oxygen) were barely adequate for the return trip. The critical problem was the hybrid trajectory and the lack of the normal Service Propulsion System of the Service Module. Accordingly, a motor burn of the Lunar Module descent engine at 61:30 GET successfully returned the spacecraft to a free-return trajectory.

The remainder of the mission consisted mainly of minimizing activity to reduce electrical power usage. Several additional orbit changes were conducted. About 2 h after passing behind the moon, a midcourse correction speeded up the spacecraft to decrease its transit time to earth by 10 h and enable the use of the original recovery area. Unfortunately, a small out-of-plane component created a trajectory that would have caused the spacecraft to enter the atmosphere improperly. This error was trimmed out by a small motor burn of 15 ft/s at 105:18 GET. The final orbit correction was conducted at 137:40 GET, only 5 h before entering the earth's atmosphere, and changed the entry flight-path angle. Shortly after this maneuver, the Service Module was jettisoned and photographs taken of the damage. The crew re-entered the Command Module, powered up its systems (using the re-entry batteries), and jettisoned the Lunar Module just 1 h before landing. Entry, splashdown, and recovery were all normal except for the deletion of all quarantine measures. The approximate event times for the *Apollo 13* mission are given in Table 2. The astronauts arrived aboard the *U.S.S. Iwo Jima*

Table 2. Approximate event times for *Apollo 13*

Event	GMT	GET
Launch	April 11, 19:13:00.65	0:00
Translunar injection	April 11, 21:49	2:36
Midcourse maneuver 2 (to "hybrid" trajectory)	April 13, 01:54	30:41
Begin Lunar Module checkout	April 14, 02:13	55:00
Service module explosion	April 14, 03:08	55:55
Lunar Module signal on	April 14, 05:10	57:57
All Command/Service Module fuel cells off	April 14, 05:11	57:58
Command/Service Module completely off	April 14, 05:53	58:40
Maneuver (to "free return" trajectory)	April 14, 08:43	61:30
Lunar occultation	April 15, 00:22	77:09
End lunar occultation	April 15, 00:46	77:33
S-IVB impact	April 15, 01:09:39	77:56:39
Maneuver ("speedup")	April 15, 02:41	79:28
Maneuver (trim)	April 16, 04:31	105:18
Maneuver (trim)	April 17, 12:53	137:40
Jettison Service Module	April 17, 13:23	138:10
Jettison Lunar Module	April 17, 16:43	141:30
Enter atmosphere	April 17, 17:54	142:41
Splashdown	April 17, 18:07:45	142:54:45

44 min after splashdown, thus ending mankind's first aborted manned deep space mission.

c. Requirements for DSN Support of Apollo 13

DSN/MSFN wing stations. As with previous *Apollo* missions, DSSs 11, 42, and 61 were committed to support *Apollo 13* under direct MSFN/MSC control starting at launch minus 2 wk through the end of the mission.

DSS 14. On previous missions, DSS 14 supported the *Apollo* mission exclusively for 6 or 7 days. With *Apollo 13*, this was not possible since the *Mariner* Mars 1969 Extended Operations mission was in its prime scientific phase and required DSS 14 support. A sharing schedule (Fig. 2) was developed by DSN Scheduling in an attempt to satisfy the critical requirements of both missions. This schedule was accepted by all parties.

Goldstone time synchronization. The MSFN required time synchronization between the various stations at Goldstone (DSS 14, DSS 11/MSFN wing, and *Apollo* Prime). The time synchronization was supplied in the same manner as on previous missions by transporting a Goldstone Standards Laboratory cesium clock to the various sites several times throughout the mission. A supplementary 1-pulse/s time tick accurate to 5μs was made available at the MSFN microwave interface at DSS 14. An additional request was received for the portable clock to be stationed within the DSS 11 MSFN wing for a 30-h period during lunar operations. The MSFN planned to conduct a series of experiments with a new hydrogen maser frequency standard and was concerned over a possible loss of absolute time reference. The DSN planned the support, and the necessary overtime was authorized. However, with the aborted mission, the plans were cancelled.

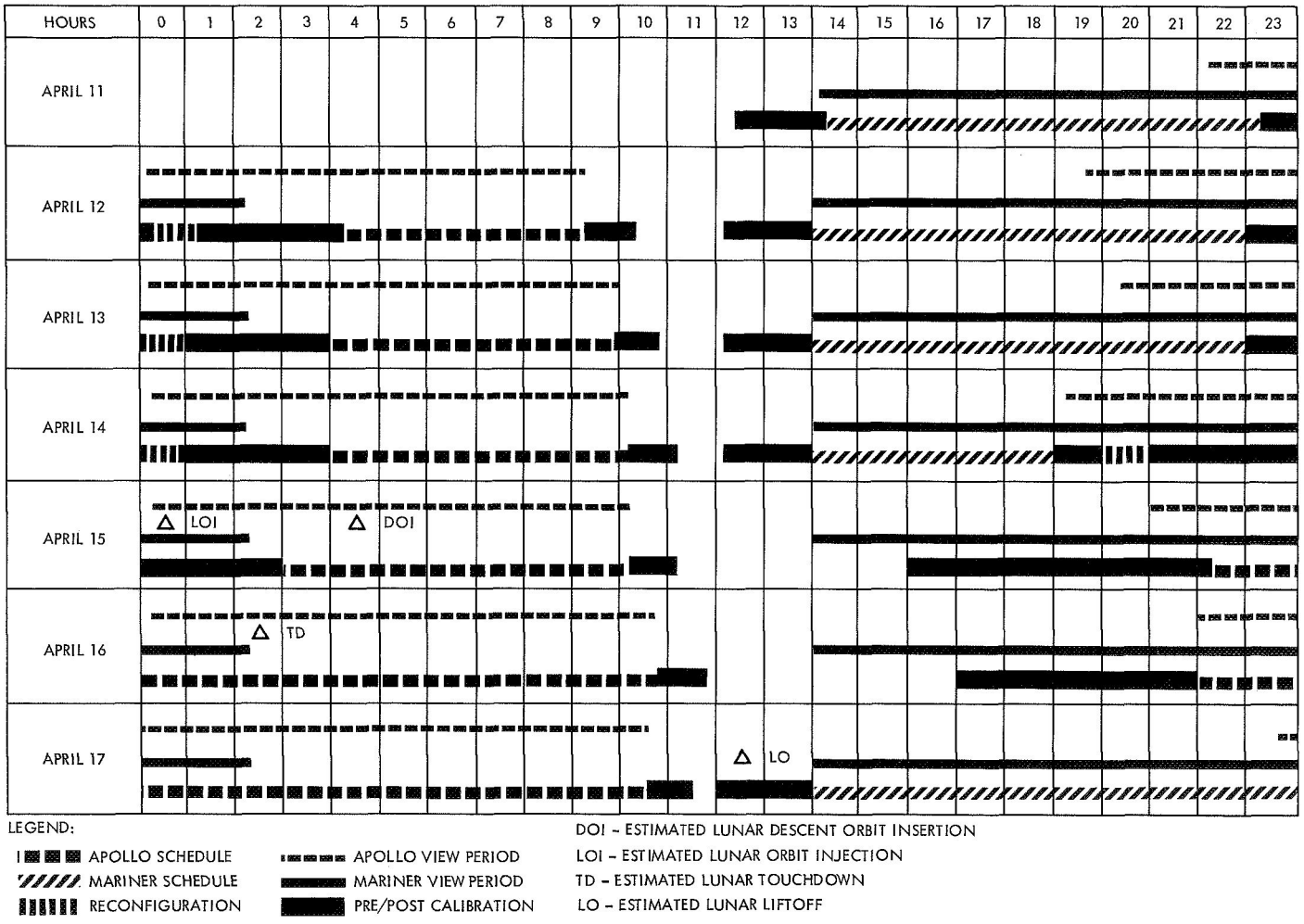

Fig. 2. DSS 14 schedule planned for *Apollo 13*

Precision doppler data. As part of a continuing study of lunar potential anomalies (mascons), DSS 14 was required to provide precision doppler recordings of the Command/Service Module during several low lunar orbits and of the Lunar Module during the descent phase. Signal strength recordings were also required during the Lunar Module descent. Additionally, MSFN stated a desire to have precision Lunar Module doppler data from DSS 62 on low lunar orbits 34 and 35. During these orbits, the Lunar Module was to be viewable only from Madrid DSCC, and the Madrid Prime and Wing sites have no doppler resolvers. Since DSS 62 is not a normal *Apollo* support station, this coverage was planned based on no interference to other missions and no additional resources required.

d. Apollo Interface Team. Between *Apollos 12* and *13*, DSN management decided that the level of DSN support to *Apollo* no longer warranted the services of a DSN Manager. Accordingly, the position of DSN Manager for *Apollo* was abolished with most of the DSN Manager duties being assumed by the DSN Project Engineer. Another "first" for *Apollo 13* was the formal transfer of the *Apollo* support capability from the Interface Team to the Mission-Independent Operations Organization. Unfortunately, the predict generation capability was not transferred. In the areas that were transferred, however, no operational problems were noted.

e. Premission testing

DSN/MSFN wing stations. DSSs 11, 42, and 61 were placed on mission status at 00:01 GMT on March 31, 1970 and from that time until splashdown, the stations were under MSFN control. Prior to March 31, each wing site conducted extensive maintenance and a long pretrack countdown to ensure the integrity of the equipment common to the DSN and MSFN.

DSS 14. Two tests were conducted at DSS 14 prior to the *Apollo 13* mission. The first test was a 12-h internal Configuration Verification Test on March 26. In the second test, DSS 14 linked up with the Goldstone Prime station for a 24-h data flow test including bit error-rate checking. During this second test, the SFOF predict transmission procedure was tested by sending center-of-the-moon predicts to DSS 14. As the results of the predicts exercise were doubtful, an additional test was conducted on April 7, during which the premission nominal predicts were successfully transmitted.

f. Apollo 13 operations

DSN/MSFN wing stations. DSSs 11, 42, and 61 successfully supported the earth-orbital translunar, and transearth phases of the mission with only the following anomalies noted:

(1) *DSS 11.* During the week prior to launch, the MSFN reported DSS 11 "red can support" due to apparent shifts of the RF boresight. The shifts were on the order of 0.060 deg, but were only observable at temperature extremes of night vs day. The DSN has no specifications for boresight shift, and the MSFN specification of 0.018 deg is felt by some to be unrealistic. Several tests were run following the first report of the problem at 17:29 GMT on April 2, and a star track was conducted to calibrate the shifts. Armed with these calibrations, the MSFN declared DSS 11 green at 23:21 GMT on April 9, two days before launch. A second premission problem at DSS 11 was the failure of maser 2, but it was returned to operational status before launch. During the first translunar pass, a circuit breaker tripped on the ac regulator for maser 1. A switch was made to maser 2 with a loss of 2 min of data.

(2) *DSS 42.* The only problem occurring at DSS 42 was the failure of transmitter power amplifier 4 during a pretrack System Readiness Test at 02:40 GMT on April 14. A fan motor bearing failed in the heat exchanger and was repaired by 04:28 GMT.

(3) *DSS 61.* About 5 h before launch, a large water leak occurred on the pump of heat exchanger 2, causing 2 min of a test to be lost. The pump was replaced, but a defective mechanical seal caused a small leak to develop 1 day later during a tracking period. The uplink was not lost, however, and the problem was corrected after the uplink was taken over by another tracking station.

DSS 14. Six passes were tracked with the planned schedule shown in Fig. 2 being altered in only two cases. On the third pass (April 14), MSFN requested DSS 14 to be on track at 01:00 GMT instead of 04:00 to cover the Lunar Module familiarization TV broadcast and telemetry. The end of the *Mariner* track was changed from 23:00 GMT to 21:30 and the post-calibration was shortened to 0.5 h for ranging only. Toward the end of this Lunar Module familiarization, the Service Module explosion occurred, which resulted in DSS 14's being requested to track horizon-to-horizon for the remainder of the mission. Since the fifth and sixth passes (April 16 and 17) were already scheduled horizon-to-horizon, the only schedule change

required was to drop the *Mariner* track on April 14 in order to track *Apollo* from horizon rise on the fourth pass (late April 14).

No problems occurred at DSS 14 affecting *Apollo* support. One problem did occur at JPL—at the end of the fourth pass, it was erroneously determined that the existing predicts would be valid for the fifth pass. Upon acquisition during the fifth pass, DSS 14 reported large offsets of 0.300 deg in both axes. These offsets were caused by the "speedup" burn 18 h earlier, which altered the trajectory enough to require new predicts. As mentioned before, predicts generation will be transferred to the Mission-Independent Operations Organization for future *Apollo* missions and this problem should not reoccur.

As in past missions, DSS 14 was able to demonstrate its unique capabilities. After the abort, the spacecraft conserved power by transmitting with low power through the omni-antenna (the high-gain antenna is electrically steered). During many portions of the mission, DSS 14 was the only tracking station to receive a solid downlink. When DSS 14 acquired the spacecraft and took over the function of downlink from an 85-ft antenna tracking station, the reduction in background noise on the astronaut's voice was immediately noticed. In addition, when the S-IVB signal interfered with the Lunar Module signal (the two craft use the same frequency causing the same problem on every mission), DSS 14 again separated the two spatially using the narrow DSS 14 beamwidth.

DSS 62. When the mission was aborted, the special support planned for DSS 62 was cancelled.

SFOF participation. The SFOF areas and equipment involved in the *Apollo 13* operations included the Operations Area, the Network Analysis Area, the displays, and the Mode IV 7044–7094 computers. These areas and functions were staffed during all DSS 14 passes and at other times to support special activities. Aside from the difficulty with predicts for the DSS 14 fifth pass, there were no problems in the SFOF.

GCF participation. The DSN GCF provided voice and teletype circuits as required to support the operations mentioned above. In addition, JPL acts as West Coast Switching Center for the NASA Communications Network and handles many non-DSN circuits in support of *Apollo*. There were no communications problems that constrained the DSN support of *Apollo 13*.

g. Concluding remarks. In concluding, it seems appropriate to quote the Houston MSC Director of Flight Operations.

> "We at MSC wish to commend the entire network for their superior performance in support of *Apollo 13*. In the midst of this most difficult and critical mission it was extremely reassuring to have a network with so few anomalies and one which provided us with the urgently needed voice and data to bring the crew back safely. We thank you for your outstanding support."

III. Advanced Engineering

A. Tracking and Navigational Accuracy Analysis

1. Introduction, *T. W. Hamilton and D. W. Trask*

The DSN Inherent Accuracy Project was formally established by the DSN Executive Committee in July 1965. The objectives of the project are:

(1) Determination (and verification) of the inherent accuracy of the DSN as a radio navigation instrument for lunar and planetary missions.

(2) Formulation of designs and plans for refining this accuracy to its practical limits.

Achievement of these goals is the joint responsibility of the Telecommunications and Mission Analysis Divisions of JPL. To this end, regular monthly meetings are held to coordinate and initiate relevant activities. The project leader and his assistant (from the Mission Analysis and Telecommunications Divisions, respectively) report to the DSN Executive Committee, and are authorized to task project members to (1) conduct analyses of proposed experiments, (2) prepare reports on current work, and (3) write descriptions of proposed experiments. The project is further authorized to deal directly with those flight projects using the DSN regarding data-gathering procedures that bear on inherent accuracy.

The various data types and tracking modes provided by the DSIF in support of lunar and planetary missions are discussed in SPS 37-39, Vol. III, pp. 6–8. Technical work directly related to the Inherent Accuracy Project is presented in SPS 37-38, Vol. III, and in subsequent *Deep Space Network* SPS volumes, and is continued in the following subsections of this volume.

The effect of the charged particles in the interplanetary space plasma and earth's ionosphere can limit the inherent accuracy of the ground-based radio tracking system. Consequently, various schemes are under consideration to calibrate the charged-particle effect so that it will not become the limiting error source for navigation by the DSN.

The three articles of this section are all concerned with the effect of charged particles. *Subsection 2* describes and evaluates the major charged-particle calibration schemes being considered—both on the basis of operational considerations and measurement resolution. These charged-particle calibration techniques are divided into two types. Type 1 are those techniques that require specific hardware implementation on the spacecraft, i.e., the dual frequency, differential phase, DRVID, and S-band faraday rotation measurements, while Type 2 are those independent of any spacecraft hardware, i.e., VHF faraday rotation (tracking

of geostationary satellites), back-scattering, and ionosonde measurements. Because of their ability to measure the charged-particle content along the tracking station–spacecraft ray path, the Type 1 methods are preferred with an "ultimate" calibration scheme, defined for use as a standard of comparison, employing the transmission of two coherent frequencies with ranging modulation on both carriers, up to and transponded down by the spacecraft.

Subsection 3 compares the results of faraday rotation measurements made at DSS 14 while tracking *Pioneer VII* with those obtained by the Stanford tracking *Applications Technology Satellite-1* (ATS-1). Both of these techniques can be used to measure the charged-particle content of the ionosphere. The ATS-1 electronic content measurements are made at a constant elevation azimuth and mapped to the *Pioneer* ray path, which passes through the earth's ionosphere at varying elevation azimuth, by correcting for differences in local time, path length through the ionosphere, and geomagnetic field strength between the two ray paths. Although the comparison is quite good on certain days, it fails to match up on other days. The likely causes for this lack of matching are discussed, and include errors in accomplishing the previously mentioned mapping.

Subsection 4 evaluates a model used to predict the diurnal behavior of the earth's ionosphere in terms of its effect on navigation accuracy. This model corresponds to the one coded in the double-precision orbit determination program and contains three input parameters. These parameters were determined by analyzing ionospheric data from 1967 through 1969 and the resultant model was tested using data from the *Mariner* Venus 67 mission. For this case, the model does improve the navigational accuracy in the declination direction but is not effective in correcting errors in right ascension.

2. Charged-Particle Calibration System Analysis,

B. D. Mulhall

a. Introduction. The charged particles in the interplanetary space plasma and the earth's ionosphere have various effects upon a transmitted radio signal. Among these effects are absorption, refraction, scintillation, polarization rotation, phase path decrease, and group path delay. For orbit determination by radio tracking, the two effects of greatest concern are phase path decrease and group path delay, since these effects corrupt measurements of radio doppler and ranging measurements, respectively. The other effects become important when attempts are made to measure the charged particles to calibrate their effect on doppler and ranging data.

Reference 1 describes the effect of a plasma on radio waves. The plasma delays the propagation of the energy in the wave, the effect being called "group path delay." The phase of the wave propagates at a rate faster than the speed of light, so that the product of the group velocity and the phase velocity remains constant. This increase in phase velocity (or decrease in phase path) is a function of the wave frequency, so the plasma has a dispersive effect on the spectrum of the radio signal.

As the number of charged particles along the ray path changes, the phase velocity increases, changing the S-band carrier frequency. This frequency shift cannot be distinguished from the doppler effect unless the change in the number of charged particles is determined. Similarly, the charged particles delay the energy of the S-band signal, which increases the round-trip propagation time and thereby corrupts ranging data since these measurements are based on the time required for the energy to propagate from the tracking station to the spacecraft and return.

The charged-particle effect on interplanetary spacecraft navigation, using radio tracking data, is discussed in a forthcoming JPL technical report.[1]

The effect of the charged particles can limit the inherent accuracy of the ground-based radio tracking system and, consequently, various schemes are under consideration to calibrate the charged-particle effect so that it will not become the limiting error source for navigation by the DSN.

The methods for measuring charged particles and, hence, computing a calibration for their effect, can be grouped as follows:

(1) Dispersive measurements.

(2) Polarization measurements.

(3) Ionospheric soundings.

Dispersive measurements. The charged particle effects on the radio signal vary as the integrated electron density along the ray path.

$$E_c = \int_{\text{path}} N(s)\, ds \qquad (1)$$

[1]Mulhall, B. D., et al., *Tracking System Analytic Calibration Activities for the Mariner Mars 1969 Mission*, Technical Report 32-1499. Jet Propulsion Laboratory, Pasadena, Calif. (to be published).

where

E_c = the integrated electron density along the ray path

$N(s)$ = the local density of charged particles

ds = the increment of path length

The charged-particle induced shift of the observed frequency is given by (Ref. 2)

$$\Delta f = \frac{-Q}{4\pi^2 f c} \frac{dE_c}{dt} \tag{2}$$

where

Δf = the shift in frequency, Hz

f = the frequency of the transmitted signal, Hz

c = the speed of light in a vacuum, m/sec

Q = 40.3 in mks units

$$Q = \frac{e^2}{8\pi^2 \epsilon_0 m}$$

where

e = the charge on an electron

m = the mass of an electron

ϵ_0 = the electric permittivity of free space

(1) *Dual frequency.* By coherently transmitting two frequencies, one of which is a multiple of the other, and measuring the difference in the phase and group velocity of the two frequencies when received, the number of charged particles in the ray path can be computed. This technique, called "dual frequency," is described in Ref. 3.

The change in path length at S-band frequencies is given by (Ref. 2)

$$\pm\Delta\ell = \frac{Q}{f^2} E_c \tag{3}$$

where $\Delta\ell$ is the change in path length (positive for group path, negative for phase).

To refine the measurement of E_c obtained from differential group path data, differences in received frequency are detected and integrated to obtain differential phase data. These data are used as a vernier to improve the resolution of the group measurement. The differential group path data are required to obtain the constant of integration for the differential phase measurement.

(2) *DRVID.* One technique for making measurements of the change in group path length versus the change in phase path length is called Differenced Range vs Integrated Doppler (DRVID).[2] The change in group path length is measured by monitoring the time required for a ranging code to be transmitted to the spacecraft and transponded back to the tracking station. The phase-path change can be measured from the counted doppler. If there were no charged particles between the tracking station and spacecraft, the quantity given by differencing range points would equal the quantity found from counting S-band cycles in the doppler counter. The apparent disagreement between differenced range and integrated doppler equals twice the change in charged particles along the ray path since the effect of charged particles is essentially equal and opposite on the group and phase measurements at S-band (Eq. 3). This technique provides a measure of the time rate of change of the integrated electron content, dE_c/dt, but does not give the total integrated content itself. The constant of integration E_c cannot be measured directly from DRVID.

(3) *Differential phase.* The dual-frequency measurement discussed previously employs measurements of differential phase path and group path. It is also possible to implement a system that provides only the differential phase path data. This is accomplished by transmitting two signals coherently; however, only one would be modulated. The second frequency can be much lower powered, and would require less equipment on the spacecraft. This "differential-phase" technique has been proposed, although it is not presently planned for any future mission. The constant of integration E_c is not determined by this technique.

Polarization measurements. In the presence of a magnetic field, the charged particles produce the effect of rotating the plane of polarization of the signal transmitted through the plasma (Ref. 2). If the plane of polarization of the transmitted signal can be determined (or referenced to some known inertial frame) and the polarization of the received signal measured, then the total electron content coupled with the magnetic field along the ray path can be determined.

$$\Omega = \frac{R}{f^2} \int_{\text{path}} \|\tilde{H}\| \cos\theta \, N(s) \, ds \tag{4}$$

[2]SPS 37-62, Vol. II, pp. 28–34.

where

Ω = the faraday rotation of the plane of polarization, rad

θ = the angle between the signal wave normal and the magnetic field vector $\tilde{H}$

$\|\tilde{H}\| \cos\theta$ = the tangential component of the magnetic field along the ray path, A-t/m

and

$$R = \frac{e^3\mu_0}{8\pi^2 cm^2\epsilon_0} = 2.97 \times 10^{-2}\,(\text{mks})$$

where μ_0 = the magnetic permittivity of free space.

From Eq. (4), it can be seen that the integrated product of the electron density and the tangential component of the magnetic field can be measured. To isolate integrated electron content, the magnetic field vector must be known or modeled. This can cause an error in ionospheric measurements made with the faraday rotation technique.

The magnetic fields of interplanetary space are generally too weak to produce the faraday rotation effect. Except when the signal passes near the sun or some planet, the charged particles in the solar wind cannot be detected by the faraday rotation technique even though they are sufficiently dense to corrupt range and doppler measurements.

Ionospheric sounding

(1) *Ionosonde.* Before the advent of artificial satellites, the only method of measuring the ionosphere was a vertical sounding technique called ionosonde. Using this method, a radio signal is transmitted vertically, reflected by the ionosphere, and received by the transmitting station. This process is repeated while increasing the transmitted frequency until the signal pierces the ionosphere. The density of electrons required to reflect a particular frequency is (Ref. 1)

$$N = Af^2$$

where

N = the density of electrons, electrons/m^3

f = the reflected frequency, Hz

A = 1.24×10^{-2}, electrons/m^3-Hz^2

By measuring the time of flight for each reflected frequency, the altitude h dependence of the electron density $N(h)$ can be determined. This method measures $N(h)$ for the lower or bottom side of the ionosphere; i.e., up to the F_2 layer. The topside, above the F_2 layer, must be estimated by employing a model for $N(h)$ in this region.

(2) *Backscattering.* The Arecibo Ionospheric Observatory has employed a monostable radar to sound the ionosphere. This device can penetrate past the F_2 layer and detect reflections from 800 to 2000 km altitude under good conditions. This provides a measure of the distribution of ionization along any line-of-sight to which the radar can be pointed.

b. Operational considerations. A comparison between schemes used in evaluating the various charged-particle calibration is discussed herein in two separate paragraphs. In this paragraph, the operational considerations are reviewed; in *Paragraph c*, the resolution capability of each scheme for measuring charged particles is discussed and compared.

The principal competing approaches currently under consideration for implementation in the DSN are the only techniques discussed in this paragraph, although there are many alternate schemes, including various combinations of the techniques. In addition to these, an "ultimate" technique is used as a base line or standard of comparison, even though it is not feasible for implementation.

Table 1 gives the various charged-particle calibration techniques grouped into two types. Type 1 techniques are those requiring a specific hardware implementation on the spacecraft. These include dual-frequency, differential-phase, DRVID, and S-band faraday rotation measurements.

The first scheme listed in Table 1 is the "ultimate" calibration scheme, which is used as a standard of comparison (e.g., as the Carnot cycle is used as a standard of comparison for internal combustion engines). This ideal scheme employs the transmission of two coherent frequencies with ranging modulation on both carriers up to, and transponded down by the spacecraft. This scheme would permit the measurement of total electron content as well as its time rate of change on both the up link and the down link. Consequently, it would provide all information that could possibly be desired for navigation.

The second scheme listed in the table is the combination of dual frequency and ranging, which permits the

Table 1. Calibration techniques

Technique	Measurement		Data type calibrated				Medium		Additional hardware requirements	
	Up link	Down link	Doppler		Range		Solar plasma	Ionosphere	Flight	Ground
			Up & down	Down only	Up & down	Down only				
Type 1 (Spacecraft related)										
Ultimate system	E_c, dE_c/dt		D	—	D	—	X	X	Dual frequency ranging transponder	Dual frequency transmitter/receiver, dual ranging equipment and comparator
Dual frequency/DRVID	dE_c/dt	E_c	D	D	T	D	X	X	Dual frequency transmitter, single frequency ranging transponder	Dual frequency receiver, ranging equipment
DRVID	dE_c/dt		D	—	—	—	X	X	Ranging transponder	Ranging equipment
Phase differential	—	dE_c/dt	T	D	—	—	X	X	Dual frequency transmitter	Dual frequency receiver
S-band faraday rotation	—	E_c, dE_c/dt	T	D	T	D	—	X	Linearly-polarized antenna	S-band polarimeter
Type 2 (Independent of spacecraft)										
VHF faraday rotation	$E_c + dE_c/dt$		M	M	M	M	—	X	None	VHF polarimeter
Back scattering	$E_c + dE_c/dt$		D	D	D	D	—	X	None	Radar equipment
Ionosonde	$E_c + dE_c/dt$		M	M	M	M	—	X	None	Ionosonde equipment

D Direct calibration is provided.
T Time translation is required.
M Space–time mapping is required.

measurement of total electron content on the down link by measuring differential phase and group path change by the dual-frequency technique, and the time rate of change of content on both up and down links by DRVID. This scheme is considered a feasible approach and has been proposed for *Mariner* Venus–Mercury 1973.

The third scheme is the use of DRVID alone. This approach is currently being evaluated on *Mariners VI* and *VII* and is planned for use as a calibration scheme for *Mariner* Mars 1971.

The fourth scheme is the use of a differential phase measurement of coherently transmitted carriers. It is distinguished from dual frequency since only one carrier is modulated and only differential phase path change can be measured.

The fifth technique is the use of S-band faraday rotation of the spacecraft carrier signal. This scheme was employed and measurements taken with the *Pioneer* series of spacecraft, since they were designed with linearly polarized antennas.

With the exception of the ultimate scheme, each calibration technique is mechanized in a manner to minimize the hardware requirements on the spacecraft. This is a desirable approach because of the higher cost of flight hardware as opposed to ground hardware; the limitations of weight, power, and volume on the spacecraft; and the more severe environment imposed on spacecraft electronics.

A second type of calibration techniques are those independent of any spacecraft hardware. These include VHF faraday rotation, back-scattering, and ionosonde measurements. These techniques have been used for some time in measuring the earth's ionosphere, and the VHF faraday rotation and ionosonde data have been used to calibrate tracking data to remove the ionospheric effect.

Table 1 indicates the measurements made by each technique. E_c indicates the measurement consisting of total electron content along the line-of-sight while the time rate of change of E_c is indicated by dE_c/dt.

The next item shows the data type (range or doppler) calibrated by each technique, and whether the calibration is directly provided (D), or whether time translations (indicated by T) or space–time mapping (M) are required to compute the calibration. It should be noted that if range points are differenced before introducing them as input data, dE_c/dt is an adequate measurement on which to base a differenced range calibration.

The next column indicates the medium being calibrated, either solar plasma or ionosphere.

The last column indicates grossly the equipment, in addition to the conventional deep-space probe S-band transponder and DSN transmitter/receiver, imposed on the spacecraft and the DSN.

Absolute measurements. The importance of measuring dE_c/dt is obvious since this is the data type required to make a doppler correction. A more subtle requirement is the need for establishing the absolute content E_c where we do not have a continuous measurement of dE_c/dt. For example, if DSSs located in California and Australia are provided with charged-particle calibration techniques, while DSSs located in Spain and South Africa are not, it will be necessary to interpolate the charged-particle effect through the missing portion of the day. This would be extremely difficult if the calibration scheme only provided dE_c/dt, especially if the electron content were increasing before the gap and decreasing after it. (It would be very difficult to decide where the derivative changed sign.) If the calibration scheme provides a measure of E_c, then the interpolation is greatly improved. The advantage of measuring E_c also becomes important when we attempt to extrapolate at the beginning of a pass to compute an up-link calibration when only down-link calibrations are available.

The ability to measure up and down links becomes more important as round-trip light time increases. In both the solar plasma and the ionosphere, E_c changes quite slowly compared to the round-trip light time for Mars and Venus missions. However, for missions to more distant planets, the ability to calibrate the up link in making two-way doppler calibrations will become increasingly important and difficult. This is discussed in the portion of this paragraph entitled *problems in time translation.*

Solar plasma vs ionospheric effect. When considering the media to be calibrated, it is clear that a calibration for the ionosphere is important since, with its diurnal rate, the ionosphere always corrupts orbit determination. In the case of solar plasma, the need for calibration is very important if short data arcs are to be used, or if the spacecraft's ray path passes near the sun. However, for missions where the spacecraft's ray path never approaches the sun, and where long data arcs can be employed, it is currently believed that the effect of solar plasma will tend to average out.

Problems in time translation. To calibrate ranging or two-way doppler data, it is necessary to compute the up-link calibration as well as the down-link effect. This capability is directly provided by the ultimate scheme and by DRVID. Down-link dual-frequency, down-link differential-phase, and S-band faraday rotation measurements do not provide this capability. Consequently, a means must be developed to translate in time down-link measurements to compute the up-link calibration. For S-band faraday rotation, this is a trivial calculation since the time for the propagation of light between the tracking station and the earth's ionosphere is negligible.

The up-link calibration of solar-plasma pulses is more difficult. Differential-phase measurements detect plasma intercepting the ray path. However, there is no indication at what point along the ray path the plasma intercepted the signal. For example, if a plasma pulse is detected on the down-link signal, there is no way to determine whether the pulse intercepted the ray path near the spacecraft—in which case, the up-link signal prior to detection should not be calibrated for the pulse—or whether the pulse intercepted the ray path near the earth—in which case, all the up-link signals for the previous roundtrip light time should be calibrated. Models of the solar wind will be required to interpret the down-link data so that the correct translation in time can be determined and the up link calibrated.

Problems in space–time mapping. For Type 2 calibrations, the mapping of measurements to the ray path in the ionosphere is quite difficult. The problem arises from making ionospheric measurements at a constant elevation angle and azimuth. To relate these measurements to the varying elevation and azimuth of the spacecraft requires time and spatial modeling of the ionospheric effect. This mapping has been undertaken in the past and is currently being used for post-flight calibration of tracking data. There will always be considerable uncertainty in the mapping technique since the dynamics of the ionosphere

will always cause errors and uncertainties in the resulting calibration. At present, the mapping techniques are accurate to about 5% of the total effect (see *Subsection 3*). Above 15-deg elevation, 5% amounts to less than 0.5 m and is usually closer to 0.1-m error.

Combined dual frequency/DRVID/S-band faraday rotation. The most powerful technique that can be implemented in the deep-space communication system for calibrating charged particles is the combination of dual frequency, DRVID, and S-band faraday rotation. This combination is not explicitly shown in Table 1; however, it would provide measurements of the interplanetary plasma and the earth's ionosphere and permit the identification and separation of these two media. DRVID and dual frequency measure the charged particles in the solar plasma and the earth's ionosphere. S-band faraday rotation measures only the earth's ionosphere (or plasma near a body with a magnetic field comparable to or greater than earth's).

The S-band faraday rotation provides a means to subtract out the earth's ionosphere, so that space plasma dynamics can be studied and space plasma modeling for missions that do not have charged-particle measurement capability can be developed. Isolating the space plasma for scientific studies of solar-plasma dynamics should not be overlooked as another advantage of S-band faraday rotation. When the space plasma is quiet, i.e., essentially constant, the dual-frequency measurement will show, with high resolution, the variation in the earth's ionosphere. This will greatly enhance the modeling of the earth's magnetic field, which is a source of error for faraday rotation measurements since the ionospheric effect can be measured directly under the circumstance.

Dual-frequency and DRVID measurements complement each other. DRVID measures both up-link and down-link paths and provides the time rate of change of electron content on both of these paths. With DRVID measurement and dual frequency, the effect on the up-link and down-link can be separated since plasma affecting only the up link would not appear in the dual-frequency measurement. On the other hand, the dual-frequency data complements DRVID by providing a total content measurement required for interpolation.

The argument for combining the three techniques (dual frequency/DRVID/S-band faraday rotation) is that they allow the isolation of various media so that individual techniques can be improved by providing accurate standards of comparison to determine measurement resolution and modeling errors.

Measurements of the earth's ionosphere should be made to complement dual-frequency and DRVID data, even if the spacecraft does not employ a linearly-polarized antenna for S-band faraday rotation measurements. These can be made by Type 2 techniques. However, it would be more accurate to make the measurement along the spacecraft–station line-of-sight and eliminate mapping errors. The spacecraft modification, employing linearly-polarized antennas, should be incorporated in future designs to permit S-band faraday rotation measurements.

Dual frequency/DRVID. As discussed, dual frequency and DRVID complement one another and are necessary to perform the entire navigation calibration of charged particles. This combined technique provides direct calibration of doppler on both the up and down links and range calibrations on the down link. Up-link range calibrations can be computed by identifying the changing densities of charged particles affecting the up link, isolating these by the differences between DRVID and dual frequency, and extrapolating the total content E_c back to the time of the up link signal transit through the plasma. Dual frequency has an operational advantage over DRVID in that the measurement of differential phase can be made continuously whenever the two carriers are locked up. DRVID requires that the ranging transponder on the spacecraft be turned on, and the ranging code transmitted to the spacecraft. In past missions, the quantity of ranging data obtained has been extremely small due to the problems of self-lock experienced with *Mariner* transponders. As charged-particle calibration for navigation becomes more important, reluctance to turn on the ranging transponder may diminish. However, new problems may continually arise due to the additional operational step required to obtain DRVID measurements. In addition to these problem areas, DRVID requires continuous monitoring of the ranging code since the DRVID measurement will be interrupted if ranging lock is broken. Dual frequency can provide a means to bridge gaps in ranging data, and, consequently, is essential if continuous charged-particle calibrations are to be computed for all tracking data.

Differential phase. As indicated in Table 1, differential-phase measurements would provide only the time rate of change of E_c on the down link. These down-link measurements could be translated in time to the up link; however, the uncertainty would be significant and would grow as

the round-trip light time increased. This technique would measure solar plasma and could be a useful approach; however, it would be extremely inferior to the other approaches described above.

Faraday rotation. The use of S-band faraday rotation measurements from deep-space probes has been evaluated by comparing these measurements to VHF faraday rotation measurements made from geostationary satellites. The experience with *Pioneer VII* (*Subsection 3*) indicates that S-band faraday rotation could be an effective means for measuring the earth's ionosphere. However, there is no indication that solar plasma is detected by this technique. In addition to this shortcoming, the implementation of S-band polarimeters would require a significant undertaking by the DSN.

The principal method for calibrating charged particles in the earth's ionosphere to date has been the use of VHF faraday rotation measurements. These measurements have two inherent problems: First, they require a geostationary satellite within the view of each DSS. Second, there are the inaccuracies that result from converting the Faraday rotation measurement to electron content and in mapping the electron content to the spacecraft line-of-sight. The improvement of both of these error sources, which probably amount to about 5% of the total effect (Ref. 1), is under investigation.

Figure 1 shows the location of the *Applications Technology Satellites* (ATSs) and the *Intelsat II* satellites around the world. The ATSs are equipped with beacons that can be used for faraday rotation measurements. The *Intelsat II* satellites are equipped with beacons that must be turned on before measurements can be obtained. Presently, *Intelsat II F-2* has its beacon turned on and is being used to measure the ionosphere over Australia.[3] The *Intelsat II* beacons are turned off whenever they interfere with other projects, such as *Apollo*, or when the satellite passes through the earth's shadow at equinox. The *Intelsat III* satellites are not equipped with VHF beacons. This indicates a trend in stationary satellites that, if not reversed, may make the use of VHF faraday rotation a dead-end street for future deep space missions.

Ionosonde. Ionosonde data have a problem in addition to space–time mapping since this technique only measures the lower portion of the ionosphere, leaving the upper portion (which amounts to about 75% of the total effect)

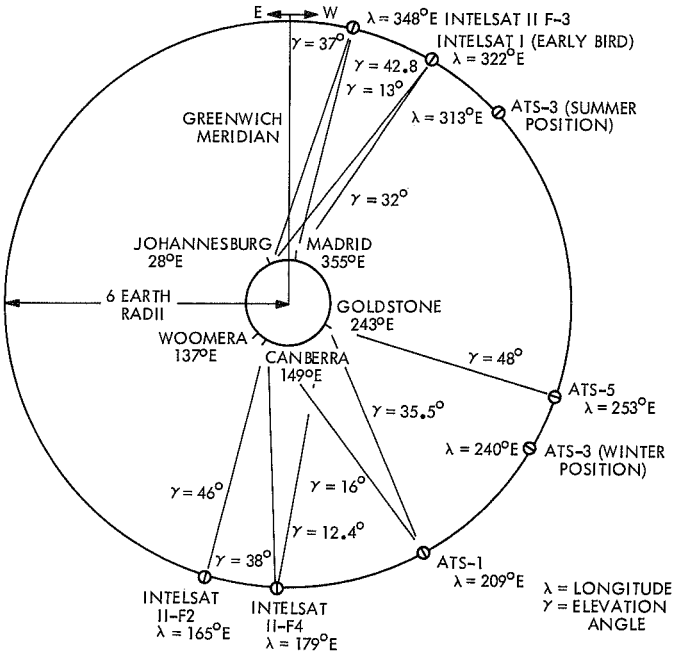

Fig. 1. Geostationary satellite locations

to be extrapolated by empirical techniques. Comparisons of ionosonde and faraday rotation measurements indicate that ionosonde data are generally less accurate for determining E_c.

c. Measurement resolution

Dual frequency. The use of the dual-frequency technique has been proposed in three configurations for future missions. These are S-band side-band dispersion, S/S-band, and X/S-band.

S-band side-band dispersion employs the present *Mariner* Telecommunication System. The S-band carrier is modulated with the ranging code and the third harmonic of the ranging side bands are monitored and compared for differences in phase.

The S/S-band technique employs the two transmitters presently used on *Mariner* spacecraft. However, both transmitters would be simultaneously active with the second S-band transmitter offset by 10 MHz above the lower carrier.

The third mechanization is the X/S-band technique, which consists of the S-band carrier at 2295 MHz and the X-band at 8415 MHz, both carriers being modulated.

Figure 2 shows the resolution capability of each of these three approaches. It is assumed that differences in

[3]Private communication with Dr. F. Hibberd, University of New England, Armidale, NSW Australia.

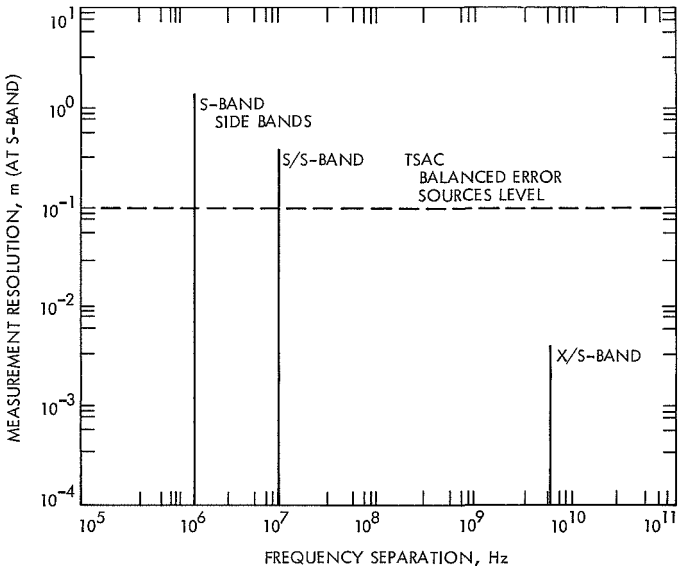

Fig. 2. Dual-frequency resolution capability for 10-deg phase difference measurement accuracy

phase can be measured to 10 deg at the lower frequency. The resolution of 10 deg is a hypothetical level based on the Stanford dual-frequency experiment, which was able to resolve phase to 7.8 deg. If experiments indicate that the equipment cannot resolve phase to 10 deg, then Fig. 2 should be changed accordingly. For example, if the capability is limited to 100 deg, then the vertical scale should be changed by a factor of 10.

Figure 2 also assumes that the difficulty in measuring differences in phase is the same for all three techniques, which all use the same lower frequency (2295 MHz).

Figure 2 indicates that for the assumed resolution, only the X/S-band dual-frequency technique will result in the calibration below the Tracking System Analytical Calibration (TSAC) balanced error sources level.

A problem with the S/S-band approach is the 10-MHz separation, which exceeds the frequency allocation provided to the DSN. A new frequency allocation will be required to use this technique. Another complication is that the 10-MHz separation exceeds the bandwidth of a single DSN receiver, thereby requiring two receivers and resulting in a comparable level of complexity with the X/S-band technique.

DRVID. Figure 3[4] indicates the stability of the Mu ranging system as indicated by the *Mariner* Mars 1969

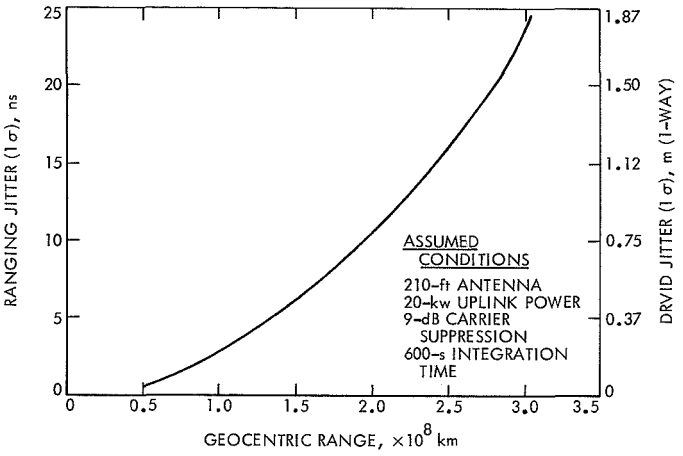

Fig. 3. DRVID resolution

experience. The figure shows the ranging jitter in nanoseconds and the resultant resolution capability of charged-particle measurements in meters of path change vs geocentric range. For most missions (i.e., missions closer than 1 AU) DRVID will approach the TSAC-level requirements for calibrating the charged particles. However, as previously discussed, ranging modulation with dual-frequency carriers is much more powerful than DRVID technique alone.

Faraday rotation. Figure 4 shows the resolution of faraday-rotation data based on a measurement accuracy of 1 deg. Figure 4 also assumes a perfect model of the geomagnetic field. The figure indicates that at S-band, the resolution of charged particles is limited (but is probably adequate) if better than 1-deg accuracy cannot be achieved. For VHF measurements, there is adequate resolution. A problem arises at VHF since there are ambiguities in the data. Typically, five to ten rotations of the VHF signal will occur during the diurnal period. Since the polarimeter (the device that measures the plane of polarization) can make measurements only over a range of 180 deg, there are ambiguities to resolve each time the signal passes through the modulo during the day. There is also a problem in establishing the absolute level with the VHF measurements since the starting point must be guessed at. Two methods for determining the absolute level of electron concentration are to compute the number of rotations that occur between the satellite and the monitoring station, based on knowledge of the satellite's inertial position, and to monitor the satellite over a period of weeks, checking that the nighttime concentrations of electrons in the ionosphere do not become unreasonably high or low, and thereby verifying that the starting point was correct.

[4]The author wishes to acknowledge the assistance of P. F. MacDoran who provided this graph.

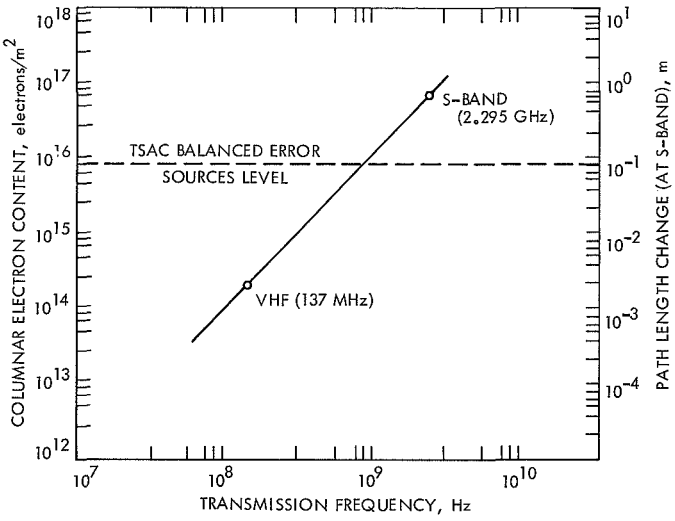

Fig. 4. Faraday rotation resolution for 1-deg measurement accuracy

At S-band there is no problem with ambiguities because the typical variation over one day is less than 10 deg of rotation.

All faraday rotation techniques suffer from the problem of determining the tangential component of the magnetic field. There are diurnal variations in the slab thickness of the ionosphere and the altitude of maximum density. As the thickness and altitude change (the entire altitude dependence of the profile changes) the tangential component of different magnetic field vector along the ray path is encountered. Averaging of the tangential component can be employed to simplify the modeling problem. However, this average should have some diurnal variation, for if it is held constant, there will be diurnal error in the conversion of faraday rotation to electron content. For navigation purposes, this is the worst possible kind of error.

d. Conclusion. Table 1 indicates that, except for the ultimate scheme, no single technique provides a complete calibration for both doppler and range. Consequently, combinations of these techniques are highly desirable, if not mandatory, in the calibration of both doppler and range data for all the charged-particle effects. The up-link measurement for dual frequency and S-band faraday rotation can be computed by making translations in time of the down-link measurement, provided the round-trip light time is short. DRVID measurements of the up link will be essential for longer round-trip propagation times.

The S-band faraday rotation technique and the Type 2 techniques failed to measure the effects of space plasma on the signal. The ionosphere will always cause an error in the estimation of navigational parameters, as discussed in *Subsection 4.* On the other hand, space plasma may or may not corrupt navigation, depending on the activity of the sun, the sun–earth probe angle of the spacecraft, and the length of the data arc used for navigation purposes (SPS 37-62, Vol. II, pp. 24–28). It is indicated in SPS 37-62, Vol. II that, for sufficiently long data arcs, the effects of space plasma averaged out to zero. It was assumed that the ionosphere was being perfectly calibrated—an assumption which will obviously never be fulfilled, and which becomes farther from the truth as the ionospheric measurement technique becomes less accurate. Where short data arcs are needed (e.g., when a maneuver is performed close to the target planet), the effect of space plasma becomes extremely important and may indeed be more significant than the ionosphere.

To adequately perform the charged-particle calibration, the combined dual-frequency/DRVID technique is required and will be significantly enhanced by S-band faraday rotation. Where dual frequency/DRVID is not available, other techniques (listed in Table 1 in order of descending merit) may be employed to partially reduce the navigation errors.

References

1. Davies, K., *Ionospheric Radio Waves*, Blaisdell Publishing Co., New York, 1969.
2. Lawrence, R. S., Little, C. G., and Chivers, H. J. A., "Survey of Ionospheric Effects Upon Earth-Space Radio Propagation," *Proc. IEEE*, Jan. 1964.
3. Koehler, R. L., *Interplanetary Electron Content Measured Between Earth and the Pioneer VI and VII Spacecraft Using Radio Propagation Effects*, Report 67-051. Standard Electronics Laboratories, Stanford University, May 1967.

3. The Ionospheric Electron Content as Determined From Faraday Rotation Measurements of an Earth Satellite and Deep-Space Probe, *B. D. Mulhall and C. T. Stelzried*

a. Introduction. Since the summer of 1969, JPL has been using measurements of the earth's ionosphere to calibrate radio navigation data for deep-space probes in order to improve orbit determination. The ionospheric effect, though small, has become an important error source on the doppler data as the orbit determination technology advances. To calibrate past missions, and present missions where no direct charged-particle measurement is provided, it is necessary to obtain measurements of the ionosphere made near DSSs and compute adjustments to these measure-

ments to relate them to the line-of-sight of the deep-space probe. By this technique, the effect of the ionosphere on the radio tracking data can be estimated to a usable accuracy.

Comparisons between ionospheric measurements have been made to evaluate the accuracy with which this modeling can be performed. One of the most valuable comparisons to date is the one discussed in this article.

Faraday rotation measurements were made at DSS 13 by a polarimeter monitoring the *Pioneer VII* deep-space probe, transmitting at 2.3 GHz. At the same time, during the fall of 1968, faraday rotation measurements were made at Stanford University in California, observing the *Applications Technology Satellite-1* (ATS-1) geostationary satellite beacon at 137 MHz. Both measurements were converted to columnar electron content. The ATS-1 electron content measurements, which were made at a constant elevation and azimuth, were adjusted or mapped to the *Pioneer* ray path, which passed through the earth's ionosphere at varying elevation and azimuth. The adjustment was calculated based on differences in time (zenith angle of the sun), path length through the ionosphere, and geomagnetic latitude. The two measurements were then compared by subtracting the VHF measurement from the S-band measurement.

The comparison was quite good on certain days (Fig. 5), and failed to match up on other days (Fig. 6). The cause for the lack of matching can be attributed to errors in the computation of the adjustment in space and time, errors in calculating the orientation of the *Pioneer VII* in inertial space relative to the tracking antenna, errors in modeling the geomagnetic field along the ray path to convert faraday rotation to electron content, motion of the *Pioneer*, and differences in ionospheric conditions between the two ray paths.

b. Errors in modeling. On the basis of this comparison, and other comparisons made between the two measurement techniques, it is felt that the mapping errors are about 5% of the effect. This amounts to about 1.5×10^{17} electrons/m^2 at 0-deg elevation, which is quite a large error. However, at higher elevation angles, 5% error in the total effect amounts to less than 10^{17} electrons/m^2, which is sufficiently accurate to produce a usable calibration for navigation. There are several improvements in the mapping technique presently being considered. These include accounting for the diurnal change in distribution of ionization. The mapping techniques are discussed in detail in a forthcoming JPL technical report.[5]

The orientation of the spacecraft in inertial space relative to the antenna on the ground receiver was computed to remove the apparent rotation due to the motion of the tracking station as the earth rotated. This is also a possible source of error, which could contribute to the lack of match.

The computation of magnetic field along the ray path at the varying elevation and azimuth of *Pioneer* is another possible source of error leading to a lack of comparison between the two measurements. A constant altitude of 400 km was used throughout to compute the tangential component of the geomagnetic field along the ray path. No adjustment of this altitude to compensate for diurnal variation of the vertical distribution of ionization was attempted. Further analysis will be performed to determine whether adjusting the altitude improves the comparison.

c. Other error sources. Taylor Howard of the Stanford University Radio Science Laboratory (whose generosity in providing the VHF data the authors wish to acknowledge) has assured us that the attitude in inertial space of the *Pioneer VII* is stable to a small fraction of a degree and could not be a cause of significant error in the S-band data.

The ionospheric reference point (400-km altitude subearth point) for the *Pioneer* as it rises over the DSS 11 horizon is about 200 mi to the east of the ionospheric reference point for the ATS-1 viewed from Stanford. Clearly, although there will be different conditions in the ionosphere at two widely separated locations, short-term variations of ionization are not as significant for navigational errors as are variations at a diurnal rate. Therefore, ionospheric measurements made by monitoring a geostationary satellite beacon can be used to calibrate deep-space probe radio tracking data, as is discussed in the unpublished technical report cited in Footnote 5.

d. Conclusions. The diurnal variation of the distribution of ionization in the ionosphere should be modeled to improve mapping techniques, especially where precise calibration for low elevation angles is required.

[5]Mulhall, B. D., et al., *Tracking System Analytic Calibration Activities for the Mariner Mars 1969 Mission*, Technical Report 32-1499. Jet Propulsion Laboratory, Pasadena, Calif. (to be published).

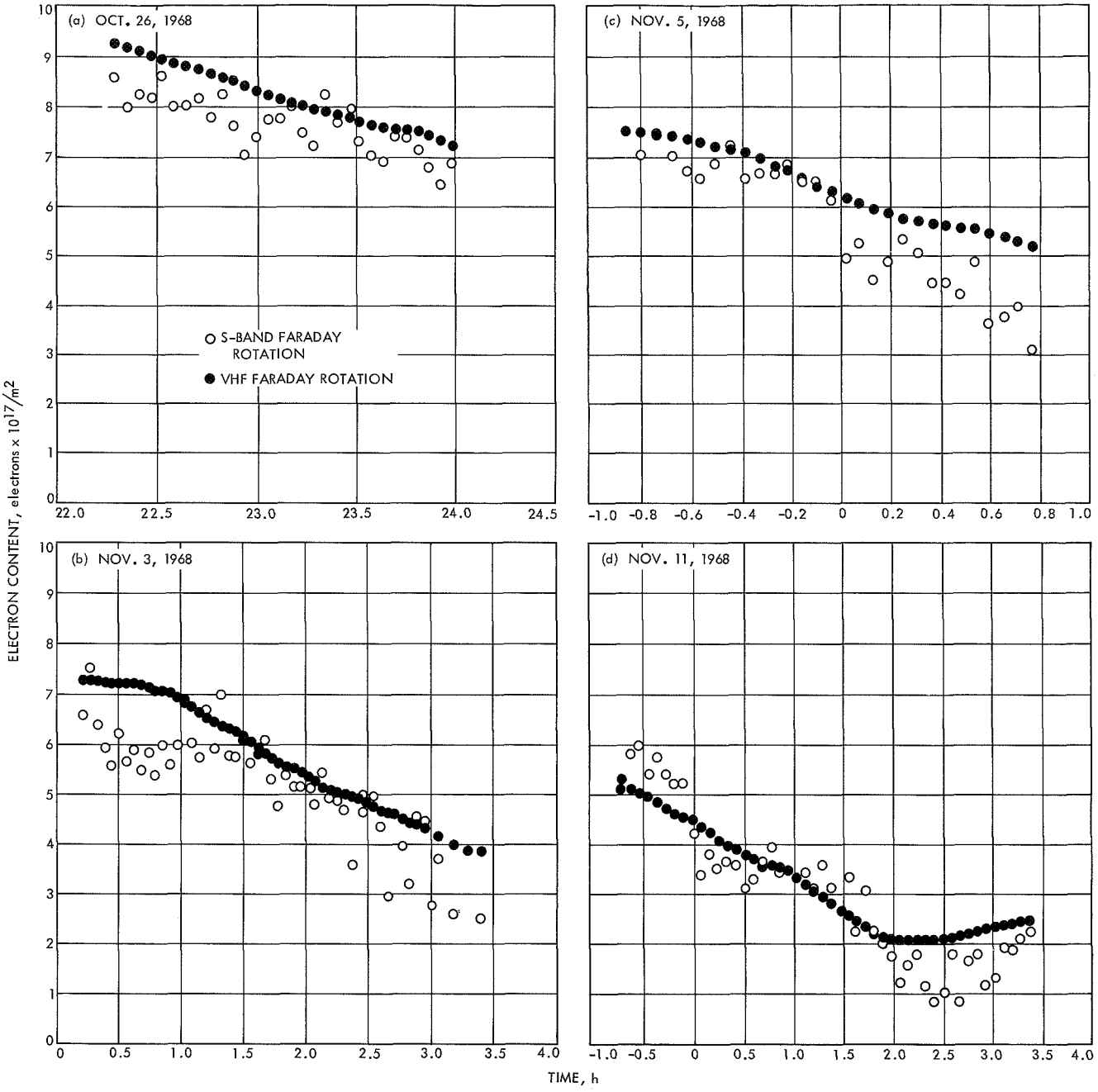

Fig. 5. Good-match comparison of S-band/VHF faraday rotation data

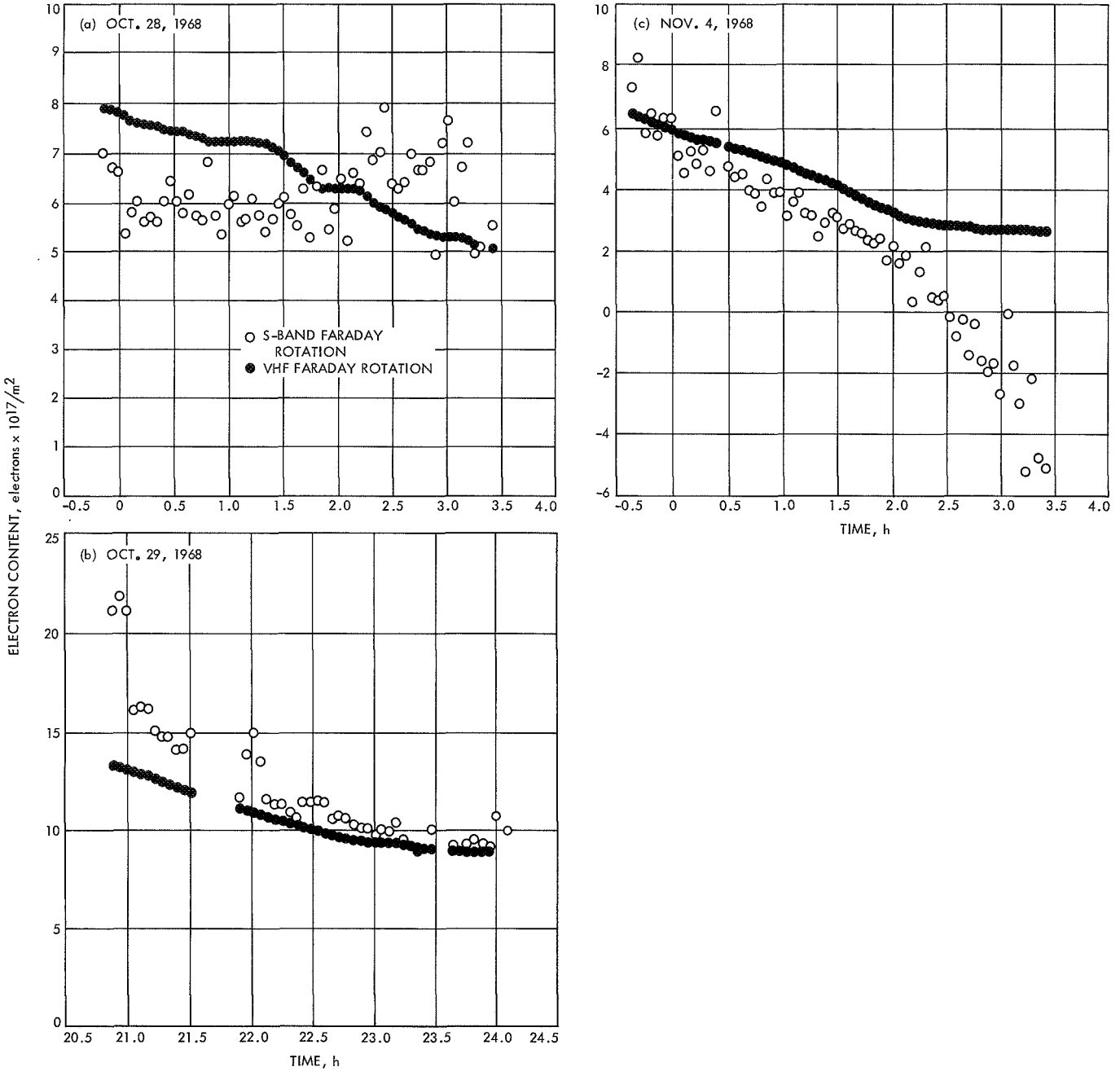

Fig. 6. Poor-match comparison of S-band/VHF faraday rotation data

4. Evaluation of the Ionospheric Model, *B. D. Mulhall*

a. Introduction. For some time, it has been hoped that a model of the diurnal variation in the ionosphere could be included in orbit-determination computer programs so that the effect of the ionosphere could be predicted and reduced with a reasonable accuracy. The model currently being used for this purpose, and which is coded in the double-precision orbit determination program (DPODP), is shown as Eq. (1). This model consists of three parameters A_c, D_c, and Φ combined as follows:

$$E_c = \begin{cases} D_c + A_c \cos \omega (t - \Phi) \\ \text{whichever is greater} \\ D_c \end{cases} \qquad (1)$$

where

E_c = total columnar electron content

ω = earth's rotational rate

t = time

D_c = nighttime concentration of ionization

A_c = amplitude of the daytime peak

Φ = time that peak concentration occurs

The three parameters are varied with season. The nighttime concentrations are higher in winter and lower in summer, while the daytime peaks are generally higher in winter and lower in summer. The parameter Φ has an average value of 1:30 p.m. local time. The uncertainty of Φ is quite great in summer and less in winter.

b. Comparison of total ionospheric effect to model residual. Data from 1967, 1968, and 1969 were employed to evaluate the model. These data were fit with the model (Eq. 1) on a daily basis, and seasonal averages of the three parameters computed. Using these seasonal averages as a composite model, the *Mariner V* mission was calibrated for the ionospheric effect. Figure 7 shows the total ionospheric effect in terms of apparent station location change. These apparent changes in station locations are computed by decomposing the doppler correction production by the program ION into the parameters of the navigation filter described in SPS 37-39, Vol. III, pp. 18–23 by the procedures described in a forthcoming JPL technical report.[6]

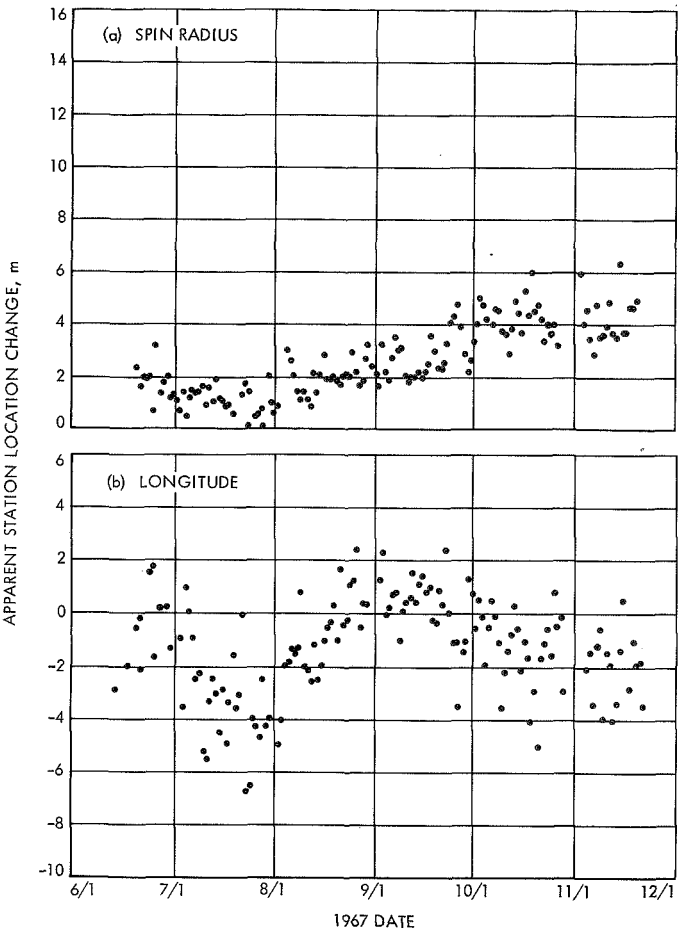

Fig. 7. Ionospheric effect on the *Mariner V* mission

Figure 8 shows the navigational error in terms of apparent station location error when the diurnal model of the ionosphere is subtracted from the actual measurements and their residuals are used as an input to the ION program. As in Fig. 7, the doppler effect is decomposed into spin radius and longitude.

From Figs. 7 and 8, it is apparent that for certain times of the year, the navigational error in longitude increases when the model is used. For example, in late July, the total ionospheric effect is slightly greater than 6 m on certain days; however, when the model is employed, the error increases to over 9 m. In fact, the error caused by the model is generally higher throughout the month of July than if the model were not used. There are other periods when longitude error is improved by employing the model (e.g., in mid-September).

Some possible causes for the increase in the longitude error, when the model is applied, can be summarized as

[6]Mulhall, B. D., et al., *Tracking System Analytic Calibration Activities for the Mariner Mars 1969 Mission*, Technical Report 32-1499. Jet Propulsion Laboratory, Pasadena, Calif. (to be published).

follows: The effect of the ionosphere on longitude is most highly correlated with the time of the peak concentration during the day. This sensitivity of the longitude error to Φ is shown in the partial derivative listed in SPS 37-57, Vol. II, pp. 29–42.

Coupled with this large sensitivity, the uncertainty in the time of peak concentration is greatest in summer, which becomes apparent when one notes the extensive scatter of the longitude error in the summer (Fig. 7b). There is also considerable scatter in October and November. However, this is due to the increased sensitivity of the longitude error as the sun–earth–probe angle decreases to 45 deg, so that smaller changes in Φ during the fall caused larger changes in longitude than earlier in the *Mariner V* mission.

A possible improvement in the current model that may be investigated is represented by

$$E_c = \begin{cases} \begin{cases} D_c + A_c \cos \omega (t - \Phi) \\ \text{whichever is greater} \\ D_c \end{cases} \\ \text{whichever is less} \\ B_c \end{cases} \qquad (2)$$

The fourth parameter B_c would be used only in summer to represent the flattened daytime characteristic of the summer diurnal variation. It may be that the *a priori* estimate of Φ would be relaxed by clipping the top of the curve, which might diminish the longitude error in summer.

The spin radius error is noticeably improved by applying the model. As shown in SPS 37-57, Vol. II, the amplitude A_c of the peak concentration is more important than Φ for r_s. A_c is a much more predictable parameter than Φ, especially in summer, and, consequently, the model performs better in the spin radius component. Figure 7a shows a gradual increase in the spin-radius error for the total ionospheric effect, which is due partially to the increase in peak concentration in the fall and winter, and partially due to the change in solar-electric propulsion during the *Mariner V* mission. Figure 8a shows that the repetitive error (monthly average) in spin radius after the model is applied is fairly constant throughout the *Mariner V* mission. An improved estimate of A_c could further reduce the remaining error.

If a day-by-day calibration of high precision is required, Fig. 7 shows that a model can never hope to accomplish

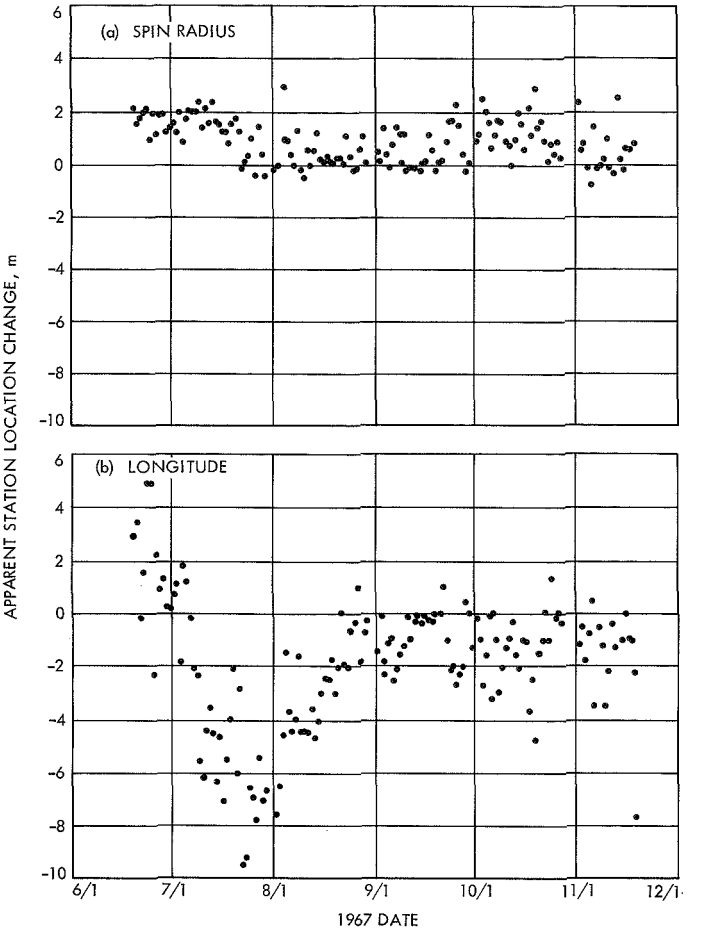

Fig. 8. Ionospheric model residual error

this end. The change either in spin radius or longitude from one day to the next can be in excess of 2 m. There are days (e.g., in mid-August and mid-September) when the ionospheric effect is repeatable for a period of a week. However, there is no apparent way to predict when a weekly trend will be suddenly changed.

c. Future model. The evaluation performed with the *Mariner V* mission shows clearly that a "canned" ionospheric model that remains unchanged in the software over long periods of time will never provide a suitable method for calibrating the ionosphere, especially where longitude is concerned. On the other hand, an adaptive model that employs the previous month's data and can be extrapolated ahead a week at a time may have value since Fig. 7 shows regular trends over the 6-mo period.

At this time, two possibilities for adaptive models suggest themselves. First, the diurnal model with the fourth parameter B_c added might be employed to predict the

path-length change by building statistical information on the four parameters of this model.

A second approach that may also be fruitful would be to perform the kind of evaluation discussed in this article using the six-parameter navigation filter.[7] The effect of the ionosphere in range, declination, right ascension, range rate, declination rate, and right ascension rate could be determined from the six-parameter navigation filter and statistics developed for these parameters. This approach has the attractive feature that navigation parameters with intuitive significance are employed rather than unfamiliar ionospheric parameters.

B. Communications Systems Research

1. Digital Telemetry and Command: Mean-Square Error and Bias of Phase Estimator for the JPL Sequential Ranging System, *J. Molinder*

a. Introduction. The JPL Sequential Ranging System (SPS 37-52, Vol. II, pp. 46–49) uses the first and third harmonics of the high-frequency squarewave to estimate the phase of the incoming signal. This estimate is then used as a reference for the remaining lower frequency components. In this article, plots of the conditional mean-square error and the bias in the estimate are given. A plot of the bias under no-noise conditions is also given.

b. Conditional mean-square error and bias. The conditional mean square error $E[(\theta - \hat{\theta})^2 | \hat{\theta}]$ and the bias $E[\theta - \hat{\theta} | \theta]$ in the phase estimate of the JPL Sequential Ranging System are given by

$$E[(\theta - \hat{\theta})^2 | \hat{\theta}] = \int_{\hat{\theta}-\pi}^{\hat{\theta}+\pi} (\hat{\theta} - \theta)^2 p(\theta | \hat{\theta})\, d\theta$$

and

$$E[\theta - \hat{\theta} | \theta] = \int_{\theta-\pi}^{\theta+\pi} (\theta - \hat{\theta})\, p(\hat{\theta} | \theta)\, d\hat{\theta}$$

where θ is the true phase and $\hat{\theta}$ is the phase estimate. The joint probability density $p(\theta, \hat{\theta})$ and the conditional probability density $p(\hat{\theta} | \theta)$ are known (SPS 37-61, Vol. III, pp. 31–33). The conditional density $p(\theta | \hat{\theta})$ can be evaluated numerically since

$$p(\theta | \hat{\theta}) = \frac{p(\theta, \hat{\theta})}{p(\hat{\theta})} = \frac{p(\theta, \hat{\theta})}{\int_{-\pi}^{\pi} p(\theta, \hat{\theta})\, d\theta}$$

Finally, the conditional mean-square error and bias can be evaluated numerically.

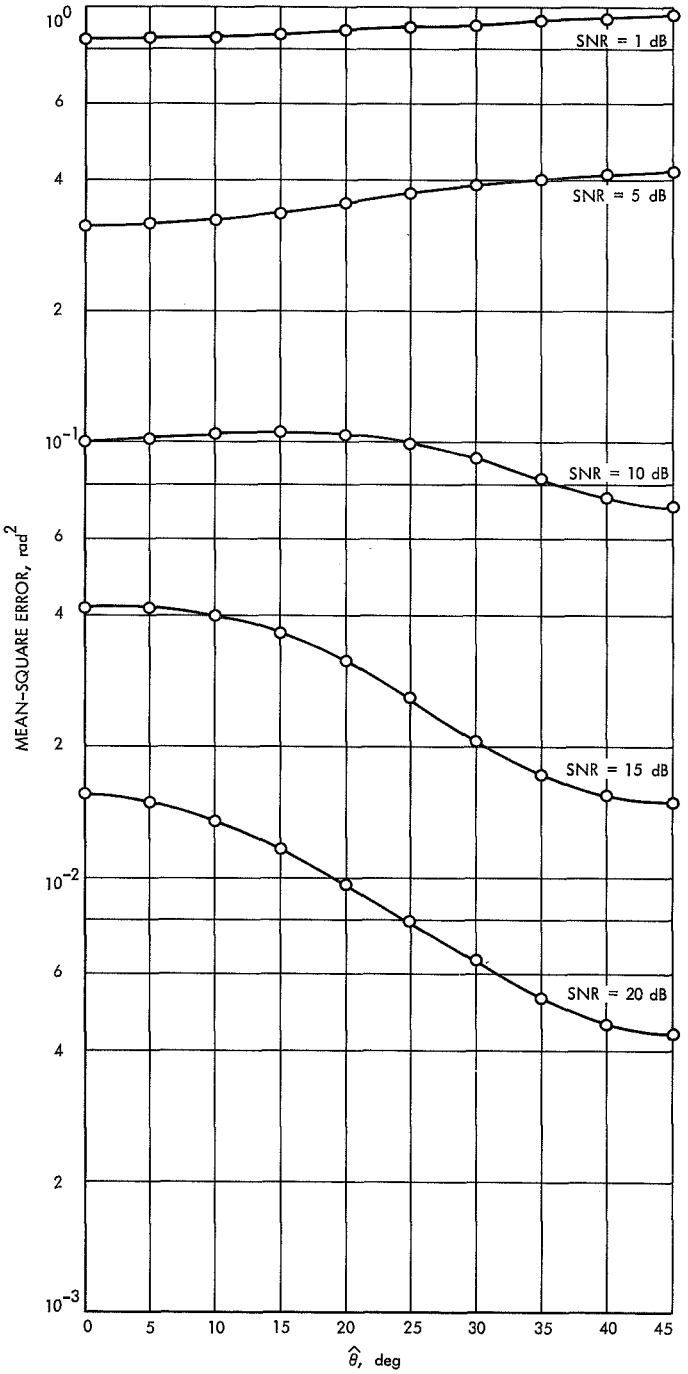

Fig. 9. Mean-square error vs $\hat{\theta}$

[7]Curkendall, D., *A Six-Parameter Model Characterizing the Doppler Information Received While Tracking a Distant Spacecraft*, May 16, 1967 (JPL internal document).

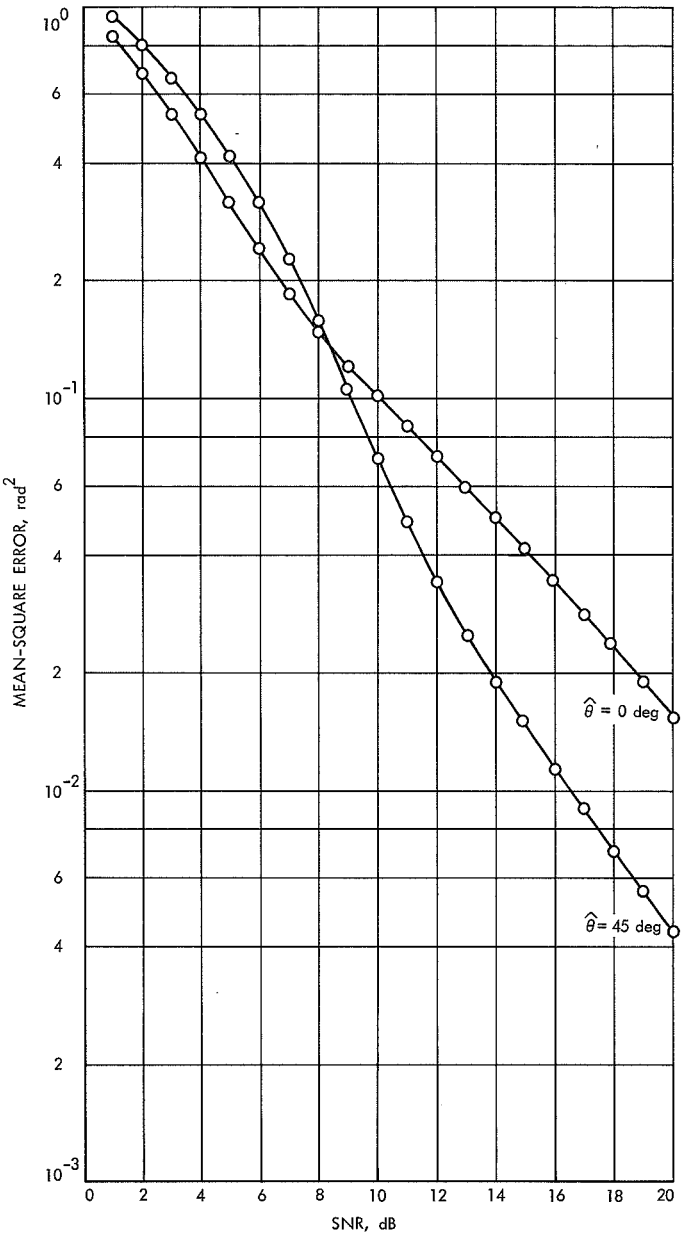

Fig. 10. Mean-square error vs SNR

c. Results. Figure 9 shows the conditional mean-square error vs $\hat{\theta}$ for specified signal-to-noise ratios (SNRs). Note that at low SNRs, the minimum mean-square error occurs at $\hat{\theta} = 0$ deg, while at high SNRs, it occurs at $\hat{\theta} = 45$ deg. In Fig. 10, the mean-square error is plotted as a function of the SNR for $\hat{\theta} = 0$ deg and $\hat{\theta} = 45$ deg. Figure 11 shows the bias vs θ for several values of SNR. Note that the estimate of $\hat{\theta}$ is unbiased at $\hat{\theta} = 0$ deg and $\theta = 45$ deg. This follows from symmetry since a sufficient condition for the conditional mean $E[\theta - \hat{\theta}|\theta]$ to be zero is that the conditional probability density $p(\hat{\theta}|\theta)$ is symmetrical

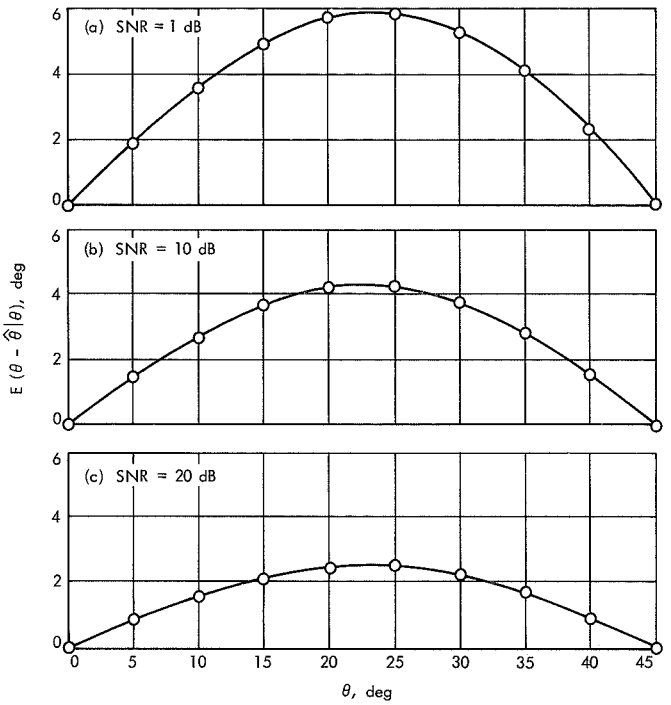

Fig. 11. $E(\theta - \hat{\theta} \mid \theta)$ vs θ

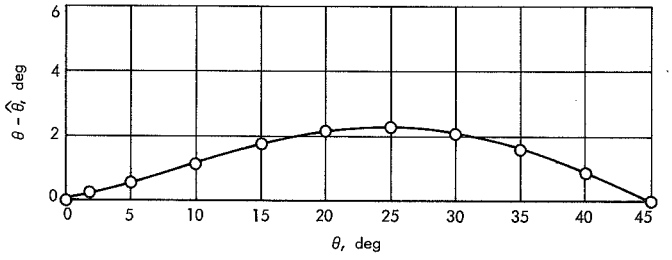

Fig. 12. $\theta - \hat{\theta}$ vs θ for no-noise conditions

about the point $\hat{\theta} = \theta$. Since

$$p(\theta \mid \hat{\theta}) = p\left(\theta \,\middle|\, \hat{\theta} + \frac{n\pi}{4}\right)$$

and

$$p(\hat{\theta} \mid \theta) = p\left(\hat{\theta} \,\middle|\, \theta + \frac{n\pi}{4}\right) \qquad n = 1, 2, \cdots,$$

results conditioned on θ or $\hat{\theta}$ need only be plotted from 0 to 45 deg. Since only the first and third harmonics of the high-frequency squarewave are used for phase estimation, there is a bias in the estimate even when there is no noise. The bias under no-noise conditions $\hat{\theta} - \theta$ vs θ is shown in Fig. 12.

2. Digital Telemetry and Command: The Asymptotic Complexity of the Green Decoding Procedure,

J. E. Savage[8]

a. Introduction. Green (SPS 37-39, Vol. IV, pp. 247–252; SPS 37-53, Vol. III, pp. 185–187) has recently introduced a simple decoding procedure for first-order Reed–Muller codes; the decoder was used to decode *Mariner* Mars 1969 high-rate telemetry. In this article the Green procedure is shown to be nearly optimal in the computational work[9] it requires to decode M code words with a small probability of error, P_e, on the additive gaussian noise (AGN) channel.

b. Computational work. Given a sequential machine with X 2-input binary logic elements and individually accessed binary memory cells which executes T cycles, we say that it performs computational work XT. In the reference cited in Footnote 9, it is shown that

$$XT \geq \frac{N}{2} \tag{1}$$

for all decoders modeled by these machines, where N is the number of decoder inputs when the channel is a completely connected discrete memoryless channel (DMC) and $P_e < P_{\min}$, the smallest channel transition probability. The additive gaussian noise channel with a finite number of inputs and a quantized output is such a channel.

The Green decoding procedure for the AGN channel performs maximum likelihood decoding of a code in which the words are rows of a $2^n \times 2^n$ Hadamard matrix H_n. Let $\mathbf{X}$ be the 2^n outputs of a matched filter quantized to q bits. Then the Green procedure calculates

$$\mathbf{y} = H_n \mathbf{X} \tag{2}$$

and determines the largest component of $\mathbf{y}$ which corresponds to the best estimate of the transmitted code word.

Green shows that H_n can be realized as a product of n matrices and that a decoder consisting of n stages can be created. The number of additions and subtractions required is $n2^n$ and each such operation involves words of length $n + q$ (q is the number of bits to represent the largest possible value of a component of $\mathbf{y}$). Therefore, an addition or subtraction requires $n + q$ clock cycles and the total number of cycles required to compute $\mathbf{y}$ is

$$T = n(n + q)\, 2^n \tag{3}$$

As these cycles are completed, the components of $\mathbf{y}$ are examined sequentially and the largest is determined.

Each of the n stages requires a fixed number of logic elements and the circuit which locates the largest component of $\mathbf{y}$ uses a number of elements proportional to n. Thus, X, the total number of logic elements, is some multiple of n, i.e.,

$$X = an \tag{4}$$

for some fixed a. Consequently, the computational work performed by the Green decoding procedure is

$$XT = a\, n^2(n + q)2^n \tag{5}$$

which for large n is bounded by

$$XT \leq 2a\, M\, (\log_2 M)^3 \tag{6}$$

where $M = 2^n$ is the number of code words in the orthogonal code.

Since the Green procedure uses $N = 2^n q$ channel outputs, we see from inequality (1) that we must have

$$XT \geq \frac{M}{2} q \tag{7}$$

From this inequality we find that inequalities (6) and (7) differ at most by a factor proportional to $(\log_2 M)^3$. It is not known whether inequality (1) is the best bound, but we conclude that *the Green procedure is near optimal in the computational work it performs to decode M code words at small P_e on the AGN channel.* (A factor of $(\log_2 M)^3$ is small compared to M when M is large.) However, the near optimality has been proved only for large M; for $M = 32$, results are harder to acquire.

---

[8]Consultant, Engineering Div., Brown University, Providence, R.I.

[9]Savage, J. E., "The Complexity of Decoders—Part II: Computational Work and Decoding Time," *IEEE Trans. Inform. Theory* (to be published in Jan. 1971).

3. Digital Telemetry and Command: The Effective Computing Power of Computer Memory,

J. E. Savage[10]

a. Introduction. Any type of computer memory which allows selective reading from storage possesses a computing power; for example, programmable telemetry decoders contain such memory. In this article we show how to measure this power and how to incorporate storage models into models for sequential machines in which the storage consists of individually accessed memory cells. In particular, if S is the size of storage and T is the number of computing cycles, we show that ST must be large to compute complex functions on general-purpose computers.

b. Models for computer memory. Consider a sequential machine as shown in Fig. 13 where L designates the logic realizing the next-state and output functions and M designates the memory unit. A standard model for storage is needed if the relative computing powers of various types of memory are to be measured. Thus, we assume that the storage consists of individually accessed cells; that is, we assume that a cell can be attached to the output of a logic element or to the output of another cell. A memory unit organized as an array of such cells has no computing power, inasmuch as all the data read into the unit is read out of it at the end of one computing cycle.

Most types of storage, such as tape and core storage, read selectively from storage cells, and consequently they possess computing power. To measure this power we replace the storage by an equivalent sequential machine with individually accessed cells. We assume that the machine receives one input and executes one cycle in which it reads from one or more individually accessed cells, overprints in these cells, and changes state. This action is easy to visualize in the case of a tape unit, since the tape head is in a given position or state, and it reads, overprints, and moves upon the command of the logic unit. A core storage control unit does not retain memory of the cells read earlier, so the control unit can be modeled by a combinational machine.

Assume that the set Ω of logic elements and some type of memory cell are available for realization of machine models. For example, the set might consist of two-input binary logic elements and the memory cells might be binary. Then, the *computing power P of a storage unit is the number of logic elements required to simulate this unit by a sequential machine with these individually accessed cells.*

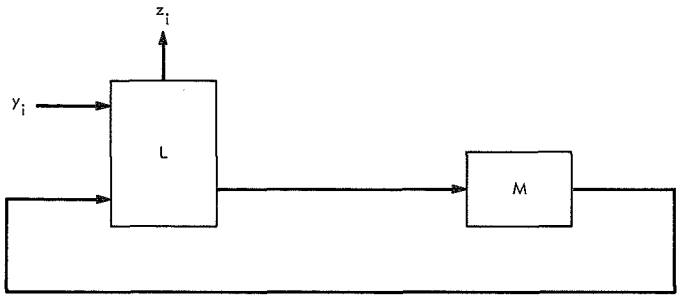

Fig. 13. Sequential machine model

P is termed "computing power" for the following reason: If X is the number of elements from Ω used in the logic unit L and P is the number of such elements used to simulate the memory unit M, then with $X + P$ logic elements the sequential machine can be put into canonical form. Let T be the number of cycles executed by the machine to compute the function f. Then, as shown earlier,[11]

$$(X + P)\,T \geqq C(f) \tag{1}$$

where $C(f)$ is the minimum number of logic elements from Ω required to realize f with a combinational circuit. We interpret the product $(X + P)\,T$ as *computational work*, since it is a number of logical operations, and by analogy with mechanical work, *we interpret T as time and P as power.*

c. Computing power of tape and core storage. If a control unit on a storage device can be directed to move from any given group of cells to another *nonoverlapping* group of cells, then

$$P \geqq S \tag{2}$$

where S is the number of cells, since at least one logic element is required for each cell to effect this kind of control. Both core and tape storage are of this type.

We now describe machines which simulate tape and core storage and derive upper bounds on P. These bounds will be proportional to S for large S.

[10]Consultant, Engineering Div., Brown University, Providence, R.I.

[11]Savage, J. E., "The Complexity of Decoders—Part II: Computational Work and Decoding Time," to be published in *IEEE Trans. Inf. Theory.*

Consider tape storage in which each tape square stores m binary digits; that is, the tape alphabet has size 2^m, and assume that two-input binary logic elements and binary memory cells are available for simulation. If the tape has S cells, the tape head can occupy S positions and the control unit simulator must have S states. In the simulator, represent the position of the head by an integer which denotes the distance of the head from the right end of the tape; then the integer can be stored in binary notation and a command to move the tape head one cell left can be realized by adding 1 to this integer. A command to move right will result in the subtraction of 1 from this integer. With $[\log_2 S]$ bits[12] of storage and as many full adders, the sequential machine simulating the tape head movements can be realized. Now, however, $[\log_2 S]$ clock cycles will be required to change the position of the tape head, since carry propagation will occur in general. Each full adder can be realized with a few logic elements, so that by "stretching" the adder, we can simulate the tape head with a machine that executes one cycle for each input and has a number of logic elements that is a small multiple of $[\log_2 S]^2$.

Once the position of the tape head is fixed by the above sequential machine, the state of this machine can be used to gate the individually accessed memory cells. We use a group of m binary cells to represent each tape square, and the jth group will be accessed when the state s of the simulator represents the integer j. Let T_j be the control signal which gates the jth group. This can be realized by a $[\log_2 S]$-input *and* gate with complementation of inputs so that the output T_j is 1 if, and only if, the state s represents j (Fig. 14). Such an *and* gate can be realized with a number of 2-input gates that does not exceed $[\log_2 S]$-1. If each T_j is realized separately, a total of $S([\log_2 S]\text{-}1)$ gates would be required. We now show that this number can be considerably reduced if we use the redundancy in these circuits.

Consider a circuit $M(n)$ which realizes all 2^n minterms in n variables (T_j is a minterm). This can be realized from

[12] $[x]$ is the smallest integer greater than or equal to x.

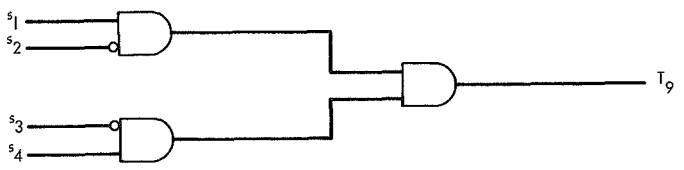

Fig. 14. Circuit realizing T_9

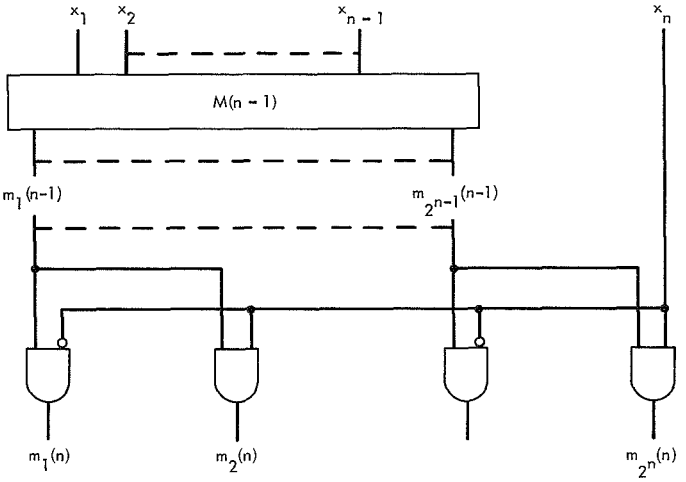

Fig. 15. Circuit for realizing $M(n)$ from $M(n-1)$

$M(n-1)$ by the addition of 2^n logic, as shown in Fig. 15. Here $x_1, \cdots, x_n$ are binary inputs, and $m_i(n-1)$ is the ith minterm in $n-1$ variables. Since a minterm in n variable is formed by the *and* of $m_i(n-1)$ for some i with x_n or $\bar{x}_n$, the circuit shown will generate $M(n)$. If $|M(n)|$ denotes the number of elements in circuit $M(n)$, we have the recursive inequality

$$|M(n)| \leq |M(n-1)| + 2^n \tag{3}$$

whose solution is

$$|M(n)| \leq 2^{n+1} \tag{4}$$

since $|M(2)| = 4$. If we let $n = \log_2 S$, we have

$$|M(n)| \leq 4 \tag{5}$$

and this circuit generates all the needed minterms $T_1, T_2, \cdots, T_S$.

In Fig. 16 we show one cell of a group of m cells which are controlled by the gating signal T_j. When $T_j = 0$, the contents of a cell are recirculated. When $T_j = 1$, the new inputs $i_1, i_2, \cdots, i_m$ are entered from the tape head input and the stored entries are read out through $[\log_2 S]$-input *or* gates. Each group of m cells has $4m$ gates associated with it. Thus, the total number of logic elements involved in this simulation of the tape and head is bounded by

$$\alpha[\log_2 S]^2 + 4S(m+1) + m\,2[\log_2 S] \tag{6}$$

where the middle term measures the number of gates used to create the T_j's and control the cells and the right-

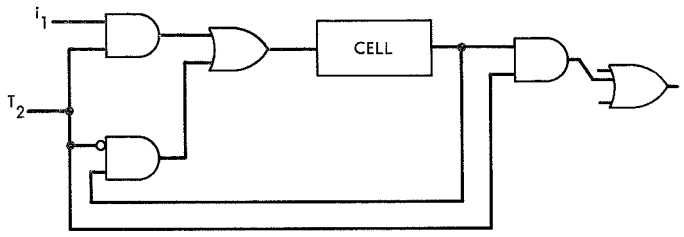

Fig. 16. Storage cell and control

hand term is a bound on the number of 2-input *or* gates needed to read out each of the m cells under examination.

Let m be fixed. Then, for large S we have the computing power of tape memory P_T bounded by

$$S \leq P_T \leq 4S(m+1)(1+\epsilon) \tag{7}$$

for some fixed $\epsilon > 0$ where S is the number of tape squares.

With core storage, the S groups of M cells to be read are identified by a pair of integers each of which has maximum size $\sqrt{S}$. Each integer can be represented by $[\log_2 \sqrt{S}]$ binary digits, and gating networks identical in form with those that compute T_j above can be formed. These gates will have $2[\log_2 \sqrt{S}] \leq \log_2 S + 2$ inputs. The memory cells and associated logic can be realized as above, and we have for the computing power of core storage P_c

$$S \leq P_c \leq 4S(m+1)(1+\epsilon) \tag{8}$$

for large S with fixed $\epsilon > 0$.

d. Conclusions. Now that replacements for the tape and core storage control units have been exhibited which use only logic elements and individually accessed cells, we can combine the logic elements of these replacements with the X logic elements of the logic unit L (Fig. 13) as is done in Eq. (1). Consider now a general-purpose computer with tape storage (such as a one-tape universal Turing machine) or core storage. If the number of storage cells S used in a computation is large, the size X of the logic unit can be neglected relative to the size of P, the computing power of storage. From Eq. (1) we have

$$PT(1+\delta) \geq C(f) \tag{9}$$

for some fixed small $\delta > 0$. Equations (7) and (8) can be used in Eq. (9), and we have for large S and sufficiently complex functions f

$$\frac{C(f)}{1+\epsilon'} \leq 4ST(m+1) \tag{10}$$

where $1 + \epsilon' = (1+\epsilon)(1+\delta)$.

This demonstrates that the product of S and T will be large on general-purpose computers that compute complex functions.

Equation (10) has a little more significance when frequently used functions are shown to be complex. Consider then the class of $n \times n$ binary matrices, there being 2^{n^2} such matrices. In Ref. 1 we show that the number of different combinational machines with p inputs and q outputs which can be constructed with C or fewer two-input binary logic elements cannot exceed $(C+p)^{2(C+q)}$. If we use such machines to create the matrix functions and choose C to satisfy

$$(C+n)^{2(C+n)} = 2^{n^2(1-\varepsilon)} \tag{11}$$

where the number of inputs and outputs are set to n, then not all matrix functions can be realized with this many logic elements. As a matter of fact, only the fraction F of these functions can be realized where

$$F \leq 2^{-n^2\varepsilon} \tag{12}$$

and F approaches zero with increasing n. Solving Eq. (11) for C we find that *almost all binary matrix operations require a C(f) satisfying*

$$C(f) \geq \frac{[n^2(1-\epsilon)/2]}{\log_2 [n^2(1-\epsilon)/2]} \tag{13}$$

which is very substantial for large n.

Reference

1. Savage, J. E., "The Complexity of Decoders—Part I: Classes of Decoding Rules," *IEEE Trans.*, Vol. IT-15, No. 6, pp. 689–695, 1969.

4. Digital Acquisition and Detection: Minimum Switching Network for Generating the Weight, in Binary Notation, of a Binary Vector, *T. O. Anderson*

a. Introduction. Implementation of the weight function, in binary notation, of a binary vector finds numerous applications in DSN coding systems. It applies not only to the encoders and decoders of both block codes and convolutional codes, but also to coding systems used in searching for good codes. This article discusses the most common implementation of this function, as well as other possible implementations. The implementation described here features maximum speed of operation with a minimum amount of hardware. The proposed switching network is entirely modular in its structure; only a single type of module is used in an iterative pattern. The module is described in detail, the modular structure is discussed, and an example of a 24-bit network is shown. The module network can be proven to be theoretically optimum for a minimum hardware, minimum propagation time network using a single type of module in an iterative pattern.

b. Application. The weight of a binary vector, i.e., the number of binary 1s in a word, is an often used function. For convenient usage, the function should be available in binary notation. One typical application is in algebraic decoding where a received word is correlated with all words in a dictionary and a search is made on the error vectors. If the weight of the error vector, i.e., the output of a bit-by-bit mod 2 comparison, can be made available in parallel in binary notation, the search can be made simply and rapidly using a qualitative binary comparator. A hold register will hold both the weight function of the error vector that has given the best correlation so far and the corresponding dictionary word.

Other applications for the weight vector occur in searches for optimum comma-free vectors for efficient block codes. In convolutional coding, searches are made for minimum weight to determine error correction capabilities.

c. General design practices. In designing digital circuitry, the speed of operation and the amount of hardware needed often result in contradicting requirements. Engineering compromises may then favor serial or parallel operation. In recent developments, speed of operation is often the major concern; therefore, parallel operation becomes the chosen concept.

d. Most-common design. The most-common design is the sequential design, which is also the minimum hardware design. As shown in Fig. 17, the data word is transferred into a shift register. The output from the register is the carry input to a binary counter. A clock common to both the shift register and the counter will shift the contents out of the register and the counter will be augmented every time a binary 1 occurs at its carry input. Accessory circuits may include a counter to count the number of shift pulses, or a gate connected to the register to detect when it is empty. If a sufficient number of shift pulses are guaranteed between transfer–counter reset pulses, no such accessory circuits are required.

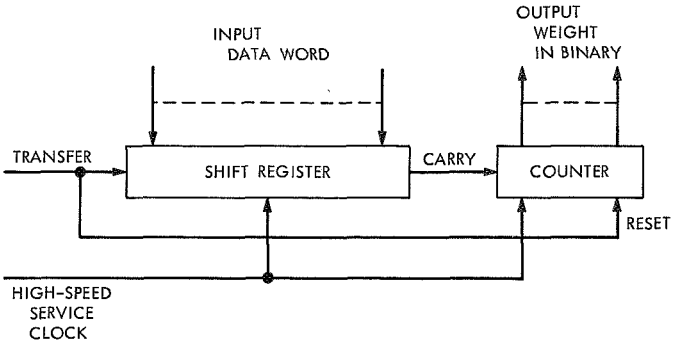

Fig. 17. Sequential design

e. Other possible designs. Recently, small-size, high-speed, medium-resolution, low-cost analog-to-digital converter modules have become available. Most of these units operate on the successive approximation principle, and the conversion times are in the order of 5 to 1 μs. In some instances, it may then prove reasonable simply to form a digital-to-analog-to-digital conversion. As depicted in Fig. 18, the digital-to-analog resistive ladder network includes resistors all of the same size.

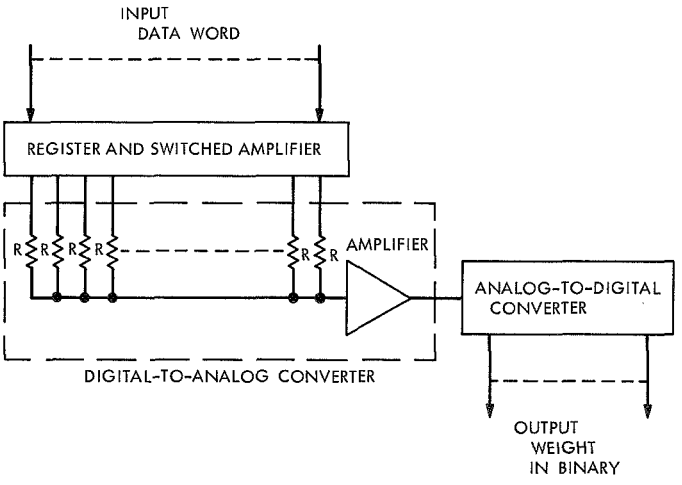

Fig. 18. Digital-to-analog-to-digital conversion design

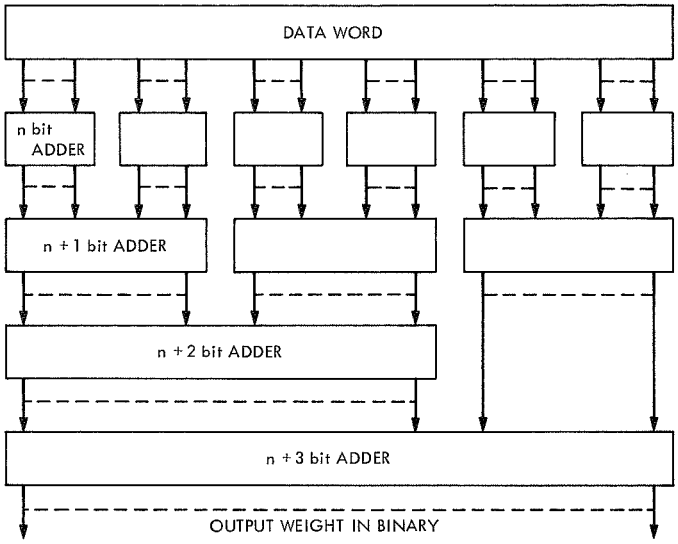

Fig. 19. Regular adder design

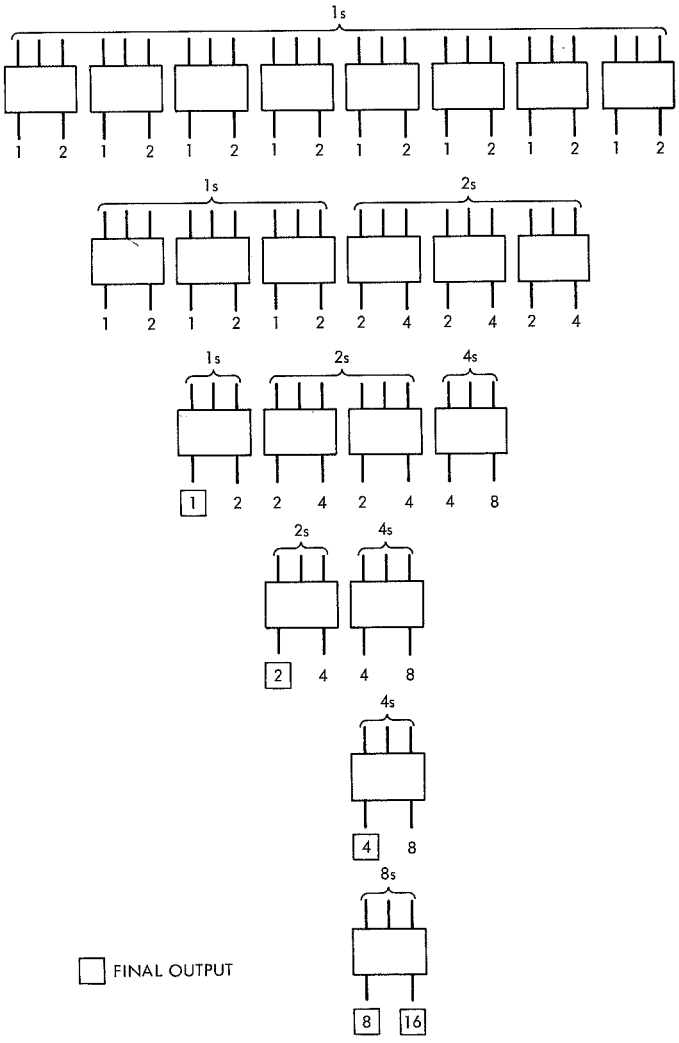

Fig. 20. 24-bit weighting network example

The third of three possible designs known is that depicted in Fig. 19. The original word is divided into smaller sections for efficient conversion from unary-to-binary. The binary outputs are then simply added in parallel binary adders increasing 1 bit for each level. For higher speed generation of the weight function, this is an acceptable method; however, this method does not immediately lend itself to modular implementation. ("Modular implementation" as used here refers to a switching network that can be constructed of a number of identical Medium-Scale Integrated Circuits (MSIs) in a repetitive manner.)

f. Present design. In this design, the original word is first divided into smaller sections with each section converted in a unary-to-binary converter or decoder. This decoder then becomes "the module" that is used in a repetitive manner for each level of the network. A 3-input–2-output module is used.

g. Network. The outputs from the first level modules are 1s and 2s respectively. (For reference, see Fig. 20.) All 1s terms are collected and entered as inputs to the second-level modules, and all 2s terms are collected and entered as inputs to other second-level modules in the same manner. Only one kind of input terms can be entered to any one module. This collecting of outputs of the same kind used as the only kind of inputs to any one module is continued until there is only one 1s, one 2s, one 4s, etc.

h. Module. The most efficient unary-to-binary converter module is one whose binary output terms are equally exercised. In terms of number of inputs, then, this means 3, 7, 15, etc. With the present MSI technology, 3-input–2-output modules appear most practical. Figures 21 and 22 show two minimum-propagation versions of such a mod-

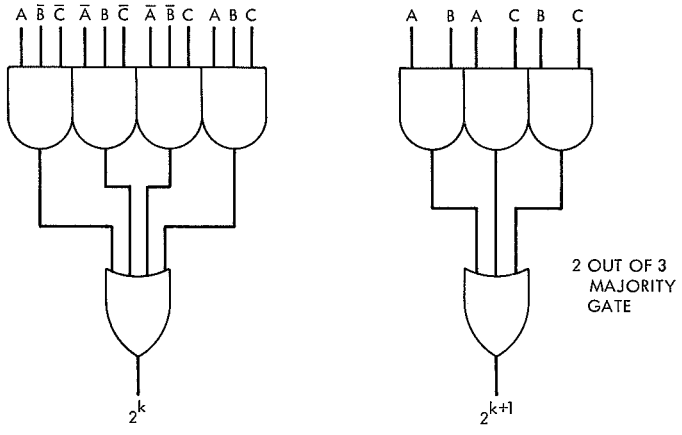

Fig. 21. Typical module

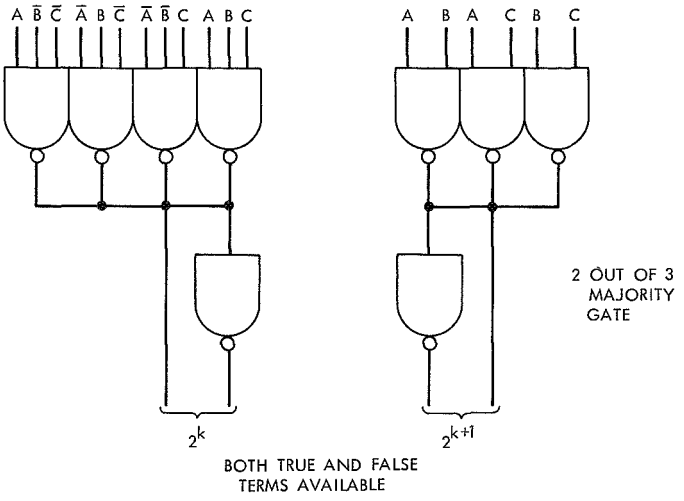

Fig. 22. Typical module collector or version

ule. (A truth table for Figs. 21 and 22 is presented as Table 2.) Figure 22 is the collector-*or* version, which may be the better since both the "true" and the "bar" terms of the outputs are readily available.

Selection of a three-input module also corresponds to a full adder, which has the same truth table. The carry-in, augend, and addend, then correspond to the inputs A, B, and C and the sum and carry-out to the 2^k and 2^{k+1} outputs, respectively (Table 2). Typical integrated circuits that are usable as "the module" are the full adders such as Sylvania's SM-10 and Texas Instrument's SN7480.

Fairchild's 9304, National Semiconductor's DM7283 and Motorola's MC9304 include two independent full adders per package.

Any 4-bit full adder, such as Signetics' 8260, can also be used as two independent 2-bit full adders. The connection is then as follows: X_1, Y_1, carry-in are inputs and Σ_1, Σ_2 are

Table 2. Truth table

Input			Output	
A (carry-in)	B (augend)	C (addend)	2^{k+1} (carry-out)	2^k (sum)
0	0	0	0	0
0	0	1	0	1
0	1	0	0	1
0	1	1	1	0
1	0	0	0	1
1	0	1	1	0
1	1	0	1	0
1	1	1	1	1

outputs for adder I. X_2 and Y_2 are wired to zero and X_3, Y_3 are tied together and form the carry input for adder II.

X_4, Y_4 are the two other inputs for adder II. Σ_4 and carry-out are the outputs in adder II. Σ_3 is not used.

i. Number of modules required. Following an argument suggested by W. J. Hurd, it can be shown that the number of modules required is always less than n. Each module with three inputs of significance 1 has one output of significance 1 and one of significance 2. Enough modules with "1s" inputs are required to reduce the number of "1s" to one. This clearly requires $n/2$ modules if n is even, and $(n-1)/2$ modules if n is odd, or $[n/2]$ modules where $[x]$ indicates the greatest integer $\leq x$. The $[n/2]$ modules with "1s" inputs have $[n/2]$ "2s" outputs. Following the same argument as above, $[n/4]$ modules with "2s" inputs are required, $[n/8]$ modules with "4s" inputs are required, etc.

The minimum number of modules required for n input variables is then

$$\left[\frac{n}{2}\right]+\left[\frac{n}{4}\right]+\left[\frac{n}{8}\right]+\cdots+$$

which series can be summed for all ns to $n-m$ where m, interestingly enough, is the "weight" of the binary representation of n. The number of modules required is then always $\leq n-1$.

j. Conclusion. As is often the case with simple designs, so it is here; once the module and the modular network have been conceived and explained, the solution appears entirely obvious. Again, for reference, see Figs. 21 and 22. It also may be of interest to note that in combination with simple comparator gates, the weighting network can also be used as a majority network. For $n-1$, where n is a power of 2, the most-significant-bit output from the weighting network is, of course, the majority output.

5. Digital Acquisition and Detection: Numerical Interactive Controller, *S. Brokl*

a. Introduction. The numerical interactive controller (NIC) gives additional versatility to the Digital Video Display System (DVDS) (SPS 37-60, Vol. II, pp. 22–28). It provides X–Y positional information to the operator to allow him to modify displayed data. The NIC is primarily designed to solve the user interface problem for two-dimensional processing of range-doppler data or for real-time data evaluation by experimenters as required in the

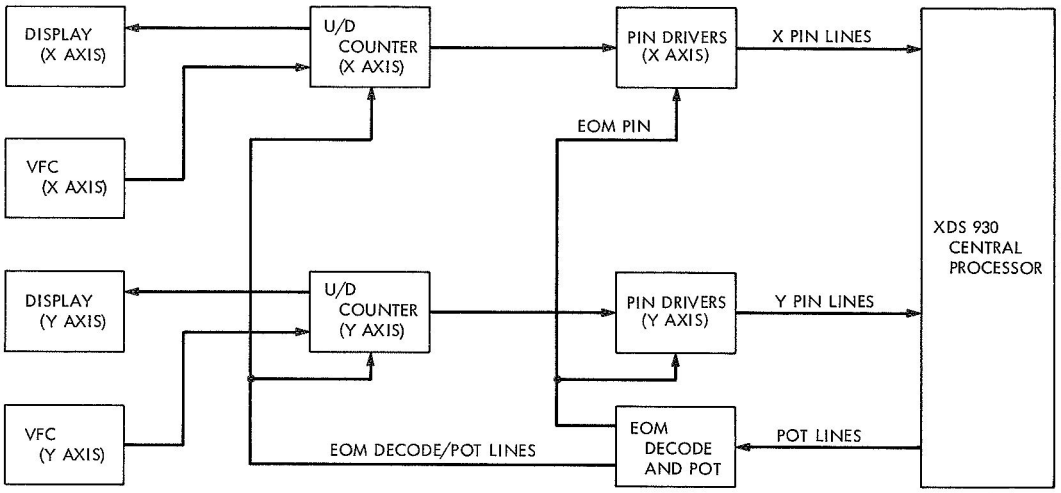

Fig. 23. NIC block diagram

SFOF Mark III. The NIC is compatible with XDS 900-series computers and can be used wherever X–Y positional information is needed.

The NIC consists of an X channel and a Y channel. Each channel contains a binary-coded decimal (BCD) up/down (U/D) counter, a variable-frequency clock oscillator, and a numerical display. Together, the channels can generate decimal numbers corrresponding to any point in a cartesian coordinate system. The U/D counters can also be preset and work as registers that display the numbers set into them.

b. Design considerations. The NIC was required to be compatible with XDS 900-series computers (SPS 37-39, Vol. III, pp. 52–65), and easily operated. Also, the NIC required a numerical display that could operate from existing supply voltages and be compatible with transistor–transistor logic. A clock source independent of the computer and with variable frequency had to be generated. The counters had to be presetable from the computer and generate BCD numbers for the display. The control console for the NIC could not be larger than a telephone receiver because of the available operating space.

c. Hardware. Figure 23 is a block diagram of the NIC. The NIC supplies and displays BCD numbers to the SDS 930 computer. It also stores and displays BCD numbers set into it from the computer.

The circuit consists of two variable frequency clocks (VFC) controlled from a joystick; two sets of presetable U/D three-digit BCD counters; two three-digit and sign light-emitting diode (LED) displays; and an EOM decode, PIN/POT control logic.

Figure 24 is a photograph of the NIC control console. The control console contains the joystick, the VFC, and LED displays.

Figure 25 is a photograph of the X and Y channel counters and EOM decode, PIN/POT, control logic cards.

Fig. 24. NIC control console

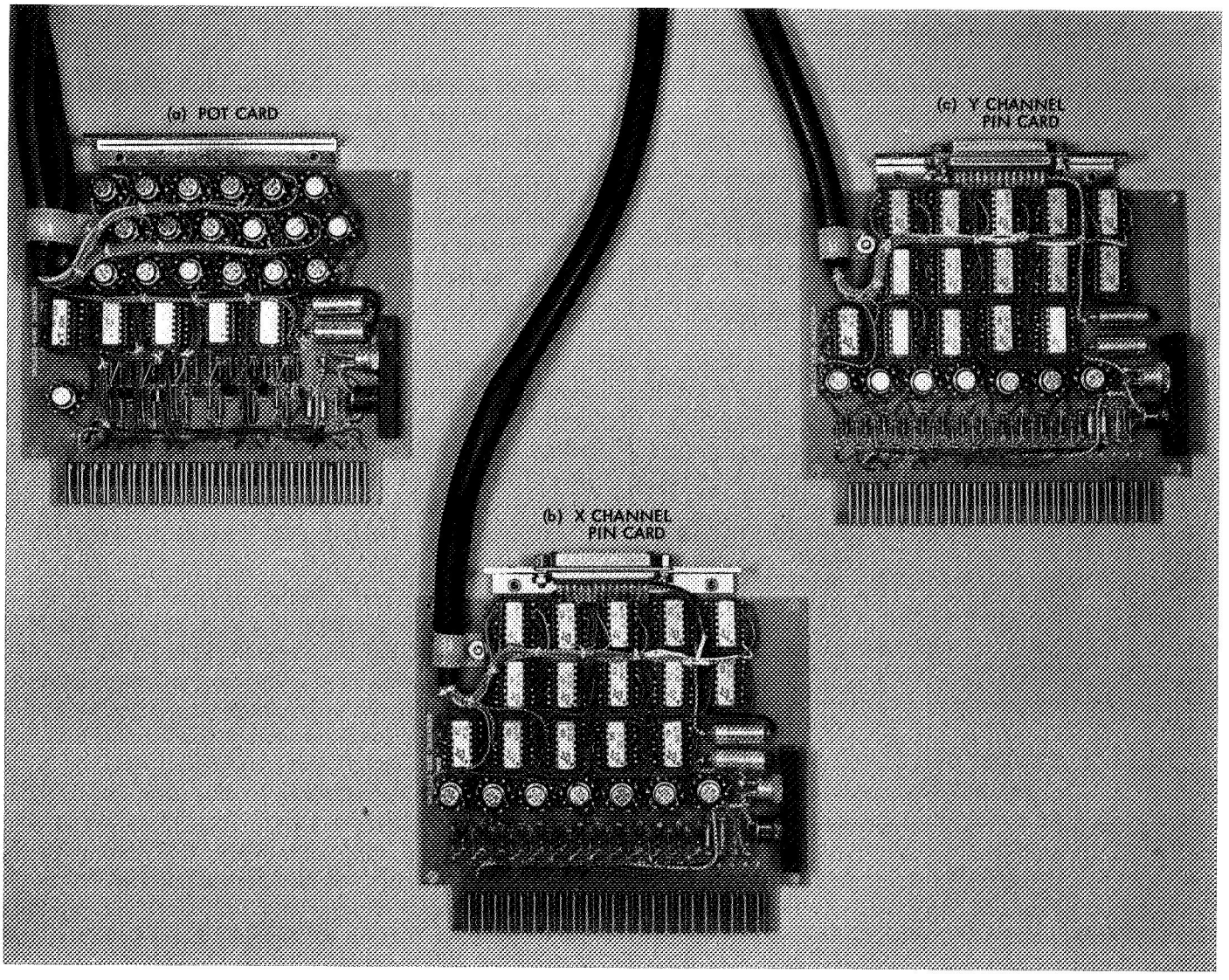

Fig. 25. POT card, X channel PIN card, and Y channel PIN card

The two PIN cards are identical, one each for the X and Y channels. The NIC control console connects to the PIN cards through a 30-ft cable.

d. Operation. A joystick controls the VFC rates and the direction of the U/D counters. The VFC rate is proportional to the amount of displacement of the joystick and the position of the clock rate switch. The lowest rate (1 Hz) is for zeroing in on a single point; the highest rate (1 kHz) is for slewing between separated points. A reset is provided to zero the U/D counters. The power on/off affects only the control console power.

e. Software and interface. Table 3 illustrates the EOM code and describes the functions it performs with a PIN or POT instruction. Table 4 illustrates the BCD interface connections used with the XDS 930 computer. NIC programming is dependent upon its use.

Table 3. EOM codes and function

EOM Code				Function
Instruction	System	Function code	Class-unit	
EOM	3	01	22	Load X: POT—load contents of computer C register into NIC X register. PIN—load contents of NIC X register into computer C register.
EOM	3	02	22	Load Y: POT—load contents of computer C register into NIC Y register. PIN—load contents of NIC Y register into computer C register.
EOM	3	03	22	Reset NIC X and Y registers.

Table 4. PIN/POT data interface connections to XDS 930 computer

PIN/POT lines	BCD	Function
$\overline{C0}$	+	Sign
C0	—	
C8	8	Most significant digit-100s digit
C9	4	
C10	2	
C11	1	
C14	9	10s digit
C15	4	
C16	2	
C17	1	
C20	8	1s digit
C21	4	
C22	2	
C23	1	

f. Conclusion. The NIC is versatile and can be adapted for use in a wide variety of applications where positional information is needed. In conjunction with the DVDS or an X–Y plotter, it can be used for drawing pictures and finding or moving data points.

6. Digital Acquisition and Detection: Solution of a Toeplitz Set of Linear Homogeneous Equations, *S. Zohar*

a. Introduction. The solution of a set of linear equations whose associated matrix has a Toeplitz structure can be effected with remarkable speed when algorithms exploiting the special structure are applied (SPS 37-61, Vol. III, pp. 65–73).

To be more specific, let us denote by K the number of arithmetic operations required to multiply a kth order arbitrary matrix by a compatible column matrix and adopt this number ($K = 2k^2$) as a yardstick for comparison. The referred algorithms require $3K$ operations to solve a set of k linear equations. When the associated Toeplitz matrix is Hermitian, this number drops to $2K$.

These numbers can be further reduced when the set of equations is homogeneous. Equation sets of this type occur in various fields. As a specific example, let us mention the construction of a gaussian quadrature formula. The sample points for such a formula are the roots of a polynomial whose coefficients are the solution of a homogeneous Toeplitz set of linear equations. We propose to show here that the solution in this case requires $2K$ operations when the associated Toeplitz matrix is non-Hermitian and K operations when it is Hermitian. In other words, the solution of a Hermitian Toeplitz set of k linear homogeneous equations can be implemented in about the time it takes to multiply a $k \times k$ matrix by a compatible column matrix!

b. Preliminaries. We adopt here the following notation conventions: Greek letters are used for scalars; capital letters are for square matrices; lower case letters are for column matrices; and transposition is indicated by the symbol $\sim$. Thus,

L_k is a $k \times k$ matrix.

g_k is a $k \times 1$ matrix.

$\tilde{g}_k$ is a $1 \times k$ matrix.

λ_k is a scalar.

In the framework of this notation we reserve the symbol I_k to the kth-order identity matrix and the symbol 0_k to a zero column matrix. Another symbol which will appear quite often in the derived algorithms is the reversal symbol $\wedge$. Given the column matrix g_k, we use $\hat{g}_k$ to denote the reversed order version of g_k; that is,

$$(\hat{g}_k)_{i,1} = (g_k)_{k+1-i,1} \tag{1}$$

Applying this notation, a homogeneous set of $(n+1)$ linear equations is expressed as

$$L_{n+1}\, s_{n+1} = 0_{n+1} \tag{2}$$

We are concerned here with the case where L_{n+1} is a Toeplitz matrix which we express as follows:

$$L_{n+1} = \begin{bmatrix} 1 & \tilde{a}_n \\ r_n & L_n \end{bmatrix} \tag{3}$$

where

$$\tilde{a}_n = [\rho_{-1}\, \rho_{-2} \cdots \rho_{-n}]$$

$$\tilde{r}_n = [\rho_1\, \rho_2 \cdots \rho_n]$$

Note that we have assumed L_{n+1} to have units along its main diagonal. The algorithm developed here is limited to the case where all of the principal minors of L_{n+1} (in Eq. 2) are nonzero. Hence, it is always possible to bring L_{n+1} to the form of Eq. (3).

Straightforward application of the general algorithm (SPS 37-61, Vol. III, pp. 65–73) to Eq. (2) is pointless, as it yields the trivial solution 0_{n+1}. To get the nontrivial solution, one should convert the homogeneous set of $(n+1)$ equations to a nonhomogeneous set of n equations. (We are restricting the discussion here to the case in which the rank of L_{n+1} is n.) It can be shown, however, that in following this course some of the computations are redundant and can be eliminated, thus leading to a faster algorithm. In the following we establish this algorithm in a more direct way.

c. Derivation of the algorithm. The set of equations considered is

$$L_{n+1}\, s_{n+1} = \begin{bmatrix} 1 & \tilde{a}_n \\ r_n & L_n \end{bmatrix} s_{n+1} = 0_{n+1} \tag{4}$$

in which the rank of L_{n+1} is n; that is,

$$|L_{n+1}| = 0;\ |L_n| \neq 0 \tag{5}$$

But, in general (Ref. 1),

$$|L_k| = \prod_{i=1}^{k-1} \lambda_i \tag{6}$$

Hence

$$\lambda_n = 0;\ \lambda_{n-1} \neq 0$$

The parameters λ_i are known functions of ρ_{-k}, ρ_k $(1 \leq k \leq i)$ (Ref. 1). Therefore, any modification of ρ_{-n}, ρ_n will leave intact λ_i $(1 \leq i < n)$ and modify λ_n.

Let us now perturb ρ_{-n}, ρ_n slightly (using primes to denote perturbed quantities) so as to ensure

$$\lambda'_n \neq 0$$

The perturbed L'_{n+1} is no longer singular, and we express its inverse as follows:

$$(L'_{n+1})^{-1} = \frac{1}{\lambda'_n} \begin{bmatrix} 1 & \tilde{e}'_n \\ g'_n & M'_n \end{bmatrix} \tag{7}$$

noting that e'_n, g'_n are known finite functions of a'_n, r'_n (Ref. 1). Multiplying Eq. (7) by L'_{n+1} we get

$$\begin{bmatrix} 1 & \tilde{a}'_n \\ r'_n & L_n \end{bmatrix} \begin{bmatrix} 1 & \tilde{e}'_n \\ g'_n & M'_n \end{bmatrix} = \lambda'_n I_{n+1}$$

and hence

$$\begin{bmatrix} 1 & \tilde{a}'_n \\ r'_n & L_n \end{bmatrix} \begin{bmatrix} 1 \\ g'_n \end{bmatrix} = \begin{bmatrix} \lambda'_n \\ 0_n \end{bmatrix} \tag{8}$$

At this point we introduce a limiting process leading back to the unperturbed quantities

$$\rho'_{-n} \to \rho_{-n}; \qquad \rho'_n \to \rho_n; \qquad \lambda'_n \to \lambda_n = 0$$

getting

$$\begin{bmatrix} 1 & \tilde{a}_n \\ r_n & L_n \end{bmatrix} \begin{bmatrix} 1 \\ g_n \end{bmatrix} = 0_{n+1} \tag{9}$$

This means that s_{n+1}, the desired solution of Eq. (2) is given by

$$s_{n+1} = k \begin{bmatrix} 1 \\ g_n \end{bmatrix}, \qquad k \text{ arbitrary} \tag{10}$$

All that is needed to solve Eq. (2) is the application of a known algorithm (Ref. 1) to evaluate g_n. Furthermore, it has been shown (SPS 37-61, Vol. III, pp. 65–73) that this algorithm requires $4n^2$ arithmetic operations for a non-Hermitian L_{n+1} and $2n^2$ arithmetic operations in the Hermitian case. This, then, verifies the claim stated in the introduction.

We conclude this presentation with a complete specification of the algorithms in these two cases.

Algorithm for homogeneous Toeplitz equations of rank n (non-Hermitian case)

Problem Formulation

$$L_{n+1} s_{n+1} = 0_{n+1}$$

$$L_{n+1} = \begin{bmatrix} 1 & \tilde{a}_n \\ r_n & L_n \end{bmatrix}$$

$$\tilde{a}_i = [\rho_{-1}, \rho_{-2}, \cdots, \rho_{-i}], \qquad 1 \leq i \leq n$$

$$\tilde{r}_i = [\rho_1, \rho_2, \cdots, \rho_i], \qquad 1 \leq i \leq n$$

$$s_{n+1} = ?$$

Initial Values for Recursion

$$e_1 = -\rho_{-1} \qquad g_1 = -\rho_1$$

$$\lambda_1 = 1 - \rho_{-1}\rho_1$$

Recursion of $\hat{e}, g, \lambda$ $(i = 1, 2, \cdots)$

$$\eta_i = -\rho_{-(i+1)} - \tilde{a}_i \hat{e}_i \qquad \gamma_i = -\rho_{i+1} - \tilde{g}_i \hat{r}_i$$

$$\hat{e}_{i+1} = \begin{bmatrix} \dfrac{\eta_i}{\lambda_i} \\ \hat{e}_i + \dfrac{\eta_i}{\lambda_i} g_i \end{bmatrix} \qquad g_{i+1} = \begin{bmatrix} g_i + \dfrac{\gamma_i}{\lambda_i} \hat{e}_i \\ \dfrac{\gamma_i}{\lambda_i} \end{bmatrix}$$

$$\lambda_{i+1} = \lambda_i - \frac{\eta_i \gamma_i}{\lambda_i}$$

The Solution

$$s_{n+1} = k \begin{bmatrix} 1 \\ g_n \end{bmatrix}, \qquad k \text{ arbitrary}$$

Solvability Constraint

$$\lambda_n = 0$$

Or, equivalently

$$1 + \tilde{a}_n g_n = 0$$

Or, equivalently

$$1 + \tilde{\hat{r}}_n \hat{e}_n = 0$$

Algorithm for homogeneous Toeplitz equations of rank n (Hermitian case)

Problem Formulation

$$L_{n+1} s_{n+1} = 0_{n+1}$$

$$L_{n+1} = \begin{bmatrix} 1 & \tilde{r}_n^* \\ r_n & L_n \end{bmatrix}$$

$$\tilde{r}_i = [\rho_1, \rho_2, \cdots, \rho_i], \qquad 1 \leq i \leq n$$

$$s_{n+1} = ?$$

Initial Values for Recursion

$$g_1 = -\rho_1$$

$$\lambda_1 = 1 - |\rho_1|^2$$

Recursion of $g, \lambda (i = 1, 2, \cdots)$

$$\gamma_i = -\rho_{i+1} - \tilde{g}_i \hat{r}_i$$

$$g_{i+1} = \begin{bmatrix} g_i + \dfrac{\gamma_i}{\lambda_i} \hat{g}_i^* \\ \dfrac{\gamma_i}{\lambda_i} \end{bmatrix}$$

$$\lambda_{i+1} = \lambda_i - \frac{|\gamma_i|^2}{\lambda_i}$$

The Solution

$$s_{n+1} = k \begin{bmatrix} 1 \\ g_n \end{bmatrix}, \qquad k \text{ arbitrary}$$

Solvability Constraint

$$\lambda_n = 0$$

Or, equivalently

$$1 + \tilde{\hat{r}}_n \hat{g}_n^* = 0$$

Reference

1. Zohar, S., "Toeplitz Matrix Inversion: The Algorithm of W. F. Trench," *J. Assn. Comp. Mach.*, Vol. 16, No. 4, pp. 592–601, October 1969.

7. Information Systems: Performance of Short Constraint Length Convolutional Codes and a Heuristic Code-Construction Algorithm, J. W. Layland

a. Introduction. The simulated bit-error performance of short constraint length convolutional codes discussed in SPS 37-54, Vol. III, pp. 171–177 has created considerable interest, both at JPL and elsewhere, in the application of Viterbi's optimal decoding algorithm to actual communications. However, the original simulation results included only three codes, thus providing only a part of the information needed to make a decision on the design constraint length of a hardware optimum convolutional decoder. The decoder would be able to decode at least one code of each constraint length less than or equal to the design constraint length, but none larger.

This article presents simulated bit-error probability curves for convolutional codes of constraint lengths K = 3 to K = 10. The K = 3 and K = 4 codes are those discussed previously (SPS 37-54, Vol. III, pp. 171–177 and SPS 37-58, Vol. III, pp. 50–55). All codes of longer constraint length were constructed using a hill-climbing algorithm discussed in *Paragraph b* of this article. The simulated bit-error rates were obtained using the software optimum convolutional decoder described in SPS 37-62, Vol. II, pp. 61–66.

b. The code-construction algorithm. A convolutional code with constraint length K and rate 1/V is normally represented as a shift register of length K coupled with V multi-input mod-2 adders. Each information bit to be encoded is shifted into the shift register and the outputs of the V adders are sampled and transmitted sequentially. Such a code can be made into a block code of h information bits and $V(K + h - 1)$ channel symbols by requiring that all information bits before time 1 and after time h be identically zero. This is the technique used to determine the best known bounds to the free-distance of a convolutional code. (SPS 37-50, Vol. III, pp. 248–252.)

In a similar manner, one may approximate the bit-error probability of the convolutional code by considering only those error patterns that differ from the true sequence only in h or less consecutive positions. If the contribution to the bit-error probability from error events of length longer than h is sufficiently small, this will be a good approximation to the bit error probability. Since the free-distance bound becomes increasingly loose as h increases beyond a critical value, there seems to be some heuristic justification in assuming that there is a value of h, not too large, such that the contribution to the bit-error probability from error events longer than h is negligible.

Let I_i represent a bit sequence that is the binary expansion of the integer i, $C * I_i$ represent the coder output sequence corresponding to the input I_i, and $W_H(x)$ be the Hamming weight of the sequence x. Then a "union bound" to this approximate bit-error probability is given by (Ref. 1)

$$P_e^h \leq \sum_{\substack{i=1 \\ i \text{ odd}}}^{2^h - 1} W_H(I_i) \operatorname{erfc}\left(\frac{W_H(C * I_i) E_b}{V \cdot N_0}\right) \qquad (1)$$

where E_b is bit energy, and N_0 is the one-sided noise spectral density, assumed white and Gaussian. This bound, in turn, is upper bounded by

$$P_e^h \leq P_e'^h = \sum_{\substack{i=1 \\ i \text{ odd}}}^{2^h-1} W_H(I_i) \exp\left(\frac{-W_H(C * I_i) E_b}{V \cdot N_0}\right) \qquad (2)$$

The code construction technique discussed here uses $P_e'^h$ as a measure of the performance of the code. A hill-climbing algorithm is given that makes changes in the code's parity check equations; these changes effect the steepest descent in $P_e'^h$. The specific algorithm is as follows: Select a set of parity check equations from which to begin. This starting point may be arbitrary, but the most success has been achieved using check equations that are either all "zeros," or else have "ones" at the first and Kth positions only. $P_e'^h$ is computed for this starting code and for all $V \cdot K$ alternate codes within a radius-one Hamming neighborhood of the original code; i.e., all codes that differ from the original code in exactly one position. The code with the smallest $P_e'^h$ is selected as the starting code for the next iteration. The process terminates when none of the alternate codes have smaller $P_e'^h$ than does the base code of that iteration. No provision is made to prevent catastrophic error propagation in the constructed code. If the final code is catastrophic, the best alternate code from the last iteration is usually the desired code. If not, a small amount of trial-and-error searching will locate a good non-catastrophic code within a radius-two Hamming neighborhood of the terminal code.

Construction of the codes discussed in this article has been performed in all cases with the block-size $h = K$, $K+1$, or $K+2$, and with $\exp\{-E_b/V \cdot N_0\} = 0.1$. When starting from check equations with very few "ones," the algorithm has been observed to always add "ones," resulting in termination in approximately $KV/2$ steps, after examining about $\frac{1}{2}(KV)^2$ codes, a small subset of the 2^{KV} possibilities. Since the algorithm uses $P_e'^h$ only for selecting a code change, $P_e'^h$ need be completely computed for only one code, with $P_e'^j, j \leq h$, computed for all others. The index j need only be large enough to guarantee that these codes are poorer than the chosen code.

The results obtained with this algorithm are aptly illustrated by Fig. 26, which compares the simulated bit-error probability of the $K = 8$, $V = 3$ code constructed with the algorithm and the $K = 8$, $V = 3$ code constructed by J. Odenwalder using a global search of all codes with a free-distance criterion as code performance (Ref. 1). The algorithm is thus not only an easy way to construct reasonably good codes, but perhaps the best way to construct codes for the bit-error probabilities presently of interest in space communications.

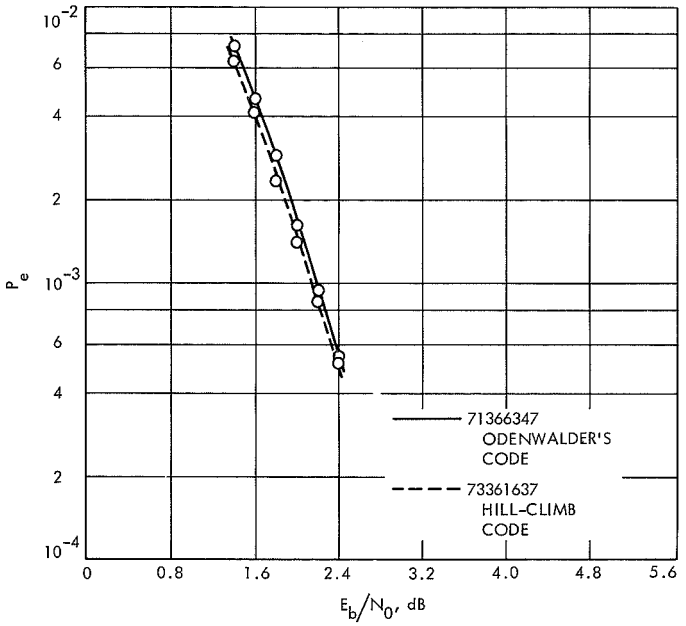

Fig. 26. Bit error probabilities of two $K = 8$, $V = 3$ codes

c. Simulation results. Figure 27 shows the simulated bit-error rate for eight convolutional codes with $K = 3$ to $K = 10$, when decoded by Viterbi's optimal decoding algorithm. The random noise was produced by the multiplicative-congruential generator ultimately adopted by Heller (SPS 37-56, Vol. III, p. 83). Codes in this figure are represented in octal, e.g., '313' represents the $K = 3$, $V = 2$ code which has

$$\begin{pmatrix} 101 \\ 111 \end{pmatrix}$$

for its parity-check equations, and '7567' represents the $K = 4$, $V = 3$ code,

$$\begin{pmatrix} 1111 \\ 1011 \\ 1101 \end{pmatrix}$$

As expected, bit-error performance is monotonic improving with constraint length, but the rate of improvement diminishes rapidly at $K = 8$ or $K = 10$.

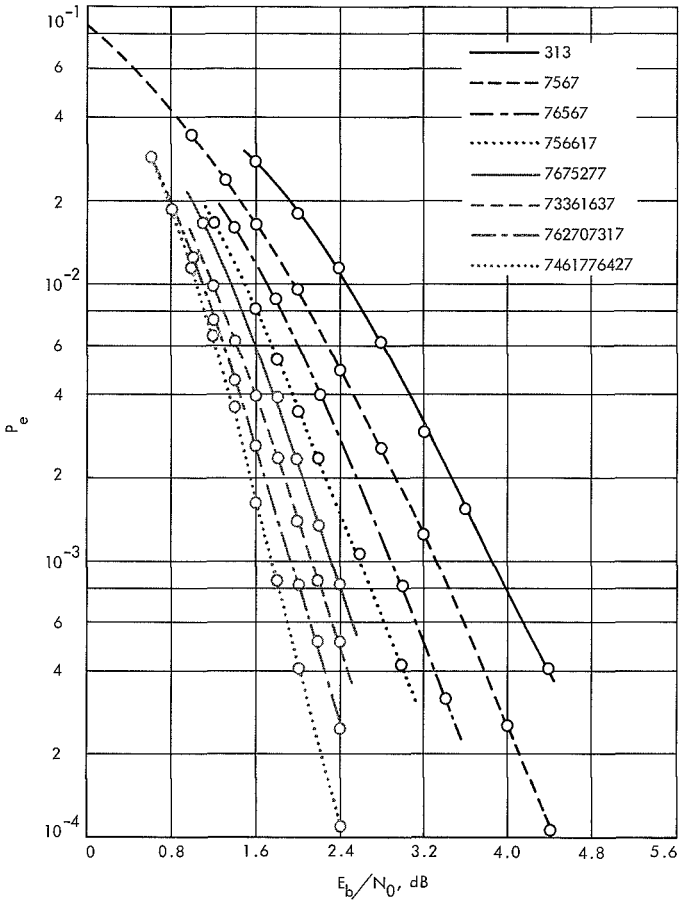

Fig. 27. Bit error probabilities of eight convolutional codes, $K = 3$ to $K = 10$

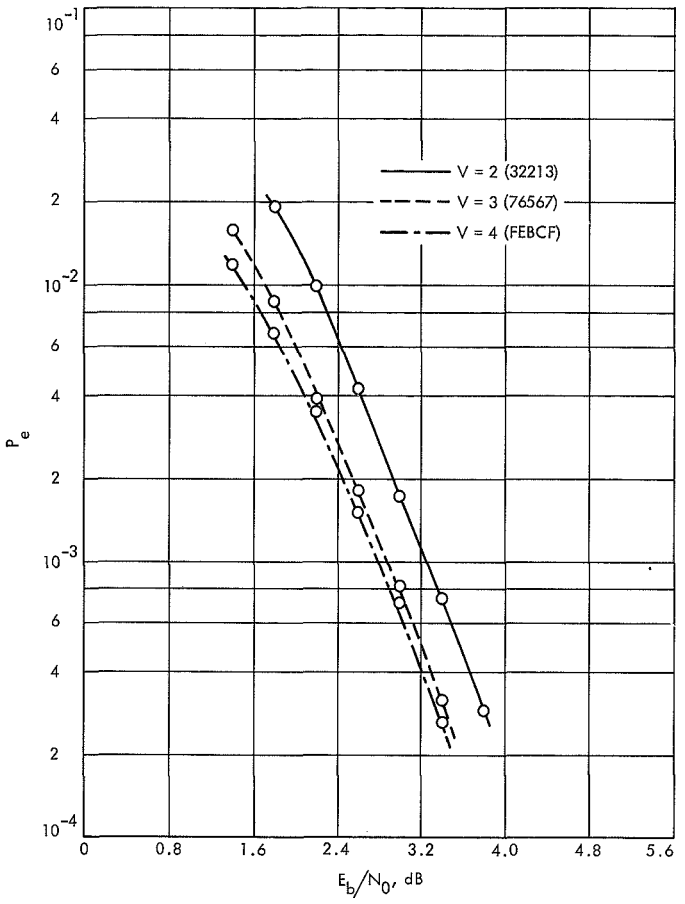

Fig. 28. Bit error probabilities of $K = 5$ codes of rate $V = 2$, $V = 3$, and $V = 4$

The effect of the code rate is illustrated in Fig. 28, which shows simulated bit-error rates for three $K = 5$ codes with rates $V = 2$, $V = 3$, and $V = 4$. The rate $V = 4$ code is given in hexadecimal notation with the symbols 0 to 9, A to F representing integers 0 to 15. The variation of the bit-error rate with code rate occurs similarly at other constraint lengths and agrees well with the behavior of the noisy-channel error rate exponent (Ref. 2).

d. Decoder complexity. An interesting view of the value of coding may be obtained by examining the "complexity" needed to achieve a design-goal bit-error rate as a function of the E_b/N_0 (Refs. 3 and 4). The complexity of an optimum convolutional decoder is approximately

$$\chi = 5K \cdot 2^{K-1} + \left(2 + \lfloor \log_2\left(\frac{KV}{2}\right) \rfloor + Q\right) 2^K + (\lfloor \log_2 (V) \rfloor + Q)\, 2^{V-1} \quad (3)$$

The notation $\lfloor x \rfloor$ represents the least integer greater than x and Q is the number of bits of quantization per symbol. Only the major components of the decoder are contained in Eq. (3). The first term is survivor storage, the second represents the state metric, and the last is caused by computing branch correlations.

Figure 29 shows the complexity as a function of the E_b/N_0 needed to achieve a 5×10^{-3} bit-error rate for the eight codes of Fig. 27. When presented in this form, the codes with $3 < K < 6$ appear to be the most desirable. For $K > 7$, the decoder complexity increases at a much faster rate than the required E_b/N_0 decreases.

Also shown in Fig. 29 for comparison is the complexity of the decoder for a bi-orthogonal block code at 5×10^{-3} bit-error probability. The block decoder is the optimally organized "Green machine" (SPS 37-39, Vol. IV, pp. 247–252). For both the block and convolutional decoders, 4-bit channel symbol quantization is assumed. At any fixed but

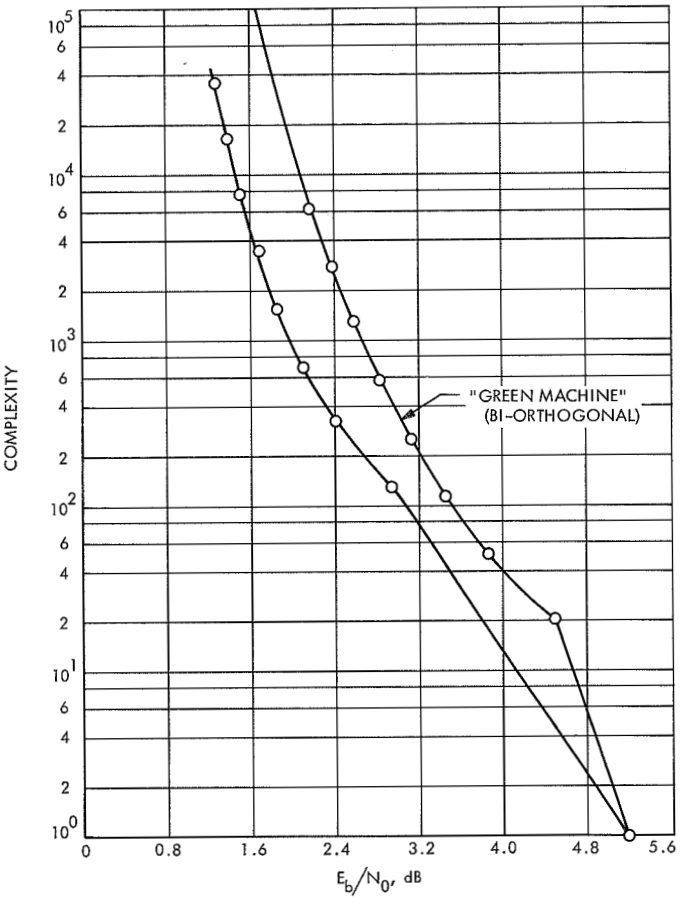

Fig. 29. Variation of decoder complexity with E_b/N_0 needed to achieve a 5×10^{-3} bit-error probability for the eight codes of Fig. 27

moderately large complexity, the convolutional codes require about 0.6 dB less E_b/N_0 to achieve the 5×10^{-3} bit-error probability than do the comparable block codes.

References

1. Odenwalder, J. P., *Optimal Decoding of Convolutional Codes*, Ph.D. dissertation. University of California at Los Angeles, Los Angeles, Calif., 1970.

2. Jacobs, I. M., "Sequential Decoding for Efficient Communications from Deep Space," *IEEE Trans. Commun. Technol.*, Vol. COM-15, pp. 492–501, Aug. 1967.

3. Savage, J. E., "Complexity of Decoders: Part I—Classes of Decoding Rules," *IEEE Trans. Inform. Theory*, Vol. IT-15, No. 6, Nov. 1969.

4. Savage, J. E., "Complexity of Decoders: Part II—Computational Complexity," Brown University Report, Providence, R.I., July 1969.

8. Information Systems: Synchronizability of Convolutional Codes, *J. W. Layland*

a. Introduction. There has been considerable interest recently in the practical application of Viterbi's optimal algorithm for decoding convolutional codes. Much of this interest arose as a result of the simulation work performed by Heller (SPS 37-54, Vol. III, pp. 171–177). These simulations, and most others, have assumed that branch synchronization is known to the decoder; i.e., that the decoder is informed as to which subgenerator of the code generates each symbol, and need not determine this from the code itself. Final coder synchronization is then achieved automatically by the decoding algorithm itself.

Although branch synchronization could be established by the use of a sync sequence periodically inserted into the data, it is much more desirable to use some property of the code itself for this purpose. For a block code, the comma-free property provides a sufficient means to establish synchronization in the *Mariner* Mars 1969 High-Rate Telemetry System. It seems intuitive that the subgenerators of any good code will be dissimilar enough that improper branch synchronization would be easily identified statistically, using the assumption that the data source is random. The truth of this notion is demonstrated by the simulation results presented in *Paragraph e* of this article. Synchronization can be achieved with more certainty, however, if some property can be found which will guarantee that only a finite number of code symbols need to be examined to identify a branch sync error. *Paragraphs b* and *c* determine the conditions that must be placed upon a convolutional code for this property to exist.

b. Convolutional codes. In its *standard form*, a constraint length K convolutional code with rate $1/V$ is represented as a shift register of length K, coupled with V parity-check adders. Each data bit to be encoded is shifted into the coder register and the oldest bit therein is shifted out. The V parity-check adders are then sampled sequentially and these binary symbols are transmitted through a channel. Figure 30 shows the encoder, channel, and decoder and the coder state diagram for a constraint length 3, rate ½ code. The output symbols for each state transition appear above each branch, and the input data bit appears below.

The channel adds a sample of white gaussian noise to each symbol. Since the channel does not explicitly provide synchronization information, the first symbol received by

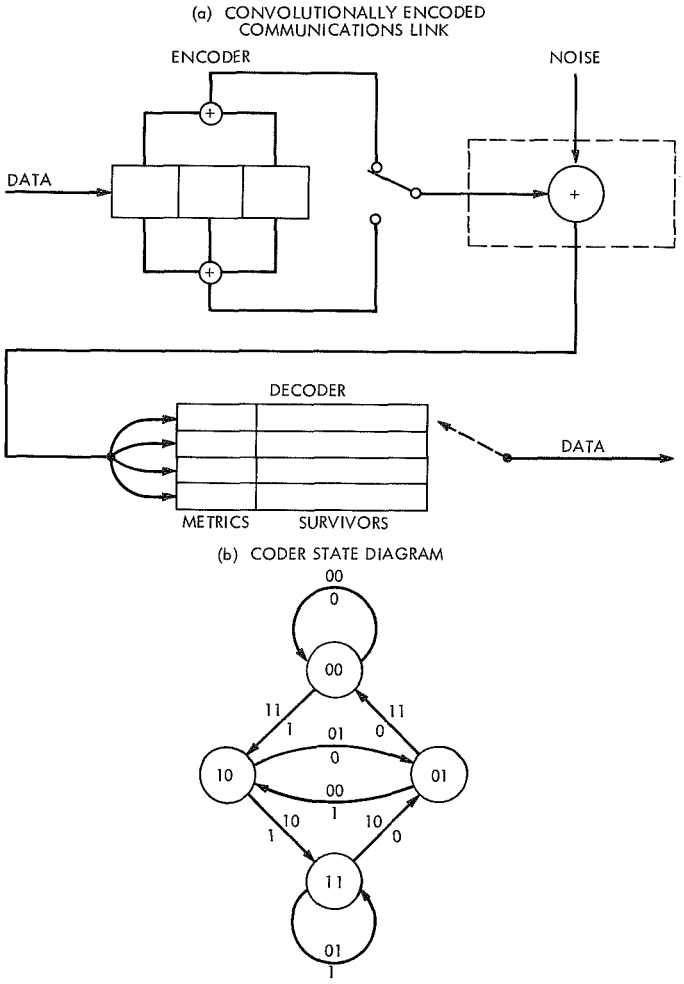

Fig. 30. A rate ½ constraint length 3 convolutional code

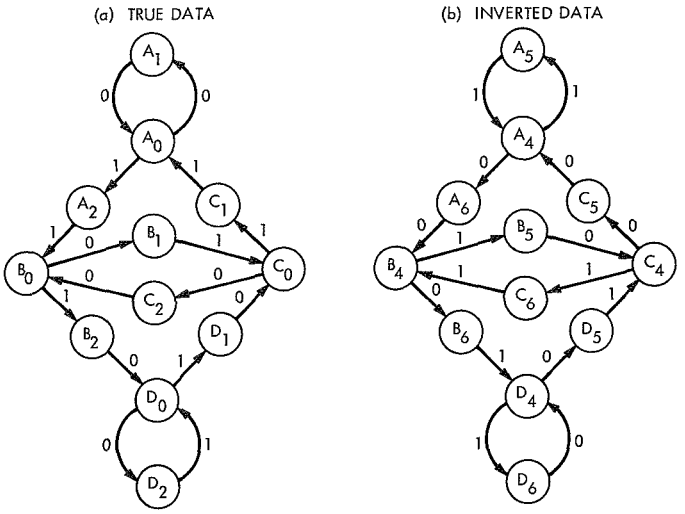

Fig. 31. Unsynchronized state diagram of the code of Fig. 30

the decoder from the channel may be the first *or second* symbol of some branch in Fig. 30b. To the decoder, then, the coder state diagram must appear as in Fig. 31a, where the $V \cdot 2^{K-1}$ states represent the starting points of all possible received symbol streams. The channel can add one further complication in the form of an ambiguity in sign of the received symbols. This ambiguity appears as a result of estimating subcarrier phase and frequency using the data signal instead of a pilot tone. This effects another two-fold increase in the number of states of the apparent data source. Fortunately, however, the channel delay and sign change very infrequently and can be regarded as constant throughout a relatively long transmission. Hence, these parameters can be estimated once and removed from the decoding process. While estimating the sync parameters, the data source state diagram is essentially that of Fig. 31. If the sync parameters are correctly estimated, the state diagram reduces to that of Fig. 30b for decoding.

c. Synchronizability. The synchronizability criterion which seems to be the least restrictive for convolutional codes is that used by Even (Ref. 1): A code is *synchronizable* if and only if, for some finite integer M, the knowledge of M or more consecutive output digits uniquely identifies some state in the coder state diagram. This definition is equivalent to the requirement that any two paths in the coder state diagram of length M or longer which have identical output symbols must pass *simultaneously* through at least one state. If branch synchronization and sign ambiguity have been resolved, the requirement that a code be synchronizable is clearly equivalent to the requirement that the coder possesses an inverse as discussed by Massey and Sain (Ref. 2). Codes which do not possess an inverse are usually referred to as *catastrophic*. In the following, a code will be called *branch synchronizable* if it is synchronizable over the $V \cdot 2^{K-1}$ states which represent the coder with unknown branch synchronization. A code will be called *fully synchronizable* if it is synchronizable over the $2 \cdot V \cdot 2^{K-1}$ states which represent the coder with unknown sign and unknown branch synchronization.

THEOREM 1. *No convolutional code in standard form is branch synchronizable.*

Proof. The output symbols of a convolutional code in standard form are exactly the linear sum (mod-2) of some subset of the K most recent input bits. If the input bit stream is identically *zero*, the output symbols are also *zero*. Delay shifts of an all-*zero* symbol stream cannot be identified, which proves Theorem 1.

If a periodic sequence of period p is added to the output, some convolutional codes can be made synchronizable. This is exactly the technique used in adding the comma-free property to the biorthogonal block code. The most desirable addition has period $p = V$; since, in that case, no more timing resolution is needed to delete the periodic sequence before decoding than is needed to perform the decoding itself. If $p \neq V$, timing resolution to the least common multiple of p and V is needed.

Some of the necessary conditions for a code to be made synchronizable by this technique are easily derived. The results are described in terms of codes with rate k/n, with k input bits and n output symbols per encoding step. As such, they apply to codes whose added sequence has period $p \neq V$, using the code parameters $n = \mathrm{LCM}\{p,V\}$, $k = n/V$.

Theorem 2. *A convolutional code of rate k/n can be made branch synchronizable only if $2^k \leq |C_{2,n}|$, where $|C_{2,n}|$ is the number of words of length n in Eastman and Even's maximal synchronizable dictionary over a 2-symbol alphabet (Ref. 3).*

Proof. If each of the k input data streams is constant, the state of the encoder must be identical at each encoding step. Since there are 2^k possible values for the input streams, there must be 2^k states in the coder state diagram which have output branches returning to themselves. If the code is not catastrophic, the sequence of n symbols corresponding to each of these 2^k branches must be distinct. Each of these sequences must also be distinct from the cyclic shifts of itself and each of the other sequences; i.e., it is equivalent under a rotational transformation to a unique word of $C_{2,n}$. This proves the theorem.

Theorem 3. *A convolutional code of rate k/n can be made totally synchronizable only if $2^{k+1} \leq |C_{2,n}|$.*

Proof. Each of the 2^k sequences considered in the proof of Theorem 2 must be distinct from the complement of any of these sequences, and from the rotational transformation of any of these sequences or their complement if the code is totally synchronizable. There are then 2^{k+1} distinct sequences, each of which is equivalent under a rotational transformation to a unique word of $C_{2,n}$. This proves the theorem.

Clearly, no code of rate $1/V$ for $V < 5$ can be made totally synchronizable by the addition of a sequence of period $p = V$ to the code words. For a complementary rate ½ code, an even stronger result is possible.

Theorem 4. *No complementary rate ½ code can be made branch synchronizable by the addition of any binary sequence to its output stream.*

Proof. The proof consists of the construction of a closed loop in Even's testing graph (Ref. 1), i.e., of two semi-infinite paths in the coder state diagram which have identical output values, and which never pass simultaneously through the same state. Referring to Fig. 31a, denote the coder states with two outgoing branches as *base states*, and the coder states with only one outgoing branch as *auxiliary states*. There are 2^{k-1} base states which correspond to the states of the coder with known branch synchronization. Each of the 2^k auxiliary states corresponds to the middle of a branch.

The needed paths are constructed as follows: Begin with any base state and any auxiliary state. Since the auxiliary state has only one branch leading from it, the symbol value on it must be the value of the first symbol on the paths being constructed. The base state has two outgoing branches, however, and since the code is complementary, the symbol on exactly one of these branches is equal to the already determined symbol on the path from the auxiliary state. The branch from the auxiliary state ends in a base state, and the branch from the base state ends in an auxiliary state, re-establishing the original configuration. The two paths can therefore be extended arbitrarily, and since each point on the dual path consists of one base state and one auxiliary state, the two paths never simultaneously occupy the same state. This is true regardless of the addition of any fixed bit pattern to the output symbol stream, and the theorem is proved.

For a rate ½ code, the only available techniques for establishing branch synchronization and data sign are the periodic insertion of a sync sequence, or to synchronize using the random source assumption. Random source synchronization is explored in *Paragraph e.*

d. Branch synchronizable rate ⅓ codes. The necessary and sufficient conditions for a rate ⅓ code to be made branch synchronizable are derived in this section. A series representation, such as the D-transform notation of Massey (Ref. 2), is convenient for this purpose. The D-transform of a sequence of binary input digits $i(0)$, $i(1), \cdots$ is given by

$$I(D) = \sum_{j=0}^{\infty} i(j) \cdot D^j \qquad (1)$$

The code is represented by the three polynomials $G_i(D)$, $i = 1, 2, 3$, where $G_i(D)$ is the D-transform of the tap selection sequence for the ith subgenerator of the code. The D-transform of the output symbol sequence from the ith subgenerator is the transform product

$$T_i(D) = G_i(D) \cdot I(D) \tag{2}$$

A factor, $f(D)$, of the polynomial, $P(D)$, is said to have multiplicity e if e is the greatest integer such that $[f(D)]^e$ divides $P(D)$.

In this notation, the addition of a period-3 sequence to the output symbol stream is represented by the addition of $\alpha_i/(1+D)$ to the output of the ith subgenerator, where the sequence $(\alpha_1, \alpha_2, \alpha_3)$ is equivalent to one of the words of $C_{2,3}$. If a code is not branch synchronizable, then there must exist information sequences $I_1(D)$ and $I_2(D)$ such that there are only a finite number of symbols which differ in the output sequence corresponding to $I_1(D)$ and the output sequence corresponding to $I_2(D)$ delayed by one or two symbol times. If a solution exists for a one-symbol delay, a solution can be constructed for the two-symbol delay by delaying both symbol streams by two symbol times, and interchanging the roles of $I_1(D)$ and $I_2(D)$. Equivalently, then, if a code is not branch synchronizable, there exist information sequences such that the error vector,

$$E(D) = \begin{bmatrix} G_1(D) & D \cdot G_3(D) \\ G_2(D) & G_1(D) \\ G_3(D) & G_2(D) \end{bmatrix} \cdot \begin{bmatrix} I_1(D) \\ I_2(D) \end{bmatrix} + \begin{bmatrix} (\alpha_1 + D \cdot \alpha_3)/(1+D) \\ (\alpha_2 + \alpha_1)/(1+D) \\ (\alpha_3 + \alpha_2)/(1+D) \end{bmatrix} \tag{3}$$

is a vector of polynomials. Denote by $\Delta_i(D)$ the determinant of the ith 2×2 submatrix of $\mathbf{G}(D)$, the 3×2 matrix in Eq. (3), and let $\Delta(D) = \text{GCD}\{\Delta_1(D), \Delta_2(D), \Delta_3(D)\}$.

THEOREM 5. *A non-catastrophic rate ⅓ convolutional code can be made branch synchronizable by the addition of a period-3 sequence if and only if the multiplicity of $(1 + D)$ as a factor of $\Delta_i(D)$ is not the same for each i.*

Proof of necessity. Suppose the condition of the theorem is not satisfied, the multiplicity of $(1+D)$ in $\Delta_i(D)$ is e for all i, and yet the code is to be made branch synchronizable by the addition of $\alpha = (1, 0, 0)$. The error vector is then

$$\begin{bmatrix} G_1(D) & D \cdot G_3(D) \\ G_2(D) & G_1(D) \\ G_3(D) & G_2(D) \end{bmatrix} \mathbf{I}(D) + \begin{bmatrix} 1/(1+D) \\ 1/(1+D) \\ 0 \end{bmatrix} \tag{4}$$

To show that the code is not branch synchronizable is to exhibit and $\mathbf{I}(D)$ which makes $\mathbf{E}(D)$ polynomial. Let

$$I_1(D) = \frac{G_2(D)}{\Delta(D) \cdot (1+D)}$$

$$I_2(D) = \frac{G_3(D)}{\Delta(D) \cdot (1+D)}$$

Then

$$\mathbf{E}(D) = \begin{bmatrix} \dfrac{G_1(D) \cdot G_2(D) + G_3(D) \cdot G_3(D) \cdot D}{\Delta(D) \cdot (1+D)} \\ \dfrac{G_2(D) \cdot G_2(D) + G_1(D) \cdot G_3(D)}{\Delta(D) \cdot (1+D)} \\ 0 \end{bmatrix} + \begin{bmatrix} \dfrac{1}{1+D} \\ \dfrac{1}{1+D} \\ 0 \end{bmatrix} \tag{5}$$

or

$$\mathbf{E}(D) = \begin{bmatrix} \Delta_3(D)/(\Delta(D) \cdot (1+D)) \\ \Delta_2(D)/(\Delta(D) \cdot (1+D)) \\ 0 \end{bmatrix} + \begin{bmatrix} 1/(1+D) \\ 1/(1+D) \\ 0 \end{bmatrix}$$

Now since $(1+D)$ divides each of the $\Delta_i(D)$ exactly e_0 times, it also divides $\Delta(D)$ e_0 times and hence $\Delta_i(D)/(\Delta(D) \cdot (1+D))$ is $p_i(D) + 1/(1+D)$. The $p_i(D)$ are polynomial and therefore $\mathbf{E}(D)$ is a vector of polynomials. An identical argument holds for each possible α, and necessity is proven.

Proof of sufficiency. Assume $(1+D)$ divides $\Delta_1(D)/\Delta(D)$ but does not divide $\Delta_2(D)/\Delta(D)$. If the theorem is true, there is an α, say (0, 0, 1), that will make this code

branch synchronizable. Assume that it does not and that an $\mathbb{I}(D)$ exists such that

$$\mathbf{E}(D) = \begin{bmatrix} G_1(D) & D \cdot G_3(D) \\ G_2(D) & G_1(D) \\ G_3(D) & G_2(D) \end{bmatrix} \mathbb{I}(D) + \begin{bmatrix} 1/(1+D) \\ 0 \\ 1/(1+D) \end{bmatrix} \quad (6)$$

is a vector of polynomials. To begin, let

$$I_1(D) = I_1^*(D) + \frac{G_1(D)}{\Delta(D) \cdot (1+D)}$$

$$I_2(D) = I_2^*(D) + \frac{G_2(D)}{\Delta(D) \cdot (1+D)}$$

By substitution of these into Eq. (6), the requirement that $\mathbf{E}(D)$ be a vector of polynomials is clearly equivalent to the requirement that

$$\mathbf{E}^*(D) = \begin{bmatrix} G_1(D) & D \cdot G_3(D) \\ G_2(D) & G_1(D) \\ G_3(D) & G_2(D) \end{bmatrix} \cdot \mathbf{I}^*(D) + \begin{bmatrix} 1/(1+D) \\ 0 \\ 0 \end{bmatrix} \quad (7)$$

is also a vector of polynomials. To determine $I^*(D)$, proceed at first as if to compute the inverse of the 3×2 matrix $\underline{\mathbf{G}}(D)$ (Ref. 2). Equation (7) is separated into each of the possible 2-row equations, and the ith equation premultiplied by the ith 2×2 submatrix of $\underline{\mathbf{G}}(D)$:

$$\begin{bmatrix} G_1(D) & D \cdot G_3(D) \\ G_2(D) & G_1(D) \end{bmatrix} \cdot \begin{bmatrix} E_1^*(D) + 1/(1+D) \\ E_2^*(D) \end{bmatrix} = \Delta_1(D) \cdot \mathbf{I}^*(D) \quad (8a)$$

$$\begin{bmatrix} G_2(D) & G_1(D) \\ G_3(D) & G_2(D) \end{bmatrix} \cdot \begin{bmatrix} E_2^*(D) \\ E_3^*(D) \end{bmatrix} = \Delta_2(D) \cdot \mathbf{I}^*(D) \quad (8b)$$

$$\begin{bmatrix} G_3(D) & G_2(D) \\ G_1(D) & D \cdot G_3(D) \end{bmatrix} \cdot \begin{bmatrix} E_3^*(D) \\ E_1^*(D) + 1/(1+D) \end{bmatrix} = \Delta_3(D) \cdot \mathbf{I}^*(D) \quad (8c)$$

Since all entries in the left-hand side of Eq. (8b) are polynomials, $\Delta_2(D) \cdot \mathbf{I}^*(D)$ must also be polynomial. Therefore, neither denominator of $I^*(D)$ can contain $(1 + D)$ to a higher multiplicity than $\Delta_2(D)$ does. This, however, means that the right-hand sides of Eqs. (8a) and (8c) do not contain $1/(1 + D)$ as a term. In order to satisfy Eq. (8a) without a $1/(1 + D)$ term on the right-hand side, $(1 + D)$ must divide both $G_1(D)$ and $G_2(D)$. Similarly, Eq. (8c) can be satisfied only if $(1 + D)$ divides both $G_2(D)$ and $D \cdot G_3(D)$. But if $(1 + D)$ divides $G_i(D)$, for $i = 1, 2, 3$, the code is catastrophic. Therefore, there does not exist an $I^*(D)$ which satisfies Eq. (7) unless the code is catastrophic. This, however, means that the code has been made branch synchronizable, thus proving the sufficiency of the condition.

Two results follow easily by application of this theorem: (1) A rate ⅓ code can be made branch synchronizable if exactly two of its subgenerator polynomials, $G_i(D)$, are divisible by $(1+D)$; and (2) a rate ⅓ code cannot be made branch synchronizable if exactly one of its subgenerator polynomials, $G_i(D)$, is divisible by $(1+D)$. The second result could also be proven directly using the arguments from the proof of Theorem 2.

Rate ⅓ codes that have no subgenerator which is divisible by $(1+D)$ require the computation of $\Delta_i(D)$ to determine whether or not they can be made branch synchronizable by adding a period-3 sequence. Each of the $\Delta_i(D)$ are divisible at least once by $(1+D)$, but no further restriction on the multiplicity of $(1+D)$ as a factor of the $\Delta_i(D)$ is known. These codes have the property that if the information sequence is complemented, the output symbol stream is also complemented, and conversely. This means that the resolution of a sign ambiguity is transferred from the decoder to the ultimate data user. Since the ultimate user will always have preliminary knowledge of some of the received data, such transfer is desirable, provided good codes can be found in this class.

e. Random source synchronization. Even if the code cannot be made branch synchronizable, synchronization of the decoder can be achieved by statistical means, provided the data source is sufficiently random. In many applications, the data to be transmitted can be assumed to consist of independent bits, which take the values of *zero* and *one* equiprobably. A delayed or inverted code symbol sequence will then, on the average, be some non-

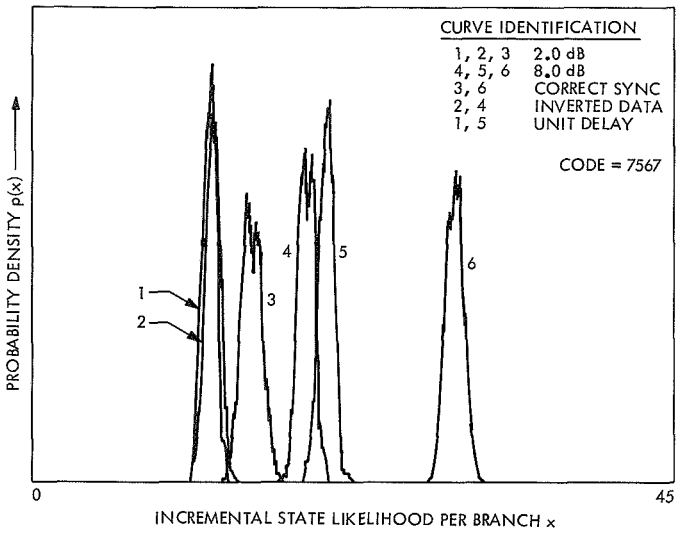

Fig. 32. Experimental densities of the incremental state likelihoods for a $K = 4$, rate ⅓ code

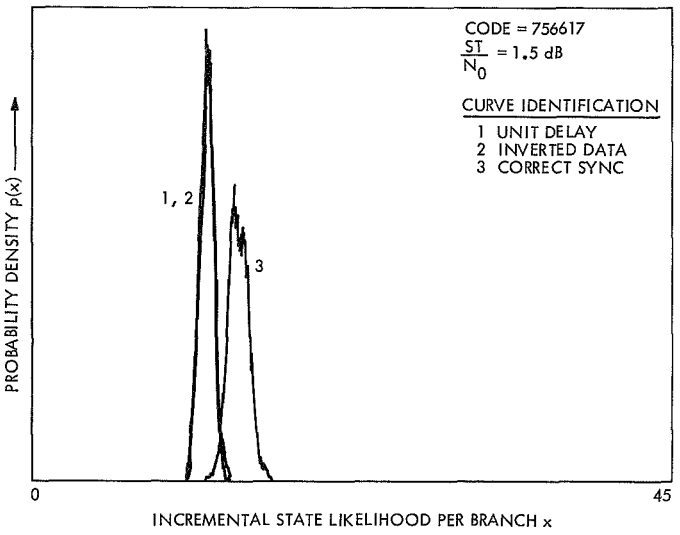

Fig. 33. Experimental densities of the incremental state likelihoods for a $K = 6$, rate ⅓ code

zero Hamming distance from the nearest true code sequence. This distance will appear in the state likelihoods of the Viterbi decoder and provide a means for determining whether or not the coder has achieved synchronization.

Simulations have been carried out using a software Viterbi decoder to estimate the probability density of the per-branch increase in decoder state likelihoods for several short-constraint-length codes. Figure 32 shows these estimated densities for the $K = 4$, rate ⅓ code, and is representative of the results obtained. Two hundred samples were taken to define each density. Each sample represents the average increase of the decoder state likelihoods over 128 branches of the code tree. The data source is pseudo-random with *ones* and *zeros* equiprobable. Curves 1, 2, and 3 of Fig. 32 represent correct sync, inverted data, and one-symbol delay, respectively, at $ST/N_0 = 2.0$ dB, where decoded bit error probability is 10^{-2}. Curves 4, 5, and 6 represent these same conditions at $ST/N_0 = 8.0$ dB. As indicated by these curves, correct sync can be identified for this code quite reliably using only 128 branches, provided the signal strength is known accurately. Some lack of knowledge of signal strength and other parameters could easily be accommodated by extending the measurement time to perhaps 256 branches. Figure 33 shows the same sync conditions for a $K = 6$ code, taken at $ST/N_0 = 1.5$ dB, where bit error probability is about 10^{-2}.

The effect of the randomness of the data source is shown in Fig. 34, for a $K = 6$ code. These experiments

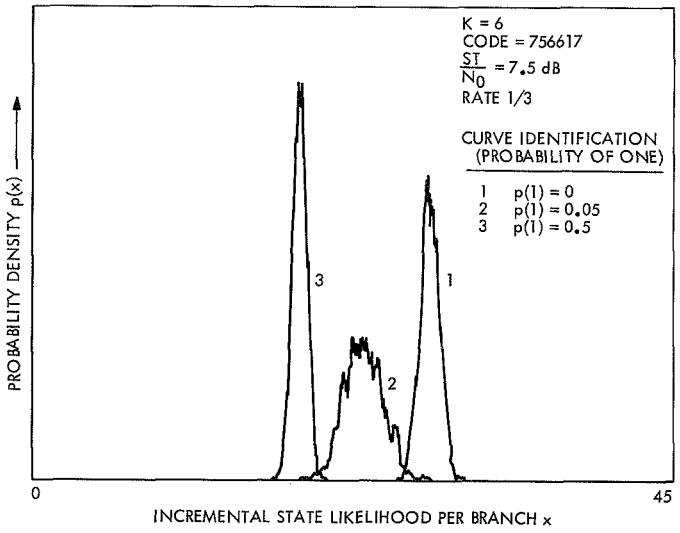

Fig. 34. Variation of the incremental state likelihoods with source statistics

were performed at $ST/N_0 = 7.5$ dB, in order to provide a reasonably expanded scale upon which to display the decoder likelihood behavior. Each of these curves represents 500 samples with a 128-bit measurement time. Each curve was generated with a one-symbol time delay between encoder and decoder. Curve 1 is an all-*zero* data stream and its sampled likelihood distribution is identical to that for correct synchronization. Curve 2 is a data stream whose bits are independent but where the probability of a *one*-bit is 0.05. Curve 3 is a data stream with equiprobable *ones* and *zeros*. This $K = 6$ can be made branch synchronizable by the addition of the period-3

sequence (010). If this is done, all curves with timing offset, including all-*zero* data, are identical to the curve for equiprobable *one*-and-*zero* data, thus demonstrating the desirability of making the code branch synchronizable. This does not help, however, if the sign ambiguity exists, since the all-*zero* code sequence, delayed and inverted, is identical to the all-*one* code sequence. Decoder synchronization is again subject to the variability of the data source. Although Fig. 34 is an extreme example, extention of the measurement time to about 512 branches is desirable to accommodate some variability in source statistics while providing adequate sync identification.

From the appearance of the experimental densities, it seems reasonable to assume that the incremental decoder state likelihoods are gaussian. Assuming that they are gaussian, the probability of false sync indication is 10^{-4} for the $K = 4$ code with equiprobable data at $ST/N_0 = 2.0$ dB, using a 512-branch measurement time, and 6×10^{-4} for the same code with 20% *ones* in the data stream. For the $K = 6$ code at $ST/N_0 = 1.5$ dB, the figures are 3.5×10^{-3} for equiprobable data and 5×10^{-3} with 20% *ones,* using a 512-branch measurement time.

f. Concluding remarks. Synchronization of a Viterbi algorithm convolutional decoder can be easily obtained using the decoder state likelihoods integrated over several hundred code branches, assuming only that the data source is sufficiently random. Attempts to endow convolutional codes with a guaranteed synchronizability have produced a sequence of non-existent results for the rate ½ and ⅓ codes of greatest interest. Fortunately, however, the randomness requirements on the data source are mild, and decoder branch synchronization can be identified almost as easily if the probability that a data bit is a *one* is 0.2, as if *zeros* and *ones* are equiprobable in the data stream.

References

1. Even, S., "Test for Synchronizability of Finite Automata and Variable Length Codes," *IEEE Trans. Inform. Theory,* pp. 185–189, July 1964.

2. Massey, J., and Sain, M. K., "Inverses of Linear Sequential Circuits," *IEEE Trans. Computers,* pp. 330–337, Apr. 1968.

3. Eastman, W. L., and Even, S., "On Synchronizable and PSK-Synchronizable Block Codes," *IEEE Trans. Inform. Theory,* pp. 351–356, Oct. 1964.

9. Information Systems: Multiple-Mission Sequential Decoder—Comparing Performance Among Three Rate ½, $K = 32$ Codes, *J. W. Layland*

a. Introduction. The multiple-mission sequential decoder (MMSD) is a high-speed special-purpose digital processor for decoding convolutional codes by the Fano algorithm. Its organization and user interface have been described in SPS 37-50, Vol. II, pp. 71–78, and in SPS 37-58, Vol. II, pp. 33–37. This article presents the results of a series of tests of this machine using rate ½, constraint length 32 codes. Two of these codes are of particular interest to *Pioneers F* and *G*: (1) the systematic code originally proposed for those missions, and (2) the "quick look" nonsystematic code which is currently under consideration. The third code is a nonsystematic code constructed by hill-climbing techniques.

b. Three $K = 32$, rate ½, convolutional codes. All three codes to be discussed are rate ½, with two channel symbols per information bit, and constraint length 32, the longest which can be used with the MMSD. Code A is the systematic code originally proposed for use on *Pioneers F* and *G*. Systematic codes have a useful property wherein the information bits appear unmodified in the symbol stream, but they are known to have poorer error performance than nonsystematic codes of the same constraint length.

Code B was constructed by Massey and Costello (Refs. 1 and 2). The subgenerators of this code differ only in the second position, so that the information bits can be constructed as the mod-2 sum of the two symbols on each branch of the code tree. This is only a slight degradation in "quick look" capability from that of the systematic code. Since this code is nonsystematic, it should have better error performance than code A.

Code C is an unconstrained nonsystematic code constructed by the hill-climbing algorithm, which is shown in *Section B-7* of this chapter to be extremely effective in construction of short constraint-length codes. In this case, the block length used (14) was much less than code constraint length to make computation time acceptable. This had the effect of making the minimum weight nonzero code word over the constructing block length somewhat greater than the code's free distance. This may mean that a better code will be found using other techniques.

c. Computing code distance properties. The free distance of a convolutional code is defined as the mini-

mum Hamming distance between any two infinite code words whose information sequences differ in at least one position (reference SPS 37-50, Vol. III, pp. 248–251). At high signal-to-noise ratios, the error performance of the code is completely determined by the free distance, and even at low signal-to-noise ratio, there is a strong correlation between large free distance and low bit error probability. The best known method for calculating the free distance of a code is the search technique suggested by Forney (Refs. 3 and 1). If the free distance of a code is 15 or less, a general-purpose computer can determine it within a few minutes, but the search time appears to grow faster than exponentially with free distance. However, the search for a minimum free distance code word is almost identical to the Fano algorithm for sequential decoding, and the computations can be performed by the MMSD itself.

To induce the decoder to compute free distance of a code, the control card (SPS 37-58, Vol. II, p. 34) is punched as if for decoding with that code except for the metric table: the all-*zero* branch has a *zero* branch metric, and each *one* on the branch adds one negative threshold step. A data simulator supplies enough blocks of noiseless data to the MMSD to fill its buffer and stops transmission prior to the tail. The data block consists of all *zeros* except for the last bit which is a *one*. The data from the simulator is encoded as if the coder were cleared at the end of the data block, but the decoder is not given the coder clear option. The single *one* at the end of the block is sufficient to guarantee correct frame sync location. It also acts to induce an error event at the beginning of the block, since the encoded data and any path the decoder can find must be separated by at least one information bit, the forced *one* at the end of the previous block which cannot now be changed. The free distances of the three codes are listed in Table 5. Computation of the distance for code B took approximately 20 min, while code C took about 10 h. Since the MMSD performs the Fano algorithm calculations between 10 and 100 times faster than the fastest available general-purpose computer, performing these calculations without the MMSD would have been virtually impossible.

The best upper bound known for the free distance of a rate ½, $K = 32$, convolutional code is 36, considerably above the best code found. This may mean that the bound is loose, that much better codes can be found, or both.

d. Test configuration. Figure 35 shows the test equipment configuration used to obtain bit error probability and block erasure probability data on the same three codes from the MMSD. The XDS 910 computer acts as both a data logger and an experiment controller. Only the gross output terminal behavior is logged in this way, rather than the detailed computational structure which is usually recorded for a software decoder.

Table 5. Parameters for the three codes tested

Code	Check equations (octal)	Free distance
A	3101010110010111000110110011 0111	16
B	3130330333030330333303333303 3303	23
C	3110203022113120100021320210 2333	28

The data source provides noisy all-*zero* data. Since the code is linear, there is no loss in generality attendant in using all *zeros* instead of a random data stream. Use of the all-*zero* data allows the computer to easily control the signal-to-noise ratio (SNR) by varying the voltage output from a digital-to-analog (D/A) converter. This control operates at two levels. At one level, the SNR is optionally stepped by 0.05 dB between sample points. At the other, the symbol error probability at the input to the decoder is used as a control signal to maintain the SNR to within about 0.05 dB despite thermal variation in the amplifiers of the signal/noise mixer.

Calibration of this equipment is achieved by setting the SNR for a 10% symbol error probability, and adjusting the gain of the signal/noise mixer to provide a signal

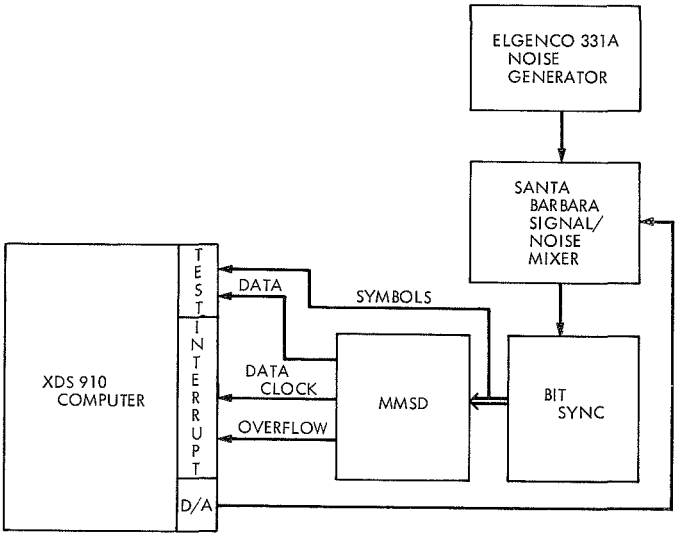

Fig. 35. Test configuration

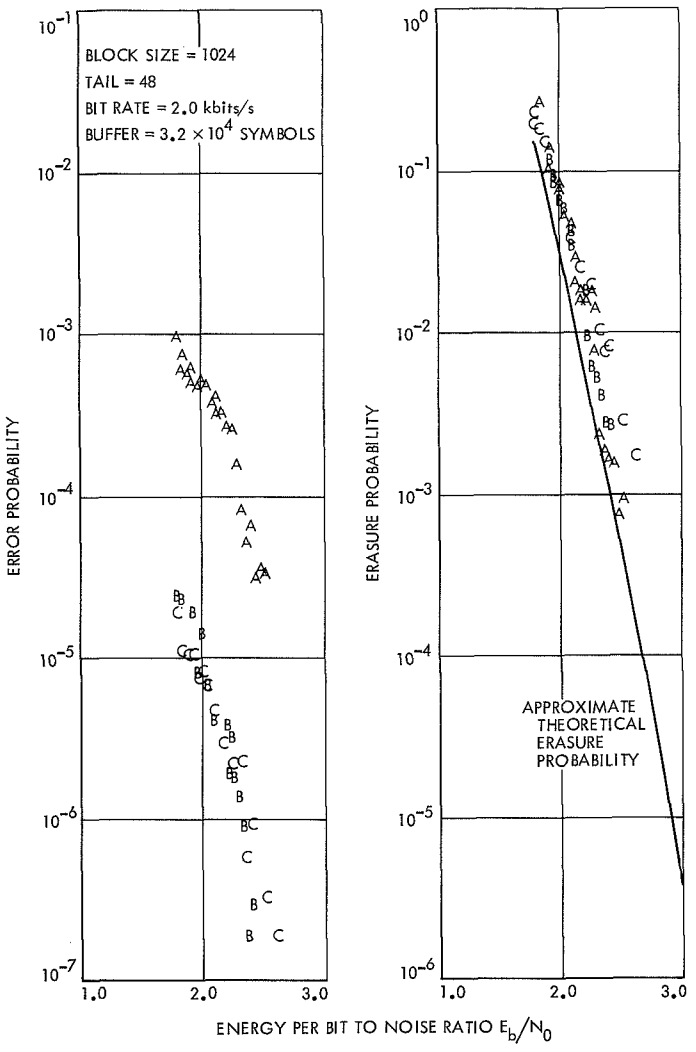

Fig. 36. Bit error and block erasure probabilities for MMSD

of approximately 140 mV at the input to the bit synchronizer. The variable actually observed is the probability that the second bit of the quantized symbol output from the bit synchronizer is a *one*, since this provides a much more sensitive observation than does metering of the signal voltage itself.

e. Test results. Figure 36 shows the experimental bit error probabilities and block erasure probabilities obtained for the three codes. Each point represents between 4×10^5 and 3×10^7 decoded bits, depending upon event probabilities within that sample. The tests were conducted at 2.0 kbits/s, with the MMSD buffer set to its maximum value of 3.2×10^4 symbols. Data block size was 1024 bits with a 48-bit tail. The approximate theoretical erasure probability is also shown on Fig. 36 for comparison. The constants used for the theoretical curve were derived on software simulations (SPS 37-58, Vol. III, pp. 36–42).

As expected, the bit error probability of the systematic code is much higher than that for either nonsystematic code. The closeness of the error probabilities for the two nonsystematic codes suggests that free distance alone is a relatively weak criterion for codes of this length. The erasure probabilities of all three codes are virtually identical, and are much greater than the error probabilities of any of the three codes. Unless errors are considerably less acceptable than erasures, there appears to be little reason for preferring the nonsystematic rate ½ codes, even with a decoder as sophisticated as the MMSD.

In some application, the information bits must be constructed from the raw channel symbols whenever a decoder erasure occurs. The bit error probability during an erasure is equal to the symbol error probability for the systematic code, approximately twice the symbol error probability for the nonsystematic "quick look" code, and essentially one-half for the general nonsystematic code. In such applications, the overall error probability is least for the systematic code at all erasure probabilities greater than 10^{-3}

f. Conclusion. The conclusion to be reached by examination of the data presented here depends greatly upon the requirement or desire by the data user for the "quick look" capability. If data loss to erasures is much less serious than errors, one of the nonsystematic codes should be chosen. If, however, data is to be extracted during an overflow using the "quick look" capability, the systematic code has better overall performance.

References

1. Massey, J. L., "Nonsystematic Convolutional Codes for Sequential Decoding," First NASA Coded Communications Conference, Feb. 26–27, 1970.

2. Costello, D. J., *Construction of Convolutional Codes for Sequential Decoding,* Technical Report EE-692. University of Notre Dame, Ind., Aug. 1969.

3. Forney, G. D., *Final Report on a Study of a Simple Sequential Decoder,* Appendix A, U. S. Army Satellite Communication Agency Contract DAA B 07-68-C-0093. Codex Corporation, Watertown, Mass., Apr. 1968.

10. Information Systems: Multiple-Mission Sequential Decoder Interface Buffer, *A. Zygielbaum*

a. Introduction. The multiple-mission sequential decoder (MMSD), described by Lushbaugh in SPS 37-58, Vol. II, pp. 33–37, decodes convolutionally encoded telemetry data more efficiently than can be done by a software-programmed general-purpose computer. In the DSN, decoding for the *Pioneer* spacecraft is currently being done by the XDS 920's. This article describes an MMSD-to-computer buffer which is compatible with the existing *Pioneer* decommutation software. This buffer is one example of the variety of MMSD-to-computer interfacings that can be achieved.

b. Design considerations. Conventional decoding of *Pioneer* probe data requires two computers (Ref. 1). The first, the decoder, sequentially decodes the received telemetry data. The second synchronizes and decommutates the data.

The computers are linked by an interface buffer that packs the serial data stream from the decoder into a parallel word format for the decommutating computer. The word is 1, 7, or 14 bits to accommodate the spacecraft data word format.

The operational computer can execute an EOM–POT sequence that sets the interface buffer to pack 1 or 7 bits into the word. If no EOM–POT is executed, 14 bits are packed (Ref. 2). When the required number of bits has been received, the computer is interrupted and executes an EOM–PIN to input data. If it again requires 1 or 7 bits, another EOM–POT must be executed.

The following instructions are used to control the interface buffer:

EOM 31777 PIN LOC	input data to the operational computer
EOM 31777 POT = 1	pack 1 bit
EOM 31777 POT = 0100	pack 7 bits

When the sequential decoder replaces the decoding computer, the MMSD computer buffer is used in place of the interface buffer. The computer buffer was therefore required to be compatible with the operational computer programming.

The MMSD output interface, described in SPS 37-58, Vol. II, pp. 33–36, consists of a serial data line and a synchronizing clock line. For reliability of operation, the clock is reconstructed in the computer buffer using a monostable multivibrator which then clocks the data into the word packing shift register.

c. Programming. An EOM–POT instruction sequence requires 32 μs to be executed. To facilitate higher speed operation, decoding of 3 additional EOMs was included in the computer buffer. Executing one EOM sets the buffer to continuously pack 1, 7, or 14 bits until one of the other EOMs is executed. These new EOMs are:

EOM 32177	start 1-bit packing
EOM 32277	start 7-bit packing
EOM 32377	start 14-bit packing

Any one of these instructions requires 8 μs for execution and eliminates all EOM–POT sequences.

Referring to the block diagram in Fig. 37, the most essential portion of the system is the 14-bit word packing shift register. The register is preset with a *one* in bit 13. When this bit shifts into the shift complete interrupt generator, an interrupt fires which informs the computer that 14 bits are packed and waiting. When the computer executes its EOM–PIN, the register is cleared and preset.

For a 1- or 7-bit shift, an EOM–POT can be used to preset the register. POT line C23 (POT = 1) is used to preset bit 0 of the register for a 1-bit shift and C17 (POT = 0100) is used to preset bit 6 for a 7-bit shift.

The new start 1-, 7-, or 14-bit shift instructions cause the register to be automatically cleared and preset after the computer executes the input EOM–PIN, as signalled by $\overline{Rt_i}$. This eliminates the need for a succeeding EOM–POT.

d. Hardware. The computer buffer is constructed on printed circuit boards following the J-card technique initiated by Martin (SPS 37-39, Vol. III, pp. 52–65). The system contained on three boards, uses integrated circuits

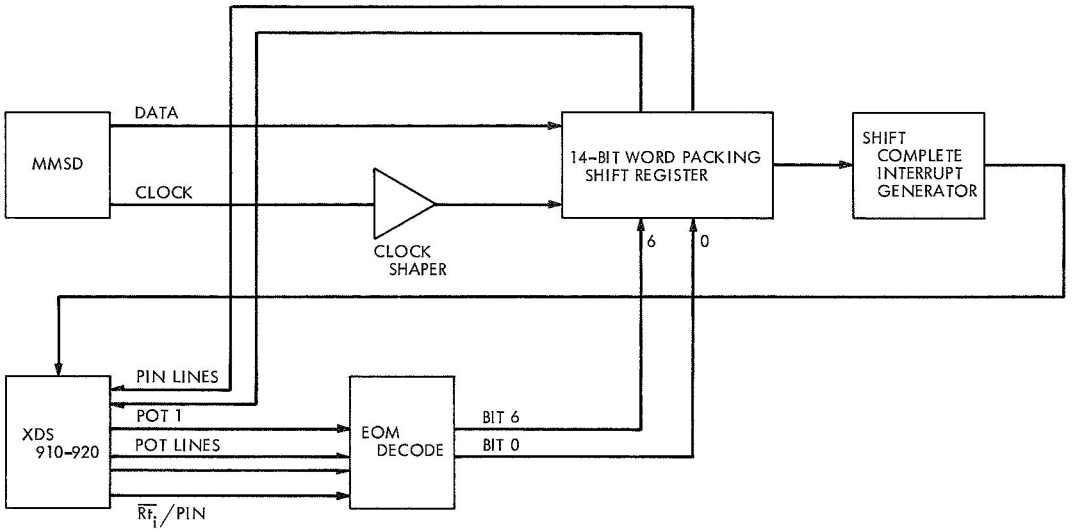

Fig. 37. MMSD computer buffer

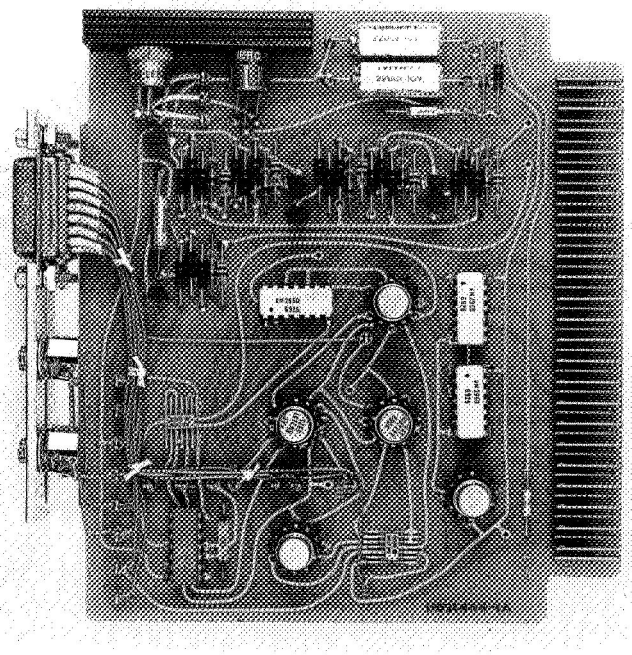

Fig. 38. Circuit card POT A

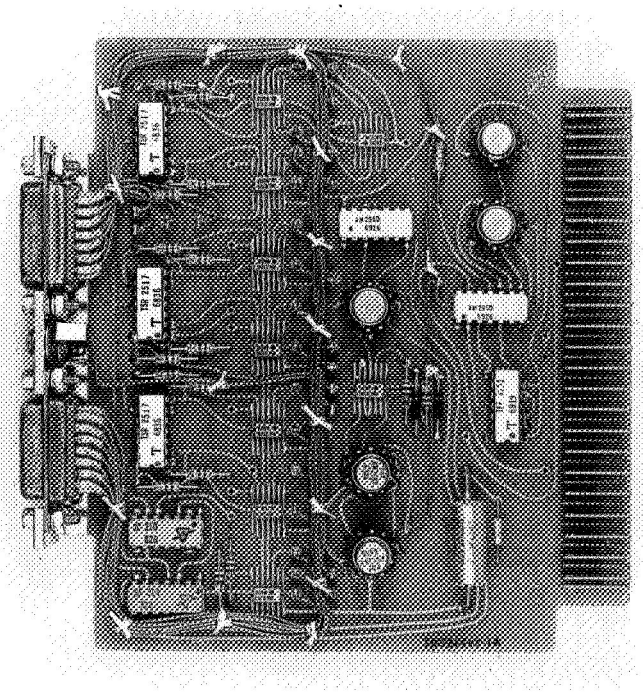

Fig. 39. Circuit card POT B

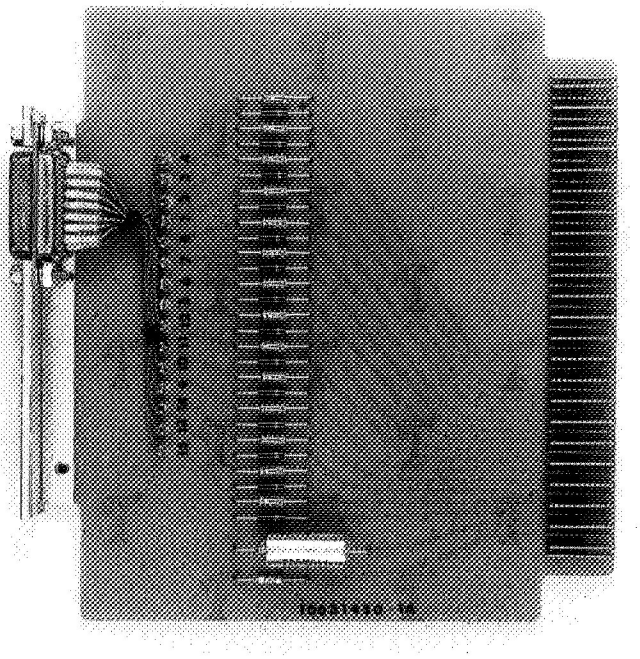

Fig. 40. Circuit card PIN

with a minimal number of discrete components. The boards are shown in Figs. 38, 39, and 40.

Board POT A contains EOM decode, the POT line receivers, the monostable clock restorer, and a 5-V power supply for the boards. The word packing register, interrupt generator, and PIN line drivers are constructed on POT B. The PIN board contains the PIN line decouplers required to interface TTL logic with the SDS 9-series computers.

References

1. *Telemetry Data Extractor,* Manual 2568-6003-TU000, Pioneer Program Ground Operational Equipment, NASA Ames Research Center, Moffett Field, Calif.
2. *Operational Decoder Program,* Manual PN-D-0-0, Pioneer Program Ground Operational Equipment, NASA Ames Research Center, Moffett Field, Calif.

11. Frequency Generation and Control: The Measurement of Phase Jitter, *R. Meyer and A. Sward*

a. Introduction. Phase noise or phase jitter is one of the limitations of sensitivity in coherent communication systems. Phase noise measurements of voltage-controlled oscillators have been made in the past without too much difficulty. This is achieved by phase-locking two oscillators in a phase-locked loop arrangement and observing the phase noise at the input of the tracking filter. However, until only recently have low level phase jitter measurements of solid-state amplifiers been possible. The advent of low-noise mixers such as the Schottky barrier diode mixers, as well as low $1/f$ noise (flicker noise of phase) transistors, has enabled very low level measurements to be made.

b. Analysis of system. A typical phase noise measurement system for an amplifier is shown in Fig. 41. The input signal is split into two channels using a power splitter. One channel is then shifted 90 deg relative to the other before being introduced into the phase detector. The two signals are then phase-detected, low-pass-filtered, and amplified. Any phase perturbations caused by the signal generator will cancel out. This can be shown as follows. Assume the two inputs to the phase detector are

$$V(t) = A \sin(\omega t + \phi(t))$$

$$V'(t) = B \sin(\omega t + 90° + \phi(t))$$

where

$$\phi(t) \triangleq \text{phase disturbance of oscillator}$$

Therefore,

$$V(t)V'(t) = AB \sin(\omega t + \phi(t)) \sin(\omega t + 90° + \phi(t))$$

$$= (AB/2)[\cos(90°) - \cos(2\omega t + 2\phi(t) + 90°)]$$

$$= -(AB/2)[\cos(2\omega t + 2\phi(t) + 90°)]$$

The low-pass filter then removes this last term. The only noise observed is that which is contributed by the amplifier in the top signal path. (The phase shifter is passive and contributes essentially no noise.)

A Schottky barrier diode double-balanced mixer is used as a phase detector with a conversion factor of approxi-

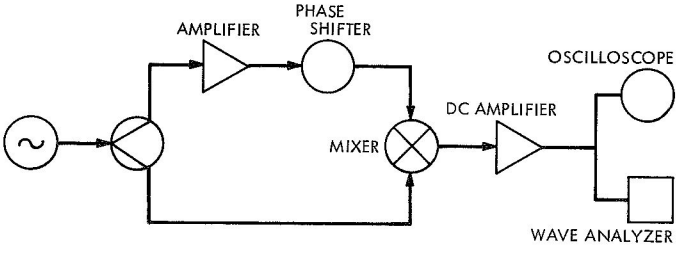

Fig. 41. Phase noise measurement setup

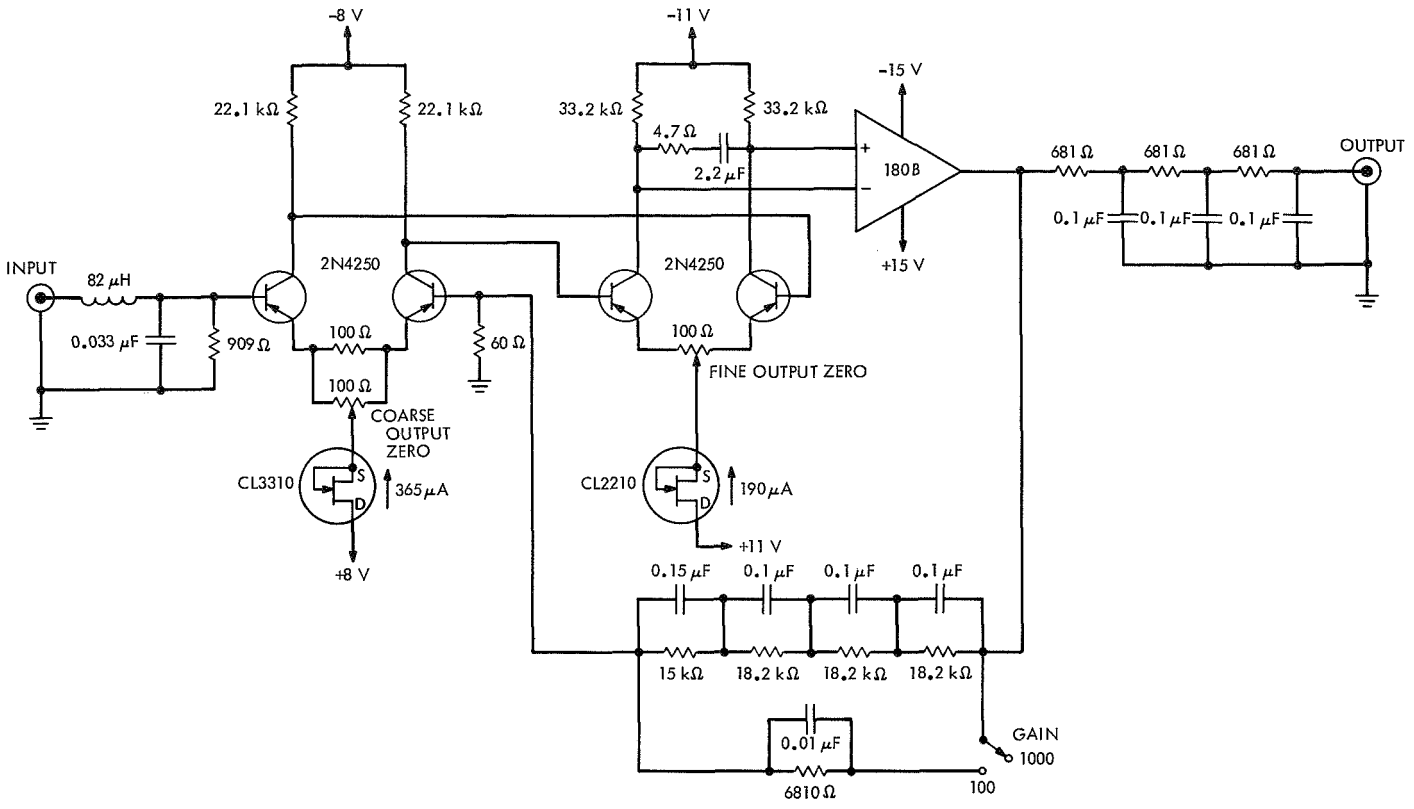

Fig. 42. Low-noise dc amplifier

mately 3 nanovolts per microdegree of phase, and a low-frequency noise spectrum of 3 nanovolts per root hertz (≈1 microdegree per root hertz). After the detected signal is amplified, it is fed into either an oscilloscope or an audio spectrum analyzer. For low level phase jitter measurements the wave analyzer is preferable because of its ability to reject 60 Hz. An approximate picture of the frequency spectrum[13] is then obtained by measuring the power in 1-Hz bandwidths over the desired frequency range.

A measure of the amount of AM noise can be obtained by adjusting the phase of the signals at the inputs of the phase detector such that they are in phase. Thus, the output becomes insensitive to phase jitter, and dependent upon amplitude changes.

[13]A standard spectrum relates power to frequency and since voltage varies as the square root of power, noise voltages are expressed on an rms volts per root hertz basis. This is the same as measuring the rms noise voltage in a one-cycle bandwidth about a particular frequency. If the noise is uniform over the spectrum, this figure may be multiplied by the square root of the bandwidth to obtain the wideband rms noise voltage. However, with $1/f$ noise this cannot be done since the noise is not uniform and increases with lower frequencies.

c. Circuit description. The low-noise dc amplifier used in the system is shown in Fig. 42. The first two stages are cascaded differential pairs that are coupled to an operational amplifier. The differential pair has many unique advantages for this type of amplifier. The dc drift is very low when the two transistors have a common heat sink. In addition it has a very high common-mode rejection. The FET diodes provide a simple constant current source for the differential pairs while the diode's high impedance (5 MΩ) produces a common-mode rejection ratio of over 15,000. An emitter potentiometer in each transistor pair compensates for unequal base–emitter voltages and also affords precise control in zeroing the dc offset at the output.

Because of the high open-loop gain (187 dB) of the amplifier, precautions had to be taken when closing the loop. A 2.2-μF capacitor was put across the collectors of the second stage, putting a pole at 1 Hz. This rolls off the response at high frequencies without introducing excessive phase shift. The resistor in series with it brings the phase shift back to zero at higher frequencies.

d. Performance. Table 6 lists the specifications of the high-gain dc amplifier. Figure 43 shows a frequency ver-

Table 6. Amplifier characteristics

Parameter	Value
Input impedance	900 Ω
Output impedance	2000 Ω
Optimum source impedance for lowest drift	50 Ω, dc-coupled
Optimum load impedance for maximum gain, minimum bandwidth	>100 kΩ
Maximum output signal	25 V p–p
Total harmonic distortion (25-V p–p output, 35 Hz)	<0.1 %
Dynamic range	129 dB (minimum detectable signal in a spectrum = 3 nV rms)
Temperature range	Unspecified, all measurements at 23°C
Frequency response:	
At gain = 1000	190 Hz, 3 dB 100 Hz, 1 dB
At gain = 100	390 Hz, 3 dB 380 Hz, 1 dB
Wide-band noise	200 μV p–p (≈2.4 nV/$\sqrt{\text{Hz}}$ rms average equivalent input noise)
Equivalent input noise:	
At 10 Hz	3.0 nV/$\sqrt{\text{Hz}}$ rms
At 100 Hz	2.2 nV/$\sqrt{\text{Hz}}$ rms
Equivalent offset and drift:	
Output zeroing	±0.5 μV
Initial drift after zeroing	1.8 μV
Subsequent 30-min drift	0.2 μV

sus noise plot of the input transistors while Fig. 44 represents the noise of the entire amplifier. Measurements indicate that the noise level of the amplifier is approximately the same as the Schottky barrier diode mixers. Shielding had to be provided for the amplifier to prevent external 60-Hz magnetic field pickup from interfering with very low level measurements.

e. Measurements. Plots of the single-sided noise density spectrum relative to carrier versus frequency are shown in Fig. 45. Both amplitude noise and phase noise can be represented in these plots. They are defined to be

$$\mathcal{P}(\omega_1,\omega_2) = \frac{P_{\omega_A}(\omega_1,\omega_2)}{2K^2}$$ (with mixer inputs in quadrature)

and

$$\mathcal{A}(\omega_1,\omega_2) = \frac{P_{\omega_A}(\omega_1,\omega_2)}{2K^2}$$ (with mixer inputs in phase)

where

$P_{\omega_A}(\omega_1,\omega_2) \triangleq$ power reading of wave analyzer for $|\omega|\epsilon[\omega_1,\omega_2]$

$K \triangleq$ peak value of S-curve

$\mathcal{P}(\omega_1,\omega_2) \triangleq$ single-sided phase noise relative to carrier for $|\omega|\epsilon[\omega_1,\omega_2]$, dB

$\mathcal{A}(\omega_1,\omega_2) \triangleq$ single-sided amplitude noise relative to carrier for $|\omega|\epsilon[\omega_1,\omega_2]$, dB

Measurements were made between 4 and 104 Hz in 1-Hz bandwidths.

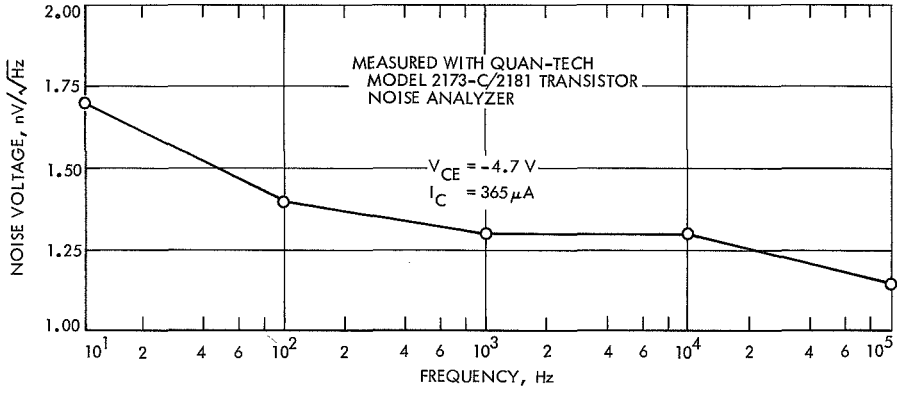

Fig. 43. Equivalent input noise voltage for 2N4250 transistor

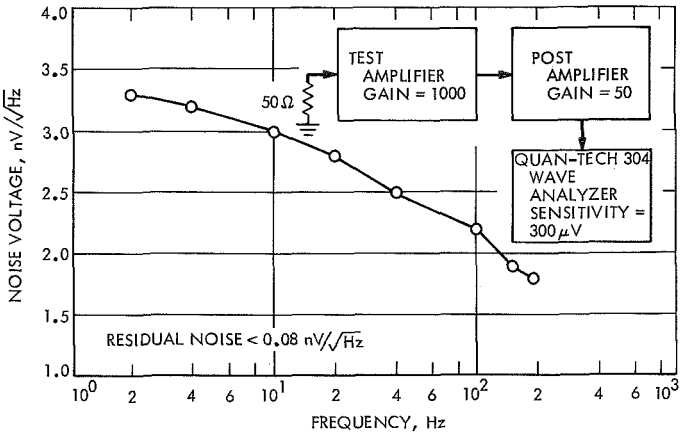

Fig. 44. Equivalent input noise spectrum

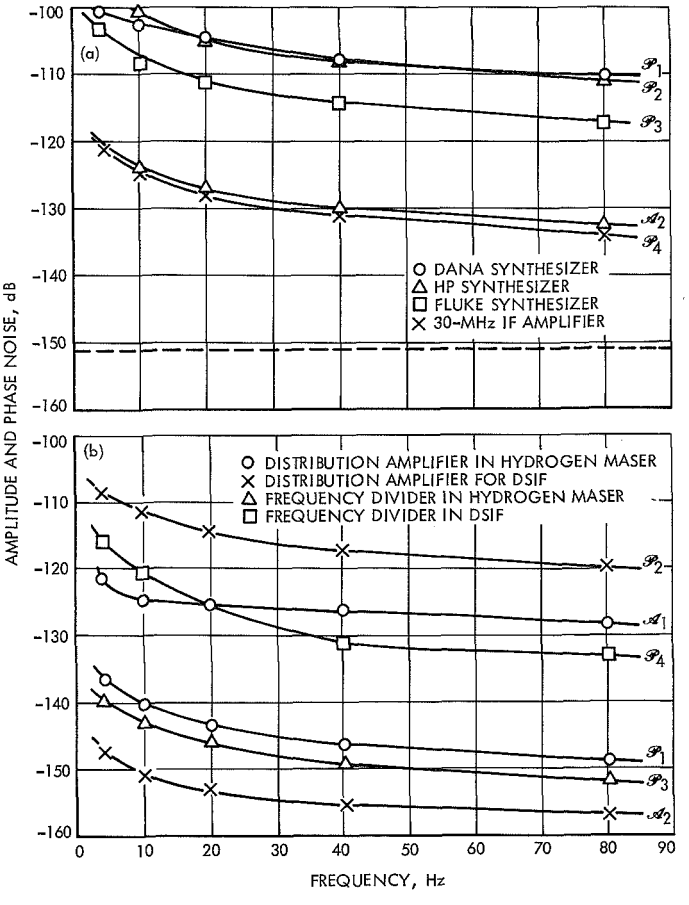

Fig. 45. Single-sided noise density relative to carrier

Most units that were measured displayed a $1/f$ frequency characteristics. Figure 45a shows the phase noise characteristic of three different synthesizers as well as a commercial IF amplifier with a noise figure of 2.5 dB. Each synthesizer was driven by an external 5-MHz signal from a cesium standard, and the 5-MHz output from each unit was used. The amplitude noise characteristic of one of the synthesizers is also included.

Figure 45b shows the phase noise of two types of distribution amplifiers; one was built for use in DSIF receivers, and the other developed for the Hydrogen Maser Frequency Standard (SPS 37-61, Vol. II, pp. 68–71). In addition the phase noise characteristic of two types of frequency dividers is shown. Again, one of the frequency dividers was designed for DSIF receivers and the other for the Hydrogen Maser Frequency Standard. Also included in the figure is a plot of the amplitude noise of the two types of distribution amplifiers.

So far it has been found that phase jitter is not related to either noise figure or gain of an amplifier. By calculating the output noise density of the IF amplifier, it can be seen that the output noise measured cannot be explained on the basis of noise figure alone. That is,

$$NF = \frac{S_i/N_i}{S_o/N_o} = \frac{S_i}{S_o}\frac{N_o}{N_i} = \frac{N_o}{GN_i}$$

where

NF = noise figure

S_i = input signal

S_o = output signal

G = gain

N_i = input noise density

N_o = output noise density = $(NF)(G)(N_i)$

but

$$N_i = kT, \text{W/Hz}$$

Letting $G = 20$ dB and $NF = 2.5$ dB, we obtain $N_o = -151.3$ dB/Hz, which is the dashed line shown in Fig. 45a.

In each of the modules developed for the Hydrogen Maser Frequency Standard, RF negative feedback was utilized in each stage to reduce phase noise. In many of the breadboard circuits, negative feedback improved the signal-to-phase noise ratio by 20 or 30 dB. Phase noise does not seem to be affected to any great degree by the type of transistor used, the collector current, or even the $1/f$ characteristic of the transistor. Hence, RF negative feedback seems to be the only thing that significantly reduces phase jitter.

12. Frequency Generation and Control: Computer-Assisted Acquisition, *K. Schreder*

a. Introduction. The acquisition of a received signal near threshold has always been a difficult problem. Some of the methods currently used are:

(1) Offset the voltage-controlled oscillator (VCO) in the direction of the doppler shift; the received signal will pass through the closed-loop bandwidth and acquire.

(2) Start the transmitter sweeping through the frequency uncertainty in the receiver; the receiver will lock to the swept signal, then acquisition has been accomplished.

This article describes a third method, where a digital computer is used to determine the offset frequency between the received signal and the local oscillator. The offset frequency can be programmed (dialed) into the VCO, and acquisition is accomplished.

b. Operation. The phase detector output function must be sampled at least at the Nyquist rate of the predetection bandwidth of the receiver. The sample points are fed into a digital computer. When all the data has been stored in the computer, a fast Fourier transform (FFT) is performed and the most likely offset frequency is outputed. The FFT program is an economical computation of the Fourier series of an input function defined by a finite number of points. The FFT algorithm and defining equations are described in SPS 37-37, Vol. IV, pp. 295–297, and SPS 37-40, Vol. III, pp. 6–8.

The implementation of this method for acquisition of a signal by a Deep Space Network (DSN) receiver could be accomplished in the following way. An analog-to-digital (A/D) converter to sample the phase detector output is required. The sampled values are fed into a digital computer. The output from the computer will tell the operator how far to offset the VCO to acquire the signal.

For a narrowband digitally controlled receiver, the implementation involves only software changes. A receiver of this type is described in SPS 37-61, Vol. II, pp. 73–86. Since the A/D converter is already sampling the IF signal, there is no additional equipment required. The computer program performs the FFT on the input data and programs the number-controlled oscillator to the correct position. The computer program mode is then switched from acquisition to track and the receiver acquires the signal.

c. Simulation. An experiment was set up in the laboratory to simulate an acquisition on the three most likely types of received signals: (1) stationary in time, (2) moving in one direction in time, and (3) a carrier and a sideband. The results from the experiment indicate that the computer could handle the above three cases. A block diagram of the experiment is shown in Fig. 46.

The signal which is stationary in time is a synchronous signal. This is probably the easiest of the three to acquire. To simulate this signal a fixed offset frequency was placed into the received signal synthesizer. The output results of the FFT are shown in Fig. 47.

The time-varying signal is probably the most likely operational case. In this example, the received signal is either moving toward or away from the observer. The VCO is set at the most likely frequency and the FFT is performed. The simulation of this type of signal was accomplished by sweeping the received signal synthesizer through a range of frequencies. The results are shown in Fig. 48. The output frequency from the computer is the average frequency for the sampled time.

The last likely signal is one in which the carrier is modulated. This signal is simulated by switching the received signal synthesizer between two frequencies. The sampled time was not divided equally between the two signals, so that one would appear as the carrier and the other the modulation. The results of this experiment are shown in Fig. 49.

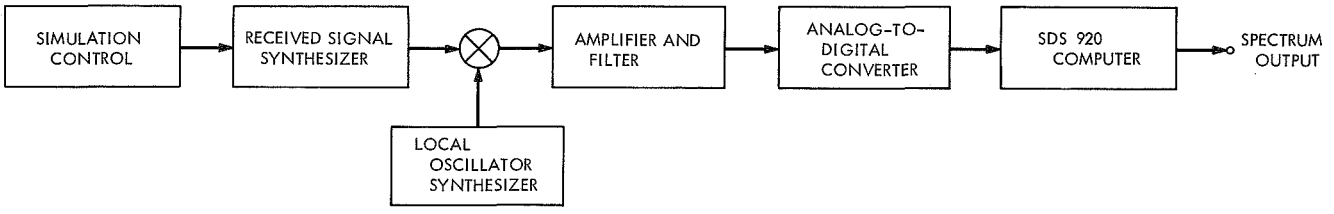

Fig. 46. Acquisition simulation block diagram

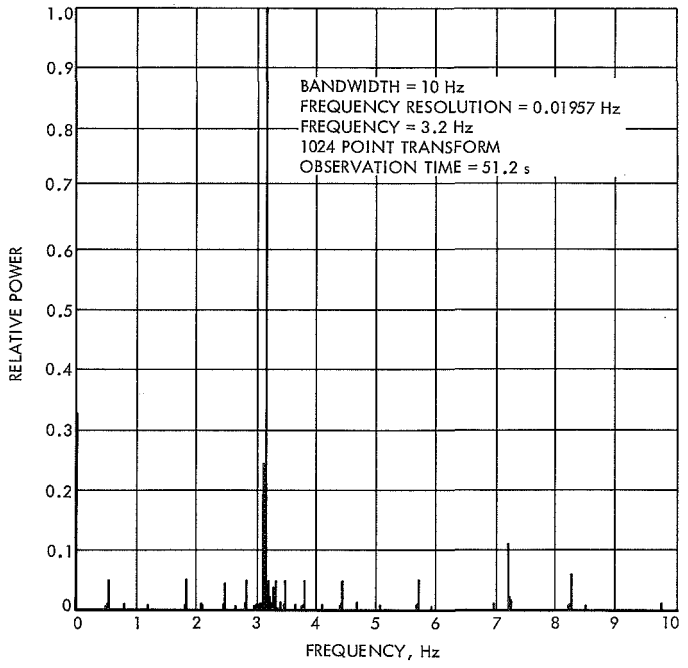

Fig. 47. Synchronous signal

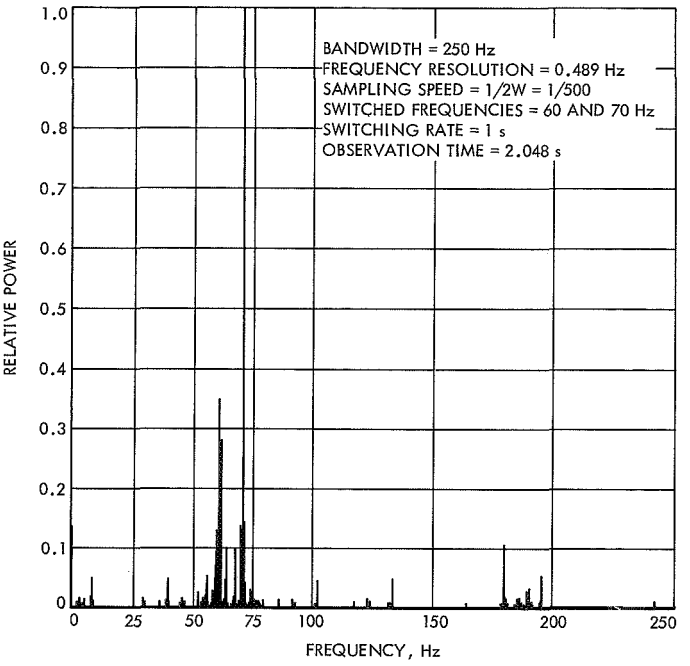

Fig. 49. Modulated signal

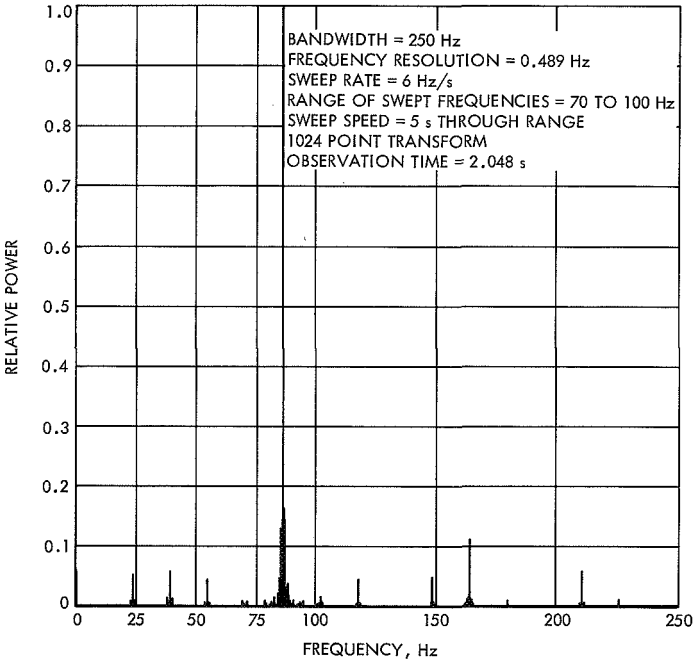

Fig. 48. Time-varying signal

In all the above cases, the computer output enabled the offset frequency to be estimated and the operator could easily tune the local oscillator for acquisition of the signal.

d. Constraint. In a phase-locked loop receiver, the error signal frequency must be less than the closed-loop bandwidth for acquisition to occur. When an FFT is used in a computer-assisted acquisition program, the frequency uncertainty (resolution) in the transform must be less than the closed-loop bandwidth.

For a signal at threshold or above and white gaussian noise, the minimum closed-loop bandwidth that insures capture of the error signal is defined in the following equation:

$$B_{L_{\min}} = \frac{R \times 2BW_{\text{pre}}}{P}$$

where

$B_{L_{\min}}$ = closed-loop bandwidth

R = ratio of sampling rate to Nyquist rate

BW_{pre} = predetection bandwidth

P = number of points taken in the transform

The reciprocal of the minimum closed-loop bandwidth is the observation time required for the transform program.

13. Loop Stress Diminution, *R. M. Goldstein, R. F. Emerson, W. L. Sjogren, and R. L. Sydnor*

a. Introduction. Radio receivers designed for space telemetry face two conflicting requirements. They must receive a signal with perhaps hundreds of kilohertz of doppler excursion; yet they must have a noise bandwidth of only a few dozen hertz. This seeming paradox was resolved at the advent of the space age by the phase-locked receivers of the Deep Space Network. These receivers have been capable of tracking any doppler rate that has been called for.

Since the first space flights, a steady pressure has existed to reduce the loop bandwidth. The reason for this is simple—the narrower the loop bandwidth, the less the power that must be allotted to the carrier signal. The bandwidth of the standard DSN receiver now is 12 Hz. An example of the need for less bandwidth can be seen in *Pioneers VI* and *VII*, where the data rate is limited by the instability of the noisy reference. Theoretically, a 3-Hz loop could almost double the data rate.

Both the uplink and downlink carrier margins would improve with the narrowing of the loop. However, a condition is soon reached where the loop might be too narrow to allow for rapid doppler acceleration. Indeed, this condition has been reached for *Mariner* Mars 1971, where the loop has been intentionally widened for this purpose.

If *a priori* knowledge of the doppler accelerations were to be used, and the loops assisted accordingly, then the loops could again be narrowed. This article presents the results of an experimental investigation of such a procedure.

b. Experimental procedure. Use has been made of two ephemeris-tuned oscillators (ETOs) which were developed for the Laboratory's planetary radar program. When supplied with a suitable ephemeris, they can tune a receiver (or transmitter) to an accuracy of about 0.02 Hz. One was used to tune the transmitter at DSS 14 to the predicted rest frequency of the *Pioneer VI* voltage-controlled oscillator (VCO), and the other to tune the receiver to remove the predicted downlink loop stress.

Under the constraints of the DSN, it must be possible to receive telemetry, transmit commands, and track two-way doppler for orbit determination—all simultaneously. However, with the uplink frequency programmed to remove loop stress, the standard doppler counter no longer produces valid data.

For this experiment, the doppler extractor was connected to a fixed reference frequency. In this mode of operation, it yields not doppler counts, but rather a number related to the received frequency. The ETO controlling the uplink was modified to record (on punch tape) the total number of transmitter cycles. These two data types (uplink and downlink frequency, nondestructively counted) are sufficient for precision orbit determination.

Figure 50 is a block diagram of the experimental configuration. It shows in greatly simplified form the standard DSN transmitter/receiver/doppler extractor. The dashed lines show the changes (all through Engineering Change Orders) that were made for the loop stress diminution (LSD) experiment. The two ETOs were located in the pedestal room at DSS 14. Each day's ephemerides were loaded into the machines in the form of polynomials, stored on punch tape.

Altogether, data was taken on three days. At the beginning of a pass, the station was configured according to the block diagram. As soon as the cables were connected and the antenna on point, both downlinks (the standard DSN on receiver 2, and the experimental system on receiver 1) were locked. Thus, telemetry throughout almost the entire pass was made available to the *Pioneer* Project.

A slow frequency sweep of ±600 Hz (at S-band) was initiated on the uplink. Normally, two-way operation

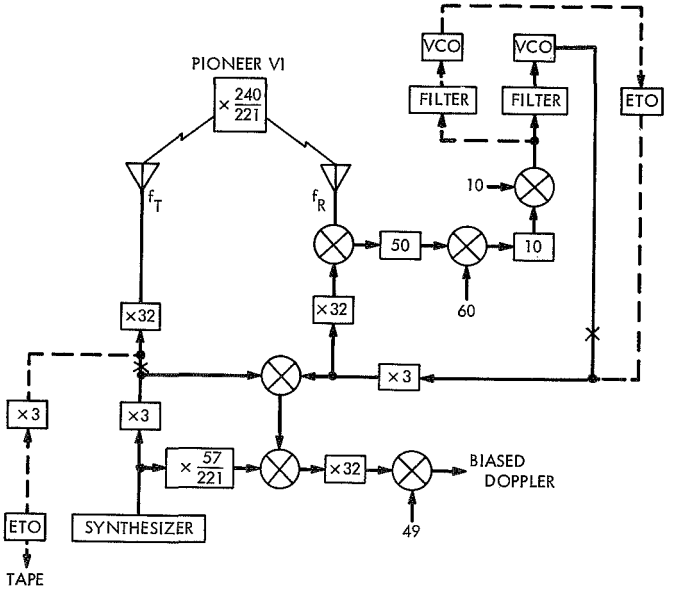

Fig. 50. Loop stress diminution experiment

was established soon after the round trip time-of-flight had elapsed.

Measurements of the receiver VCO frequency provided a real-time indication of system performance. If the uplink and downlink predictions were correct and, further, if the ETOs performed properly, then the receiver VCO would be at its rest frequency of 24 MHz. In practice it was found to be offset by only a few thousandths of a hertz. Thus, the downlink stress was essentially removed.

Uplink performance was monitored in real time from the telemetry stream of *Pioneer VI*. Precision measurements were not possible since the loop stress was quantized in steps greater than 1 kHz. However, the loop stress was less than one quantum since the telemetered readings remained zero throughout the pass.

At the end of each pass, of course, it was necessary to reconfigure the station to its standard form.

c. Receiver/transmitter. A block diagram of the basic configuration of the receiver/transmitter as reconfigured for the LSD experiment is shown in Fig. 50. Two changes were made in the station to implement this block diagram.

First, the exciter synthesizer and the exciter loop were replaced by a programmed oscillator so as to control the uplink frequency from the ephemeris. The synthesizer normally used to control the transmitter frequency was set to SYNFREQ (the normal transmitter frequency) to drive the doppler extractor for obtaining doppler data.

For the second change, the receiver VCO was replaced by a programmed oscillator running in "assist" mode. In this mode, the output frequency of the programmed oscillator is the sum of the frequency controlled by the ephemeris and the frequency of a VCO in the phase-locked receiver. Since the loop gain in the receiver is changed by the substitution of the special VCO in the programmed oscillator, a new tracking filter was supplied. The receiver noise bandwidths available with this tracking filter–VCO combination were 12, 3, and 1 Hz. A diagram of the filter is shown in Fig. 51; the pertinent constants are given in Table 7.

During operation in two-way mode, any errors in ephemeris or in the operation of the programmed oscillator are compensated for by changes in the VCO frequency from its rest frequency of 24 MHz. Thus, the

Table 7. Characteristics of the tracking filter

Parameter	Value
Phase detector constant, K_ϕ	301 mV/deg
VCO constant, K_{VCO}	50 Hz/V (gain factor = 1.1111111)
Signal suppression at threshold, α_0	
For 12 Hz	0.068485667
For 3 Hz	0.034303221
For 1 Hz	0.019812747
Multiplication factor in receiver local oscillator	96
Noise temperature of receiving system, T_n	55°K
Loop bandwidth components:	
For 12 Hz	R_1 = 813.3583 kΩ
	R_2 = 329.34 Ω
	C = 380 μF
For 3 Hz	R_1 = 6.5525 MΩ
	R_2 = 1.3153 kΩ
	C = 380 μF
For 1 Hz	R_1 = 33 MΩ
	R_2 = 3.9463 kΩ
	C = 380 μF

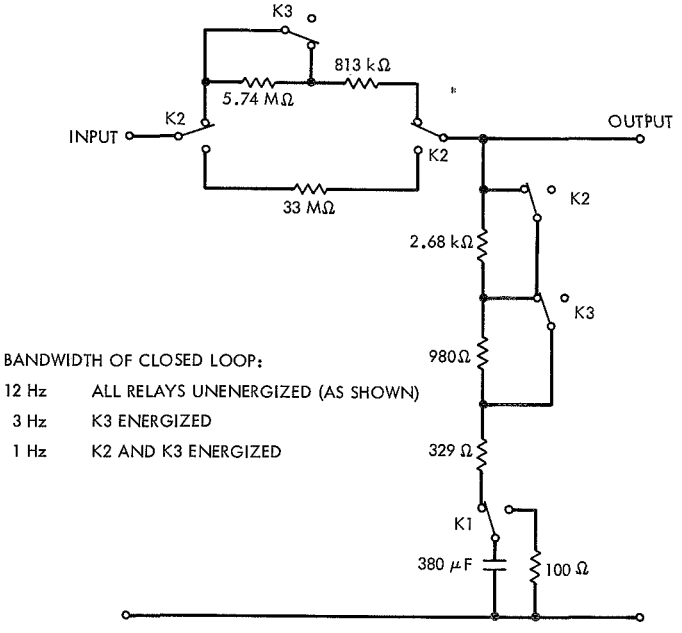

Fig. 51. Tracking filter configured for 12-, 3-, or 1-Hz loop bandwidth

VCO frequency is a good indication of the total loop stress in the ground receiver. A recording counter was used to monitor this frequency. The gate time on the counter was 90 s; the resolution was 1 millihertz. The output record displayed the frequency difference from 24 MHz. With this resolution at the VCO frequency, and the ensuing 96 multiplication, the loop stress at S-band could be read to an accuracy of 96 millihertz.

During an 8-h pass on December 22, 1969, the difference frequency drifted slowly from 0.009 to 0.004 Hz. This corresponds to a drift of less than 0.5 Hz at S-band.

Comparisons were made of the automatic gain control (AGC) with receiver loop bandwidths of 12 and 1 Hz. An increase in AGC corresponding to ≈ 0.3 dB in signal power was noted when the bandwidth was changed from 12 to 1 Hz. This corresponds directly to a 0.3-dB drop in the losses associated with the noisy reference. A larger improvement was anticipated. Since the uplink was close to threshold, the difference was attributed to the phase jitter in the downlink signal transmitted by *Pioneer VI*.

d. Ephemeris-tuned oscillator. The ETO is a software–hardware symbiotic system consisting of a stored program controller, an attendant program, a frequency synthesizer, and a special interface between the two. The block diagram for the system is given in Fig. 52 (reference SPS 37-32, Vol. III, pp. 36–47).

The output frequency is controlled in three ways. First, the ephemeris information is transformed into two parts —that which is above 100 Hz and that which is below. The controller, through the interface, selects the decade switches of the synthesizer to control the high-order part of the frequency and selects the search oscillator to control the low-order part. The controller then drives, in closed loop, the search oscillator to the value of the low-order part. Lastly, if desired, an external 24-MHz VCO may be connected to the synthesizer instead of a locally generated 24-MHz standard. Then the receiver may be phase-locked to the signal, with the 24-MHz VCO removing whatever errors remain in the ephemeris tuning system. This last feature was necessary in this experiment for the receiver tuning, but was not used for the transmitter.

The control loop for the search oscillator is a third-order sampled-data servo loop. The block diagram for the loop is given in Fig. 53. A complete description of the operation and stability of the loop is given in SPS 37-36, Vol. III, pp. 54–65, and SPS 37-39, Vol. III, pp. 71–77.

The ephemeris frequency is calculated from precomputed Chebyshev polynomial coefficients. The value of the polynomial is then appended to SYNFREQ or XMTREF (for receiver or transmitter) and separated into the low- and high-order parts. For the receiver:

$$f_{\text{ref}} = \frac{\left(\text{SYNFREQ} \times 96 \times \frac{240}{221} - 50\,\text{MHz}\right) - \left(\frac{P}{10^3} - 1\,\text{MHz} + \text{BIAS}\right)}{96}$$

and for the transmitter:

$$f_{\text{ref}} = \text{XMTREF} + \frac{P}{10^3} + \frac{\text{BIAS}}{96}$$

$$f_{\text{ref}}(\text{decade}) = \text{AMOD}\,(f_{\text{ref}}, 100)$$

$$f_{\text{ref}}(\text{search oscillator}) = f_{\text{ref}} - f_{\text{ref}}(\text{decade})$$

where

P = output of the polynomial

BIAS = an additive constant used for acquisition

SYNFREQ = uplink transmitter VCO frequency

XMTREF = best lock frequency of spacecraft receiver VCO

f_{ref}(decade) = high-order part

f_{ref}(search oscillator) = low-order part of desired frequency

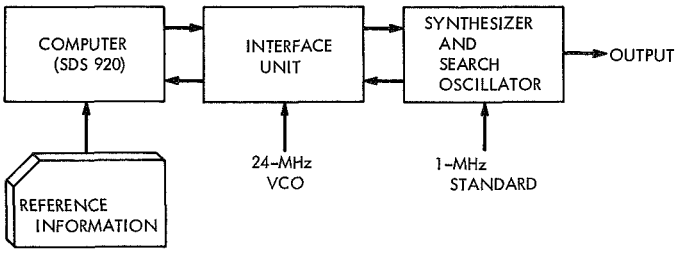

Fig. 52. Ephemeris-tuned oscillator

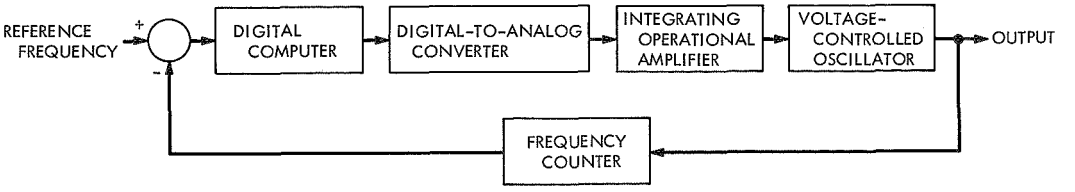

Fig. 53. Sampled data servo loop

The ETO has been subjected to tests for phase noise (SPS 37-39, Vol. III, pp. 71-77) and spectral purity (SPS 37-54, Vol. II, pp. 31–34). The phase noise was found to be 0.03 deg rms for $2B_L = 5$ Hz. The spectral width at the 3-dB point was found to be 0.015 Hz.

Three modifications had to be made in the existing control program for the loop stress experiment.

In order to determine the spacecraft orbit, it is necessary to know the number of radio frequency cycles actually transmitted during each interval. To accomplish this, the counter was never reset to zero, but rather was read "on the fly." Thus, the output data was the nondestructively counted transmitter frequency as a function of time from the start of the experiment. This value was punched out on paper tape, along with the time, every 30 s. Since the counter would overflow several times in a 30-s interval, the high-order part was computed and appended to the data before it was delivered for analysis.

Originally the program was designed to operate only in the receiver configuration. For the loop stress experiment it was expanded to handle the transmitter case. Part of this expansion involved a sweep mode. This mode was placed under control of breakpoint (BP) switches. Figure 54 gives a flow diagram of this modification. The routine was placed in the 1-s loop so that the sweep would be comparable to that normally used by operating personnel at DSS 14 (300 Hz/min).

The desired cycle count was computed from the polynomial. This was then compared against the actual cycle count from the counter data. From this the average frequency error over each interval was determined. A histogram of these values was plotted and is shown in Fig. 55. The mean of the error is 0.0113 Hz with a standard deviation of 0.00246 Hz.

e. Use in orbit determination. In the usual process of reducing coherent two-way doppler data, the transmitter signal is held constant. However, in this case, with a variable transmitter frequency, a simple internal hardware subtraction of the transmitter reference frequency does not produce the doppler tone, for the signal transit time must be accounted for. Equation (1), below, shows the terms involved in the calculations.

$$\text{Doppler}_{\text{LSD}} = \frac{1}{T}\int_T \left\{\omega_3 + \omega_4 f_c - \omega_4 f_T\left[1 - \frac{2\dot{\rho}}{c} + H\right]\right\} dt$$

$$= \omega_3 + \omega_4 f_c - \frac{\omega_4}{T^1}\int_{T^1} f_T\, dt + \frac{\omega_4}{T}\int_T f_T\left[\frac{2\dot{\rho}}{c} + H\right] dt \qquad (1)$$

① ② ③ ④

where

T = time interval between the doppler counter readings

ω_3 = 1-MHz bias to keep all readings positive

ω_4 = 96 (240/221), the 96 to bring the reference frequency to S-band and the 240/221 a multiplier in the spacecraft

f_c = constant reference frequency from the synthesizer = 21.985280×10^{-6} Hz

f_T = variable transmitter frequency before the 96 (240/221) multiplication $\approx$ 21,985, 2xx Hz

$\left[\frac{2\dot{\rho}}{c} + H\right]$ = theoretical doppler effect

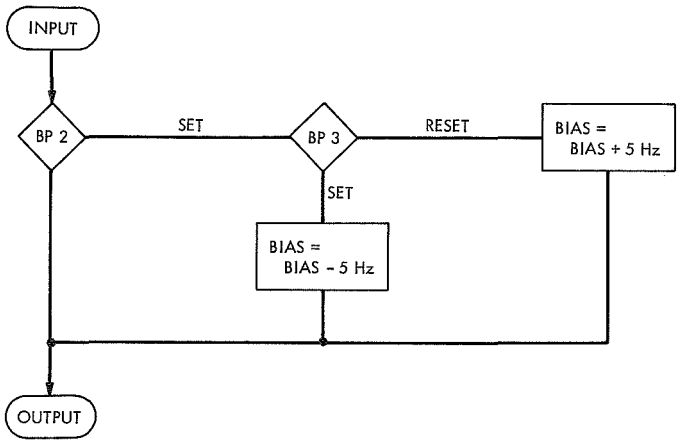

Fig. 54. Control of acquisition sweep by breakpoint switches

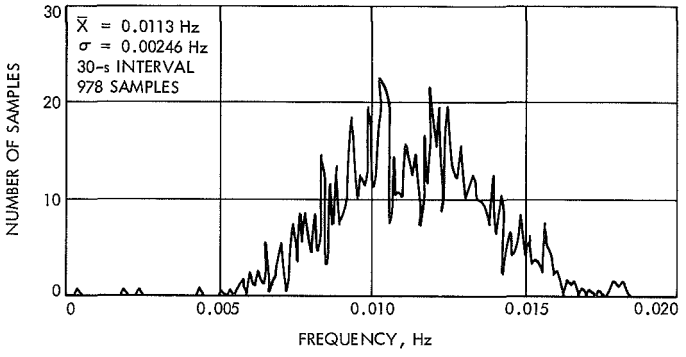

Fig. 55. Histogram of error between ephemeris frequency and actual counted frequency

$\dot{\rho}$ = station–probe range rate ≈ -1 km/s in this case

c = speed of light = 299792.5 km/s

H = higher-order terms of order c^{-2}

T^1 = integration time interval for f_T, which is slightly larger than T due to light time variation over the count interval

In the two-way coherent mode, terms ② and ③ are identical and, therefore, nullify each other, leaving only terms ① and ④. The sensitivity of term ④ is approximately 1 Hz for a 1000-Hz error in f_T. However, in term ③ the sensitivity is 1 to 1 and this holds the key to the data quality. To evaluate term ③ the signal transit time must be known to good accuracy. An error in light time (Δt) is linearly related to a frequency error by

$$\Delta f = \dot{f}\Delta t$$

where $\dot{f}$ is the rate of change in frequency ($\sim$0.3 Hz/s). If a bound of 0.001 Hz is set on Δf, than Δt is 0.0033 s, which reflects a 500-km position error in the spacecraft location. This is much larger than our uncertainty in the spacecraft's position and should not be a contributing error source.

Evaluation of Eq. (1) was performed on the Univac 1108,[14] using the theoretical doppler shift and light time values computed by the Single-Precision Orbit Determination Program (SPODP) (Ref. 1). Double precision was used in the Univac 1108 calculations to carry the necessary accuracy in the transmitter frequency.

The orbit of *Pioneer VI* was established using the SPODP with approximately 3 mo of two-way doppler data.[15] Another reduction of additional two-way doppler data straddling the time of our LSD data acquisition was made using the *a priori* position from the initial 3-mo orbit fit. The data in this last reduction consisted of 12 days of only 2-h coverage over a period of 22 days from DSS 14 (210-ft dish). The reason for the short 2-h tracking periods was due to the spiral radiation experiment, which required telemetry data while in a one-way mode.

Figure 56 shows typical two-way doppler residuals on December 21, 1969 and December 24, 1969 (the LSD data was taken on December 22, 1969). It is evident that

[14]Programmed by S. G. Finley.
[15]Data editing by N. Thomas and data fitting by G. Sievers.

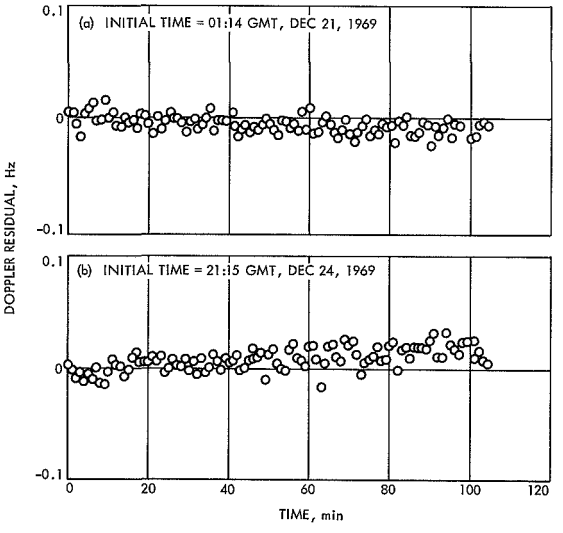

Fig. 56. Frequency residuals measured before and after LSD experiment

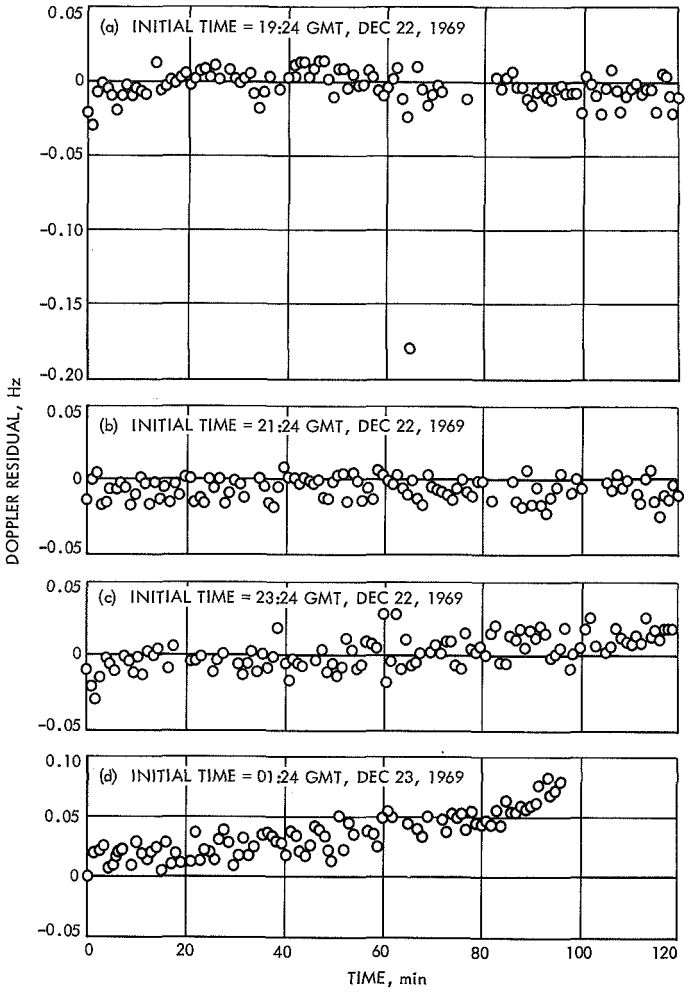

Fig. 57. Frequency residuals from LSD experiment at 60-s count interval

there are small biases in this fit which will definitely bound the evaluation of biases which may be present in the LSD data. This orbit estimate was then used to predict the doppler shift and signal transit times for the LSD data period.

The evaluation of Eq. (1) was performed on some 430 one-min observations. The observations were handled in precisely the same manner as the two-way doppler observations. The counter readings were differenced and the resolver information added. The result was divided by the count time and the time tag was placed at the center of the counting interval. Each observation was differenced with the theoretical value obtained from Eq. (1), producing residuals.

In Fig. 57, the residuals of LSD data on December 22, 1969 are shown. Comparison of this data result with the two-way data (Fig. 56) is indeed very good. The biases are of the same order with no increase in high-frequency noise. The systematic error in the last portion of Fig. 57d is attributable to atmospheric effects (troposphere and ionosphere) commonly seen in two-way doppler taken near the horizon.

In Figs. 58 and 59, the residuals are shown for count intervals of 300 and 600 s, respectively (previous residuals had 60-s count intervals). The reduction in noise now shows quite plainly a −0.005-Hz bias, which could easily be due to the orbit fitting process in the SPODP.

The LSD data obtained using the counted transmitter frequency is definitely on par with the present use of two-way doppler data in the orbit determination process. An orbit estimated using solely the LSD data should

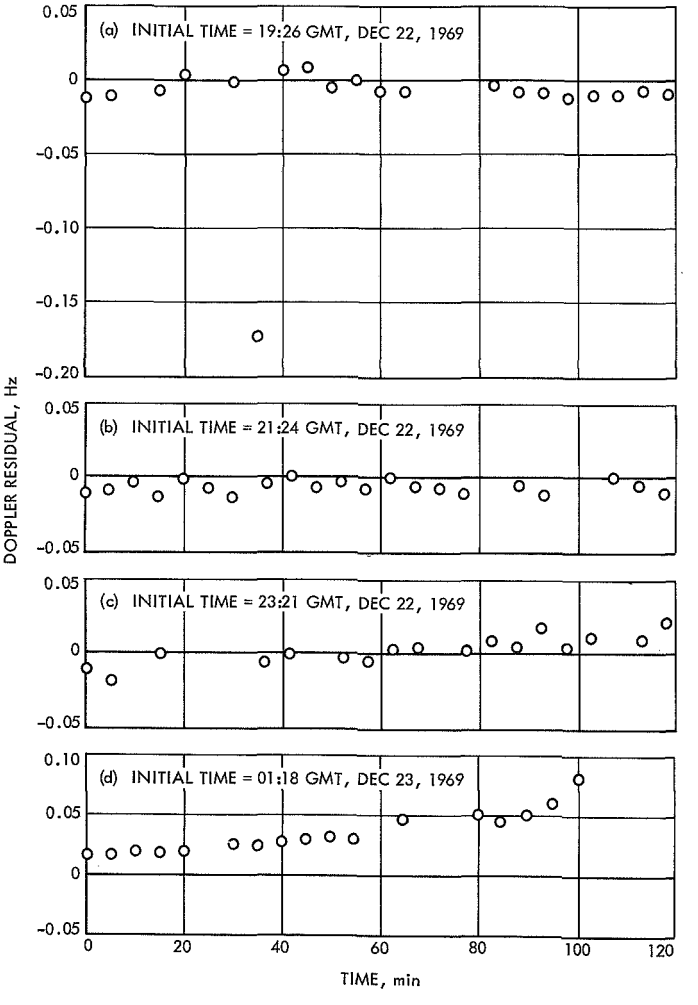

Fig. 58. Frequency residuals from LSD experiment at 300-s count interval

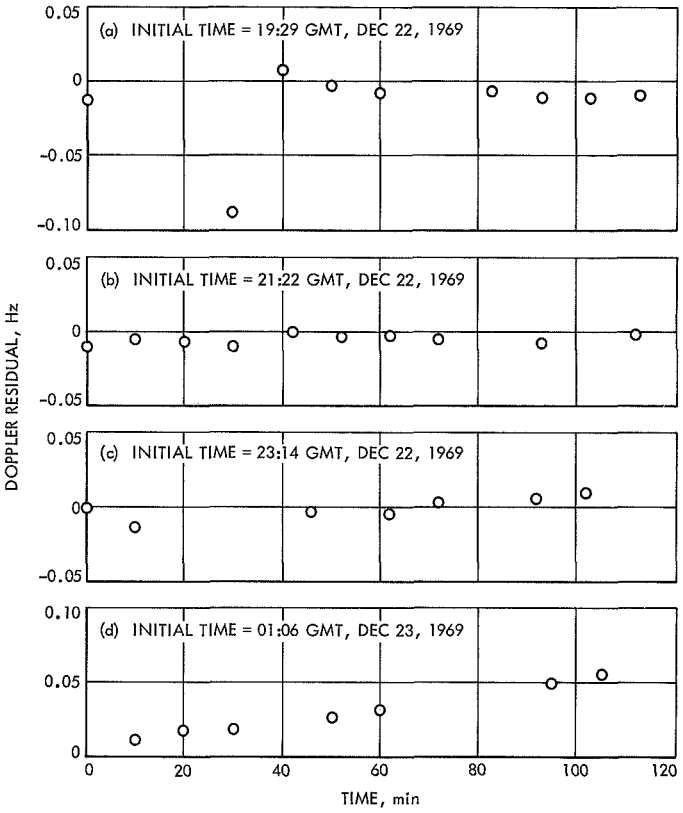

Fig. 59. Frequency residuals from LSD experiment at 600-s count interval

provide as good a solution as the two-way data. This assumption, of course, is based on these initial SPODP results. Reduction using the Double-Precision Orbit Determination Program (DPODP) might show definite small biases attributed to the LSD system. This will be done when refinements are made in the DPODP and more data are collected with the LSD system.

f. Conclusions. The signals received by, and from, *Pioneer VI* were weaker than was desirable for this experiment. Both links were close to threshold. This was due in part to polarization problems in *Pioneer VI*. Circular polarization was transmitted and received at DSS 14, but *Pioneer VI* was polarized linearly.

As a consequence, the doppler data was noisy and cycle slipping occurred occasionally. Cycle slipping in the programmed mode, however, was less than that in the normal mode. The extra noise in the uplink probably precluded most of the downlink improvement expected from a narrower loop bandwidth.

Antenna time with the stronger signals from *Mariner* spacecraft was not available. Because of the experimental nature of this demonstration, normal data could not be guaranteed during a pass. The *Pioneer* Project was, fortunately, willing to take that risk.

The experiment has demonstrated that it is practical to program both the uplink and downlink so as to essentially remove the loop stress. Furthermore, precision two-way doppler data can be obtained that is at least as good as that obtained previously. It was found that the programmed mode in no way interfered with the normal flow of commands and telemetry.

Advantage may be taken of this technique to design tracking loops with at least an order of magnitude reduction in bandwidth. A corresponding reduction of carrier power could then be realized. In addition, the so-called noisy reference loss could be reduced substantially.

Reference

1. Warner, M. R., and Nead, M. W., *SPODP—Single Precision Orbit Determination Program*, Technical Memorandum 33-204. Jet Propulsion Laboratory, Pasadena, Calif., Feb. 15, 1965.

C. Communications Elements Research

1. Tracking and Data Acquisition Elements Research: Improved RF Calibration Techniques—Precision Compact Rotary Vane Attenuator, T. Y. Otoshi

a. Introduction. In SPS 37-46, Vol. II, p. 73, a modified theoretical law was derived for rotary vane attenuators. The modified law was essentially verified when excellent agreement was obtained between theoretical and measured attenuations of a compact rotary vane attenuator which had a total dynamic range of about 30 dB. Experimental results on the compact attenuator were presented in SPS 37-62, Vol. II, pp. 81–87, and in SPS 37-63, Vol. II, pp. 29–33.

Two limiting cases of a rotary vane attenuator design are to: (1) make the resistive loss of the center vane as large as possible so that the attenuator obeys the well-known idealized $\cos^2\theta$ law, and (2) make the resistive loss approach zero so that the attenuator performs as a phase shifter. This article presents results to show that the modified theoretical law is also valid in the limiting case where the rotary vane attenuator performs as a low-loss phase shifter.

b. Modified law. As derived in SPS 37-46, Vol. II, p. 73, the modified attenuation law for rotary vane attenuators is

$$A_{dB} = -10\log_{10}\left[\cos^4\theta + 10^{-L_{dB}/20}\left(2\cos\varphi\cos^2\theta\sin^2\theta\right) + 10^{-L_{dB}/10}\sin^4\theta\right] \quad (1)$$

where

θ = the true rotary vane angle measured relative to the plane of the vanes in the stators. (It is assumed that there is no misalignment between the vanes in the stators.)

L_{dB} = attenuation of the tangential component relative to the normal component at the rotor output, dB. (It is related to the power loss ratio L by $L_{dB} = 10\log_{10} L$.)

φ = phase shift difference between the tangential and normal electric field components at the rotor output.

The differential phase shift at any vane angle setting relative to the zero degree vane angle setting is given by

$$\begin{aligned}\Delta\psi &= \Delta\psi_y(\theta) - \Delta\psi_y(0)\\ &= \arg\left[\frac{E_y(\theta)}{E_y(0)}\right]\\ &= \tan^{-1}\left[\frac{-10^{-L_{dB}/20}\sin\varphi\sin^2\theta}{\cos^2\theta + 10^{-L_{dB}/20}\cos\varphi\sin^2\theta}\right]\end{aligned} \quad (2)$$

where

$E_y(\theta), E_y(0)$ = total vertical component of the voltage wave at the rotor output when the vane angle is at the θ- and 0-deg settings, respectively.

$\psi_y(\theta), \psi_y(0)$ = phase angles of $E_y(\theta)$ and $E_y(0)$, respectively.

It is of interest to note that in the limiting case where L_{dB} approaches infinity, Eq. (1) reduces to the familiar unmodified law. In the other limiting case, L_{dB} approaches zero so that the attenuator performs basically as a low-loss phase shifter.

In order to use the modified law it is necessary that the parameters L_{dB} and φ be known. It can be seen from Eqs. (1) and (2) that when $\theta = 90$ deg, A_{dB} becomes L_{dB} and $\Delta\psi$ becomes $-\varphi$. Therefore, these two parameters can be experimentally determined by measuring the incremental attenuation and differential phase shift when the vane angle is set at 90 deg.

c. Experimental results. In the referenced SPS articles, a description of a precision compact rotary vane attenuator was given. It was also reported that the differential phase shift at the 90-deg vane angle setting varied significantly with frequency. This phase shift change with frequency was much larger than was anticipated. To facilitate a better understanding of the properties of rotary vane attenuators, it is important to determine the cause of the large differential phase shift change. The results of an experimental study made on the compact attenuator are shown in Fig. 60. Measured differential phase shifts over a broad band of frequencies are shown for the cases where: (1) the center vane was made from a thin film of resistive material deposited on a dielectric card, and (2) the center vane was made from the same dielectric card material as case (1), but with the resistive film removed. It can be seen that the main cause of the large differential phase shift change with frequency is due to the presence of the resistive film and not the dielectric material.

Additional calibrations were made on the compact attenuator in the configuration where the resistive film was removed from the center vane. This was done to test the validity of the modified law in the limiting case where the rotary vane attenuator performs as a phase shifter. The effects of possible mismatch errors were first investigated by measuring the reflection coefficient char-

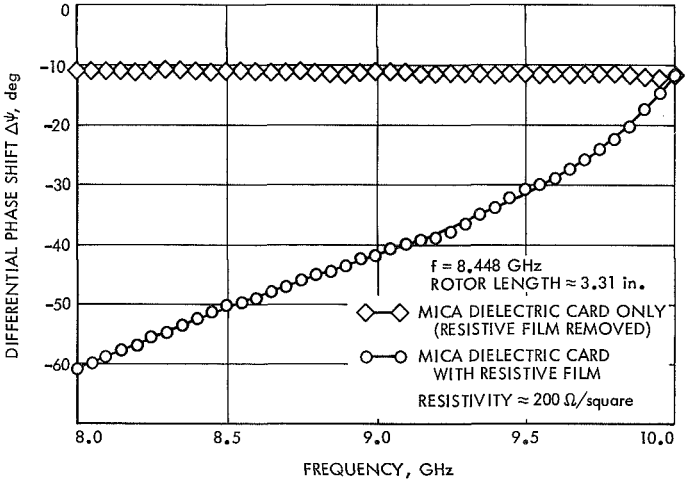

Fig. 60. Frequency response of differential phase shift when vane angle is set at 90 deg

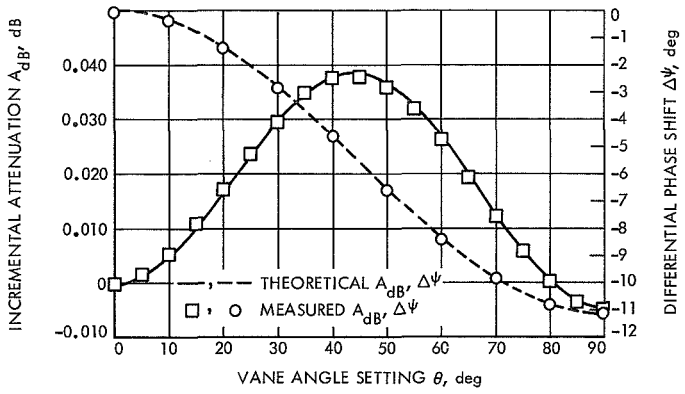

Fig. 61. Comparisons of experimental and theoretical values of incremental attenuation and differential phase shift (resistive film was removed from center vane)

acteristics. It was found that at 8448 MHz the reflection coefficients varied according to the equation

$$|S_{11}| \approx |S_{22}| = 0.006 \cos^2\theta + 0.018 \sin^2\theta \qquad (3)$$

where $|S_{11}|$ and $|S_{22}|$ are the magnitudes of the voltage reflection coefficients as seen looking into the input and output ports, respectively, when the opposite port is terminated in a nonreflecting load. It was concluded that if the attenuator is calibrated in insertion loss and phase measurement systems that were tuned to VSWRs of 1.01 or less, the effects of mismatches would be negligible. A comparison of theoretical and experimental values of incremental attenuation and differential phase shift as a function of vane angle setting may be seen in Fig. 61. The theoretical values were obtained by substitution of measured 8448 MHz values of $L_{dB} = -0.0045$ dB and $\varphi = 11.1$ deg in Eqs. (1) and (2). A negative value of L_{dB} indicates that there is less loss at the 90-deg setting than at the 0-deg setting. The agreement between theoretical and measured values of attenuations is better than ± 0.001 dB and the agreement of phase shift values is better than ± 0.1 deg. From the test results, it appears that the rotary vane attenuator can be made to perform as an accurate phase shifter or as a precision variable attenuator having a total dynamic range of a few hundredths of 1 dB.

d. Conclusions. It has been demonstrated that the modified attenuation law is still valid in the limiting case where the resistive film in the center vane is removed and the attenuator performs as a phase shifter. It was also shown that even when the total dynamic range was reduced to approximately 0.04 dB, the attenuation characteristics as a function of angle setting could still be predicted accurately by the modified law. Such a device might be useful as either a phase shifter (with limited dynamic range) or as an accurate variable attenuator in conjunction with some types of low loss calibrations.

2. Tracking and Data Acquisition Elements Research: Improved RF Calibration Techniques—System Operating Noise Temperature Calibrations of Low Noise Cones, *M. S. Reid and C. T. Stelzried*

The system operating noise temperature performance of the low noise cones in the GDSCC is reported. The operating noise temperature calibrations were performed with the ambient termination technique (SPS 37-42, Vol. III, p. 25). The cones on which this technique was used during this reporting period are:

(1) S-band polarization ultra (SPU) cone at DSS 12.

(2) S-band research operational (SRO) cone at DSS 13.

(3) S-band megawatt transmit (SMT) cone at DSS 14.

(4) S-band Cassegrain ultra (SCU) cone at DSS 14.

The averaged operating noise temperature calibrations for the various cones, and other calibration data, are presented in Table 8 for the period February 1 through May 31, 1970.

The calibration data was reduced with JPL computer program number 5841000, CTS20B. The indicated errors in Table 8 are the standard deviation of the individual measurements and of the means, respectively. They do not include instrumentation systematic errors. The averages were computed using only data with:

(1) Antenna at zenith.

(2) Clear weather.

(3) No RF spur in the receiver passband.

(4) Probable error in operating temperature due to measurement dispersion ($pe_{T_{op}}/D$) less than 0.1 °K (from computer program).

Table 8. Averaged system operating noise temperature calibrations for the low noise cones from Feb. 1 through May 1, 1970

Station	DSS 12	DSS 12	DSS 13	DSS 13	DSS 14	DSS 14	DSS 14
Cone (Serial No. 1 Modification 0)	SPU	SPU	SRO	SRO	SMT	SCU	SCU
Configuration	Low noise path Antenna-mounted	Diplexed Antenna-mounted	Antenna-mounted	Ground located	Antenna-mounted	Antenna-mounted	Antenna-mounted
Frequency, MHz	2295	2295	2388	2388	2295	2295	2388
Maser serial number	96S5	96S5	96S2	96S2	96S3	96S4	96S4
Maser temperature, °K	3.7	3.7	5.0	5.0	4.1	4.2	4.2
Maser gain, dB	57.0 ±0.19/0.06 10 Measurements	57.0 ±0.23/0.06 17 Measurements	38.0 ±1.20/0.27 20 Measurements	36.5 ±0.84/0.60 2 Measurements	50.5 ±1.8/0.73 6 Measurements	47.2 ±0.61/0.18 11 Measurements	33.2 ±0.41/0.20 4 Measurements
Follow-up noise temperature contribution, °K	1.2 ±0.33/0.18 9 Measurements	0.49 ±0.03/0.008 17 Measurements	0.66 ±0.22/0.05 21 Measurements	0.74 ±0.41/0.22 2 Measurements	0.22 ±0.06/0.02 6 Measurements	0.81 ±0.12/0.04 11 Measurements	4.9 ±0.48/0.24 4 Measurements
System operating noise temperature, °K	17.4 ±0.38/0.12 10 Measurements	24.4 ±0.34/0.08 17 Measurements	16.6 ±1.16/0.27 19 Measurements	14.3 ±2.11/0.33 2 Measurements	17.4 ±0.50/0.21 6 Measurements	17.0 ±0.97/0.30 11 Measurements	23.9 ±0.84/0.42 4 Measurements

D. Supporting Research and Technology

1. DSS 13 Operations, *E. B. Jackson*

During the period April 16 through June 15, 1970, the Venus Deep Space Station (DSS 13) maintained a full schedule of clock-synchronization transmissions, continued its support of the program of pulsar observations, and participated in cooperative planetary radar experiments with DSS 14. Additionally, DSS 13 supported the *Mariner* Extended Mission Project by taking high-resolution spectrograms of the radio frequency carrier from the *Mariner VI* spacecraft and both carrier and the first telemetry sideband from the *Mariner VII* spacecraft, while the spacecraft were operating in two-way mode, with the ground transmitter maintaining the spacecraft receiver in phase-lock.

A 100-kW, 2115-MHz transmitter was completed and installation commenced into the electronics room on the 85-ft-diameter antenna. This transmitter, when installation is completed, can provide up-link operation to spacecraft and act as backup during critical periods of a mission.

An experiment, planned for a 2-mo duration, to accurately determine the resolution of the clock-synchronization system, commenced on June 1, 1970. The National Bureau of Standards (NBS) and the United States Naval Observatory (USNO) are actively cooperating in this experiment and operate clock-synchronization receiving stations for real-time comparison between the master clock at DSS 13 and the clocks at USNO and NBS. Transmissions to these two stations, plus the other DSIF stations, are made daily for a 30-min period each, and the data are reduced and sent to JPL on a weekly basis.

In cooperation with DSS 14, bistatic planetary radar experiments have been conducted with the planet Mercury as the target. In these experiments DSS 13 illuminates the target with the 85-ft-diameter antenna and the 450-kW transmitter. DSS 14 receives the reflected signal with the 210-ft-diameter antenna and microwaves the 455-kHz video signal to DSS 13, where it undergoes processing to produce spectrograms. During this experiment, both matched and cross-polarized total power spectrograms were obtained over a period of several weeks until Mercury orbited out of acceptable range.

As part of the *Mariner* Extended Mission Project a developmental receiver at the Mars Station (DSS 14) received the signals from *Mariners VI* and *VII* spacecraft. The local oscillator for this receiver is under real-time computer control so that the doppler, when the spacecraft is in two-way lock, can be compensated for, thus maintaining the incoming signal in the receiver passband. This signal was mixed down to 455 kHz, microwaved to DSS 13, and processed to produce high-resolution spectrograms. These spectrograms, taken before, during, and after the spacecraft are occulted by the

sun, can be examined for spectral broadening caused by the sun's effects. This broadening was observed in real time on each of the spacecraft as they were occulted by the sun at approximately a 10-day interval.

In cooperation with the Massachusetts Institute of Technology (through their Haystack facility) and DSS 14, a planetary radar experiment was conducted at 7840 MHz with the Jovian moon Callisto as the target. This experiment was conducted for 6 nights with excellent results from the test target (the planet Venus), but results from Callisto are uncertain.

2. Planetary Ranging Demodulator, D. W. Brown

a. Introduction. A redesign and rebuild of the Planetary Ranging Subsystem (known as "Tau" ranging) has been recently completed, with programming and overall checkout nearing completion. This equipment was initially implemented in 1966–1967 (SPS 37-42, Vol. III, pp. 52–56) for the purpose of ranging *Mariner*-type spacecraft to planetary distances and saw service with *Mariner* Venus 67 and *Mariner* Mars 1969. After Mars flyby late in 1969, the equipment was returned for extensive updating.

The objectives were:

(1) To improve maintainability.

(2) To improve self-test, automated calibration, and operational techniques and procedures.

(3) To improve the operational capabilities of the software.

(4) To improve the ranging measurement accuracy and long-term stability.

Significant improvements have been made in all areas. It is planned to reinstall the subsystem at Mars Deep Space Station (DSS 14) in the near future. This article discusses only the analog equipment, known as the Planetary Ranging Demodulator; the subsystem also includes digital hardware and an SDS 920 computer.

b. Initial implementation. The original analog hardware consisted of most of the shaded blocks of Fig. 34 of SPS 37-42, Vol. III, p. 54, and was housed in the two-bay assembly described in SPS 37-45, Vol. III, pp. 70–72, together with the 1-MHz cleanup loop reported in SPS 37-46, Vol. III, pp. 89–92. Not reported in the latter article, but included in this installation, was the additional equipment required to synthesize and distribute reference frequencies of 10, 10.1, and 60 MHz.

The "analog" items included the dual signal channels at the left of the figure (Fig. 34, SPS 37-42, Vol. III, p. 54) and all of the shaded blocks below the RC network and 500-kc VCO excepting the coders and channel swap switching.

c. Present configuration. A block diagram of the modified equipment is shown in Fig. 62. The following significant changes were made to the signal channels:

(1) The phase switch was relocated from the 10.1-MHz reference to the 10-MHz signal path and a narrow-band crystal filter installed at the signal input of the mixer to avoid folding of the noise image frequency into the 100-kHz passband. This change was made between initial reporting and initial implementation. All other improvements occurred during the 1969–1970 rebuild.

(2) Current boosters were added to the coherent detectors to allow driving a 50-Ω load to ±5 V full scale (rather than ±1 V), thus improving the dynamic range (defined here as the ratio of maximum linear output to residual dc offset level) from 54 to 74 dB.

(3) The 100-kHz amplifiers were refitted to improve bandpass symmetry and reliability, primarily of the 10-Hz crystal filters.

(4) The step attenuator was relocated from the module slide to the front panel to ease operational setting to signal and noise predicts; dc panel meters were also front-panel-mounted to allow pre-calibration setting of added trim attenuators (located on module slide), which normalize channel gains for nominal input and output levels with a nominal setting of the step attenuator. This rearrangement allows separation and simplification of maintenance and operational procedures.

(5) The post-mixer gain of the mixer was increased by 23 dB, which, together with the increased carrier signal level from −66 to −55 dBmW at the receiver output, offsets the gain changes resulting from items (2) and (4) above.

Table 9 presents the gain distribution before and after recent modifications. Also given are the calibration nominals whereby the trim attenuators are set to produce channel outputs of 1.0 Vdc with a noiseless input of

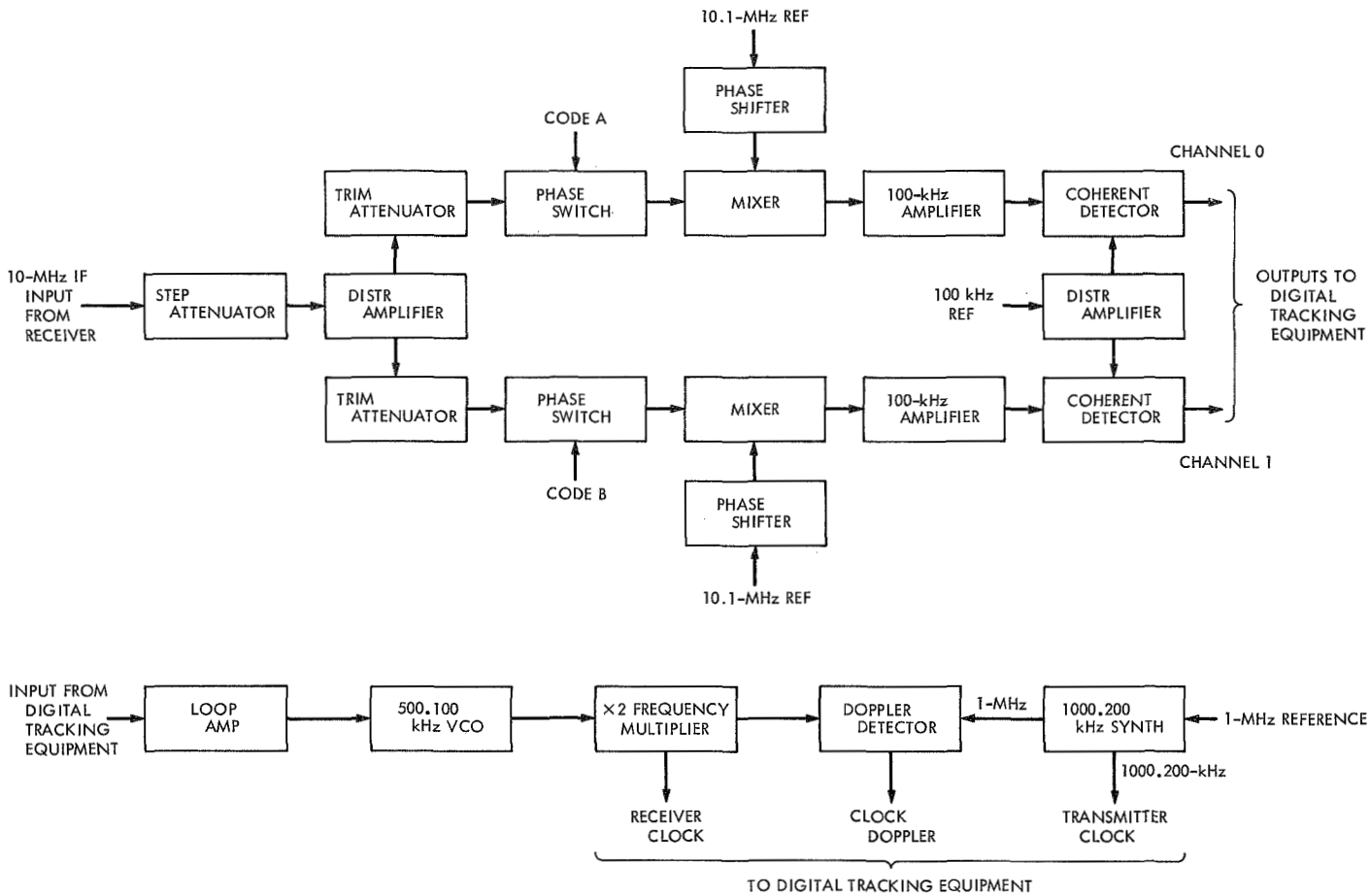

Fig. 62. Planetary ranging demodulator block diagram

−66 dBmW and a step attenuator setting of 43. Also shown is the formulation established in the software such that given predicts of P_c (carrier power), P_r (ranging power), and T_s (system noise temperature), a printout specifies the correct attenuator setting, (Aset), so that the output signal level will be maximized within the linear capability of the hardware. Constants inserted in the program are as follows:

V_{cal} = 1.0 Vdc

V_{pk} = maximum desired excursion of the fully correlated signal plus $p\sigma$ noise (usually chosen 1 or 2 dB less than the nominal hard limiting level of ±5.0 Vdc)

p = peak to rms noise ratio for desired probability of excursion beyond V_{pk} (typically taken as $p = 3$)

K = Boltzmann's constant

B_{IF} = noise bandwidth of 100-kHz amplifier (may be taken as the nominal 10 Hz)

The combined result of these hardware changes and computer-aided setup procedures enhances both the operational reliability and the ratio of signal to imperfections (dc offsets, correlated leakages, analog-to-digital converter biases, and resolution) by approximately 20 to 30 dB. It is expected that similar techniques will be combined with a computer-controlled attenuator to provide fully automated operation in next generation equipment.

Figure 62 (and Fig. 34 of SPS 37-42, Vol. III) shows that the remaining hardware has been significantly simplified. Specifically, the clock switch loop and the analog phase shifters have been eliminated, with equivalent functions absorbed into the digital hardware and software areas. Also, the commercial frequency synthesizer and ×½ (frequency multiplier) have, in effect, been replaced by a ×2 frequency multiplier and a 1000.200-

Table 9. Ranging demodulator signal gain distribution

	1967	1970
Distribution amplifier	+15 dB	+15 dB
Trim attenuator	None	−5 dB
Phase switch	−2 dB	−2 dB
Mixer	+23 dB	+46 dB
100-kHz amplifier	+40 dB	+40 dB
Coherent detector	+20 dB	+14 dB
Maximum gain	96 dB	108 dB
Step attenuator (A_{cal})	−33 dB	−43 dB
Net gain (at calibration)	+63 dB	+65 dB
Input level (carrier)	−66 dBmW	−55 dBmW
Output level (noncoherent)	−3 dBmW	+10 dBmW
Output voltage (coherent)	224 mV	1.0 V
Maximum linear output	1.0 V	5.0 V

Calibration conditions: $P_c = -66$ dBmW, $A_{cal} = 43$
set trim for 1.0 Vdc output

Operational setting:

$$A_{set} = A_{cal} + 10 \log_{10}\left(\frac{V_{cal}}{V_{pk}}\right)^2 \frac{P_r}{P_c}\left[1 + \frac{p}{\sqrt{2}}\sqrt{\frac{KT_sB_{IF}}{P_r}}\right]^2$$

kHz synthesizer. This latter change is largely responsible for an improvement of two orders of magnitude in the overall stability of the ranging modulation transit time, resulting in a stability in range number approaching 1 ns.

This stability is achieved by incorporating the ×2 frequency multiplier *within* the phase integrating tracking loop and through the development of a highly stable transmitter clock synthesizer, offset from 1 MHz to create a biased doppler and to avoid subharmonics of the 10-MHz input signal frequency (SPS 37-63, Vol. II, pp. 42–44).

In addition to the hardware shown in Fig. 62, auxiliary subassemblies mounted within the standard receiver include a UHF doppler isolation amplifier and a three-decade attenuator (for setting exciter modulation level). The demodulator is also dependent upon a coherent reference generator that has been reimplemented as a separate subsystem to support a number of upcoming requirements at the Mars Deep Space Station.

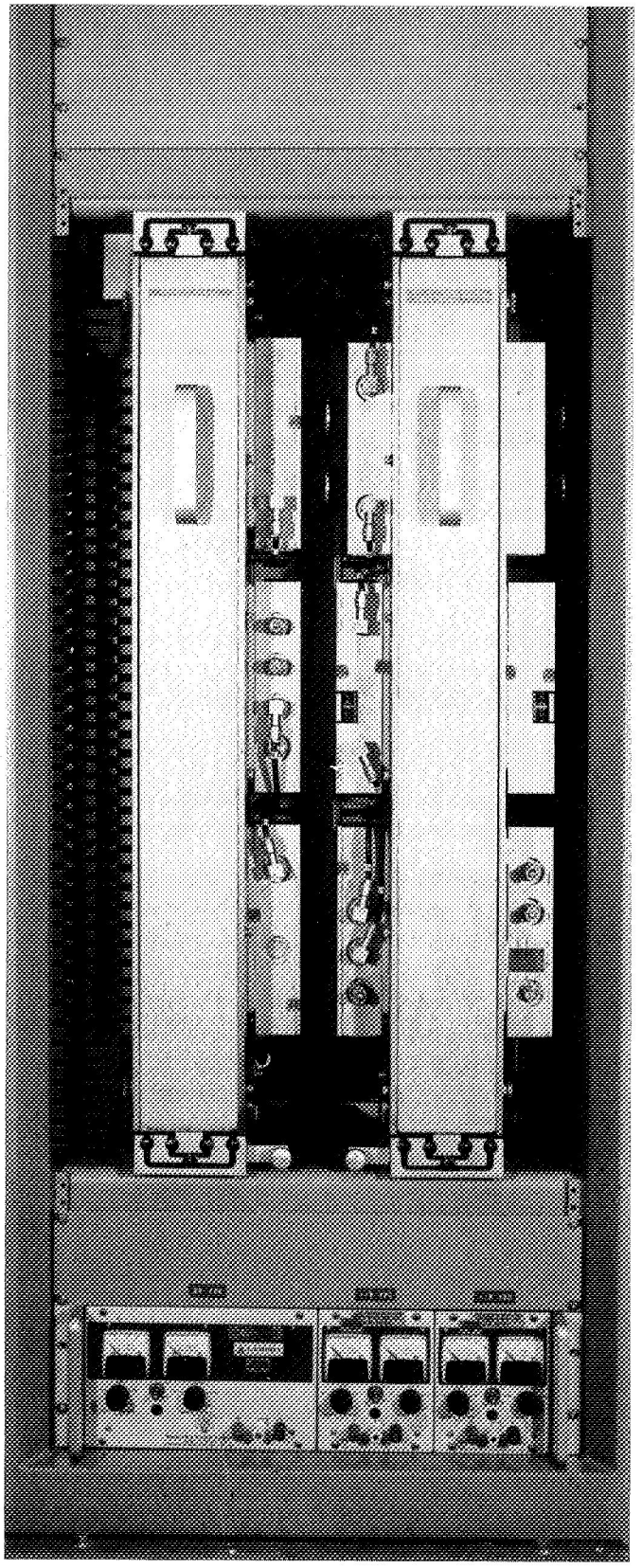

Fig. 63. Planetary ranging demodulator

d. Concluding remarks. The Planetary Ranging Demodulator has been significantly improved in all intended areas primarily through:

(1) Increasing dynamic range.

(2) Increasing modulation stability.

(3) Providing for more straightforward maintenance and operational procedures.

(4) Providing 100% spare subassemblies with the equipment.

(5) Eliminating all commercial test equipment and reducing the number of controls and indicators to a minimum.

(6) Reducing the size from two bays (partially filled) to one bay (partially filled) (Fig. 63). (Panel meters and step attenuator have been subsequently mounted in the blank panel area).

In addition, this effort has provided a measure of transition and evolution toward next generation standard equipment for the 210-ft antenna network.

3. Thirty-Degree Reflector Mockup Study: Comparisons of Measured and Predicted Deflections, *R. Levy*

a. Introduction. A full-size mockup of one-twelfth (30-deg central angle) of a representative 85-ft-diameter JPL reflector constructed at GDSCC provides favorable opportunities to collect important data with respect to the behavior of antenna structures. The mockup, which was originally constructed for the Welded Joint Integrity Study Program, is a source of practical information for thermal distortions and the effect of surface coatings, hysteresis behavior, joint slippage, precision of typical theodolite readings for surface distortions, and the agreement of measurement with analysis for distortions due to applied loading. This article refers to the load/deflection aspects only.

b. Structure and analytic model. The framework of the mockup is sketched in Fig. 64. The structure weighs about 5,200 lb with an additional 800 lb of reflector surface panels forming a skin over the top chords of the ribs. The structural members are typical steel tees and angles that weigh from 2 to 4 lb/ft. The connections were initially bolted, but at the time of load testing, supplementary welds were added to prevent joint slippage. The structure is supported on a concrete foundation at nodes 1, 33, and 35. There is an additional frame (Section B) to brace the structure in a lateral direction. The connections to this frame at nodes 50 and 51 are removable. The load tests were described as "supported" or unsupported, depending upon whether or not the lateral frame connections were present or removed. The analytical model of the structure typically idealized the member connections as pinned because the welds that had been applied were judged not capable of developing substantial continuity. Nevertheless, chord members of the ribs and the members forming the outer hoop that were continuous across joints were modeled as such, and bending resistance about the principal axes was included. Examination of Fig. 64 shows that the analytical model would be unstable without this continuity. A parallel analysis in which full continuity at every node was hypothesized showed only minor differences in the computer deflections. In fact, the difference in deflections for the analytical models with and without full continuity were relatively smaller for this structure than for the structure that was compared similarly in SPS 37-57, Vol. II, pp. 109-111.

c. Data generation. A total of 31 targets (see Fig. 64) for field measurement were located in 7 circumferential rings. Each of the 5 outer rings contained 5 targets; 2 inner rings each contained 3 targets. The targets were read by a theodolite stationed above the vertex (node 3) of the generating paraboloid. Predetermined elevation angles were established for reading the seven target rings, and the deflections from these angles normal to the line of sight were obtained to the nearest 0.001 in. by optical micrometer. Targets were read in the unloaded and loaded condition; the difference in readings was used as the measure of deflection due to load.

The following three independent cases of vertical loads were applied:

(1) A single 985-lb load at node 69, "unsupported."

(2) A single 985-lb load applied at node 59, "unsupported."

(3) A set of 34 sandbag loads totaling 1800 lb, at top chord nodes, "supported."

The field loading tests were performed in the late evenings or early mornings so that the structure could have an opportunity to reach thermal equilibrium. The procedure was to read the 31 targets before the loads were applied, to suspend the loads from the structure and reread, to remove the loads and reread, reload, and continue cyclically until the particular work period ended.

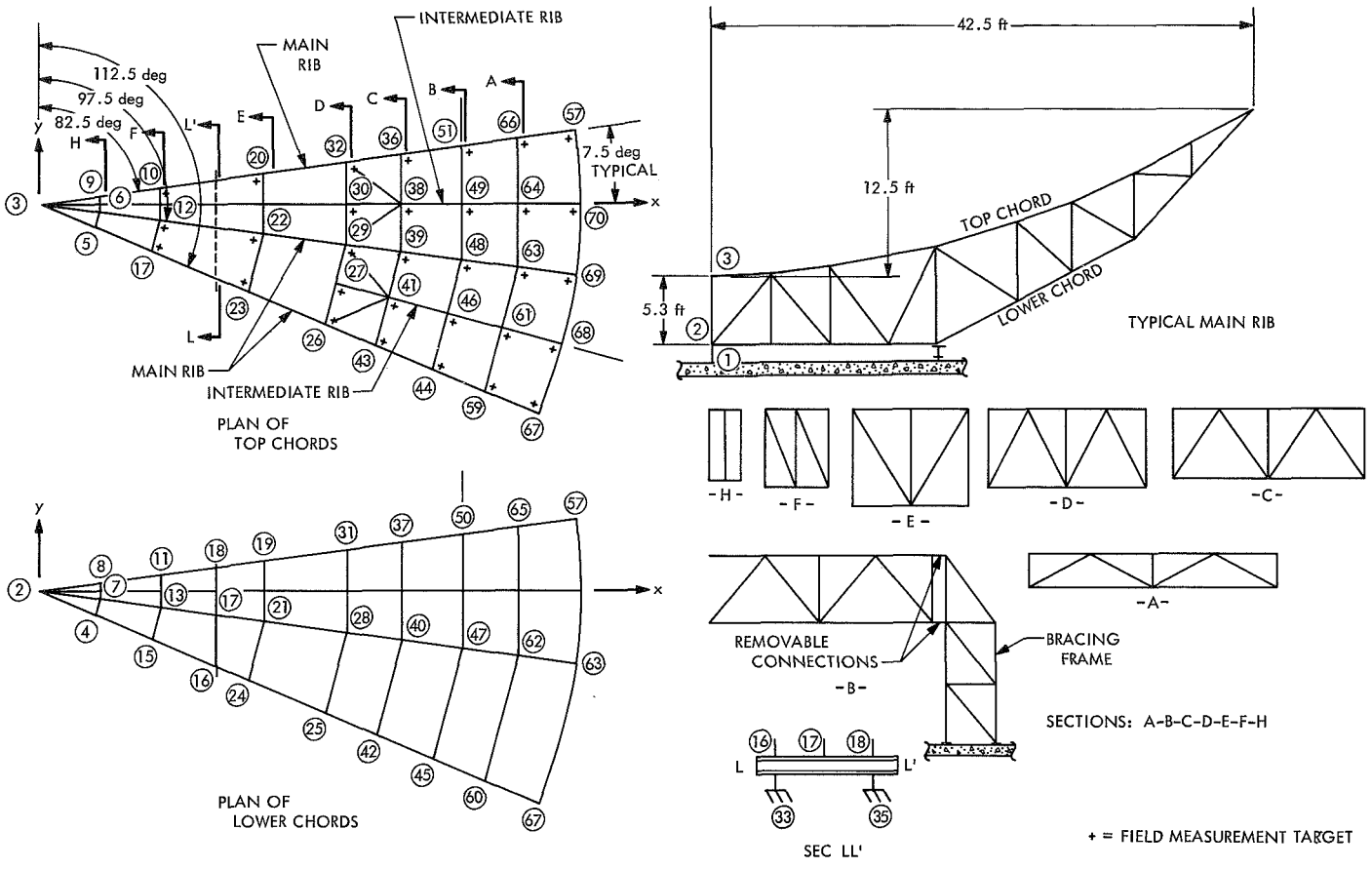

Fig. 64. Thirty-degree central angle mockup of 85-ft-diameter reflector

Consequently, for each loading case there are available several possible repeat sets of the measurements, depending upon selection of the pair for the unloaded/loaded combination. Nevertheless, for cases 1 and 2, the only combinations that have been examined so far are those in which a particular loaded reading set was matched with the unloaded reading set that occurred either directly before it or after it. This resulted in five repeat sets of data for each of these cases. Two sets of loaded readings were taken for case 3, and these were combined with the average of two unloaded readings taken during the period of this test. Each set of readings, unloaded or loaded, was assigned a code number, and identification of the particular test combinations is in the form of unloaded code No./loaded code No.

An analytical model of the structure was processed on the 1108 computer by the NASTRAN program to provide the predictions of deflections. These were converted (SPS 37-61, Vol. II, pp. 102–107) to the hypothetical field target reading differences that would have been observed as the result of these deflections.

During the field tests, the level vials of the theodolite showed significant shifts when comparing the states of load application and removal. These shifts were attributed to foundation movement resulting from changes in bearing pressure, progressive thermal changes in the soil and concrete, and loading distortion of the structure supporting the theodolite. During the applied load periods, incomplete recovery upon load removal was noted. Therefore, there was no consistent datum from which to reference the unloaded/loaded target reading differences and from which comparisons with the analytical predictions could reasonably be made. An approach of establishing immobile reference targets to fix accurate measuring planes was regarded as being both inconvenient and also impractical due to the additional measurement error that would be reflected in the establishment of these planes. The aforementioned anomalies were resolved by best-fitting the field target differences to the analytic prediction. A three-degrees-of-freedom rigid body motion was applied to the field reading coordinate system to minimize the rms variations between field measurement and analysis for the 31 targets. This was

clearly the most convenient and optimistic way to treat the data.

d. Data fitting. The procedure for best-fitting, which supplied a reference field datum, was equivalent to repositioning the theodolite used in the measurement. Two angular rotations and one vertical translation constituted a three-degrees-of-freedom theodolite adjustment. The relationships are developed below.

Figure 65 shows a typical field target with coordinates x, y, and distance R from the target in the X-Y plane. The slope distance S of the target from the theodolite is equal to R sec α, where α is the pre-set measuring angle. The perpendicular distance T_0 is read from the target to the line of sight of the theodolite in its original position; T_1 is the corresponding reading after the theodolite has been rotated through the best-fitting angle ϕ_x and ϕ_y, directed along the respective coordinate axes, and H_0 is the best-fitting vertical shift of the theodolite. In the plane of measurement, ϕ_R is the resultant of ϕ_x and ϕ_y.

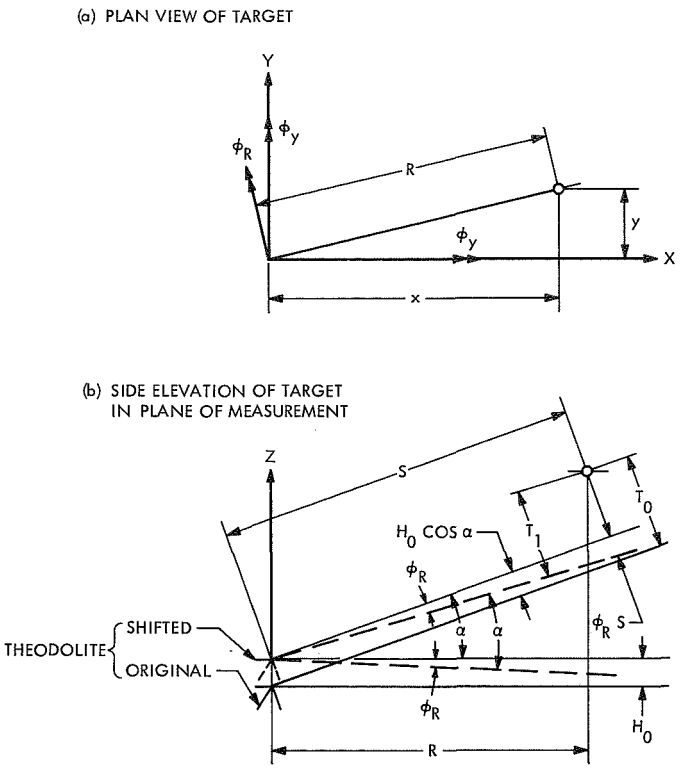

Fig. 65. Geometrical relations for fitting field readings

As shown in Fig. 65b,

$$T_1 = T_0 + S\phi_R - H_0 \cos \alpha \tag{1}$$

$$S = \frac{R}{\cos \alpha} \tag{2}$$

Since these angles are all small,

$$\phi_R = \phi_y \frac{x}{R} - \phi_x \frac{y}{R} \tag{3}$$

Substituting Eqs. (2) and (3) in Eq. (1) gives

$$T_1 = T_0 + \phi_y \frac{x}{\cos \alpha} - \phi_x \frac{y}{\cos \alpha} - H_0 \cos \alpha \tag{4}$$

The residual variation V between T_1 and A, the analytic prediction at this point, is therefore

$$V = T_0 - A + \phi_y \frac{x}{\cos \alpha} - \phi_x \frac{y}{\cos \alpha} - H_0 \cos \alpha \tag{5}$$

The following matrix equation is provided by letting the original difference between field and analytic, $T_0 - A$, be represented by D and expanding Eq. (5) to include all of the points:

$$\{V\} = \{D\} + [B]\{\phi\} \tag{6}$$

where

$$[B] = \left[\left\{ \frac{-y}{\cos \alpha} \right\} \left\{ \frac{x}{\cos \alpha} \right\} \{-\cos \alpha\} \right]$$

and

$$\{\phi\} = \begin{Bmatrix} \phi_x \\ \phi_y \\ H_0 \end{Bmatrix}$$

Summing the squares of the differences, we obtain

$$\sum V^2 = \{V\}^t \{V\} = 2\{\phi\}^t [B]^t \{D\} + \{\phi\} [B]^t [B] \{\phi\} + \{D\}^t \{D\} \tag{7}$$

Taking the partial derivatives of the sums of the squares with respect to each of the components of $\{\phi\}$ and setting them to zero results in the least squares normal equations, e.g.,

$$\frac{\partial(\Sigma V^2)}{\partial \phi_i} = 0$$

or

$$\{0\} = [B]^t \{D\} + [B]^t [B] \{\phi\} \quad (8)$$

The solution of Eq. (8) for the $\{\phi\}$ vector, when substituted back in Eq. (4), provides the adjusted field readings that have been best-fit to the analytical predictions.

e. Data processing. Data were processed by a computer program designed specifically to treat comparative reflector surface target data. The following operations were performed by the program:

(1) Read in punched cards of nodes and coordinates.

(2) Read in the analytical NASTRAN punched card output of nodal displacement components and assigned the nodal coordinates to them.

(3) Converted the analytical displacements to equivalent hypothetical field target readings and stored these for reuse and comparison with multiple sets of field readings.

(4) Read in punched cards for pairs of sets (unloaded/loaded) of field readings, performed the subtractions, and assigned the coordinates for each node. For this input, the field target readings were recorded in a format designed to serve as a key punch coding form.

(5) Performed the best-fit computations.

(6) Determined the averages, standard deviations, root mean squares, and some additional statistics for the vectors of best-fit field readings, analytical predictions, and the corresponding differences. This part of the program represents a statistical analysis phase that is currently undergoing additional developments, which makes it necessary to postpone reporting the full set of related findings.

(7) Generated SC-4020 plots for comparison of field and analytic target readings. The plots are produced optionally along selected circumferential bands of constant radius or along selected radial cuts of constant central angle.

f. Results and discussion. Table 10 contains a summary of results and related statistics for the variations

Table 10. Summary of results

Case	Test identification	Residuals, in.		Ratios for comparison		
	(unloaded/loaded)	rms $= M_V$	Maximum magnitude $= \lvert V \rvert m$	$\frac{M_V}{M_A}$, %	$\frac{\lvert V \rvert m}{M_V}$	$\frac{\lvert V \rvert m}{M_A}$, %
Load at node 69	1/2	0.0087	0.019	14.4	2.18	31.4
(predicted rms = 0.0605 in., M_A)	3/2	0.0085	0.014	14.0	1.65	23.1
	9/10	0.0074	0.021	12.2	2.83	34.7
	11/10	0.0092	0.023	15.2	2.51	38.0
	11/12	0.0060	0.015	9.9	2.48	24.7
Load at node 59	3/4	0.0059	0.013	10.9	2.21	24.0
(predicted rms = 0.0541 in., M_A)	5/6	0.0044	0.009	8.1	2.06	16.6
	7/6	0.0074	0.017	13.7	2.31	31.4
	7/8	0.0073	0.016	13.5	2.20	29.6
	9/8	0.0041	0.012	7.6	2.92	22.2
Sandbag loads	Av/75	0.0128	0.025	28.8	1.95	56.1
(predicted rms = 0.0445 in., M_A)	Av/87	0.0060	0.012	13.5	2.00	26.9

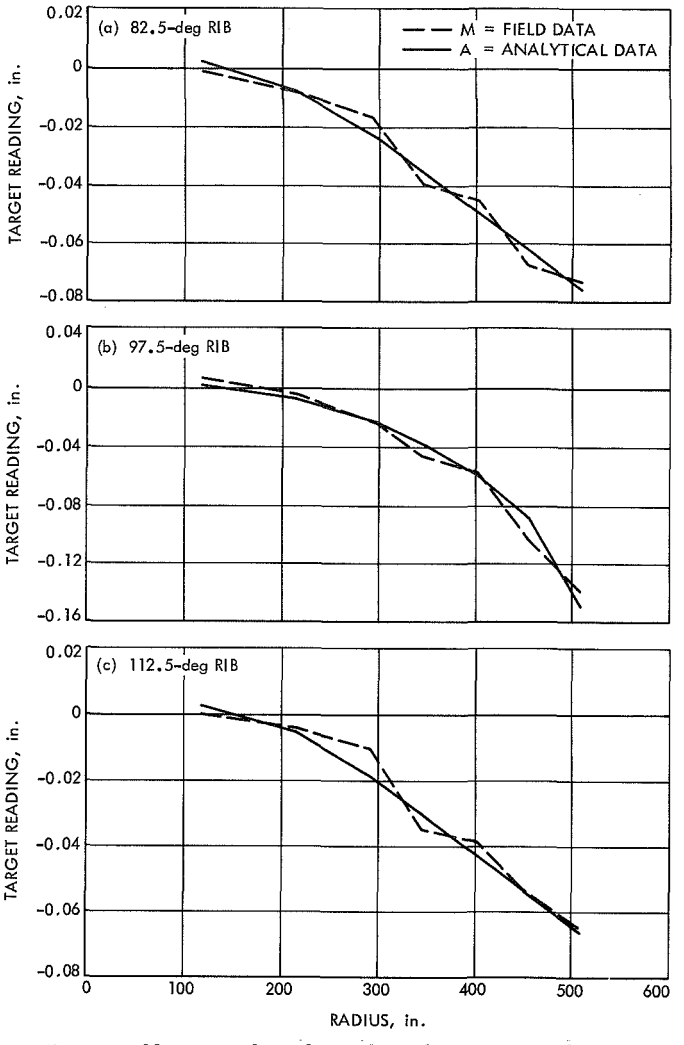

Fig. 66. Measured and predicted target readings, main ribs case 1

between the target measurements and the predictions. Figures 66–68 show curves of the point-by-point measurements and predictions for the three main ribs (7 targets per rib). The curves in these figures are the tests for each loading case that had the smallest ratio of rms variation to rms predictions. These are also the tests within each case for which the agreement of the curves was judged to be the closest. Except for case 3, AV/75 test, all the pairs of curves appeared to agree almost as well as those shown. The tabulated magnitudes and ratios also indicate almost comparable agreement.

The circumstances under which the field measurements were obtained were more favorable than for the usual set of measurements that are taken for a full reflector at variable elevation attitudes. The relatively smaller number of targets and the always-vertical theodolite axis for the mockup measurements tended to reduce operator fatigue and the consequent human error of reading. The analytical model was also developed with possibly more attention to detail than for the usual analysis of the much more cumbersome model of a full-size reflector. The present results, as qualitatively evaluated from the curves, appear to be in satisfactorily close agreement, consistent with the expectation of especially good agreement because of the better-than-average conditions of these tests.

g. Conclusions. It would be preferable if the comparisons of target measurements with predictions could be made quantitatively in terms of some concise measure that is descriptive of the extent of agreement. Although additional statistical evaluations of these and other data are currently in progress, these evaluations have not

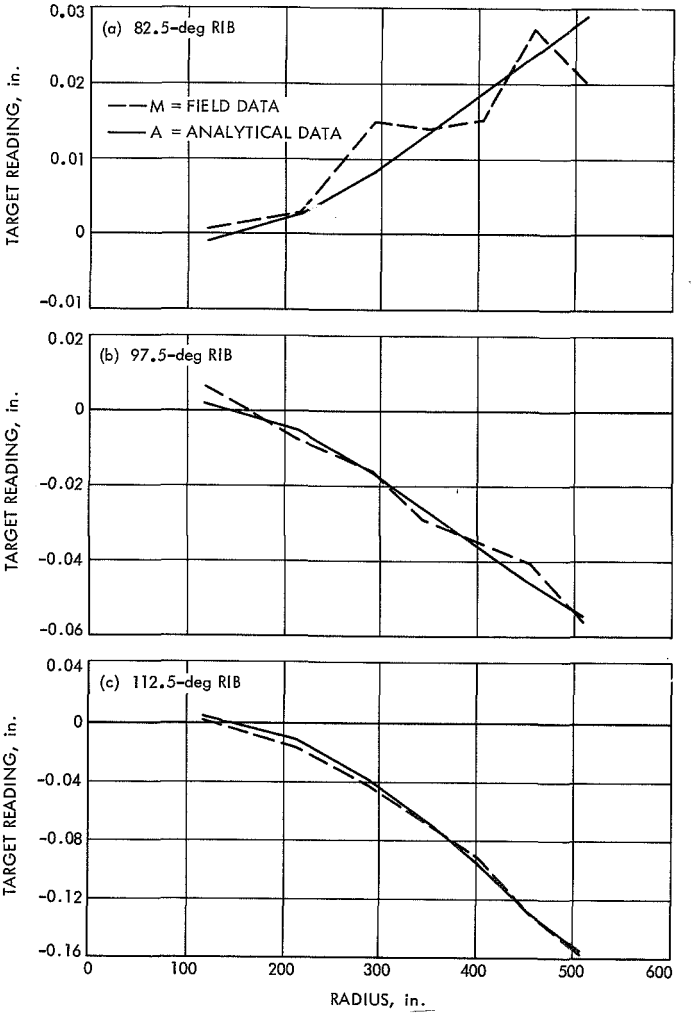

Fig. 67. Measured and predicted target readings, main ribs case 2

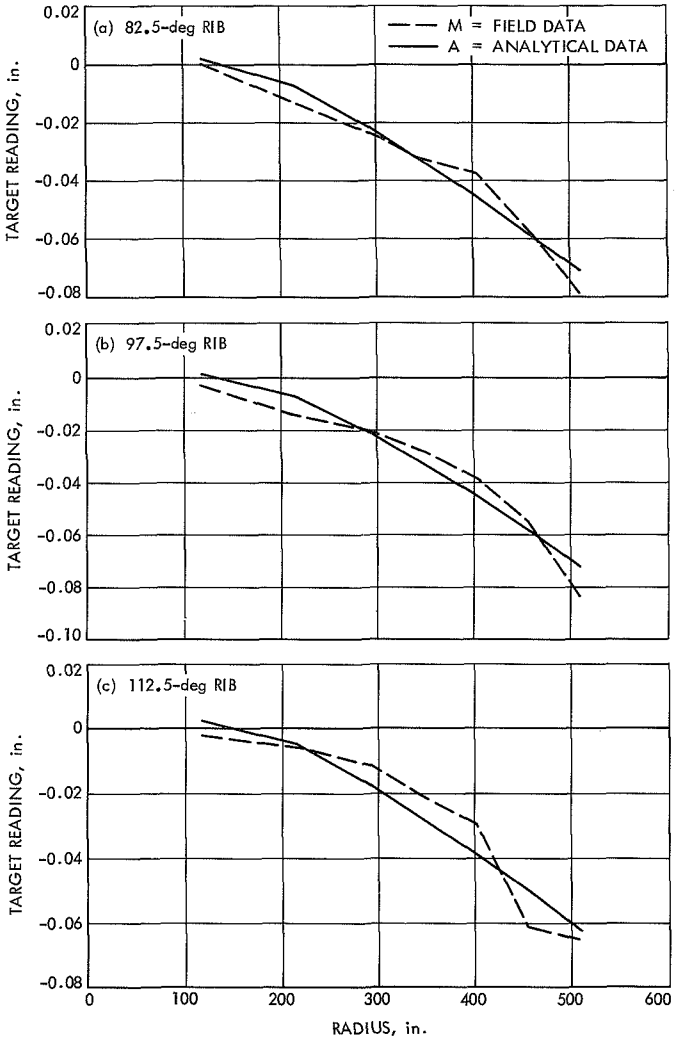

Fig. 68. Measured and predicted target readings, main ribs case 3

progressed to the specification of a particular comparison measure. Nevertheless, it is reasonable to recommend that the following properties are desirable for measures that could be proposed:

(1) Relate to the magnitude of the vector of variations between target measurements and predictions. The relationship might be based upon size (vector norm) or upon the distributions of individual components, or upon the largest magnitude of components.

(2) Contain a normalization factor that would tend to effect independence with respect to the magnitude of loading and possibly, the structural configuration.

(3) Distinguish the variations to consist of two parts, e.g., the part due to measurement error and the part due to idealization error in the analytical model.

The last property listed above appears to be both the most difficult to achieve and yet the most important to attain for antenna reflectors. The difficulty is in the requirement to perform statistical analyses of multiple sets of field measurements that are not readily available and that are expensive to obtain. The capability to separate measurement and modelling errors provides the following important advantages:

(1) The ability to identify and quantify the associated error supplies the opportunity to develop valid ways to improve measurement techniques and modeling approaches.

(2) Knowledge of the field measurement error could permit closer correlation of and close the gap between RF measurements of gain-loss and current theories of performance. The significance here is that specifications for reflector surface accuracy for given performance could be stated more precisely than at present.

(3) Knowledge of the modeling error provides the basis for a valid estimate of the future performance, permitting a realistic evaluation of proposed new designs and modifications to existing reflector structures.

4. Welded Joint Integrity Study, V. Lobb and W. Kissane

a. Introduction. A 30-deg test segment of an 85-ft antenna reflector and backup structure was constructed between March 17 and April 3, 1969, and tested between April 7 and June 20, 1969, at the antenna engineering yard at the DSS 12 site. The reflector segment was used to research possible future antenna design changes, maintenance procedures, and thermal changes and will be used for prototype development of improved measuring systems. The test segment was used to study the following items:

(1) Variation of structure rms due to welding distortion caused by welding the test structure's joints.

(2) Temperature variation of the test structure members in relation to ambient temperature for different finishes.

(3) Thermal variation of structure rms due to different finishes on the test structures.

(4) Creep of tower-bolted reflector structures.

(5) Thermal variation of test panel rms.

(6) Correlation of radial and vertical movements of the test structure.

b. Test structure and instrumentation. The test structure was built to fabrication drawings made from the antenna manufacturer's drawings of the DSS 85-ft HA-dec reflector. Surplus L-band aluminum panels from DSS 12 were used for the test structure surface. The clips and tees for attaching the panels to the upper chord of the ribs were doweled to the ribs and to each other to minimize any movement of the panels relative to the ribs. The structure members were hot-dip galvanized, and bolted together with galvanized tower bolts. The fasteners were installed to a wrench-tight condition, the same as were the fasteners used in the reflector of the DSS antennas. The center post and a wide-flange beam were used for the supporting girder of the test structure and were bolted to a reinforced slab foundation. A theodolite, fitted with an optical micrometer to measure the vertical parallel displacement of the line of sight, was mounted on the top of the center post (as it is in the antenna) 13.000 in. above the vertex (see Fig. 69). The optical micrometer range was 0.000 to 0.250 in 0.001 increments.

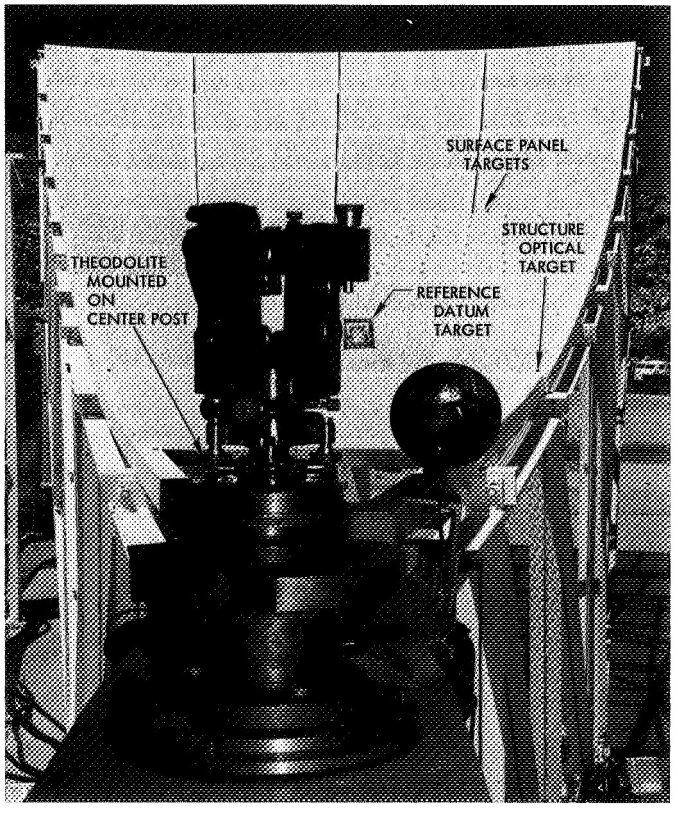

Fig. 69. Test stand targets and theodolite mounting

A reference datum target of the wide-flange girder was established by using the leveled theodolite and a gravity plane containing the datum target (see Fig. 69). The panels were rough set and 31 targets were installed on the panels at the test structure's surface joints (see Fig. 69). The targets were installed at given angles for each row of targets measured from the leveled theodolite and the datum target plane. The targets were set to lie within ± 0.020 in. of the target angle. This was permissible because only differences in rms were required. Also, a reference set of micrometer measurements would be subtracted from the micrometer measurements corresponding to a desired condition.

A total of 73 thermocouples was used on the test structure. One thermocouple was placed at each intersection of the members of the structure (see Fig. 70) (joints of the computer model of the structure) and three thermocouples were placed on one aluminum panel surface. The NASTRAN Program, which was used to determine computer-calculated thermal deflections and resulting rms, takes the member temperature as the average of its end point temperatures, hence the need for joint temperatures. No attempt was made to prepare the galvanized structure other than minimal cleanings to remove dust and dirt from the surface. The thermocouples were attached to the structure by Eccobond 57C adhesive, using aluminum caps. The thermocouple-measuring junctions were formed by arc fusion techniques. Individual thermocouple wires employed were made from duplex-style Chromel Constantan 26 gauge solid premium grade cable with FEP Teflon insulation. JPL standards lab calibration of the thermocouple wire showed no larger than $\pm 0.2°C$ over the range of -45 to $+150°C$. These thermocouple cables were connected to a Pace oven or reference junction located on the ground at the wide flange girder area of the test structure (see Fig. 70). The reference oven was set at 33°F. The gauge cables running from the reference oven to the recording equipment (located in the engineering yard trailer for environmental protection) was made from 20 gauge twisted and shielded pairs of copper wire (see Fig. 70). The recording equipment (two racks) each had a capability of fifty channels. Each channel was switched consecutively into a potentiometer strip chart recorder. The signal was received in millivolts (mV) and displayed on the recorder which had a conversion chart. The range of the recorder was 32–176°F and had a relative accuracy of $\pm 5°F$. The overall accuracy of the instrumentation system was $\pm 1°F$.

The theodolite, equipped with an optical micrometer, for radial measurements was placed roughly normal to

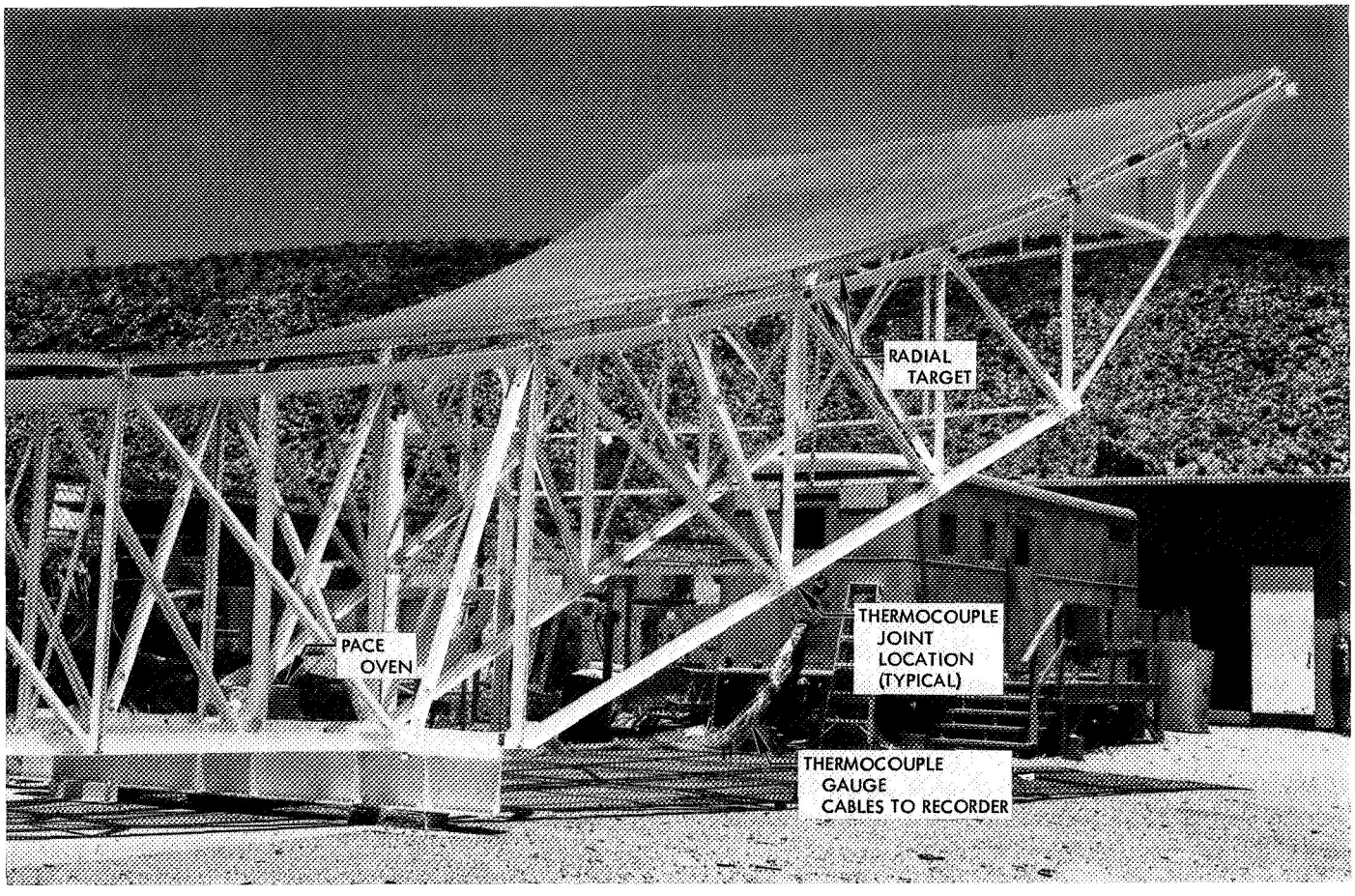

Fig. 70. Test stand thermocouple instrumentation and radial targets

the clockwise outside radial truss and was 76 ft away from the structure. This instrument had a separate foundation from the test structure's slab foundation. The instrument was mounted on a 3-in. standard pipe stand that was insulated with burlap and shaded from the direct sun by an enclosure. The radial stickon targets were set to given azimuth angles from the datum radial target, which was set on the square girder. Fourteen radial targets were used and were placed on the side of the aluminum panel frames and on the outside truss and on the faces of the chord tees near the joints where the radial movements were to be read (see Fig. 70). Only four panel frame radial targets and nine truss radial targets were installed.

One of the panels on the test structure was selected to be monitored for thermal variance due to changing conditions and panel finish. A total of 49 targets was installed in the panel (see Fig. 69), which is about one target per 100 in.^{2} of surface. These targets were installed in rows of seven targets to given vertical angles from the center post theodolite and the datum target plane. A work stand and enclosure were used to shade the center post theodolite, house the theodolite observer, recorder, and the wind gauge meter, and support the wind gauge.

A sway frame was needed to prevent damage to the test stand laterally in high wind and to prevent lateral movements that could contaminate the vertical measurements. The frame was constructed from salvaged material and was pin-connected to the test structure so that it would not constrain the test structure in vertical movements.

c. Test parameters. During the test period of April 7–June 20, 1969, the following test parameters were studied:

(1) Solar heating on a bolted, hot-dipped galvanized structure, with bare aluminum surface panels.

(2) Solar heating, wind loading, and creep on a bolted, hot-dipped galvanized structure, with bare aluminum surface panels.

(3) Welding distortions on a bolted hot-dipped galvanized structure, with bare aluminum surface panels.

(4) Solar heating, wind loading, and creep on a welded, hot-dipped galvanized structure, with bare aluminum surface panels.

(5) Solar heating on a welded, thermally painted structure with bare aluminum surface panels.

(6) Solar heating on a welded, thermally painted structure, with thermally painted surface panels.

d. Test procedures. The radial movements of the targets at the structure joints and on the 4 panels were measured by a theodolite equipped with an optical micrometer. The micrometer was set to read 0.125, as a midpoint; the theodolite was set in azimuth at a reading of 5 sec when it was aligned on the radial datum target. Set azimuth angles were turned on the theodolite, and the optical micrometer was adjusted to measure horizontal distances to give the radial movement directly in inches.

The temperatures of the structure's joints were measured by reading the thermocouple recorder display and recording the readings in numerical order.

The vertical movements of the structure's joints were measured normal to the line of sight of the theodolite. An optical micrometer was set to read 0.125, as a midpoint, and the instrument was leveled to gravity and aligned to a datum target at a vertical angle setting of 0°0′0″. The theodolite (a Hilger-Watts Mark II) directed the line of sight in a horizontal plane when it was leveled and the vertical angle was 0°0′0″. The 0.125 micrometer setting was allowed to vary from 0.110 to 0.140 since the target readings were corrected by the recorded micrometer setting. Set vertical angles were turned and the optical micrometer was adjusted to give the normal to line of sight movement directly in inches.

The above procedure was followed to measure the targets in the test panel.

Four measurements were taken daily: the first at 10:00 p.m. (which was used as a reference), the second at 9:00 a.m., the third at 12:00 noon, and the fourth at 4:00 p.m. The times were selected so as to give different sun angles on the structure and surface panels at various ambient temperatures.

Wind loads equal to 2.5 lb/ft^2 were simulated by sand bags applied to the joints of the structure at the surface to correlate computer-calculated deflections and to check the structure for creep; loads were maintained for periods of 6 to 15 days.

e. Data reduction. The data reduction of field data to an engineering rms involved the use of a FORTRAN computer program. The data were reviewed and corrected, then listed and coded for card punch as input for the program. The program takes a referenced set of field measurements and subtracts them from other sets to give the change that occurred. The program calculates the resulting standard deviation rms from these data. The equation used is the standard deviation as a 1-σ value of the rms of a series of measured points on a surface having normal distribution. (When the term rms is used in this article, the preceding is its definition and is the normally acceptable term for antenna surface measurements in the antenna field.) This program was used with several variations. One was to use day/night cycle comparisons, with the night field data used as a reference for the day change. This method corresponded best with the NASTRAN use of one reference temperature. A second variation was the use of one starting night as a reference for several days of field readings to show the overall effects of different conditions, such as welded, loaded, painted, etc.

A third variation was to use this program to calculate rms on the NASTRAN card output from which the computer calculates the deflections that correspond to the measured joint temperatures input from the test structure. These processed data are printed on the same tabular form as the field data for easy cross-checking and reference.

f. Results and conclusions. The ranges of joint temperatures throughout the test structure for different sun angles and ambient temperatures are shown in Table 11. The beneficial effect of painting the structure is most apparent as shown by the 63% reduction of the maximum daily temperature range of members in the test structure. Painting surface panels had little effect on the structure's temperatures, but did reduce the panel's average, maximum, and minimum temperatures.

All the test structure's members were welded at their connections so as to develop the capacity of the member. The distortion in the structure due to this welding was 0.030 rms; maximum joint movement was 0.090 in. The

Table 11. Structure temperature ranges

Temperature variation	Aluminum panels and galvanized structure, °F	Aluminum panels and painted structures, °F	Painted panels and structures, °F
Structure maximum below ambient	−15	−12	−5
Structure maximum above ambient	+35	+10	+16
Structure maximum daily range	40	15	15
Structure minimum daily range	4	5	2
Structure average daily range	15	9	9
Structure average from ambient	+5.1	−0.7	+1.4
Surface panel maximum below ambient	−9	−12	−7
Surface panel maximum above ambient	+19	+12	+7
Surface panel average from ambient	+1.9	+1.4	0

small distortions and change in rms caused by welding the structure certainly indicates that this would be a more acceptable method than present methods of tightening or replacing bolts on antenna reflector structures. The variation in the test structure's rms for different sun angles and ambient temperatures are shown in Table 12.

Table 12 shows the trend for a reduction in rms in total magnitude and in daily range when the structure is thermally painted. For a given change in temperature ($T = 21°F$) the reduction in rms with thermal painting is apparent. The comparison of NASTRAN-computed rms to measured rms varies from very good to very poor correlation. Generally, the computer calculated thermal rms was smaller than the measured rms. Many uncontrolled variables and tolerances are inherent with this type of study and indeed with the actual antenna. Some of these factors that cause variation of computer-calculated thermal rms and measured thermal rms are listed as follows:

(1) The measuring tolerance. On this study, a maximum allowance of 0.003 rms should be allowed for reading errors, repeatability, instrument error, human errors, etc.

(2) Foundation movements. Daily variations in the foundation of the test stand were noted, probably caused by thermal movements of the concrete and earth.

(3) Wind on the structure. Movements due to wind on the test structure effect the thermal measurements. The wind also affects the structure's temperature distribution during the short time period (1 to 1½ h) of measurement.

(4) Surface panel/structure interaction. The computer model of the test structure does not account for the structural action of the aluminum panels as they expand and contract.

Table 12. Structure thermal rms ranges[a]

Rms variation	Bolted structure	Welded structure			Computed thermal rms
	Aluminum panels galvanized structures	Aluminum panels galvanized structures	Aluminum panels painted structures	Painted panels and structures	
Minimum	0.005	0.009	0.005	0.006	0.001
Maximum	0.025	0.023	0.017	0.023	0.012
Minimum daily range	0.013/0.014	0.020/0.022	0.005/0.008	0.020/0.021	0.007/0.007
Maximum daily range	0.013/0.025	0.009/0.023	0.006/0.017	0.006/0.017	0.005/0.012
Same temperature range	Measured 0.012	0.010	0.006	0.007	
$T = 21°F$	Calculated 0.006	0.009	0.004	0.005	

[a]For ambient temperature ranges of 40–160°F.

(5) The creep effect. The structural creep that occurred in the structure over the entire bolted period had to have an effect on the night/day readings of individual daily cycles.

Table 12 shows an unexpected increase in the rms when the surface panels were painted. Apparently with the panels held near ambient temperature by the thermal coating, the panels constrained the structure and increased the structure's rms as shown on a graph (see Fig. 71) of the average rms against a daily time cycle. The curve that hits the highest peak is the one in which the dish surface is painted. This daily cycle curve also shows the improvement in the painted structure over the bolted or welded galvanized structure. The bolted or welded structure's daily cycle rms is almost identical, except that the welded structure responds earlier in the day to solar heating than does the bolted structure. This may be caused by better heat transfer between members at their connecting joints.

The effect of joint slippage and structural creep is shown on Fig. 72. The bolted structure showed a high rate of creep initially and then a lessening of the rate with time. The welded structure showed an initial creep, but this leveled off to no further creep with time. To minimize the effect of creep on the measured thermal data, the day measurements were based on a night reference that was used to get the rms changes for the three daytime measurements. This method also agreed with the use of the NASTRAN program, which used one reference temperature as a base to get all bar temperature changes. At night, the test structure's temperatures were generally within ±2°F of ambient and this ambient temperature was used for the NASTRAN reference, hence the temperature change that occurred from the

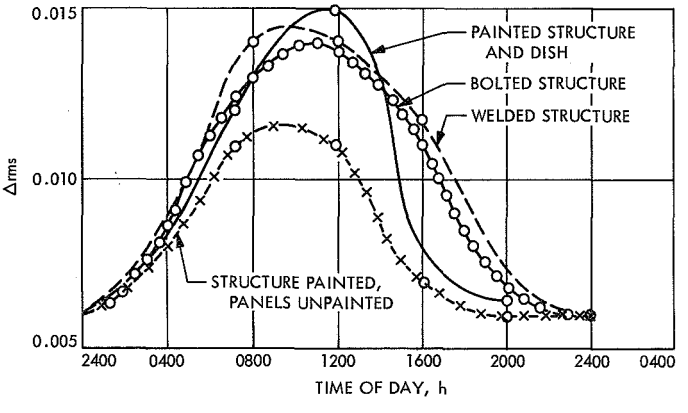

Fig. 71. Average daily cyclic change in rms

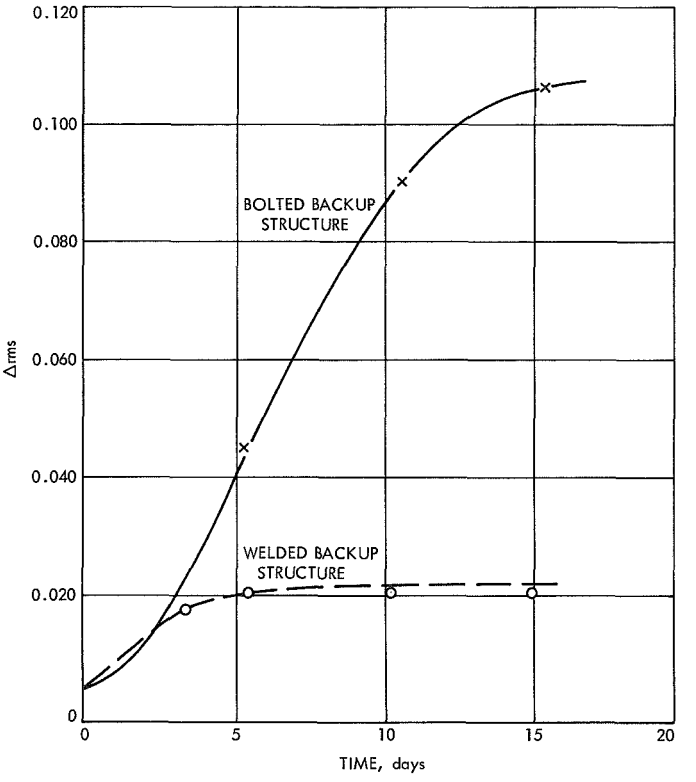

Fig. 72. Structure creep curve

night reference temperature to the following day corresponded to changes in temperatures that occurred for the day measurements.

The creep in the structure was also demonstrated when the sand bag loads were loaded and unloaded on the test structure. In this case, the structure was measured at night unloaded. Then the structure was loaded the following day and measured four nights later. This process was worked in reverse a week later when the structure was unloaded. The measured deflection difference over this period was caused by creep of the structure. The load and unload cycle was done on both the bolted structure and on the welded structure with quite different results. The change in rms on the bolted structure was 0.007 rms (0.047 − 0.040). This change was creep, caused by the joint slippage and set the structure took after the application of the load. The change in rms on the welded structure was 0.001 rms (0.031 − 0.030). This slight change falls within the error budget of the measurements.

The maximum average daily temperature rms for a bolted, galvanized reflector structure with bare aluminum panels was 0.014 in. (see Fig. 69). Since this is a

Table 13. Night/day reference rms vs one reference rms

rms variation	Bolted structure				Welded structure						Painted dish also	
	No load		Loaded		No load		Loaded		Painted			
	Night/ day	1 Ref	Night/ day	1 Ref	Night/ day	1 Ref	Night/ day	1 Ref	Night/ day	1 Ref	Night/ day	1 Ref
Minimum	0.005	0.005	0.007	0.008	0.009	0.009	0.008	0.006	0.005	0.005	0.006	0.006
Maximum	0.024	0.024	0.025	0.070	0.033	0.033	0.023	0.027	0.018	0.017	0.023	0.024
Minimum daily range	0.011/ 0.013	0.013/ 0.014	0.013/ 0.014	0.024/ 0.025	0.020/ 0.022	0.018/ 0.022	0.014/ 0.019	0.010/ 0.019	0.005/ 0.007	0.005/ 0.008	0.009/ 0.011	0.011/ 0.012
Maximum daily range	0.005/ 0.024	0.005/ 0.024	0.013/ 0.025	0.046/ 0.070	0.009/ 0.033	0.009/ 0.033	0.008/ 0.023	0.006/ 0.025	0.006/ 0.018	0.006/ 0.017	0.011/ 0.023	0.006/ 0.017

30-deg segment of a parabola, the thermal rms were not best-fitted by rotation and focal length change which is normally done on a complete reflector. Normally, such best-fitting reduces the rms about 50%, and in this case would give an average thermal rms of 0.007. Also, the test structure rms should be greater than a whole dish as the test structure was a segment and hence received more direct sun than a whole dish. The average thermal rms of 0.007 in. compares with previous work on an 85-ft galvanized reflector structure (DSS 11) with bare aluminum surface panels that had a thermal rms of 0.006. This test structure showed larger peak thermal rms, but this is probably caused by more structure getting direct sun than in the whole dish. Painting the test structure reduced the average rms 25%, but painting the surface caused a 30% increase in the rms. Therefore, from these data and considering a best fit of a thermally distorted parabola, the thermal allowance for an 85-ft reflector structure, thermally painted with thermally painted aluminum surface panels should be 0.006 rms. This thermal allowance will be verified on an 85-ft antenna, thermally painted which will be field measured for various sun and antenna positions (DSS 13, 85-ft az-el antenna).

Changes of rms as a function of ambient temperature relationships were tried, but the relationship was random. The effects of wind, clouds, and temperature distribution nullify any relationship of structure rms change with ambient temperatures.

The use of night/day cycles to minimize the effect of creep is shown in Table 13. The data were reduced by subtracting the night measurements from the following day measurements to get the change that occurred. Also, one reference set of measurements was used to subtract from all the following measurements for any one structure condition, load, or finish. The table shows that the rms values that result are essentially the same with variations of from 10 to 20%. The main difference between the day/night and one reference rms is the effect of structural creep in the loaded bolted structure causing differences of 200–300%. This same creep factor shows to a slight degree in the loaded welded structure.

The night temperature distribution readings for the structure were used in the NASTRAN program to calculate the rms. For a welded, painted structure, the average of the rms for three nights was 0.002. The average of the three nights of the measured rms was 0.004. These results show that the structure's thermal rms (measured and calculated) is a small number at night and is within the range of the measuring tolerance of 0.003 rms.

The test panel thermal rms ranges are shown in the Table 14, which shows a reduction in the panel rms magnitude with a painted structure, probably caused by the panel not being moved as much by the structure from its proper position, since the structure's thermal rms was significantly reduced by painting. The painting of the panel itself increased the rms even further. A thermal allowance for this type of panel (original perforated plate L-band panels) when thermally painted of 0.017 rms would be sufficient.

The new improved S-band panels have more members that support the surface skin better. These members are deeper and hence stiffer than the old panel members. These factors should decrease the thermal rms allowance to 0.010 rms. A direct empirical evaluation of this thermal allowance on one of the improved S-band panels will be measured as installed on the DSS 13 85-ft az–el antenna.

Table 14. Test panel rms ranges[a]

rms variation	Bolted structure	Welded structure		
	Galvanized structure aluminum panel	Aluminum panels galvanized structure	Aluminum panels painted structure	Painted panels and structure
Minimum	0.003	0.005	0.003	0.006
Maximum	0.022	0.020	0.011	0.021
Minimum daily range	0.005/0.007	0.017/0.020	0.006/0.010	0.006/0.011
Maximum daily range	0.010/0.022	0.005/0.015	0.003/0.010	0.006/0.021
Average daily range	0.007/0.012	0.006/0.015	0.005/0.010	0.008/0.017

[a]For ambient temperature ranges of 40—106°F.

The correlation of radial and vertical movements of the test structure against the computer-calculated movements was not too successful. Many difficulties were encountered, such as the theodolite azimuth reference setting being lost twice because someone had tampered with it, targets removed by painters, movements of the theodolite foundation and difficulties in getting repeatable readings. The measurements, when compared with the computer-calculated movements, varied from good correlation to poor correlation. For example, radial movement was 0.010 for both the computer and field measurement, with vertical movements of 0.007 computer calculated vs 0.013 measured. The movements being measured averaged 0.020 radial and 0.010 vertical. The movements were small since the usable data were taken after the structure was thermally painted. The repeatability on vertical measurements is 0.003–0.006 in. and on the radial measurements it is 0.005–0.010 in. This factor, along with previously mentioned problems, would account for the lack of any consistent correlation.

The main points learned from this research are as follows:

(1) Welding the reflector joints causes only minor distortion of the dish, hence this procedure should be used, if needed, to minimize or eliminate resetting of the dish and rebolting of the backup structure (existing maintenance procedure).

(2) Welding the reflector joints is an effective way to eliminate bolted structure creep (0.007–0.001 rms for load to unload cycle).

(3) Actual temperature ranges throughout the structure and how much they are reduced by a thermal coating (for example, the maximum daily range throughout the test structure was 40°F, which was reduced to 15°F after thermal coating).

(4) A basis for thermal allowances for rms budgets used in antenna structure design or modification. The structure thermal allowance for rms budgets determined from this study was 0.006 in.

(5) Bolted structures that use plain tower bolts show creep under sustained load. On this structure the change in rms due to creep was 0.100 in. over a 15-day load period.

(6) The thermal rms on this structure follows a cyclic variation during a 24-h period. This change in rms, on the average, was 0.008 in.

(7) Painting the structure reduces the thermal rms; the amount varies, but was generally 0.004 in. rms reduction (0.014 to 0.006).

(8) Painting the surface increases the thermal rms of the structure and of the test panel; the amount of increase varied from as low as 0.001 to 0.006 rms.

(9) Depending on wind velocity, the equilibrium time (cool off) of the structure was from 1 to 2 h after sunset.

IV. Development and Implementation

A. DSIF Development

1. DSIF Monitor System Development, *F. B. Leppla*

The DSIF Monitor System software is being developed within the DSIF in order to provide the capability for monitoring the performance and alarm status of various subsystems within each DSS.

During the past 6 mo, the software development effort has been transposing the system functional requirements into detailed functional and interface descriptions. The DSIF Software Requirements Document (SRD), which defines the detailed processing to be accomplished and interfaces to be utilized, is approximately 90% complete at this time. In general, the system and subsystem interface descriptions are complete while the detailed processing and DSIF output formats still require some detail definition.

The present software development utilizes new Digital Instrumentation Subsystem equipment as outlined in SPS 37-60, Vol. II, pp. 147–148. This new equipment usage presents many new requirements for the DSIF Monitor Subsystem. These new equipments and their use are described in the following paragraphs of this article.

The high-speed data (HSD) input/output capabilities will be increased to 4800-bits/s rates with 1200-bit blocks. These faster rates will be used to output more discrete DSS configuration and status information to the SFOF. Various status indicators will be output at a resolution rate of 1/s. The total DSS configuration will be output once every 5 s. The DSIF HSD receive capability will be used to replace TTY inputs. This input to the DSIF will consist of tolerance, limit, and prediction information.

The cathode-ray tube and keyboard will provide an interactive computer terminal at the station monitor and control console. This terminal will be used for input (software control) and DSIF monitor display of selected parameters. The output formats will be defined by the DSIF operations personnel to output up to 20 parameters with alarms appearing on the lower portion of the display. The X–Y plotter will output up to five performance parameters at any time. These will also be selectable by DSIF operations personnel.

In summary, the DSIF Monitor Software System Development is continuing on schedule in order to meet functional requirements for the 1971 era.

2. Simulation Conversion Assembly, *E. Garcia*

a. Introduction. The Simulation Conversion Assembly (SCA), an assembly of the DSIF telemetry and command data (TCD) handling subsystem, has been designed to provide the DSSs with a mission-independent spacecraft telemetry simulation capability. The SCA will be used in support of spacecraft projects and for test and calibration of the DSS's multiple-mission telemetry (MMT) equipment (SPS 37-61, Vol. II, pp. 121–147 and SPS 37-62, Vol. II, pp. 3–5).

b. General description. The SCA consists of one Xerox Data Systems (XDS) 910 computer and two SCA buffer cabinets. The XDS 910 computer, its programs, and the peripheral hardware that comprise the SCA (Fig. 1) will:

(1) Receive demultiplexed Automatic Data Switching System (ADSS) formatted blocks, received over one or two high-speed data (HSD) circuits, from the DSN Simulation Center. Received blocks contain simulated telemetry data, SCA control data and operator instructions text data.

(2) Output received telemetry data in formats defined by the received data blocks or modified by SCA control blocks on one to four independent telemetry output channels.

(3) Output telemetry test data, self-generated by the SCA computer with its "stand-alone" software, on one to four telemetry output channels.

(4) Output telemetry test patterns on one to four telemetry output channels in the SCA hardware manual mode.

(5) Provide block coding capability on two of the telemetry output channels with 32/6 or 16/5 Reed–Muller biorthogonal codes.

(6) Provide convolutional coding capability on one of the telemetry output channels with the following coding configurations:

(a) Systematic 1/2 (S 1/2).

(b) Systematic 1/3 (S 1/3).

(c) Non-systematic 1/2 (NS 1/2).

(d) Non-systematic 1/3 (NS 1/3).

Parity constraint length will be up to 32 states with a "tail" length of 24 bits or less in the SCA manual mode. Tail length and frame length in the computer mode will be variable to any length. Frame length in the manual mode will be variable to 2047 bits maximum.

(7) Perform signal conditioning of the telemetry data streams as required for injection at various test input points of the DSS's MMT equipment.

c. Implementation plan. The SCA implementation plan calls for the following two configurations to be implemented:

(1) SCA–antenna-pointing subsystem configuration. In this configuration, the SCA consists of two SCA buffer cabinets and the antenna pointing subsystem (APS) XDS 910 computer. Usage of the computer for SCA purposes is constrained to non-tracking periods.

During tracking periods or APS maintenance, the SCA buffer provides a hardware manual mode used to generate fix test patterns for MMT equipment testing. The DSSs to be provided with this configuration, and the dates of implementation, are as follows:

(a) DSS 11, June 1971.

(b) DSS 12, August 1970.

(c) DSS 41, October 1970.

(d) DSS 42, April 1971.

(e) DSS 51, September 1970.

(f) DSS 61, March 1971.

(g) DSS 62, February 1971.

(2) SCA–XDS 910 configuration. In this configuration, the SCA is implemented with its own XDS 910 computer and the same two SCA buffer cabinets used with the SCA–APS configuration. The stations to be provided with this configuration, and the dates of implementation, are as follows:

(a) DSS 14, January 1971.

(b) The Compatibility Test Station at Cape Kennedy, December 1970.

(c) The Compatibility Test Area at JPL, June 1970.

d. SCA hardware description. The SCA consists of an XDS 910 computer, and two standard Goldstone duplicate standard cabinets defined as SCA buffer cabinet 1 and SCA buffer cabinet 2.

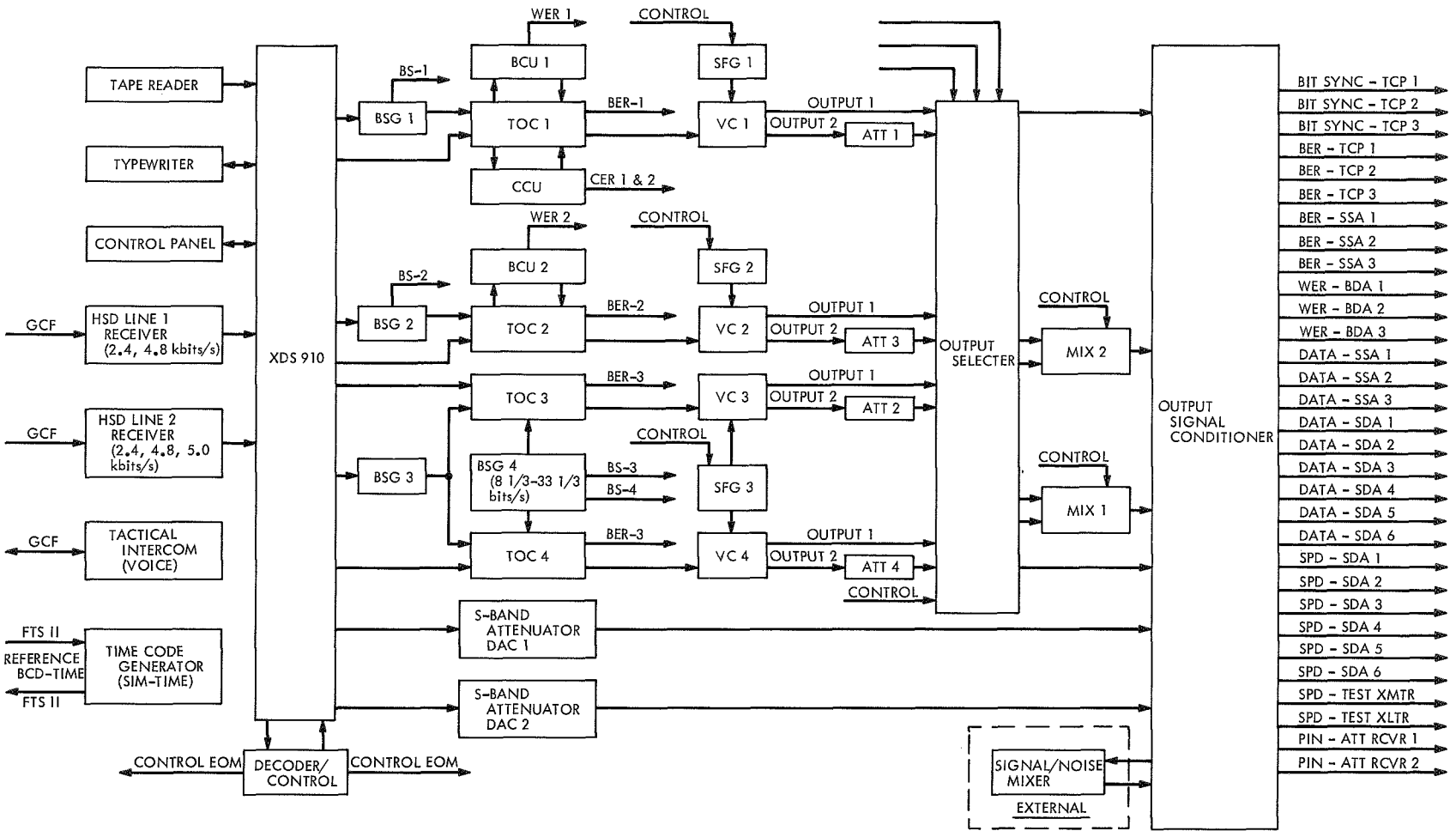

LEGEND

APS	ANTENNA POINTING SUBSYSTEM
ATT	MIX-RATIO ATTENUATOR
BCD	BINARY-CODED DECIMAL
BCU	BLOCK CODE UNIT
BDA	BLOCK DECODER ASSEMBLY
BER	BIT ERROR RATE
BS	BIT SYNC
BSG	BIT SYNC GENERATOR
CCU	CONVOLUTIONAL CODE UNIT
CER	CONVOLUTIONAL ERROR RATE
DAC	DIGITAL-TO-ANALOG CONVERTER
EOM	END OF MESSAGE
FTS	FREQUENCY AND TIMING SUBSYSTEM
GCF	GROUND COMMUNICATIONS FACILITY
HSD	HIGH-SPEED DATA
MIX	MIXING AMPLIFIERS
NRZ	NON-RETURN-TO-ZERO
PIN	PARALLEL INPUT
POT	PARALLEL OUTPUT
SDA	SUBCARRIER DEMODULATOR ASSEMBLY
SFG	SUBCARRIER FREQUENCY GENERATOR
SPD	SUBCARRIER-PLUS-DATA
SSA	SYMBOL SYNCHRONIZER ASSEMBLY
TCP	TELEMETRY AND COMMAND PROCESSOR
TOC	TELEMETRY OUTPUT CHANNEL
VC	VIDEO CONDITIONER
WER	WORD ERROR RATE

Fig. 1. SCA block diagram

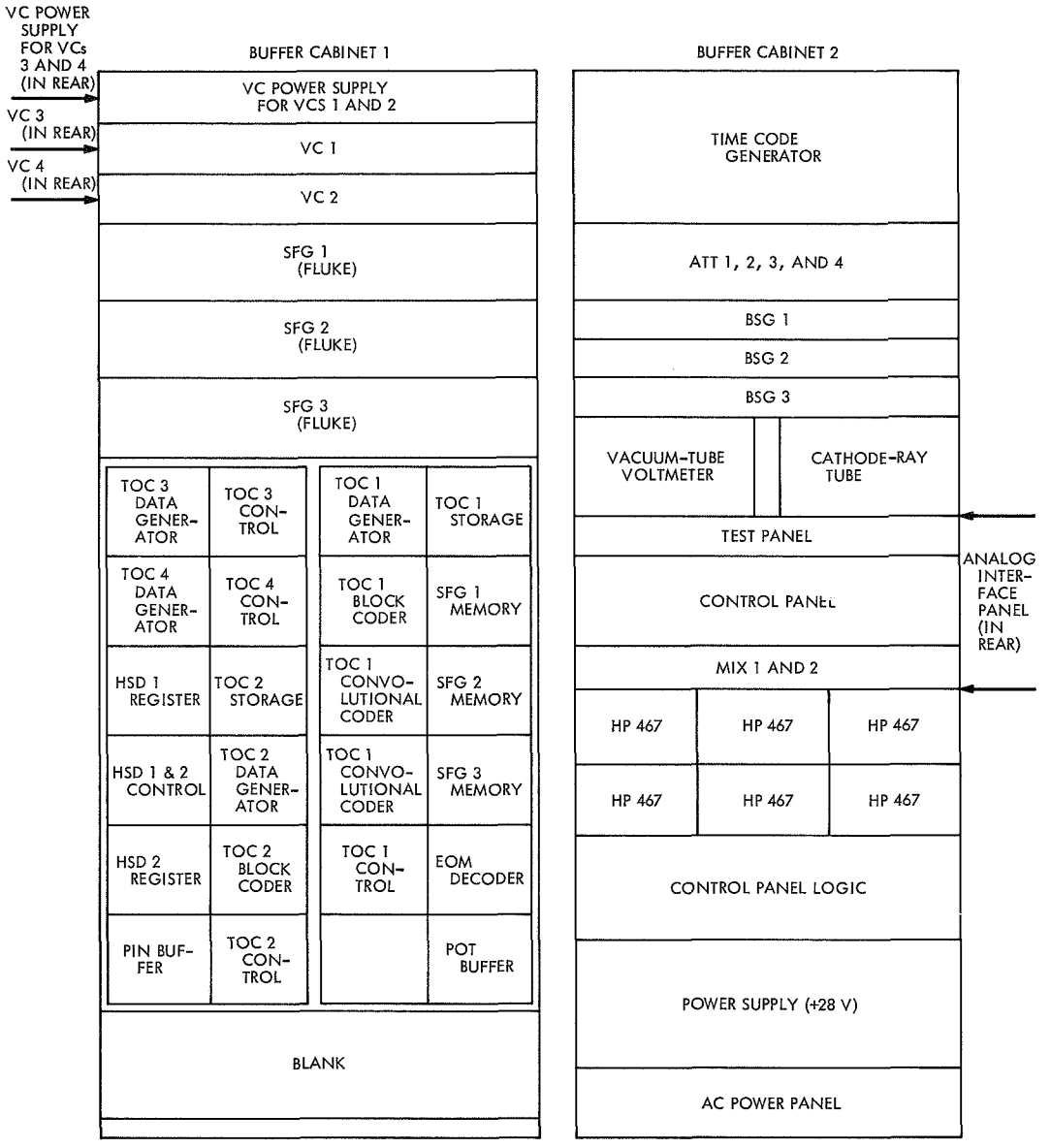

NOTE
SEE FIG. 1 LEGEND FOR DEFINITIONS OF ABBREVIATIONS

Fig. 2. SCA buffer cabinets 1 and 2

Previous SPS articles have presented detailed descriptions of the XDS 910/920 computers, their capabilities, and standard peripheral hardware. Thus, this article will not attempt to describe the XDS 910 computer, but rather will present a summary description of the SCA buffer cabinets.

The SCA buffer cabinets 1 and 2 (Fig. 2) contain all the digital and analog hardware required to interface the XDS 910 computer with external SCA interfaces, as well as the hardware required to provide the capabilities defined in *paragraph b* and subsequent paragraphs.

Telemetry output channel (TOC) 1. TOC 1 (Fig. 3) has been designed to provide simulated telemetry data at programmable data rates ranging from 8 bits/s to 250 kbits/s in any one of its various operating modes. TOC 1 operating modes are as follows:

(1) Manual mode. In this mode of operation, control over TOC is set via the SCA control panel and can be programmed to generate any one of the following uncoded or coded data types (block coded 32/6 or 16/5; convolutional coded S 1/2, S 1/3, NS 1/2, NS 1/3):

(a) Infinite bit. This data type selection forces the output of the TOC to a constant logic one.

(b) Square wave. This data type selection forces a fix pattern of logical ones and zeros to be loaded in parallel from the TOC 1 data storage buffer into TOC 1 data generator register for serial non-return-to-zero (NRZ) output.

(c) Pseudo-random noise (PN). This data type selection uses the first 11 stages of TOC 1 data generation shift register to generate PN data with a 2047-bit sequence.

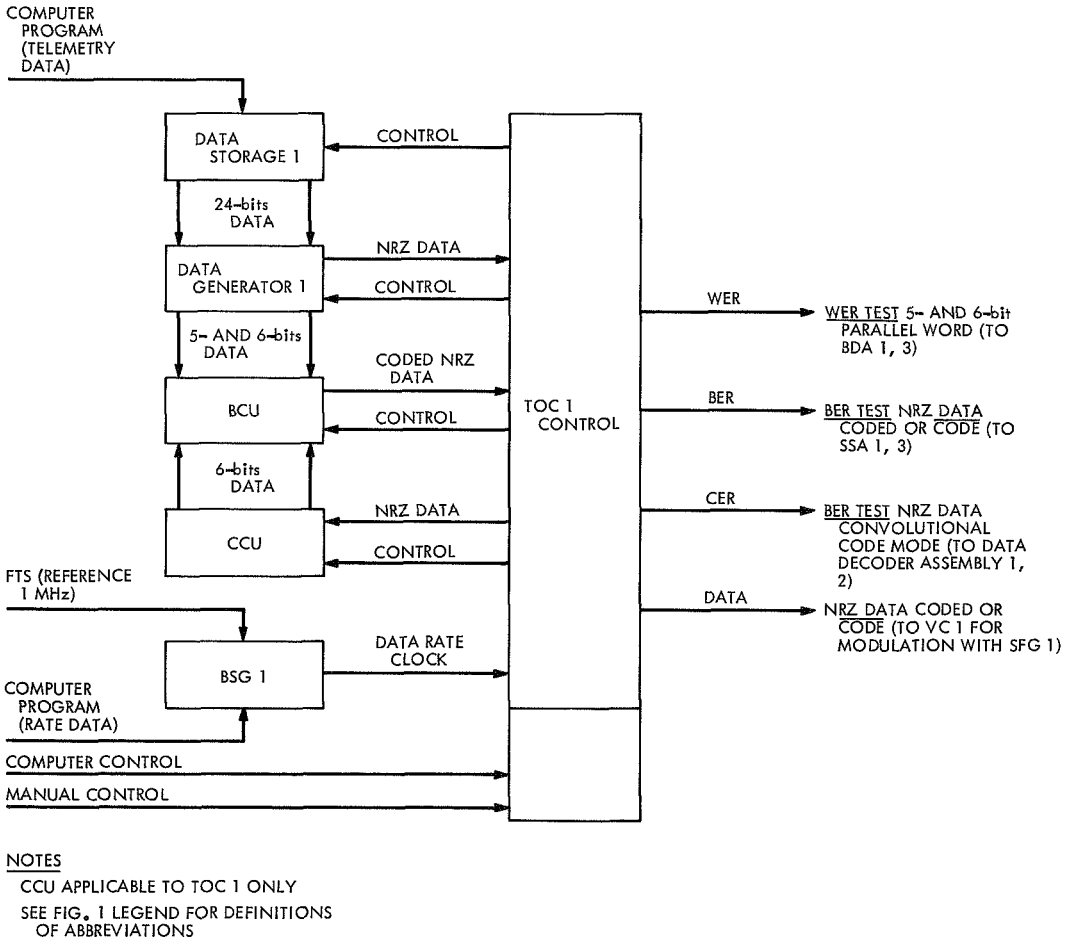

Fig. 3. TOCs 1 and 2

(d) Fixed data. This data type selection loads 6 bits of data preset at the SCA control panel (block-coded fixed data switches). Data loaded into TOC 1 storage buffer from the control panel is continuously reloaded into data generator 1 for serial NRZ output.

(2) Computer mode. In this mode of operation, control over the TOC is set via the SCA computer interface circuits. The TOC can be programmed to generate data types defined by the SCA computer software in the uncoded or coded formats. Software supplied with the SCA will provide the capability to output repetitive fix patterns, data inputted from HSD circuits, and SCA self-generated spacecraft data.

TOC 2. TOC 2 is identical to TOC 1 except that it does not have the capability for convolutional coding.

TOCs 3 and 4. TOCs 3 and 4 (Fig. 4) are identical and have been designed to provide simulated telemetry data at selectable fix rates of 8-1/3, 16-2/3, 33-1/3, and 133-1/3 bits/s, or at programmable data rates from 1 to 2500 bits/s. The TOC 3 and 4 operating modes are similar to TOC 1 except that they do not include block code or convolutional code capabilities.

HSD input registers. The SCA provides the capability for accepting, simultaneously, data from two HSD circuits, both operating at data rates of 4.8 kbits/s, or from one at 4.8 kbits/s and the other, connected to a wide-band data line, of 50 kbits/s.

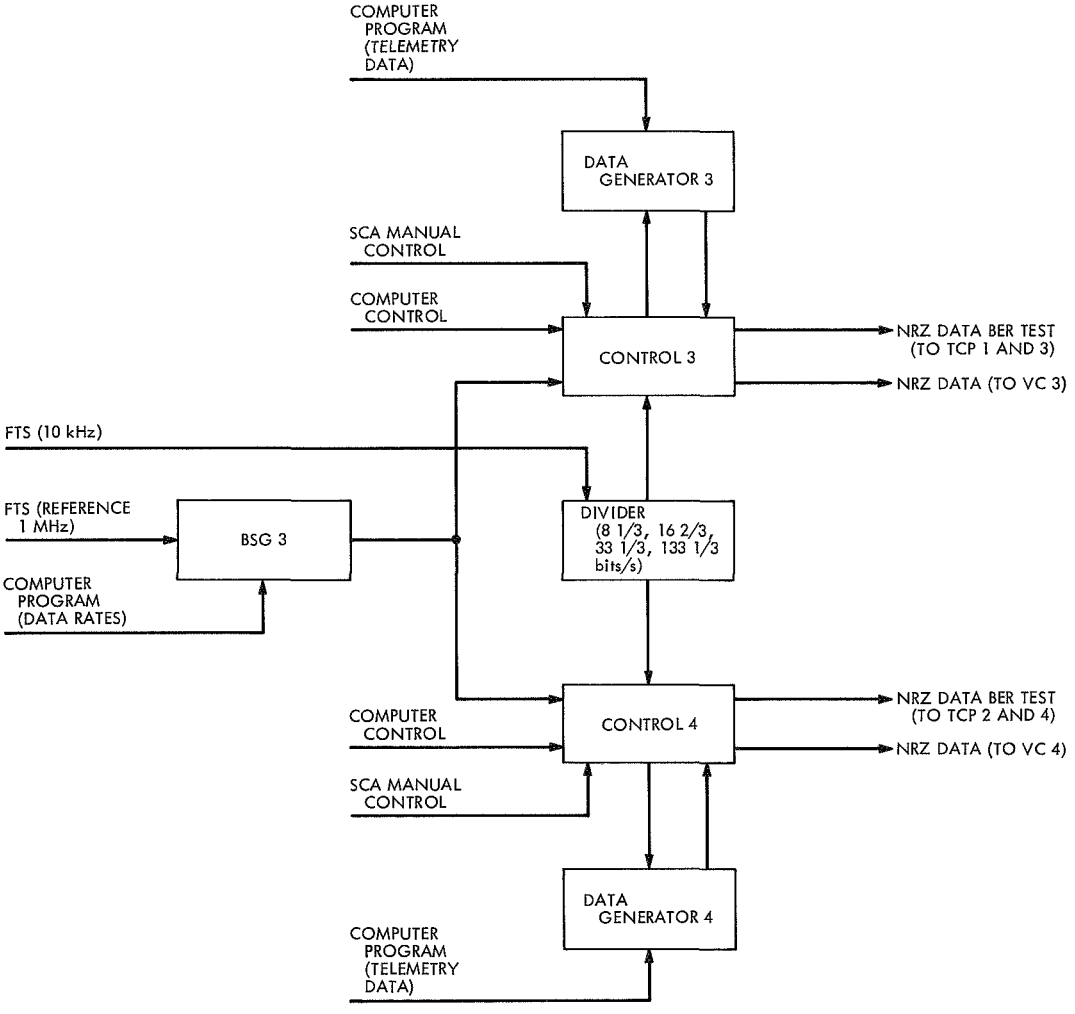

NOTE
SEE FIG. 1 LEGEND FOR DEFINITIONS OF ABBREVIATIONS

Fig. 4. TOCs 3 and 4

The functions performed by the HSD registers (Fig. 5) are:

(1) Convert serial input data to 24-bit parallel required by the computer.

(2) Provide ADSS data block sync detection for the purpose of identifying to the computer the start of an incoming ADSS data block. The sync-detector circuitry provides the capability of allowing up to three random errors in a sync word; sync error is set by a manual switch.

Computer interface. SCA cabinet buffer 1 contains the required logic elements used to interface the XDS 910 computer with the TOCs, programmable data-rate generators [bit-sync generators (BSGs)], subcarrier frequency synthesizers [subcarrier frequency generators (SFGs)], programmable mix-ratio attenuators (ATTs), digital-to-analog converters (DACs), and HSD registers.

The hardware used provides (1) 24 line drivers used to transmit parallel data to the computer, (2) 24-bit line drivers used to transmit parallel data from the computer to the various computer-programmed subassemblies, and (3) a computer-control decoder (EOM decoder) used for control of discrete hardware functions, as well as for steering control of all computer input/output data transfer (see Fig. 6).

SCA manual control. The SCA provides a manual-control capability designed to supplement the computer mode of operation whenever the XDS 910 is being employed for other uses, or when the sum total data rates for any one or all TOCs combined exceed 90 kbits/s. In

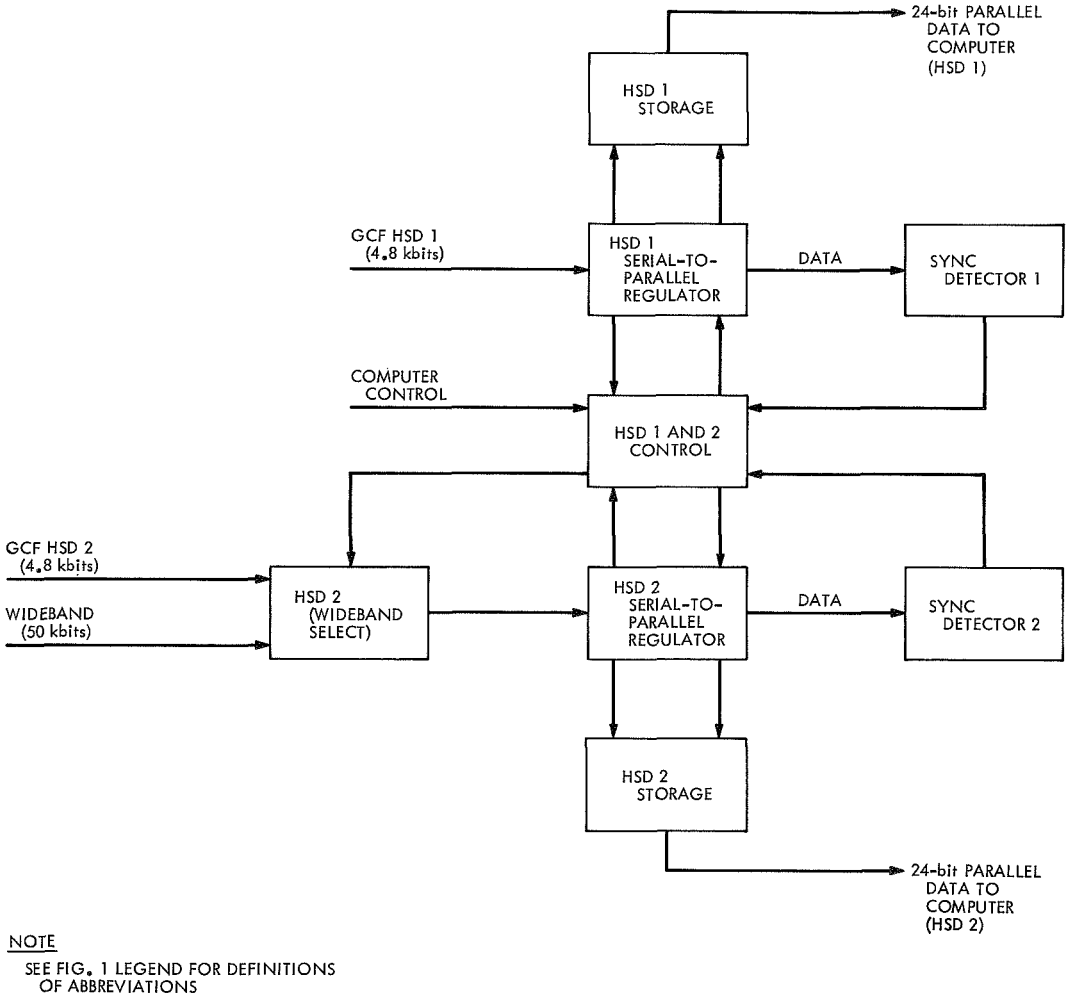

Fig. 5. HSD 1 and 2 registers

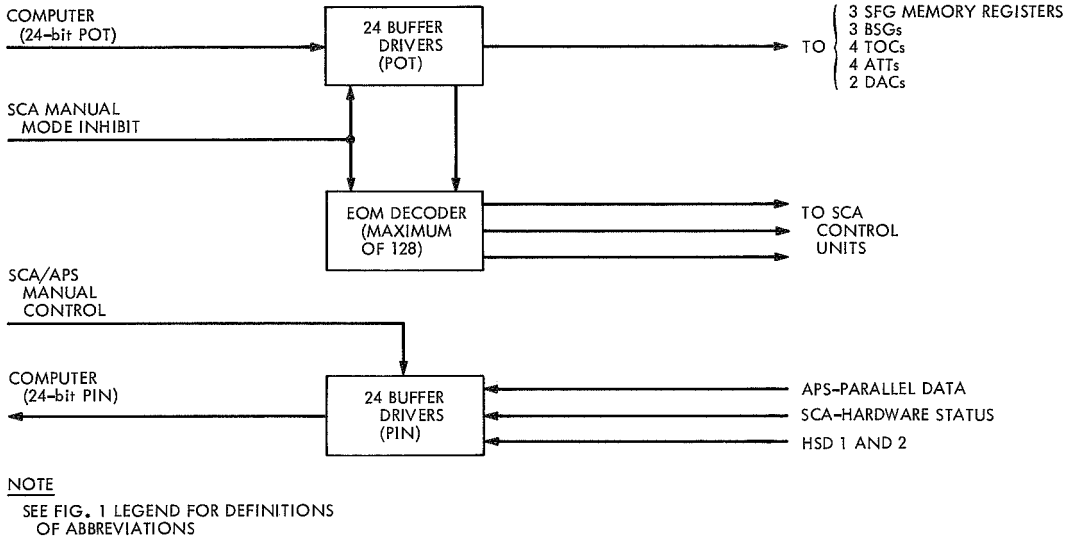

Fig. 6. SCA–XDS 910 interface

the manual mode, any one or all four TOCs are capable of operating at data rates up to 250 kbits/s.

In the manual mode, each TOC is capable of being set independently to the following configurations:

(1) Data type:

(a) XDS 910 (computer mode).

(b) Infinite bit (fixed data equal to logical one).

(c) Square wave.

(d) PN (2047-bit sequence).

(e) Block-coded fixed data (manual set; 5- or 6-bit data word used with 16/5 or 32/6 block coding; channels 1 and 2 only).

(2) Data format:

(a) Uncoded (all channels).

(b) 16/5 block coded (TOCs 1 and 2 only).

(c) 32/6 block coded (TOCs 1 and 2 only).

(d) S 1/2 convolutional (TOC 1 only).

(e) S 1/3 convolutional (TOC 1 only).

(f) NS 1/2 convolutional (TOC 1 only).

(g) NS 1/3 convolutional (TOC 1 only).

(3) Fixed data rates:

(a) 8-1/3 bits/s (TOCs 3 and 4 only).

(b) 16-2/3 bits/s (TOCs 3 and 4 only).

(c) 33-1/3 bits/s (TOCs 3 and 4 only).

(d) 133-1/3 bits/s (TOCs 3 and 4 only).

In addition to TOC manual control, the SCA control panel provides display indicators for the purpose of monitoring all TOCs and HSD input registers, as well as control of the SCA analog interface routing of data or subcarrier-plus-data to the following interfacing equipment: (1) eight subcarrier demodulator assemblies (SDAs), (2) four symbol synchronizer assemblies (SSAs), (3) four telemetry and command processors (TCP), and (4) two test transmitters.

Other manual control functions available are from individual front-panel controls for each SFG and each BSG when selected to local control.

BSGs 1, 2, and 3. The SCA provides three computer-programmable or local, front-panel programmed, square-wave frequency synthesizers capable of setting data rates in the range of 1.00000 bits/s to 1.00000 Mbits/s.

BSG 1 is connected to TOC 1, BSG 2 is connected to TOC 2, and BSG 3 is capable of driving TOCs 3 and 4 either simultaneously or individually.

SFGs 1, 2, and 3. The SCA provides three computer-programmable or local, front-panel programmed, sine-wave frequency synthesizers capable of setting subcarrier frequencies in the range of 2 Mhz to 500 Hz in 1-Hz steps.

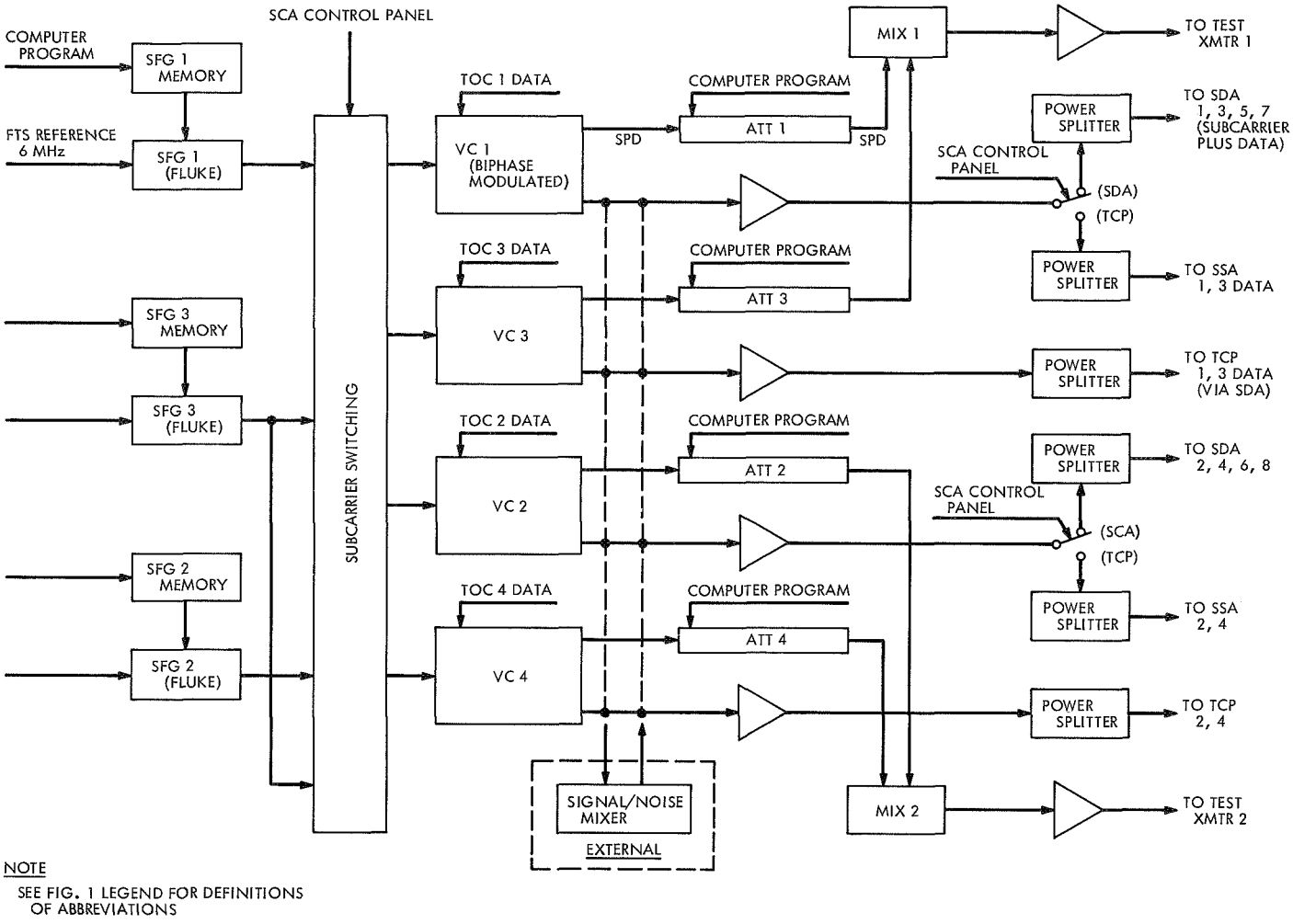

Fig. 7. SCA analog interface

SFG 1 is connected to Video Conditioner (VC) 1, SFG 2 is connected to VC 2, and SFG 3 is connected in parallel to VCs 3 and 4.

SFG remote program memory is supplied external to the synthesizers in SCA buffer cabinet 1.

VCs 1, 2, 3, and 4. VCs 1 through 4 are used to bi-phase modulate the subcarrier frequency with the data generated by each of the TOCs.

ATTs 1, 2, 3, and 4. The SCA provides four computer-programmable ATTs capable of attenuating the output of the VCs in 0.1-dB steps through the range of 0 to 100 dB. The ATTs are used to set the mix ratios between two subcarrier-modulated signals being mixed by the SCA mixing amplifiers (MIXs).

MIXs 1 and 2. The SCA provides two 4-input MIXs with a gain of $\times 1$. At the present, the MIXs are used to mix two subcarriers modulated by data. MIX 1 mixes the modulated signals from TOCs 1 and 3 and MIX 2 mixes the signals generated by TOCs 2 and 4.

The output of MIX 1 is used to modulate the DSIF test transmitter 1 and MIX 2 modulates DSIF test transmitter 2.

Power amplifiers. The SCA provides six power amplifiers used to drive "power splitters" to interfacing equipment (Fig. 7).

3. Transmitter Phase Modulation as a Result of Beam Voltage Ripple, C. P. Wiggins, E. B. Jackson, and T. W. Rathbun

a. Introduction. High-resolution, narrow-band spectrograms of the down-link signals from *Mariners VI* and *VII* were taken in support of the *Mariner* Mars 1969 Extended Mission. It was noted that the *Mariner VII* spectra taken on the second day showed 9.9 Hz phase modulation sidebands, about 16 dB below the carrier level, while the first-day spectra were reasonably clean. (The spacecraft was in a two-way lock with DSS 14.) Spurious phase modulation of the up-data-link transmitter can produce such modulation of the spacecraft transmitter which is phase-locked to the up-link by the spacecraft receiver. An examination of DSS 14 records showed that the 20-kW transmitter was in use the first day and the 400-kW transmitter was in use the second day. The latter, delivering 200 kW, was being used on a best-efforts basis since it was still under construction and not scheduled to become operational until November 1970. The same exciter was used to drive both transmitters.

Amplitude modulation of the transmitter high-voltage supply can result in phase modulation of the RF output, due to the "phase-pushing" characteristic of the klystron. An examination of the power-supply ripple data showed a frequency component corresponding to the spacecraft modulation. Compensation of the power-supply feed-back loop reduced this amplitude modulation, which then reduced the spacecraft down-link modulation below the threshold of the spectrum analyzer.

b. Spectrographic analysis. Figure 8a, which was taken on April 27, 1970, is the down-link signal from *Mariner VII* (received signal strength is −167.5 dBmW). The spurious phase modulation sidebands are approximately 9.9 Hz and about 16 dB below the carrier level. Assuming the spacecraft has faithfully reproduced the input or up-link signal and transmitted it back, it can be concluded that each sideband contains about 5 kW of up-link power. The chart covers a bandwidth of ±50 Hz about the carrier.

Figure 8b was taken on April 29, 1970 after compensating the ground transmitter power supply. The phase modulation is gone and the increased carrier amplitude is due, in part, to the energy removed from the sidebands now in the carrier since the spectrum analyzer's internal gain was the same. Small variations in the signal-to-noise ratio would have also affected the data.

c. Spectrum analyzer. These data were taken by the R&D receiver at DSS 14, receiving the *Mariner VII* signal

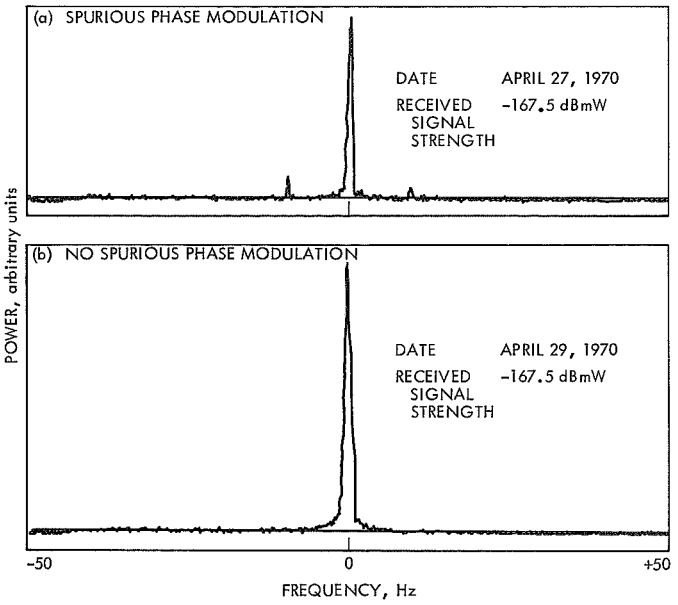

Fig. 8. Spectrogram of *Mariner VII* signal in two-way operation

by utilization of a programmed local oscillator. The receiver output was mixed to 455 kHz, microwaved to DSS 13, mixed to a center frequency of 50 Hz, pre-filtered for a 100-Hz bandwidth, and entered into the computer.

The computer analog-to-digital converter that sampled the incoming signal was operated with a precision clock to take samples at intervals of 5 ms (the Nyquist rate for a bandwidth of 100 Hz). The Fast Fourier Transform was used to analyze the energy per unit frequency in the frequency domain, and the result plotted.

d. 400-kW transmitter power supply. Optimization of the high-voltage power supply feed-back loop, so as to suppress low-frequency modulation, was in process at DSS 14 on April 27, 1970 when the spurious modulation was observed. In preparation, tests were made to determine the amount and frequency of ripple present in the system. Using a transfer function analyzer, phase and gain characteristics of the feed-back were determined and photographs were made of the ripple present. Figure 9 shows the test configuration.

Data correlation indicated the system was near an oscillatory condition at 0.01 to 10.5 Hz, i.e., the phase margin was less than 30 deg, and the gain was greater than unity at these frequencies. Specifically, at 10 Hz, the gain was +6 dB with a phase angle of 160 deg lead. Photographs confirmed the above findings, showing ripple present in the order of 2% at 50 kVdc.

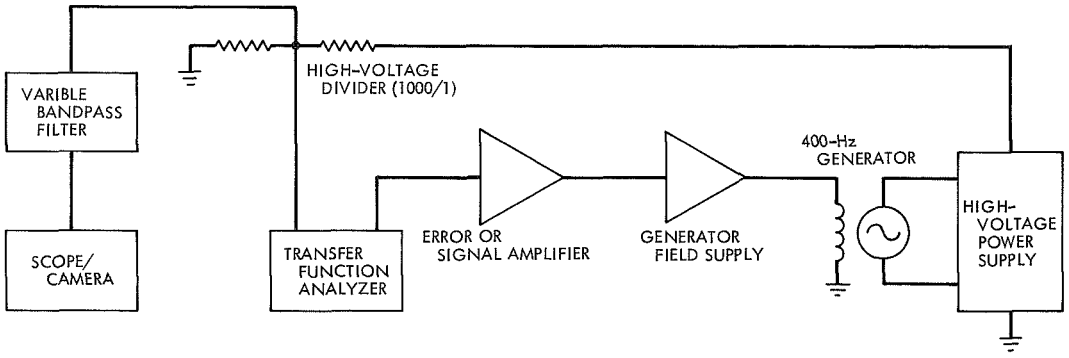

Fig. 9. High-voltage system test configuration

Data taken after a compensating network was installed in the error amplifier showed ripple to be reduced to approximately 0.2%, worst case, at the frequencies concerned. Phase-gain characteristics were improved with the phase margin now greater than 50 deg and gain at unity or less.

Further spectrum tests (Fig. 8b) showed that the sidebands had been reduced significantly.

4. Antenna Acceleration: Impact Damage Modifications, *V. Lobb*

As discussed in SPS 37-48, Vol. II, pp. 139–142, a deceleration–impact damage investigation revealed structural clip damage and failures developing in the hour-angle wheel counterweight cage support areas of DSSs 11, 12, 41, and 51. From this investigation, a change was instigated to modify all the antennas in the DSN. After engineering and prototype development, modification kits were procured that consisted of A490 high-strength bolts, welded-plate assemblies, and individual clips. The modifications were accomplished at DSSs 11, 12, 41 and 51 during the upgrades of these DSSs.

The first implementation, accomplished under an Engineering Change Order, was at DSS 42. For this implementation, DSS 42 was out of service from January 15 to February 15, 1970. This modification was completed in the polar-wheel counterweight cage area and consisted of the following:

(1) Removal of ladders and braces in the work area.

(2) Removal of the face plate in the areas to be modified by burning that section free.

(3) Removal of the counterweight billets behind the face plate and marking them for future reinstallation.

(4) Removal of the existing clips, brackets, and bolts.

(5) Cutting and modifying of areas and sections of the existing members to engineering documentation.

(6) Setting and tack welding the new welded assemblies and clips in place.

(7) Installing new A490 bolts in the clips and welded assemblies. In addition to the bolting, heavy welds were used to tie the new assemblies and clips to the existing members.

(8) Replacing the counterweight billets.

(9) Replacing the face plate and rewelding it where it was burned.

This installation was performed as a joint effort of the cognizant operations and cognizant development engineers. This was done to provide a training period for this modification that would enable the cognizant operations engineers to implement the modification at DSS 61 and DSS 62, which are planned for installation late this year. The DSS 12 antenna modification (and others throughout the DSN) has been subjected to service conditions for more than 2 yr, and, to date, the modified areas exhibit no evidence of fatigue or wear.

5. Clock-Sync Antenna Installation at the U.S. Naval Observatory, *W. Kissane*

With the mechanical installation of a clock-sync receiving antenna at the U.S. Naval Observatory in Washington, D.C. (Fig. 10), that government facility is now capable of receiving coded timing signals from the DSS 13 30-ft-diam antenna.

During the early part of January 1970, U.S. Naval Observatory personnel installed a steel fabricated platform on the roof of the Time Service Building so that the

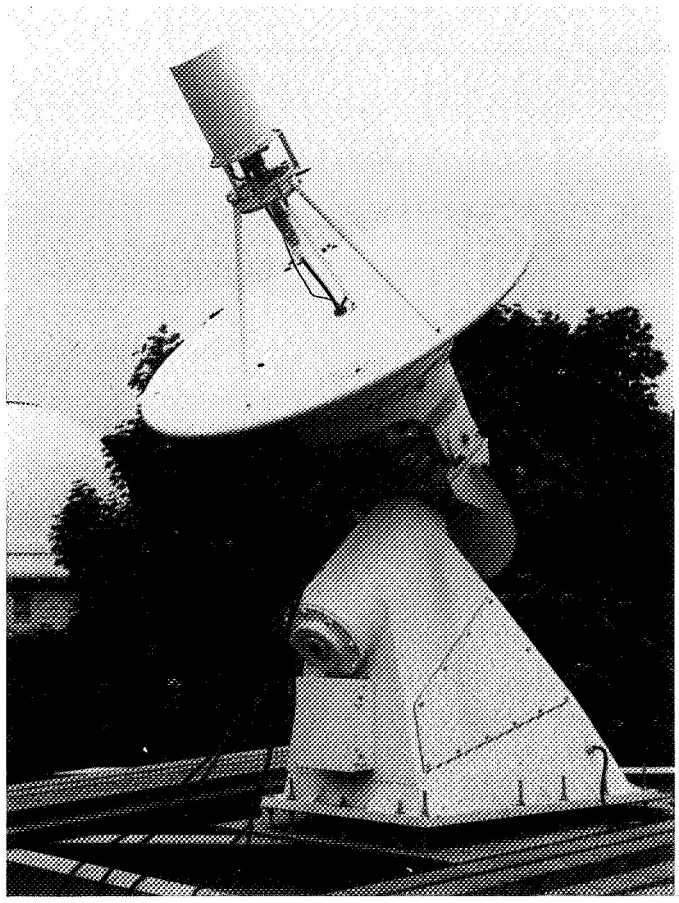

Fig. 10. Clock-sync receiving antenna installation (4-min phase)

antenna could be as close as possible to the frequency and timing subsystem hardware and still be protected from the interference of unauthorized personnel.

In early March 1970, JPL Antenna Engineering personnel supervised the mechanical installation of the clock-sync antenna utilizing U.S. Naval Observatory personnel. JPL-developed optical procedures[1] and optical sighting of Polaris (Ref. 1) were used for the final alignment of the antenna. The antenna was aligned to within 30 s of arc of the true station latitude and meridian.

The antenna is located at the following coordinates:

(1) *Astronomical*
Latitude N 38°55′11.″48
Longitude W 77°03′53.″66

(2) *Geodetic*
Latitude N 38°55′13.″50
Longitude W 77°03′59.″72

(3) *Elevation*
287.0 ft above mean sea level

The astronomical coordinates of the photographic zenith tube at the U.S. Naval Observatory were used in determining the position of the antenna. East–west and north–south distances from the photographic zenith tube and Station A of the clock-sync antenna were measured. Using conversion factors (Ref. 1), the astronomic location of the antenna was determined. The photographic zenith tube is located 592 ft north and 156 ft west of the antenna.

The geodetic coordinates of the satellite camera, located 25 ft due south of the antenna, and conversion factors (Ref. 1) were used to determine the geodetic position of the antenna.

The elevation of the antenna centerline was measured to the ground contour and was determined using the U.S. Geological Survey map of Washington, D.C. The map shows the ground elevation at this point to be 260 ft above mean sea level. The antenna centerline was found to be 27 ft above the ground for the satellite camera (the map was dated 1956, polyconic projection, 1927 North American datum).

At a later date, U.S. Naval Observatory personnel will install a wooden platform and railing on the antenna steel platform, trim the pedestal attach bolts, and grout between the steel fabricated platform and the antenna pedestal.

At the completion of antenna installation, a 360-deg horizon mask of the area was measured from the antenna centerline and forwarded to the JPL DSIF Digital Systems Development Section.

Reference

1. *Manual of Second and Third Order Triangulation*, Special Publication 145, U.S. Department of Commerce Coast and Geodetic Survey, Washington, D.C.

[1]JPL Procedure DOA-1336-TP B (JPL internal document).

6. DSS 51 Antenna Mechanical Subsystem Upgrade,

J. Carpenter, V. Lobb, A. Nicula, and D. Nelson

The antenna mechanical subsystem upgrade at DSS 51, as with the other upgrades at DSSs 11, 12, and 41, was implemented to restore the original specification agreement relative to the addition of the declination wheel electronics house, provide for the use of acquisition patterns and snap-on tests, increase tracking coverage, and attain a stiffer structure for S-band tolerances and thereby

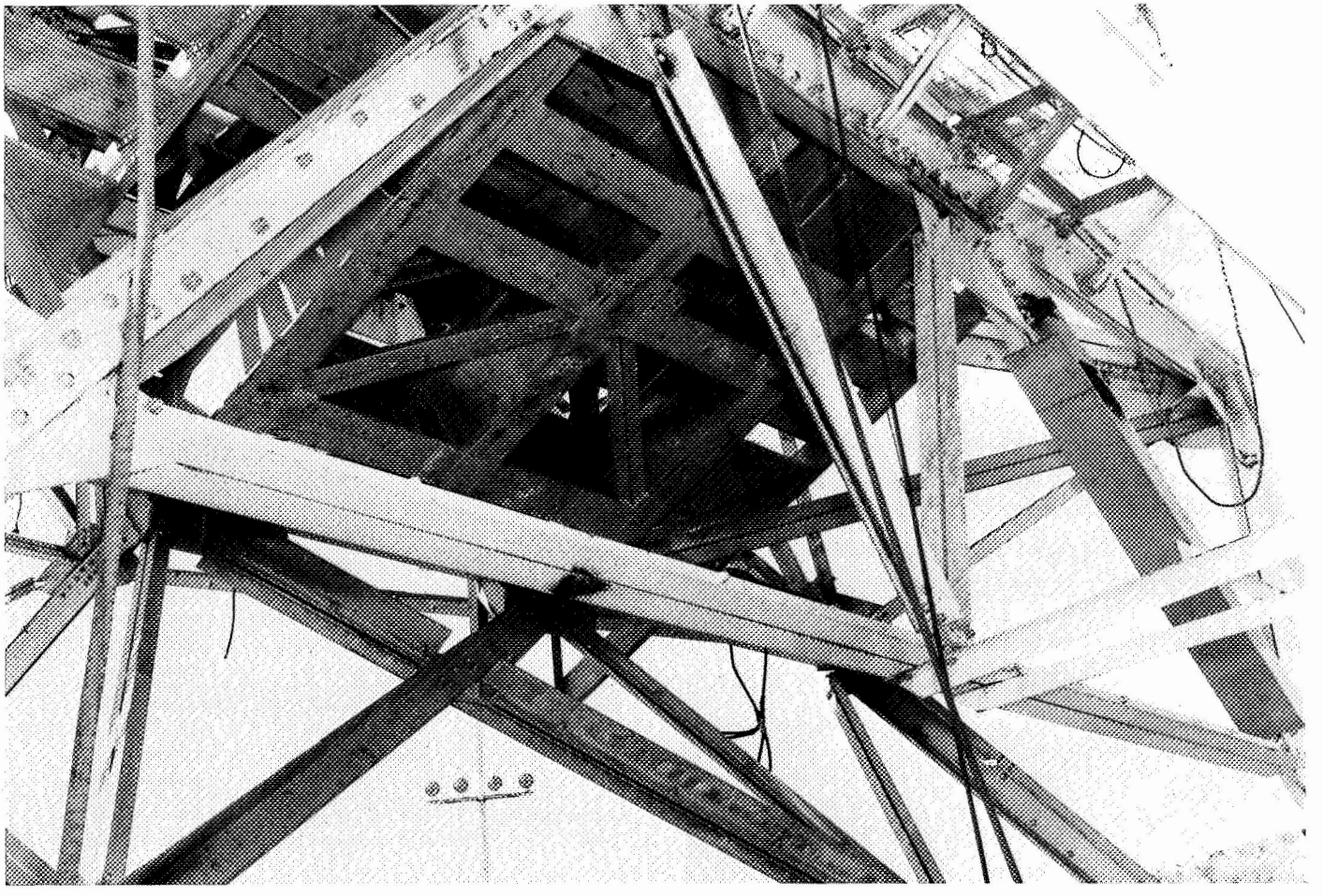

Fig. 11. Pedestal structure stiffening

achieve compatibility with the four-legged antennas at DSSs 42, 61, and 62.

The upgrade was started by JPL and DSS 51 personnel on September 2, 1969 by stripping all equipment, cables, cable trays, and coolant lines from the DSS 51 85-ft-diam antenna structure. This phase of the upgrade was required to be completed prior to commencement of the contracted work.

The contracted phase of the upgrade, started on September 8, 1969 and performed by a steel-erection company under the direction of JPL representatives, covered the following work:

(1) The addition of structural steel to decrease the antenna structure's deflections. This was done in the antenna pedestal and hour-angle and declination-angle wheels. One hoop row near the edge of the reflector structure also was stiffened (Figs. 11 and 12).

(2) Replacement and alignment of all drive skids and resetting of drive gears to increase tracking coverage by 12 deg (Table 1).

(3) Rebolting of the complete structure with ASTM A490 high-strength bolts to reduce structural hysterisis effects on tolerances and to minimize structural joint slippage (Fig. 13).

(4) The addition of 18,000 lb of lead for counterbalancing the antenna.

(5) Replacement of all cable trays on the antenna (Fig. 14).

This phase of the upgrade was completed on November 22, 1969.

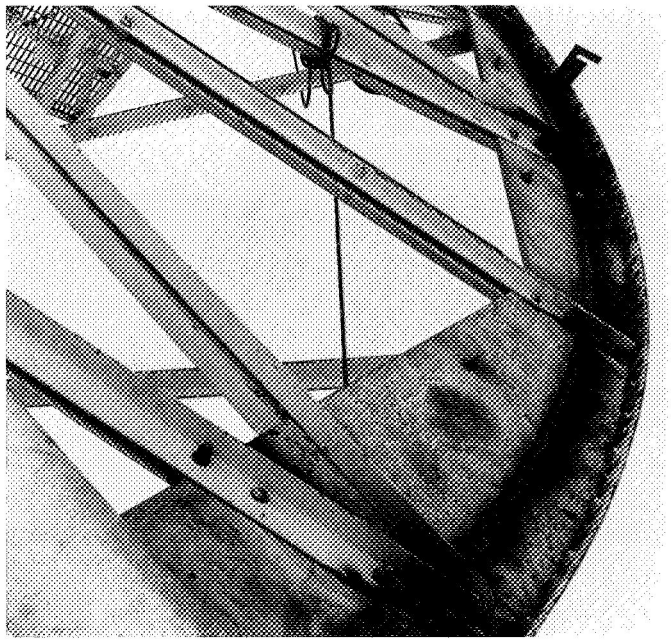

Fig. 12. Hour-angle wheel stiffening

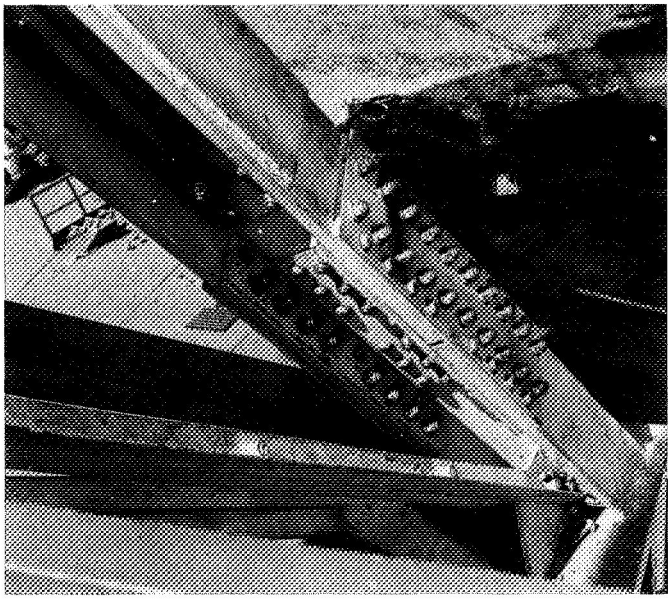

Fig. 13. Structural rebolt

The final phase of the upgrade was started by JPL and DSS 51 personnel on November 24, 1969 and covered the following work:

(1) Fabrication and installation of improved hydraulic drive assemblies on both hour-angle and declination axes (Fig. 15).

Table 1. DSS 51 upgrade acceptance test data

Item	Specification requirement	Actual achievement
Reflector surface		
Manufacturing	0.060 in. rms	< 0.060 in. rms
Setting at zenith	0.060 in. rms	< 0.040 in. rms
Counter balance		
Hour angle		500 lb maximum (counter weight heavy)
Declination		800 lb maximum (dish heavy)
Total in-line read-out of gears		
Hour angle	0.030 in.	0.030 in.
Declination	0.030 in.	0.025 in.
Running clearances		
Hour Angle	0.050/0.100 in.	0.035/0.058 in.
Declination	0.025/0.050 in.	0.040/0.068 in.
Cone ring alignment	6-3/8 ± 1/32 in. above vertex ring attach holes to be concentric within 0.060 in. with dish mechanical axis	6-3/8 above vertex concentric within 0.050 in. and parallel within 0.030 in. with dish datum plane
Hyberbola alignment	Concentric within 0.030 in. and parallel within 1 min of arc	Hyperbola axis is coincident within 0.025 in. with reflector mechanical axis
Optical tracking aid	Within 10 s of arc with dish mechanical axis	+3.5 s of arc in declination and +7.8 s of arc in hour angle
Optical acquisition aid	Within 10 s of arc with mechanical axis	−6.3 s of arc in declination and +5.8 s of arc in hour angle
Dish mechanical axis primary datum plane	13.00 in. above vertex parallel within 10 s of arc with declination axis of rotation	13.00 above vertex parallel within 7 s of arc with dec. axis of rotation
Secondary datum plane	Parallel within 5 s of arc with primary datum plane	Parallel within 5 s of arc

(2) Installation, rerouting, connection, and checkout of all antenna-mounted cables (Fig. 16).

(3) Replacement of all antenna-mounted equipment, such as the receiver racks, maser, junction boxes, wave guides, etc.

(4) Rerouting and replacement of all transmitter and air-conditioning coolant lines (Fig. 14).

(5) Repair and replacement of the antenna-mounted, acquisition-aid antenna (Table 1).

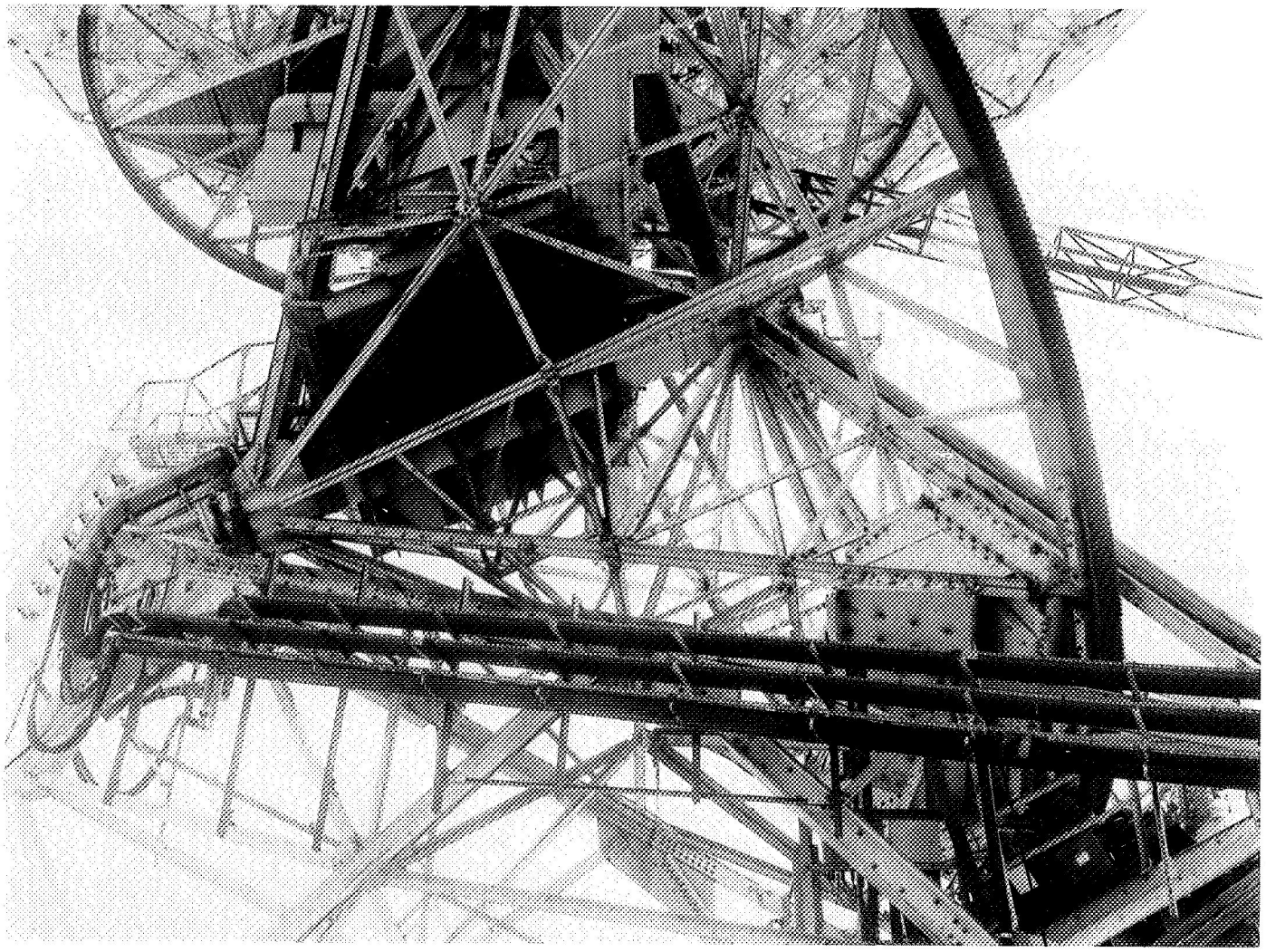

Fig. 14. Cable tray layout

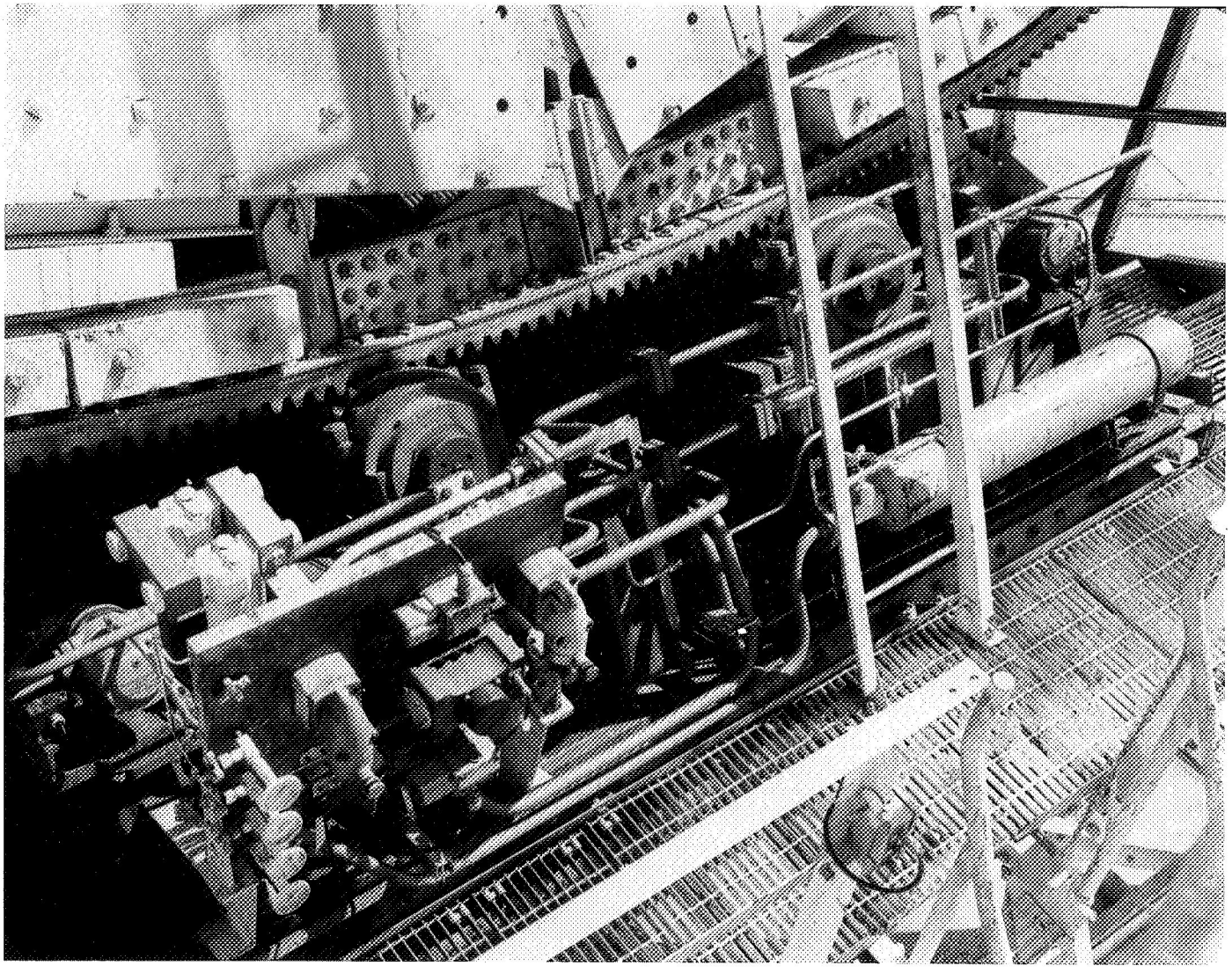

Fig. 15. Typical hydraulic drive assembly

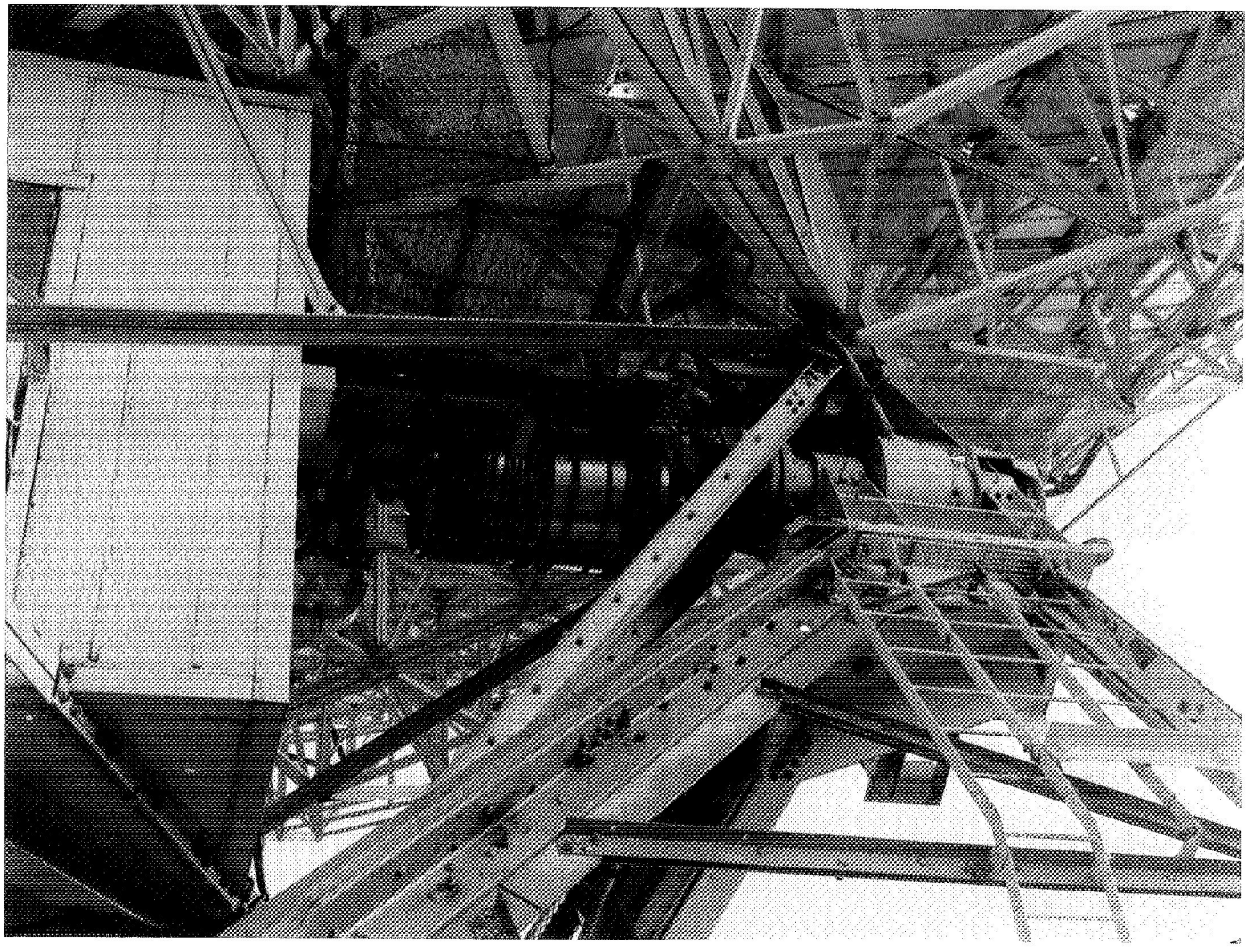

Fig. 16. Typical cable installation

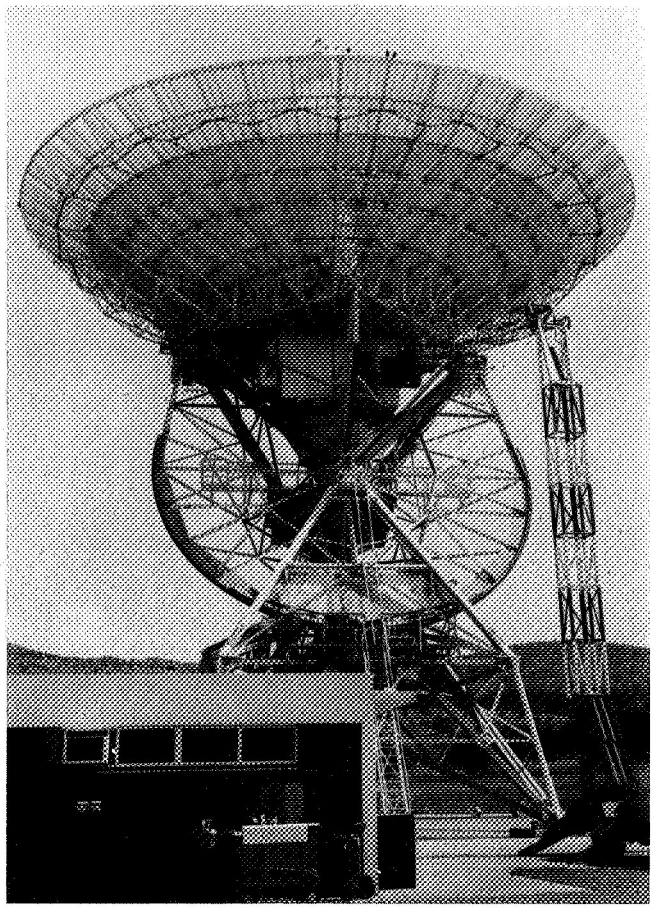

Fig. 17. Upgraded antenna

(6) Optically measuring and resetting the antenna surface panels to a deviation of less than 0.040 in. rms relative to S-band tolerances (Table 1).

(7) Optical alignment of the cassegrain system (Table 1).

(8) Installation of optical targets to a gravity reference for future verification measurements of surface rms deviation (Table 1).

(9) Running new antenna-mounted coax cables to replace the existing 15 cables plus five additional spare coax cables.

This final phase of the upgrade, with the exception of servo hydraulic testing, was completed on December 31, 1969 and the antenna was turned over to the subsystem engineers for systems integration tests (Fig. 17).

The servo hydraulic testing was started on January 4, 1970, along with the systems integration tests, and covered the following:

The hydraulic upgrade at DSS 51 was mated to the electronics upgrade approximately 1 yr earlier. The hydraulic installation included five major units: (1) declination skid assembly, (2) hour-angle skid assembly, (3) main electrical controller assembly, (4) hydraulic power unit assembly, and (5) heat exchanger assembly. The latter three assemblies were tested in conjunction with each other. The skids were checked for leaks, as were the replumbed lube subassemblies on the skids. The operation of the five assemblies was adjusted, tested, and found to be satisfactory. As part of a previous modification, only one tachometer had been installed in high and low speed of each axis; this oversight was corrected.

The complete subsystem was checked out and tested in accordance with JPL test procedure TP1078 to verify conformance with JPL detail specification DOA 1146-DTL A. All parameters of the specification were met, with the exception of the high-speed position loop response in both axes. This problem exists at other sites and is under investigation at DSS 11. The probable outcome of this investigation will be to reduce the specification requirements to a more realistic value. As part of running the test procedure, the hydraulic counterbalance valves were adjusted to provide anti-backlash with the existing structural unbalance, the limit switch contour was checked and reset where necessary, and one of the emergency disable stations was repaired.

V. Operations and Facilities

A. DSN Operations

1. Network Allocation Schedules, *D. G. Tustin*

a. Introduction. The Network Allocation Schedules are a part of the DSN Operations and Analysis function, and are the means by which all operational activities of the Deep Space Network are committed and scheduled.

The need for a means of scheduling the network at varying levels of detail and time became apparent several years ago. With the scheduling methods then in use, it was not possible to commit support and schedule activities more than several weeks in advance. Under these conditions it was impossible to size the network and/or user's requirements far enough in advance for proper replanning of support or activities when a conflict occurred. The Network Allocation Schedules described in this article have been instrumental toward solving this problem.

b. Function. The Network Allocation Schedules provide the means of sizing the network and committing its resources to the various users. These commitments are made far enough in advance, and iterated enough times, to allow for adjustment in the resources (i.e., staffing) and/or changes in the user's basic project design, thus compensating for any period when the requirements exceed the base resources. Under this system, when the time of the planned activity is reached, the resources necessary for adequate support are available with no need to make last minute changes in plans, nor is there a large quantity of unused resources remaining idle.

c. Elements. The Network Allocation Schedules consist of four levels of schedules involving ever-increasing detail regarding time and equipment required, and covering ever-decreasing periods of time. In addition, provisions exist to change any of the levels as required and these changed data are recorded, creating a file of historical data.

The levels of schedules are (1) the 130-Week Network Loading Schedule, (2) the 72-Week Network Allocation Schedule, (3) the 8-Week Operations Planning Schedule, and (4) the 7-Day Operations Schedule; their relationship as to detail, vis-a-vis time period covered, is shown in Fig. 1.

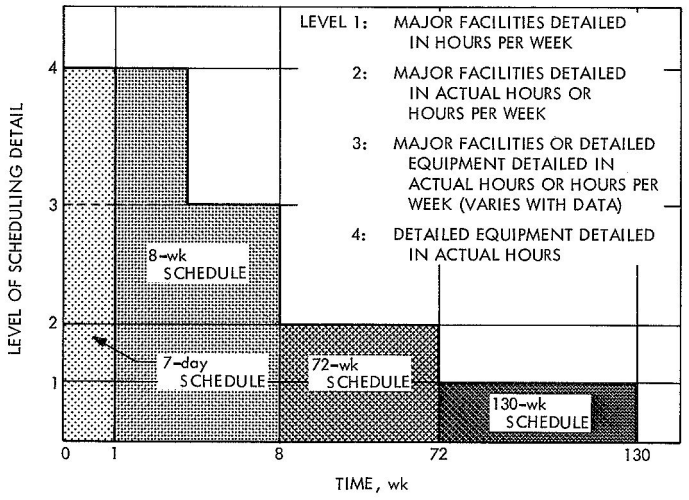

Fig. 1. Comparison of level of scheduling detail to time

d. Schedule operations. The interrelationship of the schedules and the general purpose of each can best be shown by beginning with the 130-week schedule and progressing to the 7-day schedule.

As each schedule is generated and published, it becomes the base from which the next schedule is constructed. Herein lies the key to the system. Once the requirements and resources have been sized, they are carried from one schedule to the next, requiring only some small adjustment as the detail increases.

The 130-Week Network Loading Schedule deals only with major resources (i.e., antennas, major computers, etc.) in hours per week per user, or tracks per week per user, in the case of the antennas. (When the tracks per week figure is used, it is assumed that a track equals 12 h of data acquisition or testing and includes any necessary pre- and post-track setup and calibration time.) The track allocation is based upon spacecraft view periods (trajectories), either actuals or nominals, thus avoiding a major conflict in a near-time period. With the requirements known, the staffing can now be adjusted and/or the requirements negotiated until a workable schedule is reached. This schedule is published as a part of the DSN support commitment for each project, thus allowing the project to make any necessary changes in plans well in advance of the requirement.

The above schedule, when published, becomes the basis for the 72-Week Network Allocation Schedule. This schedule expands the tracks and any other time-sensitive item to the actual day and time, and continues to carry the other items as hours per week. The level of detail for the equipment remains at major resources although a user may input a detailed equipment configuration for use in the later schedule if it is known. This schedule, when published quarterly, becomes a more detailed commitment to the network users, and is a direct input to the next level of scheduling.

The 8-Week Operations Planning Schedule takes its inputs directly from the 72-wk schedule and expands them to the maximum time and equipment configuration detail available. All activities that are missing this detail are flagged and the network users are given 3 wk to complete their planning and submit their detailed requirements. The 8-wk schedule is then published a second time showing all activities with the maximum detail as required for actual network operations. Any activities that are still deficient in detailed information are dropped from the schedule.

Every 7 days, a week is removed from the latest 8-wk schedule, updated with any last minute changes, and published as the 7-Day Operations Schedule. This schedule is used by the first level operational personnel to configure and operate the network in support of the users.

Throughout this process, changes in requirements and resources occur. When these changes are implemented into the schedules, they are also recorded in a history data bank. This data bank can then be used to determine network utilization, user planning ability, and many other items useful to management for planning and budgetary purposes.

e. Conclusion. The Network Allocation Schedules represent a large step forward for the DSN in resource management, resource commitment, and scheduling. Although the system is still growing, with new uses devised and requirements levied, it has already proven its worth both in long-range planning and near-real-time support by identifying major problems far enough in advance to allow for orderly solution and implementation. These schedules are currently being used as a model by another tracking network for the upgrading of their scheduling system.

B. SFOF Operations

1. SFOF *Mariner* Mars 1971 Mission Support Area,

B. M. Hayes

The *Mariner* Mars 1971 Mission Support Area in the SFOF has been functionally specified and the configuration determined (Fig. 2). The architectural and electrical designs for wall modifications and for the electrical power distribution system within the Mission Support Area have been completed.

To meet the required occupancy date requested by the *Mariner* Mars 1971 Project, a well-defined implementation schedule was developed. This schedule took into consideration the necessary approval cycles, installation of the new IBM 360-75 data systems (known as Mark III A), and facility construction. Before any of these events could occur, several other events that had an impact on these had to be resolved and performed. These events were: the relocation of the Flight Path Orbital Display Board, the relocation and combining of the *Mariner* Mars 1969 Extended Operations Mission and the *Pioneer VI* through *IX* Mission Support Areas, and providing an interim area for the checkout of the IBM 360-75 data system devices.

The schedule reflected the start of construction on June 10, 1970, with occupancy by the *Mariner* Mars 1971 Project on January 1, 1971. All of the construction, equipment installation, development testing, and systems checkout must be accomplished between these dates.

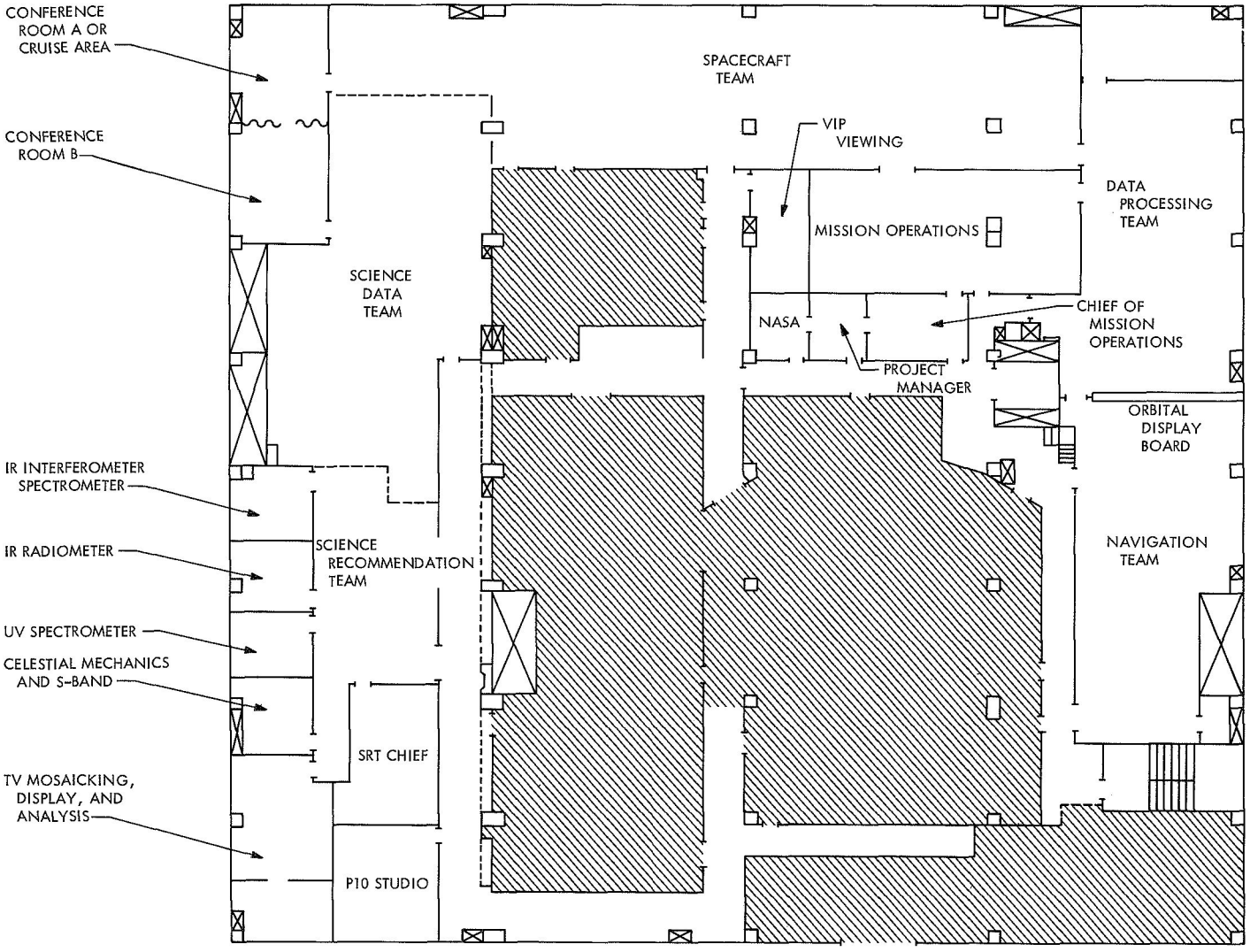

Fig. 2. *Mariner* Mars 1971 Mission Support Area

The *Mariner* Mars 1971 Project was asked to provide early inputs reflecting the types and numbers of IBM 360-75 devices required, and to define a Mission Support Area floor plan based on the requirements specified in the NASA Support Instrumentation Requirements Document. Certain constraints were placed on the *Mariner* Mars 1971 Project which were used as a guide in this planning. These were in the areas of building code, safety, equipment access, personnel access, cable runs, electrical power, communications, acoustics, and lighting.

The *Mariner* Mars 1971 mission operations area contains the following distinct sub-areas: Navigation Team, Data Processing Team, Spacecraft Team, Mission Operations, Science Data Team, Science Recommendation Team (SRT), Cruise, and the Public Information Office (PIO) studio. Additional space is also defined in these areas for a conference room, VIP viewing, NASA, Project Manager, and the Chief of Mission Operations. This Mission Support Area utilizes 13,600 ft^2 of space in the SFOF. The physical arrangement of the mission operations and analysis areas is based upon previous *Mariner* project operations and the utilization of the new Mark III A data systems. The Mission Operations room, Data Processing Team room, Navigation Team room, Spacecraft Team room, and Science areas have been located to provide a maximum degree of interaction and communication. Emphasis was placed on the maximum utilization of glass in all areas to provide the desired visual communication between these areas. The Mission Operations room will again feature one of the round six-man conference consoles used very successfully for the previous *Mariner*, *Surveyor*, and *Pioneer* mission operations. The Project Manager and Chief of Mission Operations are positioned so that they can observe all operations when necessary, but can remain separated from the operations when desired. A viewing room will permit visitors a direct view of Mission Operations and the Spacecraft Team areas from outside of these immediate areas. The Spacecraft Team room utilizes consoles for the two spacecraft team leaders and spacecraft team chief. Desks and tables have been provided for the 28 analysts. The Navigation Team room remains unchanged from previous missions with the exception of the Flight Path Orbital Display Board, which has been relocated to provide better visibility to personnel of the Navigation Team. The Science Data and Science Recommendation Team rooms provide individual, distinct rooms for the various science experimenters. Analysts and experimenters in all of the individual team areas will be provided with desks and tables.

A PIO studio is being designed for utilization during orbital operations. This PIO studio will be similar to the one used by the experimenters during the *Mariner* Mars 1969 encounter operations. An operations console will be provided which contains a switching capability to provide real-time television output to commercial television and other portions of the Laboratory. Experience gained during the *Mariner* Mars 1969 encounter operations dictated that early planning was necessary in order to eliminate the last minute problems that occurred. Emphasis will be placed on an increased working space at the console, the utilization of the special effects generator, and hard copy camera location and lighting. The room has also been designed for optimum acoustics which was a major problem during the *Mariner* Mars 1969 encounter operations.

Communications within the entire *Mariner* Mars 1971 Mission Support Area will be accomplished through the use of the voice communications network and closed circuit television. The closed circuit television will be utilized for the dissemination of digital formatted data from the IBM 360-75, time display, updated sequence of events information, as well as display of many individual elements of teletype information.

Subject Index

Subject — **Pages**

Antennas and Transmission Lines
- precision compact rotary vane attenuator 67–69
- system operating noise temperature calibrations of low noise cones 69–70
- thirty-degree reflector mockup study: comparisons of measured and predicted deflections 74–79
- deep space station antenna repairs 97
- clock-sync antenna installation at U.S. Naval Observatory 97–98
- Johannesburg Deep Space Station antenna mechanical subsystem upgrade 98–104

***Apollo* Project**
- Deep Space Network support 7–11

Computer Applications and Equipment
- effective computing power of computer memory 30–32
- numerical interactive controller for digital video display system 35–38
- multiple-mission sequential decoder interface buffer 53–55
- computer-assisted acquisition 59–60
- Deep Space Instrumentation Facility monitor system development 87
- telemetry simulation conversion assembly 88–95

Earth Atmosphere
- charged-particle calibration system analysis 13–21
- ionospheric electron content determined from faraday rotation measurements of an earth satellite and a deep-space probe 21–24
- evaluation of ionospheric model 25–27

Electronic Components and Circuits
- multiple-mission sequential decoder interface buffer 53–55
- planetary ranging demodulator 71–74

Facility Engineering
- Venus Deep Space Station operations 70–71
- Space Flight Operations Facility mission support area for *Mariner* Mars 1971 Project 107–108

Information Theory
- mean-square error and bias of phase estimator for sequential ranging system 27–28
- the asymptotic complexity of the Green decoding procedure 29
- effective computing power of computer memory 30–32
- minimum switching network for generating the weight, in binary notation of a binary vector 33–35

Subject — **Pages**

Information Theory (contd)
- digital acquisition and detection: solution of a Toeplitz set of linear homogeneous equations 38–41
- performance of short constraint length convolutional codes and a heuristic code-construction algorithm 41–44
- synchronizability of convolutional codes 44–50
- comparing performance of three rate ½, $K = 32$ codes 50–52

Management Systems
- Deep Space Network allocation schedules 105–106

***Mariner* Mars 1969 Project**
- Venus Deep Space Station support of extended mission project 70–71
- transmitter phase modulation as a result of beam voltage ripple in *Mariner VII* signal 96–97

***Mariner* Mars 1971 Project**
- Deep Space Network support 4–7
- Space Flight Operations Facility mission support area 107–108

***Mariner* Venus 67 Project**
- ionospheric effect on *Mariner V* mission 25–27

Mathematical Sciences
- solution of a Toeplitz set of linear homogeneous equations 38–41
- theorems for synchronizability of convolutional codes 44–50

Quality Assurance and Reliability
- welded joint integrity study 79–86

Radar
- Venus Deep Space Station planetary radar experiments 70–71

Solar Phenomena
- charged-particle calibration system analysis 13–21

Standards, Reference
- clock-sync antenna installation at U.S. Naval Observatory 97–98

Structural Engineering
- welded joint integrity study 79–86
- deep space station antenna repairs 97

Telemetry and Command
- Deep Space Network support of *Mariner* Mars 1971 Project 4–7
- Deep Space Network support of *Apollo* Project 7–11
- charged-particle calibration system analysis 13–21
- mean-square error and bias of phase estimator for sequential ranging system 27–28

Subject	Pages
Telemetry and Command (contd)	
the asymptotic complexity of the Green decoding procedure	29
minimum switching network for generating the weight, in binary notation, of a binary vector	33–35
digital acquisition and detection: solution of a Toeplitz set of linear homogeneous equations	38–41
performance of short constraint length convolutional codes and a heuristic code-construction algorithm	41–44
synchronizability of convolutional codes	44–50
comparing performance of three rate ½, $K = 32$ codes for multiple-mission sequential decoder	50–52
frequency generation and control: measurement of phase jitter	55–58
computer-assisted acquisition	59–60
loop stress diminution	61–67
Telemetry and Command (contd)	
telemetry simulation conversion assembly	88–95
Test Facilities and Equipment	
thirty-degree reflector mockup	74–79
welded joint integrity test equipment	79–86
telemetry simulation conversion assembly	88–95
Tracking	
Deep Space Network support of *Mariner* Mars 1971 Project	4–7
Deep Space Network support of *Apollo* Project	7–11
charged-particle calibration system analysis	13–21
mean-square error and bias of phase estimator for sequential ranging system	27–28
Wave Propagation	
frequency generation and control: measurement of phase jitter	55–58
loop stress diminution	61–67
transmitter phase modulation as a result of beam voltage ripple	96–97

NASA — JPL — Coml., L.A., Calif.